Bicycle tyre lateral characteristics and their effect on bicycle dynamics

Dell'Orto, G.

DOI
10.4233/uuid:dc549b99-0b00-4f24-995b-94a44cbf5caa

Publication date
2025

Document Version
Final published version

Citation (APA)
Dell'Orto, G. (2025). *Bicycle tyre lateral characteristics and their effect on bicycle dynamics*. [Dissertation (TU Delft), Delft University of Technology]. https://doi.org/10.4233/uuid:dc549b99-0b00-4f24-995b-94a44cbf5caa

Bicycle tyre lateral characteristics and their effect on bicycle dynamics

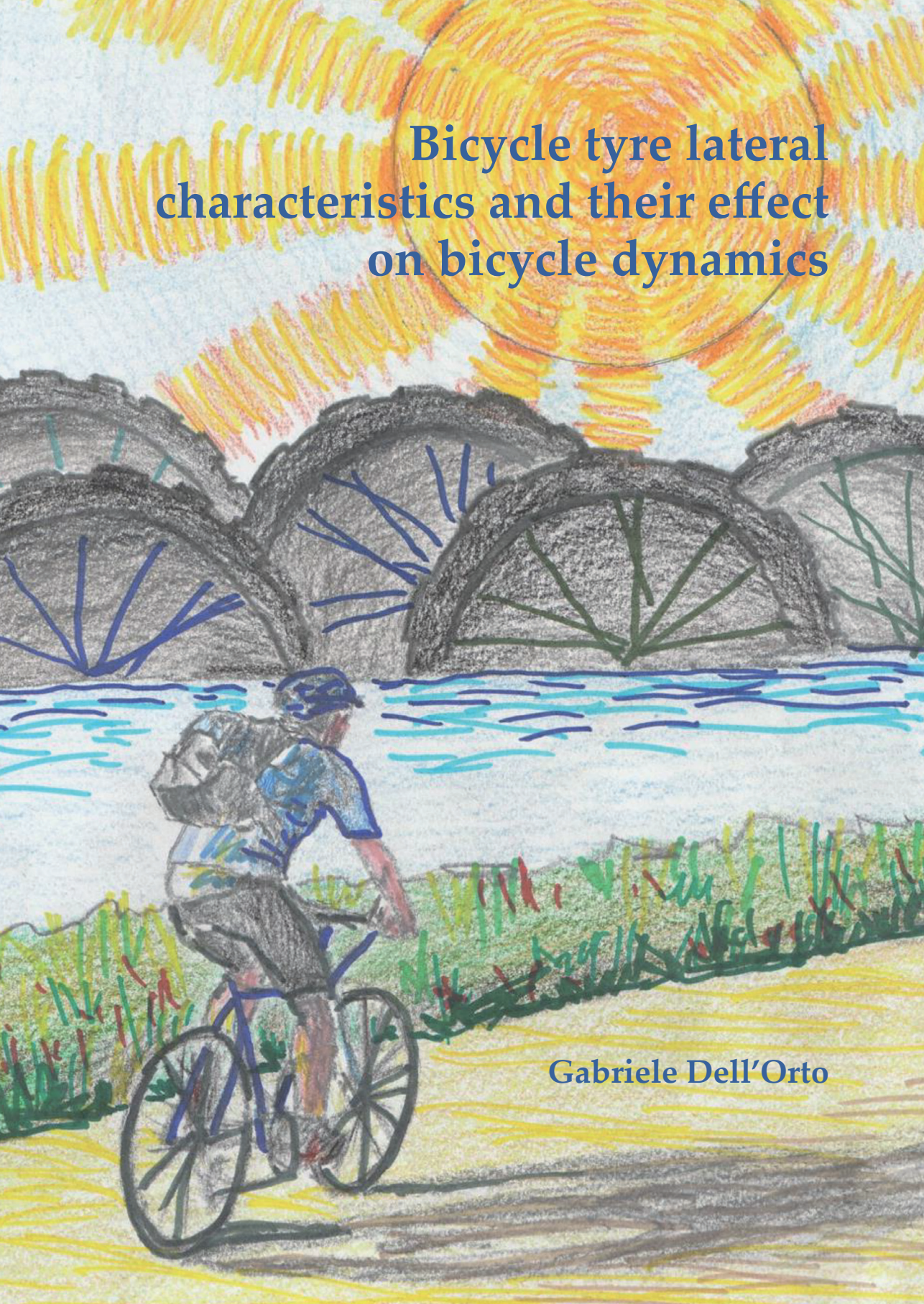

Gabriele Dell'Orto

BICYCLE TYRE LATERAL CHARACTERISTICS AND THEIR EFFECT ON BICYCLE DYNAMICS

This dissertation has been approved by the promotors.

Promotor:	Prof.dr.ir. R. Happee
Promotor	Prof.dr. G. Mastinu
Copromotor	Dr. J.K. Moore

Composition of the doctoral committee:

Rector Magnificus	chairperson
Prof.dr.ir. R. Happee	Delft University of Technology, promotor
Prof.dr. G. Mastinu	Polytechnic of Milan, Italy, promotor
Dr. J.K. Moore	Delft University of Technology, copromotor
Independent members:	
Dr.ir. I.J.M. Besselink	Eindhoven University of Technology, The Netherlands
Prof.dr. F. Van der Helm	Delft University of Technology, The Netherlands
Prof.dr. I. Kageyama	Nihon University, Japan
Dr. M. Rothhämel	KTH Royal Institute of Technology, Sweden
Reserve member:	
Prof.dr.ir. M. Wisse	Delft University of Technology, The Netherlands

The doctoral research has been carried out in the context of an agreement on joint doctoral supervision between Polytechnic of Milan, Italy and Delft University of Technology, the Netherlands

Keywords:	Tyre, test-rig, lateral characteristics, bicycle dynamics
Printed by:	ProefschriftMaken.nl
Covers:	Gianmario Rosson Original images

ISBN 978-94-6518-014-4

An electronic version of this dissertation is available at

http://repository.tudelft.nl/

BICYCLE TYRE LATERAL CHARACTERISTICS AND THEIR EFFECT ON BICYCLE DYNAMICS

Dissertation

for the purpose of obtaining the degree of doctor
at Delft University of Technology
by the authority of the Rector Magnificus prof.dr.ir. T.H.J.J. van der Hagen
chair of the Board for Doctorates
to be defended publicly on
Tuesday February 25th, 2025 at 10:00 o'clock
by

Gabriele DELL'ORTO

Master in Mechanical Engineering, Polytechnic of Milan, Italy

To my beloved grandfather.

Summary

Bicycles are among the simplest and at the same time most fascinating vehicles. Despite their apparently basic design, their stability, dynamics, performance, and safety are still largely unknown. In a world where cities suffer from critical air pollution levels and are often congested by car traffic, bicycles can represent a cost-effective and ready solution to address part of the problem. However, the increasing use of bicycles enlarges the risk of bicycle-related accidents and injuries. Many of these accidents involve falls, highlighting the need of proper studies on bicycle-rider dynamics. While research has been conducted on the effect of bicycle parameters on the handling quality properties, we still do not know enough about the specific role of tyres on bicycle-rider dynamics. To better simulate what happens in the real world, existing bicycle mathematical models need to be integrated with robust tyre models that include side slip, as they can change both the lateral and longitudinal dynamics. Actually, the use of nonlinear tyre models allows taking into account the lateral force and self-aligning torque saturation. This is needed for instance to model the wobble as a non-divergent vibration modes, contrarily to what happens when using a simple linear tyre model. These features relate directly to predict critical situations for which we need a deep knowledge of bicycle tyres, thus proper test-rigs to measure their mechanical characteristics.

This dissertation aims to address the following research objectives:

1. To develop a new test bench to measure bicycle tyre lateral characteristics, in order to provide a tyre dataset to be used in bicycle dynamics studies.
2. To provide a robust tyre mathematical model that can be added to bicycle-rider models.
3. To quantify the effect of tyres on bicycle-rider dynamics, both experimentally and numerically.

The lateral characterisation of bicycle tyres is barely addressed in academic literature. Only a few test-rigs have been presented so far, for both indoor and outdoor testing. Although field tests usually feature a simpler implementation, they do not allow the tests to be repeatable, as external conditions may vary considerably. Indoor tests are instead performed on specific test-rigs and they allow measuring tyre characteristics with a good level of repeatability, in controlled environments. To fulfil the first objective of this dissertation, I present a novel indoor test-rig for bicycle tyres lateral characterisation (Chapter 3), named VeTyT (acronym of Velo Tyre Testing). It is made of an aluminium frame reinforced with steel cables and plates to increase its stiffness and carries a bicycle wheel on top of a drum or a flat track. Using VeTyT, I conducted an extensive experimental campaign on a 26 mm wide road racing tyre, to investigate the effects of inflation pressure, vertical force, rolling speed and rolling surface

temperature on the tyre's mechanical characteristics (Chapter 4). The temperature of the rolling surface turned out to be a parameter to keep under control during the tests, as it affected considerably the outcomes especially for what concerns the self-aligning torque. An increase in the temperature of the rolling surface from 35 °C to 70 °C caused a decrease in lateral force up to 16% and self-aligning torque up to 50%, for slip angles $|\alpha| \geq 3$ deg. These variations may cause unexpected bicycles behaviour, especially when turning on paved roads featured by the presence of shaded corners during summer days. To keep the temperature within a safety threshold during the tests – in the range from 22 °C to 33 °C, found to be acceptable as it did not affect the measurements – I implemented a cooling system and checked periodically the temperature of the flat track by means of a pyrometer and/or a thermocamera.

I also evaluated the relaxation length and twisting torque of road racing tyres (Chapter 5 and Chapter 6, respectively). The twisting torque refers to the self-aligning torque for null slip angle and non-null camber. It increases with the increase of the contact patch area, which results from a larger vertical load and/or a lower pressure. Based on this, I proposed a theoretical model to predict the twisting torque, given the knowledge of the contact patch area, wheel radius and camber angle. It provided promising results for camber angles up to 10 deg. Regarding the relaxation length, I compared the results for a 26 and a 28 mm wide tyre, showing that, even though 28 mm wide tyres can generate higher lateral force under larger vertical loads, their relaxation length is longer, meaning that they are less responsive than the 26 mm wide tyres.

The second objective of this dissertation sought to close the gap between experimental research and mathematical modelling (Chapter 7). I employed VeTyT to measure lateral characteristics of city/trekking and cargo bicycle tyres. Then, I used the Pacejka's Magic Formula to develop a simple yet robust tyre model valid for bicycle tyres. Although it was originally conceived for tyres subjected to much larger loads, the Magic Formula provided valuable results for camber angles up to 20 deg, when dealing with lateral force and self-aligning torque.

The third research objective sought to move a step forward towards the full exploitation of the just presented tyre model. Looking at the larger picture, it aims to transfer the knowledge from indoor testing of bicycle tyre to bicycle-rider tests and models, thus quantifying the effect of tyres on bicycle-rider dynamics. To do that, I conceived an experimental setup using a kickplate device, typically employed to train car drivers on circuits, to laterally perturb the rear wheel when the bicycle rides over a moving plate, each time with a different tyre inflation pressure (Chapter 8). I used the nonlinear Carvallo-Whipple bicycle-rider model, extended to include the nonlinear tyre model discussed above, and including side slip. The rider was incorporated using a steering torque generating controller. I ran simulations with different tyre inflation pressures, namely tyre characteristics. The experimental campaign with kickplate confirmed that the inflation pressure affected bicycle dynamics, especially the yaw rate (the most affected parameter) and roll rate. I used

the yaw rate decay to determine the best inflation pressure relative to the vertical load applied to the wheels, i.e. the rider's weight. There is an optimal pressure per each rider which allows recovering faster from lateral disturbances.

In this dissertation, I demonstrated the significant role tyres play on bicycle-rider dynamics. Starting from indoor testing to ending with bicycle-rider model simulations and outdoor tests with kickplate, I pushed the boundaries of our knowledge in both bicycle dynamics and bicycle tyres, exploring novel testing devices. This knowledge will hopefully help policymakers, manufacturers, and fellow researchers in advancing in the field and gaining insights to enhance cycling and improve people's daily lives.

Keywords: bicycle, bicycle tyres, dynamics.

Samenvatting

Fietsen behoren tot de eenvoudigste en tegelijkertijd meest fascinerende voertuigen. Ondanks hun ogenschijnlijk eenvoudige ontwerp, zijn hun stabiliteit, dynamica, prestaties en veiligheid nog grotendeels onbekend. In een wereld waar steden kampen met ernstige luchtvervuilingsniveaus en vaak verstopt raken door autoverkeer, kunnen fietsen een kosteneffectieve en bereikbare oplossing bieden om een deel van het probleem aan te pakken. De toenemende populariteit van fietsen brengt echter ook het risico van fiets-gerelateerde ongevallen en verwondingen met zich mee. Veel van deze ongevallen betreffen valpartijen, wat de noodzaak benadrukt van grondige studies naar de dynamiek van fiets en fietser. Hoewel er onderzoek is gedaan naar het effect van fietsparameters op de bestuurbaarheid, weten we nog steeds niet genoeg over de specifieke rol van banden in de dynamiek van fiets en fietser. Om beter te simuleren wat er in de echte wereld gebeurt, moeten bestaande wiskundige modellen van fietsen worden uitgebreid met robuuste bandmodellen die ook zijdelingse slip omvatten, aangezien dit zowel de zijdelingse als de longitudinale dynamiek kan veranderen. Het gebruik van niet-lineaire bandmodellen maakt het mogelijk om rekening te houden met de verzadiging van de zijdelingse kracht en het zelfuitlijningskoppel. Dit is nodig om bijvoorbeeld het wiel trillen te modelleren als een niet-divergerende vibratiemodus, in tegenstelling tot wat gebeurt bij het gebruik van een eenvoudig lineair bandmodel. Deze kenmerken zijn direct gerelateerd aan het voorspellen van kritieke situaties waarvoor een diepgaande kennis van fietsbanden nodig is, en daarmee de juiste testbanken om hun mechanische eigenschappen te meten.

Dit proefschrift is gericht op de volgende onderzoeksdoelen:

1. Het ontwikkelen van een nieuwe testbank om de zijdelingse eigenschappen van fietsbanden te meten, met als doel een dataset voor banden te verstrekken die kan worden gebruikt in studies naar de dynamiek van fietsen.
2. Het leveren van een robuust wiskundig bandmodel dat kan worden toegevoegd aan fiets- en fietser modellen
3. Het kwantificeren van het effect van banden op de dynamiek van fiets en fietser, zowel experimenteel als numeriek.

De zijdelingse karakterisering van fietsbanden wordt nauwelijks behandeld in de academische literatuur. Slechts enkele testbanken zijn tot nu toe gepresenteerd, zowel voor indoor als outdoor tests. Hoewel veldtesten meestal eenvoudiger uit te voeren zijn, bieden ze niet de mogelijkheid om tests te herhalen, omdat de externe omstandigheden aanzienlijk kunnen variëren. Indoor tests worden daarentegen uitgevoerd op specifieke testbanken en bieden de mogelijkheid om de bandkenmerken te meten met een goede mate van herhaalbaarheid in gecontroleerde omgevingen. Om

het eerste doel van dit proefschrift te vervullen, presenteer ik een nieuwe indoor testbank voor de zijdelingse karakterisering van fietsbanden (Hoofdstuk 3), genaamd VeTyT (acroniem voor Velo Tyre Testing). Het bestaat uit een aluminium frame dat is versterkt met stalen kabels en platen om de stijfheid te verhogen en het draagt een fietswiel bovenop een trommel of een vlakke baan. Met behulp van VeTyT heb ik een uitgebreide experimentele procedure uitgevoerd op een 26 mm brede racefietsband om de effecten van bandenspanning, verticale kracht, rijsnelheid en temperatuur van het roloppervlak op de mechanische eigenschappen van de band te onderzoeken (Hoofdstuk 4). De temperatuur van het roloppervlak bleek een parameter te zijn die tijdens de tests onder controle moest worden gehouden, aangezien deze de resultaten aanzienlijk beïnvloedde, vooral wat betreft het zelfuitlijningskoppel. Een verhoging van de temperatuur van het roloppervlak van 35 °C tot 70 °C veroorzaakte een afname van de zijdelingse kracht tot 16% en het zelfuitlijningskoppel tot 50% bij sliphoeken $|\alpha| \geq 3$ graden. Wanneer de sliphoeken $|\alpha| < 3$ graden waren, daalde de variabiliteit van de gemeten zijdelingse kracht tot 2%. Deze variaties kunnen onverwacht gedrag van fietsen veroorzaken, vooral bij het nemen van schaduwrijke bochten op verharde wegen op zomerse dagen. Om de temperatuur tijdens de tests binnen een veilig bereik te houden – tussen 22 °C en 33 °C, wat werd beschouwd als acceptabel omdat het de metingen niet beïnvloedde – implementeerde ik een koelsysteem en controleerde ik periodiek de temperatuur van de vlakke baan met behulp van een pyrometer en/of een thermocamera.

Ik heb ook de relaxatielengte en de wringkoppels van racefietsbanden geëvalueerd (respectievelijk Hoofdstuk 5 en Hoofdstuk 6). Wringkoppel verwijst naar het zelfuitlijningskoppel bij nul sliphoek en niet-nul camberhoek. Ik heb de resultaten vergeleken voor een 26 en een 28 mm brede band en aangetoond dat, hoewel 28 mm brede banden hogere zijdelingse krachten kunnen genereren onder zwaardere verticale belastingen, hun relaxatielengte langer is, wat betekent dat ze minder responsief zijn dan de 26 mm brede banden. Wat betreft het wringkoppel heb ik een theoretisch model voorgesteld om het te voorspellen, op basis van de kennis van het contactvlak, de wielstraal en de camberhoek. Het leverde veelbelovende resultaten op voor camberhoeken tot 10 graden.

Het tweede doel van dit proefschrift was om de kloof tussen experimenteel onderzoek en wiskundige modellering te overbruggen (Hoofdstuk 7). Ik gebruikte VeTyT om de zijdelingse eigenschappen van stads-/trekking- en vrachtfietsenbanden te meten. Vervolgens gebruikte ik de Magic Formula van Pacejka om een eenvoudig maar robuust bandmodel te ontwikkelen dat geldig is voor fietsbanden. Hoewel het oorspronkelijk was ontwikkeld voor banden die aan veel grotere belastingen worden onderworpen, leverde de Magic Formula waardevolle resultaten voor camberhoeken tot 20 graden bij het omgaan met zijdelingse kracht en zelfuitlijningskoppel.

Het derde onderzoeksdoel was om een stap verder te gaan in de volledige benutting van het zojuist gepresenteerde bandmodel. Met het oog op het grotere geheel is het

doel om de kennis van het indoor testen van fietsbanden over te dragen naar testen en modellen van fiets en fietser, en daarmee het effect van banden op de dynamiek van fiets en fietser te kwantificeren. Om dit te bereiken, ontwierp ik een experimentele opstelling met behulp van een kickplate-apparaat, dat doorgaans wordt gebruikt om automobilisten op circuits te trainen, om het achterwiel zijdelings te verstoren wanneer de fiets over een bewegende plaat rijdt, telkens met een andere bandenspanning (Hoofdstuk 8). Ik gebruikte het niet-lineaire Carvallo-Whipple model, uitgebreid met het hierboven besproken niet-lineaire bandmodel en inclusief zijdelingse slip. De fietser werd gemodelleerd met behulp van een stuurkoppelgenererende regelaar. Ik heb simulaties uitgevoerd waarbij ik telkens de bandkarakteristieken in het model varieerde, dus met verschillende Magic Formula parameters. De experimentele campagne met de kickplate bevestigde dat de bandenspanning de dynamiek van de fiets beïnvloedde, vooral de gier (yaw) snelheid (de meest beïnvloede parameter) en de rolbeweging. Ik gebruikte de afname van de gier (yaw) snelheid om de beste bandenspanning te bepalen in relatie tot de verticale belasting die op de wielen wordt uitgeoefend, d.w.z. het gewicht van de fietser. Voor elke fietser is er een optimale druk die een sneller herstel van zijdelingse verstoringen mogelijk maakt.

In dit proefschrift heb ik de belangrijke rol aangetoond die banden spelen in de dynamiek van fiets en fietser. Beginnend bij indoor tests en eindigend met fietser modelleringen en outdoor proeven met de kickplate heb ik de grenzen van onze kennis over zowel fiets- als bandendynamica verlegd door nieuwe testapparatuur te onderzoeken. Hopelijk zal deze kennis beleidsmakers, fabrikanten en medeonderzoekers helpen om vooruitgang te boeken op dit gebied en inzichten te verwerven die het fietsen kunnen verbeteren en het dagelijks leven van mensen kunnen veraangenamen.

Keywords: fietsen, fietsbanden, dynamiek.

Sommario

Le biciclette sono tra i veicoli più semplici e allo stesso tempo più affascinanti. Nonostante il loro design apparentemente semplice, la loro stabilità, dinamica, prestazioni e sicurezza sono ancora in gran parte oggetto di studio. In un mondo in cui le città soffrono di livelli critici di inquinamento atmosferico e sono spesso congestionate dal traffico automobilistico, le biciclette possono rappresentare una soluzione economica e immediata per affrontare parte del problema. Tuttavia, l'aumento dell'uso delle biciclette comporta il rischio di incidenti e infortuni. Molti di questi incidenti coinvolgono cadute, sottolineando la necessità di studi adeguati sulla dinamica del sistema ciclista-bicicletta. Sebbene siano state condotte ricerche sugli effetti dei parametri delle biciclette sulle proprietà di handling, non sappiamo ancora abbastanza sul ruolo specifico degli pneumatici nella dinamica del sistema ciclista-bicicletta. Per simulare meglio ciò che accade nel mondo reale, i modelli matematici esistenti di biciclette devono essere integrati con modelli di pneumatici robusti che includano lo slittamento laterale, poiché questi possono influenzare sia la dinamica laterale che longitudinale. L'uso di modelli non lineari di pneumatici consente infatti di tenere conto della saturazione della forza laterale e della coppia di autoallineamento. Ciò è necessario, ad esempio, per modellare il modo di vibrare di wobble (o shimmy) come una modo di vibrare non divergente, contrariamente a quanto accade utilizzando un semplice modello lineare di pneumatici. Queste caratteristiche sono direttamente correlate alla previsione di situazioni critiche per cui è necessaria una conoscenza approfondita degli pneumatici di biciclette, quindi dispositivi di test adeguati per misurare le loro caratteristiche meccaniche.

Questa tesi si propone di affrontare i seguenti obiettivi di ricerca:

1. Sviluppare un nuovo banco prova per misurare le caratteristiche laterali degli pneumatici di bicicletta, al fine di fornire un set di dati sugli pneumatici da utilizzare negli studi sulla dinamica del veicolo.
2. Fornire un modello matematico dei pneumatici robusto che possa essere aggiunto ai modelli ciclista-bicicletta.
3. Quantificare l'effetto dei pneumatici sulla dinamica del sistema ciclista-bicicletta, sia sperimentalmente che numericamente.

La caratterizzazione laterale degli pneumatici di biciclette è un argomento poco affrontato nella letteratura accademica. Finora sono stati presentati solo pochi banchi prova, sia per test indoor che outdoor. Sebbene i test outdoor siano generalmente più semplici da implementare, questi non consentono la ripetibilità dei test, poiché le condizioni esterne possono variare considerevolmente. I test indoor, invece, vengono eseguiti su banchi prova specifici e consentono di misurare le caratteristiche dei pneumatici con un buon livello di ripetibilità, in ambienti controllati. Per raggiungere

il primo obiettivo di questa tesi, presento un nuovo banco per prove indoor per la caratterizzazione laterale di pneumatici di bicicletta (Capitolo 3), conosciuto con il nome di VeTyT (acronimo di Velo Tyre Testing). È costituito da un telaio in alluminio rinforzato con cavi e piastre d'acciaio per aumentarne la rigidità e supporta una ruota di bicicletta su un tamburo o un flat track. Utilizzando il VeTyT, ho condotto una vasta campagna sperimentale su uno pneumatico da corsa su strada di larghezza 26 mm, per indagare gli effetti della pressione di gonfiaggio, della forza verticale, della velocità di rotolamento e della temperatura della superficie di rotolamento sulle caratteristiche meccaniche dello pneumatico (Capitolo 4). La temperatura della superficie di rotolamento si è rivelata un parametro da tenere sotto controllo durante i test, poiché ha influenzato notevolmente i risultati, in particolare per quanto riguarda la coppia di autoallineamento. Un aumento della temperatura della superficie di rotolamento da 35 °C a 70 °C ha causato una diminuzione della forza laterale fino al 16% e della coppia di autoallineamento fino al 50%, per angoli di slip $|\alpha| \geq 3$ gradi. Quando gli angoli di slip erano $|\alpha| < 3$ gradi, la variabilità della forza laterale misurata è scesa al 2%. Queste variazioni possono causare comportamenti inaspettati delle biciclette, specialmente quando si percorrono strade asfaltate caratterizzate dalla presenza di curve ombreggiate durante le giornate estive. Per mantenere la temperatura entro una soglia di sicurezza durante i test - nell'intervallo compreso tra 22 °C a 33 °C, ritenuto accettabile poiché non influiva sulle misurazioni - ho implementato un sistema di raffreddamento e controllato periodicamente la temperatura del flat track mediante un pirometro e/o una termocamera.

Ho anche valutato la lunghezza di rilassamento e la twisting torque degli pneumatici da corsa su strada (Capitolo 5 e Capitolo 6, rispettivamente). La twisting torque si riferisce alla coppia di autoallineamento per angolo di slittamento nullo e camber non nullo. Ho confrontato i risultati per pneumatici larghi 26 mm e 28 mm, dimostrando che, sebbene gli pneumatici di larghezza 28 mm possano generare una forza laterale maggiore sotto carichi verticali più pesanti, la loro lunghezza di rilassamento è maggiore, il che significa che sono meno reattivi rispetto agli pneumatici di larghezza 26 mm. Per quanto riguarda la twisting torque, ho proposto un modello teorico per prevederla, conoscendo l'area del punto di contatto, il raggio della ruota e l'angolo di camber. Il modello ha fornito risultati promettenti per angoli di camber fino a 10 gradi.

Il secondo obiettivo di questa tesi mirava a colmare il divario tra ricerca sperimentale e modellazione matematica (Capitolo 7). Ho utilizzato il VeTyT per misurare le caratteristiche laterali degli pneumatici di biciclette da città/trekking e cargo. Successivamente, ho utilizzato la Magic Formula di Pacejka per sviluppare un modello di pneumatico semplice ma robusto, valido per gli pneumatici di biciclette. Sebbene fosse originariamente concepito per pneumatici soggetti a carichi molto maggiori, la Magic Formula ha fornito risultati preziosi per angoli di camber fino a 20 gradi, quando si tratta di forza laterale e coppia di autoallineamento.

Il terzo obiettivo di ricerca ha cercato di fare un passo avanti verso la piena sfruttabilità del modello di pneumatico appena presentato. Guardando al quadro generale, mira a

trasferire la conoscenza dai test indoor degli pneumatici di bici ai test e ai modelli del sistema ciclista-bicicletta, quantificando così l'effetto degli pneumatici sulla dinamica del sistema ciclista-bicicletta. Per fare ciò, ho realizzato un setup sperimentale utilizzando un dispositivo di tipo kickplate, tipicamente impiegato per addestrare i piloti di auto sui circuiti, per perturbare lateralmente la ruota posteriore quando la bicicletta passa su di una piastra mobile, ogni volta con una diversa pressione di gonfiaggio dello pneumatico (Capitolo 8). Ho utilizzato il modello bici-rider non lineare di Carvallo-Whipple, esteso per includere il modello non lineare di pneumatici discusso in precedenza, e includendo lo slittamento laterale. Il ciclista è stato inserito nel loop utilizzando un controller generatore di coppia di sterzo. Ho eseguito simulazioni con diverse pressioni di gonfiaggio degli pneumatici, ovvero diverse caratteristiche di pneumatici. La campagna sperimentale con il kickplate ha confermato che la pressione di gonfiaggio influiva sulla dinamica della bicicletta, in particolare sullo yaw rate (il parametro più esposto) e sul roll rate. Ho utilizzato il decremento logaritmico dello yaw rate per determinare la migliore pressione di gonfiaggio in relazione al carico verticale applicato alle ruote, cioè il peso del ciclista. C'è una pressione ottimale per ciascun ciclista che consente di recuperare più velocemente dalle perturbazioni laterali.

In questa tesi, ho dimostrato il ruolo significativo che gli pneumatici giocano nella dinamica del sistema ciclista-bicicletta. Partendo dai test indoor fino a concludere con le simulazioni dei modelli ciclista-bicicletta e i test outdoor con kickplate, ho cercato di fare passi avanti nella nostra conoscenza sia della dinamica delle bici che di pneumatici per biciclette, esplorando dispositivi di testing innovativi. Mi auguro che questa conoscenza possa eseere utile ai responsabili politici, ai produttori ed ai ricercatori per fare progressi in questo campo e acquisire conoscenze per migliorare il ciclismo e apportare benefici nella vita quotidiana delle persone.

Parole chiave: bicicletta, pneumatici, dinamica.

Contents

List of Figures

Chapter 1

Introduction

Climate change is forcing governments and people to reduce pollutant emissions. Transportation is a key source of environmental impact, consuming one-third of all energy in EU and accounting for more than one-quarter of total EU greenhouse gas emissions [1]. Especially in the cities, means of transportation are a relevant source of air pollution and traffic congestion. This concern is also on the United Nations Member States agenda. The Member States summarised 17 Sustainable Development Goals ("SDP") for a better world, including the urban mobility as a key factor for making cities more liveable (Goal 11) [2]. In this context, we need to develop alternative and low-impact ways of mobility for urban travels, and cycling is a simple and cost-effective solution [3] [4]. After the Covid-19 pandemic, many people have discovered the pleasure of cycling for leisure and/or commuting [5] [6]. Municipalities invested money in cycling infrastructure to foster micromobility [7], in order to improve cities' liveability, reduce air pollution levels and car traffic congestion [8], [9], [10].

As the popularity of two-wheeled vehicles grows, concerns about road safety are growing as well [11] [12]. Despite bicycles seeming to be simple vehicles, there are still many unknown aspects referring to stability, performance, and safety [13] [14]. We know that bicycle design parameters affect the handling quality properties [15]. The tyres as well can affect both the lateral and longitudinal bicycle dynamics [16], [17], [18], [19], [20], [21], [22], [23]. Getting into practice, when riding a bicycle in daily life you may face loss of control due to many unexpected but realistic situations in which tyre lateral characteristics play a large role, like slippery roads.

A wide range of studies have addressed lateral dynamics for road vehicles with four or more wheels such as cars, trucks, buses [24], [25], [26], [27], [28], [29], [30], as lateral disturbances are one of the most important causes of accident [31]. This statement is even more true for two-wheeled vehicles, such as bicycles and motorcycles. Their riding mode is featured by large camber angles, thus relying on tyre lateral characteristics to ensure optimal and safe handling [13], [32]. Regarding motorcycles, the introduction of nonlinear tyre models which account for tyre lateral dynamics, with slipping, is also necessary to predict wobble [32].

As for the bicycles, only a few studies focus on bicycle dynamics [33], [34], tyres, and their effect on lateral dynamics [35] [36] [37]. The reader may inquire about the reasons behind the lack of studies on bicycles. It's a fact that the total revenue per year of the

bicycle market is 2 and 3 orders of magnitude lower than motorcycle and passenger car markets, respectively [38], [39]. Researchers have to deal with similar troubles in dynamics, but with a much smaller budget. Public investments and universities can partially close the gap, as the research outcomes may have a direct and tangible impact on road users' safety.

By way of analogy, we might think to transfer the knowledge from motorcycles to bicycles. Two wheeled vehicles, such as motorcycles and bicycles, are indeed featured by large camber (or lean) angles when moving along a curvilinear path [40] [41] [42], with a relatively small contact patch between the tyre and road [43] [44]. As well as motorcycle tyres, bicycle tyres are featured by a toroidal cross-section of the carcass [26], [32], however they are completely different in construction and usage, being designed for much smaller loads. This is the reason why we need proper studies and testing machines to characterise and draw conclusions on bicycle tyres, which outcomes are useful to numerically study bicycle dynamics [45], [46], [47]. In [48], the authors investigated the effect of tyres on the stability of a bicycle, using an open-loop bicycle rider model and a realistic tyre model, which also introduced slipping. Similarly to what is stated by Sharp et al. in [13], and for motorcycles in [32], the authors concluded that Carvallo-Whipple bicycle model which includes simplified tyres modelled as thin knife-edge rolling without slip [49], [50] miss out the phenomena occurring following large perturbations, like wobble. To also account for wobble, the model has to be extended by laterally slipping tyres [51], [52]. Moreover, bicycle lateral dynamics is largely involved in daily life riding situations, like when hit by a gust of crosswind or a road pothole, or riding on a slippery road. In these scenarios, a different tyre inflation pressure, tyre width [53], carcass construction, or compound may change the dynamics response over time [54]. A faster recovery from the disturbance can make the difference when you are on the road, surrounded by many other road users. Therefore, we need to know bicycle tyres lateral characteristics in order to cope with dangerous situations where a deep knowledge of dynamics can make the difference.

In academic literature, only a few studies have been published on the characterisation of bicycle tyres [48], [55], [56], [57], [58], [59], [60]. Dressel et al. [55] presented an indoor test-rig for bicycle tyres, but it could achieve limited slip angles to (+/-2 deg), and conduct tests at very low speed (0.15 m/s). In [60], Doria et al. tested bicycle tyres by using a test-rig originally conceived for motorcycle tyres. It consisted of a 3 m diameter rotating disk, to allow tests at very large camber angles (>45 deg). Nonetheless, the authors pointed out the difficulties in measurements of the lateral force for small slip angles ($\alpha < 1$ deg), for which the presence of curvature force strongly reduces the signal to noise ratio.

This dissertation aims to propose a novel test-rig to measure the lateral characteristics of bicycles tyres, develop a robust meanwhile relatively simple bicycle tyre mathematical model, and extend the bicycle-rider models by introducing nonlinear

tyre model. In doing so, I can investigate the actual effect of tyres on bicycle-rider dynamics.

The dissertation opens with the presentation of a novel test-rig specific for bicycle tyres, named VeTyT (Velo Tyre Testing). The VeTyT frame can carry a bicycle tyre on top of a drum or on a flat track, eventually covered with a rough surface made up of sands of varying granularity. It makes possible tests under vertical loads up to 550 N, at speeds higher than 25 km/h, in order to collect data closer to real outdoor conditions. Tests can be performed with tyres mounted on commercial rims or a high-stiffness laboratory rim (six times stiffer in lateral direction than an aluminium commercial rim, taken as benchmark), used to avoid the effect of rim deformation and capture the tyre characteristics only (being the tyre order of magnitudes softer than the rim). I wrote a theoretical uncertainty model to provide results alongside their uncertainty, then experimentally verified. These steps were necessary to meet the standards ISO 9001-2015, thus making the VeTyT the very first certified testing machine for lateral characteristics of bicycle tyre in the world, as far as I know.

Experimental data coming from the test-rig needs to be postprocessed to have robust tyre mathematical models to be used in simulations. To this purpose, the so-called Magic Formula [61], well known and largely exploited in automotive field, can help generate mathematical models by fitting experimental data, under the assumption of good quality inputs. In this dissertation I also show that the use of a simple Magic Formula (version '89), featured by 14 parameters for the lateral force and 18 for the self-aligning torque, can provide very good tyre mathematical models that can be used in bicycle simulations. The use of a nonlinear tyre model allows indeed to take into account the lateral force and self-aligning torque saturation, and it is needed to model the wobble as a non-divergent vibration mode, as is the case when using a simple linear tyre model [45].

Once getting experimental data from a batch of different tyres (road racing, trekking, cargo bicycle tyres), I focused on the ultimate goal of this dissertation, that is the quantification of the effect of tyres on bicycle-rider dynamics, both experimentally and numerically. I developed a novel test-rig (the "kickplate") to laterally perturb the bicycle at the rear wheel, and simulate likely to occur situations as slippery roads or gusts of crosswind. Kickplate tests elicited large slip angles (>5 deg), thus it allowed catching the saturation limit and the nonlinear regime of the tyres I asked three different volunteers to ride an instrumented bicycle over the kickplate, with tyres inflated at different pressures each time. Data such as roll rate and yaw rate plotted over time is used as an index to assess the actual influence of tyre parameters on bicycle handling, for different inflation pressures. Numerical simulations were based on the Carvallo-Whipple bicycle-rider model extended with the Magic Formula for bicycle tyres, tuned on the experimental results I got from the indoor testing.

In summary, the research objectives of this dissertation are outlined below.

1. To develop a new test bench to measure bicycle tyre lateral characteristics, in order to provide a tyre dataset to be used in bicycle dynamics studies.
2. To provide a robust tyre mathematical model that can be added to bicycle-rider models.
3. To quantify the effect of tyres on bicycle-rider dynamics, both experimentally and numerically.

The reader will find in Section 1.1 "Outline" a brief summary of each chapter, in which the above mentioned research objectives are fully addressed.

1.1 Outline

This dissertation is organised in nine chapters, based on the papers published over the four years of my doctoral journey (with the exception of Chapter 8. The paper will be submitted soon following the publication of the dissertation). Each chapter opens with the list of the main authors alongside all publication details.
With this dissertation, I have tried to push the boundaries of knowledge about bicycle tyres and their effect on bicycle-rider dynamics as far as I could. Hereafter the reader will find the outlook of each chapter.

Chapter 2 presents a full overview of the testing machines and methods developed so far to measure bicycle tyre lateral characteristics [62]. The experimental methods have been classified according to two main categories, namely field tests and indoor tests.
Field tests usually feature a relatively simple implementation: a trailer in which the two test wheels are constrained by load cells. If on one hand the possibility to test tyres in real environment makes the results close to the effective working conditions, on the other hand this does not allow the tests to be repeatable. Field tests only measure the sum of the lateral forces exerted by the tyres, thus neglecting any difference or asymmetry between the two tested tyres.
Indoor tests are performed on specific test-rigs. The development of such test-rigs is proven to be difficult and still requires much attention. Although it is complex to replicate real-world conditions, indoor tests allow to measure tyre characteristics with a good level of accuracy and repeatability.

In **Chapter 3**, I present a novel test-rig specifically designed to measure the lateral characteristics of bicycle tyres. It has a reinforced aluminium frame and it can test tyres on both a flat track and a drum, under vertical loads up to 550 N. In this chapter, I describe the development procedure step by step, enlightening the main subsystems. I also present a theoretical uncertainty model for the measurements, which I experimentally verified. These steps allowed VeTyT to meet the ISO 9001-2015 standards, obtained after a certification process lasting through January 2023.

In **Chapter 4**, I present the first extensive experimental campaign with VeTyT, conducted on a 26 mm wide racing bicycle tyre [63]. I investigated the effect of inflation

pressure, vertical force, speed and rolling surface temperature on the mechanical characteristics of a road racing bicycle tyre. The reader can find the resultant lateral force as a function of slip angle, for different rolling speed (free rolling), and the cornering stiffness varying pressure and vertical load. The significant effect of rolling surface temperature is investigated on the lateral force, for different slip angles [64]. I also considered the effect of the rim stiffness, as it may change the tyre response. Carbon rims have become the natural choice for professional riders, as they ensure lightness and high radial stiffness. The use of a high-stiffness laboratory rim (steel made, six times stiffer in lateral direction than a commercial aluminium rim taken as benchmark) allowed to test the stiffest condition possible. In addition, it allowed me to test the properties of the tyre only, as the latter is order of magnitudes less stiff than the rim. As the VeTyT can test tyres on top of a drum (also used for cleat tests) and flat track, the differences in contact patches were investigated.

Another topic of interest when dealing with road racing bicycle tyres is the tyre width: should a cyclist chose a 26 mm wide tyre or go for a 28 mm wide one? Or even wider? The study presented in **Chapter 5** [53] focuses on the measurement of the relaxation length, as the ratio between cornering stiffness and lateral stiffness of the tyre. It gives an indication of tyre responsiveness, affecting both the bicycle reactiveness and the recovery from a possible disturbance. Tests were conducted on two 26 mm wide tyres, from different manufacturers, in order to investigate some peculiarities coming from the manufacturing process. Then, two tyres from the same manufacturer, one was 26 mm wide, the other one 28 mm wide tyre, were analysed.

In **Chapter 6**, I focused my attention on the self-aligning torque [65]. I analysed the outcomes at different camber angles and inflation pressure from a 26 mm road racing bicycle tyre. I also proposed a simplified theoretical model for predicting the twisting torque. It was proven the relationship between the extension of the contact patch and the self-aligning torque: the latter increases with the contact patch area. Starting from the assumption of elliptical contact patch area, the resultant ellipse was divided into infinitesimal slices, over which it was possible to theoretically evaluate the infinitesimal force. Integrating over the contact patch area, we should be able to have the resultant twisting torque. When the area is larger the stresses are more distant from the wheel median plane, thus resulting in higher twisting torque.

The steady growth of the e-bikes and cargo bicycles sector poses new challenges in terms of vertical loads applied to the wheel, high speed and aggressive accelerations. **Chapter 7** [66] focuses on the measurement of lateral force and self-aligning torque of a set of cargo bike tyres (two tyres, from different brands), and city/trekking bicycle tyres (three tyres from two manufacturers). Tyres were tested with VeTyT on flat track, for different camber angles (0, +-5), inflation pressures (300 , 400, 500 kPa), and vertical loads (343 to 526 N, according to the technical limits of the test-rig). Afterwards, I postprocessed the experimental data to have robust tyre mathematical models to be used in simulations. To this purpose, the so-called Magic Formula [61] helped generate

mathematical models by fitting experimental data. The set of coefficients for the Magic Formula model are listed in Table 7.8, and they are useful to further research on bicycle dynamics, being a dataset available to everyone.

The know-how gained on trekking bicycle tyres has been exploited in **Chapter 8**, where I investigated and quantified the effect of tyre lateral characteristics on bicycle-rider dynamics, both numerically and experimentally. The nonlinear Carvallo-Whipple bicycle-rider model was updated by adding the nonlinear tyre model (Magic Formula [61]) presented in **Chapter 7**, also including slipping. The role of the rider in lateral stabilisation was incorporated using a closed-loop steering torque generating controller. The simulations with the same tyre at different pressures showed a variation in yaw rate and roll rate following a lateral perturbation. To prove it experimentally, a novel test-rig named "kickplate" has been developed to laterally perturb a bicycle instrumented with IMU. The kickplate simulates situations which may occur daily, like hitting a pothole, slipping on a sliding surface, or a sudden gust of crosswind, while it elicits large slip angles (>5 deg). With the aim to define an optimal inflation pressure per each vertical load, I asked three riders of different weights to ride over the kickplate and control the bicycle after the disturbance. I aim to answer what is the best inflation pressure that facilitates a faster recovery after a lateral perturbation.

The discussion and concluding remarks are summarised in **Chapter 9.** The dissertation closes with a list of proposals for future research directions.

Chapter 2

Experimental methods to measure the lateral characteristics of bicycle tyres – a review

G. Dell'Orto[a,b], F.M. Ballo[a], G. Mastinu[a]

[a] *Department of Mechanical Engineering, Politecnico di Milano, Via La Masa 1, 20156 Milan, Italy*

[b] *Faculty of Mechanical Engineering ME, Delft University of Technology, Mekelweg 2, 2628 CD, Delft, The Netherlands*

CReditT author statement:
G. Dell'Orto: Visualization; Writing – Original Draft. **F.M. Ballo**: Writing – Review & Editing. **G. Mastinu**: Supervision; Writing – Review & Editing. **M. Gobbi**: Writing – Review & Editing.

Published in Vehicle System Dynamics, 61(11), 2738–2760, 2022

https://doi.org/10.1080/00423114.2022.\

2.1 Abstract

Tyre characteristics can strongly affect bicycle dynamics. In light of this, proper test-rigs are required to accurately measure tyre parameters.
The paper presents a review of the methods and devices developed for the experimental characterisation of bicycle tyres in the lateral direction. The main aspects of the known test devices are described, highlighting the respective features.
The technology of test-rigs for bicycle tyre parameter measurement seems to be just beginning.

Keywords: bicycle, dynamics, test-rig, tyre.

2.2 Introduction

Climate change is forcing governments to reduce pollutant emissions. Transportation is a key source of environmental impact, consuming one-third of all energy in EU and accounting for more than one-quarter of total EU greenhouse gas emissions [1]. Means of transportation are a relevant source of air pollution, especially in the cities. This is why we need to develop alternative and low-impact ways of mobility for urban travels, and cycling may be a simple and cost-effective solution [3] [4].
United Nations Member States summarised 17 Sustainable Development Goals ("SDP") for a better world, including the urban mobility as a key factor for making cities more liveable (Goal 11) [2]. In addition, European Commission has announced a "green deal" to fight climate change [67], considering the huge spread of cycling as a suitable way to address the issue of low-carbon urban mobility and tackle pollution and congestion in cities [68]. One billion Euros has been spent on cycling infrastructure across Europe in 2020 [69] [10], more than 2300 km of bike lanes have been announced by European cities [70]. According to Deloitte analysts, the number of people using bicycles to get to work in large cities will increase by as much as 100% by 2022 [71] [5].
As the popularity of two-wheeled vehicles grows, concerns about road safety are growing as well [11] [12]. Cyclists have a high level of vulnerability: bicycle fatalities account for 8% of the total road fatalities recorded in 2016 in EU countries [68].
Researchers have already started to study how to improve cyclists' safety. Particular attention is devoted to traffic management and urban planning [72] [73] [74] [75], unfortunately no extensive studies have been focused on bicycle design. It seems necessary to deepen the knowledge on bicycle dynamics for fatality prevention.
This paper aims at enabling the future development of accurate dynamical models of bicycles, in order to increase safety and performance of two-wheeled vehicles for micromobility. Tyre mechanical characteristics play a fundamental role in bicycle dynamics [32]. Specifically, tyre lateral properties can be measured through field testing or by indoor testing machines and are the basis for any dynamic analysis. The paper focuses on this.

After a brief section stating the motivation on why and how bicycle dynamics can be studied, comprehensive overview of the experimental methods to measure the lateral characteristics of bicycle tyres – both indoor and outdoor – is presented. Firstly, the methods for field tests are described. Then, attention will be paid to the test-rigs used for bicycle tyres characterisation.

2.2.1 The role of tyres on bicycle dynamics

Starting from the first prototype of bicycle developed by Baron Karl von Drais in 1817 [76] [77] [16], many attempts to implement mathematical models and describe the bicycle dynamics have been recorded during the last century [17] [18] [19] [20] [21] [22] [23]. The dynamics of two-wheeled vehicles is featured by large camber (or lean) angles when moving along a curvilinear path [40] [41] [42]. Therefore, tyre properties are very important to ensure stability and proper handling of the bicycles and motorcycles [78] [79] [13].

The influence of tyres on motorcycles dynamics was addressed in [30]. Three different tyre sets were tested both outdoor mounted on motorcycle and indoor with proper test-rig, to derive useful parameters. Data were then employed to tune a motorcycle multibody model and study the dynamic response. The cornering stiffnesses of front and rear tyre strongly affected the frequency at which weave and wobble modes occur. Similarly, Sharp found the wobble mode is completely missing in the motorcycle model with the no-sideslip tyre model [32].

By way of analogy, bicycles are expected to behave in a very similar way. Bicycles tyres do not only affect rider comfort, for which the tyre filtering effect combined with the rider's posture can be relevant [80], but they also have effect on performances and safety issues. The analysis of tyre properties on bicycle stability was carried out in [48], working on a bicycle-rider model implemented in ADAMS [81] [82]. The increase in vertical load from 400 N to 600 N changed the weave speed from 9.7 m/s to 8.3 m/s respectively. A sensitivity analysis of the weave speed to the single tyre properties revealed the twisting torque to have the largest effect on weave stability. A multibody model described by linearised equation of motion was used in [58] to study the influence of tyre characteristics on bicycle stability. Larger cornering stiffness increases the damping on the wobble mode, while the variation of relaxation length changes both the weave mode and the wobble. Plöchl et al. [52] used the Carvallo-Whipple model [50] [83] extended by lateral slipping tyres, frame compliance and passive rider model for numerical analysis. They found that the cornering stiffness of the front tyre is the main parameter which destabilises the wobble mode, while the camber stiffness only affects the weave mode. Similar conclusion was drawn in [47]. A multibody model of a racing bicycle including the rear frame, front assembly, rider, wheels and tyres revealed that wobble mode is largely affected by tyre properties and lateral compliance. In [45] a nonlinear model to describe the bicycle dynamics was developed. They employed numerical continuation and bifurcation analysis to enlighten the large role played by tyre stiffness in the onset of wobble. In addition, Moore et al. [36] noted

that the inaccurate modelling of tyre characteristics might be the cause of some deficiencies in the Carvallo-Whipple model, making difficult the implementation of realistic controller for bicycle.
A deeper understanding of the forces exchanged in the tyre-road contact area is therefore crucial [51], so as to update the current mechanical models of bicycles with reliable tyre parameters [60]. Specifically, the cornering stiffness, camber stiffness, self-alignment stiffness, twisting torque and relaxation length are the main parameters to be used in bicycle models [43]. In the recent years, proper methods and testing machines have been developed to characterise bicycle tyres.

2.3 Measure of the lateral characteristics for bicycle tyre

The tyre exchanges forces with the ground in all three perpendicular directions. This is necessary to carry weight, to properly handle the bicycle, and to brake and accelerate [84] [24]. Forces and moments are generated by tyre deflection that occurs as a result of the mutual interaction between tyre and road surface [28]. The acting loads are described in a reference coordinate system with the origin located at the point resulting from the intersection of the three main planes, i.e., the central (or meridian) plane of the wheel, the transverse plane of the wheel, and the plane tangent to the road (Figure 2.1) [28] [85].

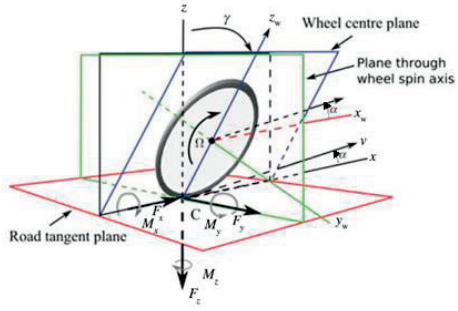

Figure 2.1 – Reference system with indicated the axis, angles and forces useful for tyre characterisation (adapted from [60]).

By the inspection of Figure 2.1, the following definition can be made. The lateral slip angle α defines the angle between the direction of the forward velocity v of the contact point tyre/road and the central plane of the wheel. The camber (or inclination [28]) angle γ is defined as the angle between the axis normal to the road and the central plane of the wheel [60]. Ω represents the angular velocity of the wheel. At the contact point, three forces (F_x, F_y, F_z) and three moments (M_x, M_y, M_z) are generated by the tyre-road interaction, acting along (or around, for the moments) the x, y, z axis, respectively. The longitudinal force F_x is also known as the "driving force" when the tyre is driven. Conversely, it is called the "braking force" when the tyre is braked. F_y

forces the vehicle to move left or right according to the direction of steering. The normal load F_z is the force of the road on the tyre, oriented downward.
From a thorough review of the scientific literature, experimental test methods aimed at characterising the lateral properties of bicycle tyres can be divided into two main categories: field (or outdoor) testing and indoor testing. Field testing is primarily based on a trailer carrying one or more wheels to test. This allows testing to be performed in real-world environment, but the presence of uncontrolled variables (including outdoor temperature, weather conditions, etc.) could affect the signal-to-noise ratio, so the repeatability of data. To overcome the disadvantages of field testing, during the last decade test-rigs have been developed to measure bicycle tyre characteristics.
Although it can be very difficult to replicate real-world conditions in a laboratory environment, indoor tests are performed due their accuracy and repeatability. The high level of accuracy of indoor test rigs allows to sense slight variations of tyre parameters. Accuracy and sensitivity of these devices is continuously improving and still is not equally attained by the known test rigs [55]. The presence of friction or small misalignments may be detrimental for measurement accuracy, often the quantities to measure are of the same order of magnitude as the disturbances [86].

2.3.1 Field testing

Field tests usually feature a relatively simple implementation: a trailer towed by motorcycle or bicycle which constrains the test wheels through load cells. In this way, tyres can be tested outdoor. If on one hand the possibility to test tyres in real environment make the results close to the effective working condition, on the other hand this does not allow the tests to be repeatable with high level of accuracy.
The first remarkable field test on bicycle tyres was performed by Roland and Lynch in 1972, at Cornell Aeronautical Laboratory [57]. By exploiting a single-wheel trailer towed behind a car on asphalt road, they measured the lateral characteristics of bicycle tyres. The vertical load on tyre was adjusted by adding weights on the trailer. The normalised cornering stiffness was measured in the range 0.15-0.35 -/deg [87], [88]. They pointed out an increase in the cornering stiffness with increasing vertical load. The repeatability of the test was poor, but the outcomes pointed out significant and expected trend of variation of cornering stiffness with respect to the change in vertical load.
In [89], Cole and Khoo presented a back-to-back test method. It consists of a transverse horizontal beam and a fork, on which two wheels are connected (Figure 2.2).

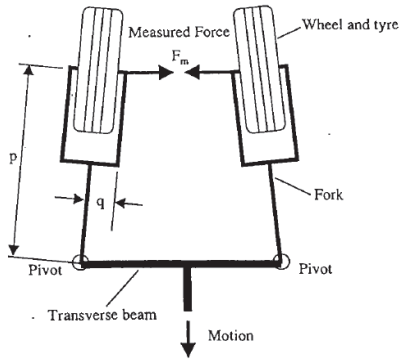

Figure 2.2 – Test set-up implemented by Cole and Khoo. The apparatus must be towed by a bicycle in accordance with the depicted direction of motion (adapted from [90]).

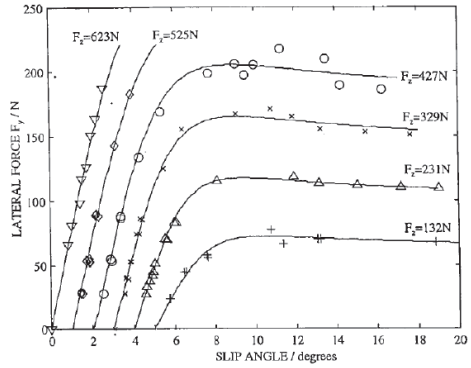

Figure 2.3 – Results pointed out by Cole and Khoo (adapted from [90]. Markers stand for measured values, while solid lines were obtained from Magic Formula [25]).

The device was conceived to be towed over the road surface by a bicycle and to measure the lateral forces of the tyres at different slip angles by means of a load cell placed between the tyres. They tested six different vertical loads (from 132 N to 623 N, Figure 2.3), set by adding weights to the beam. In Figure 2.3, the markers represent the measured data while the solid lines are interpolations of data using the Magic Formula proposed by Pacejka in [91].

The test equipment of Figure 2.2 does not allow the camber angle to be changed. Moreover, with such an arrangement, only the sum of the lateral forces exerted by the two tyres can be measured; any difference between the two tested tyres is neglected. Ply-steer or any dissymmetry of a tyre cannot be inferred from the outcomes.

In [92], the apparatus previously proposed by Cole and Khoo in [89] was replicated. Two tyres of the same type were held by two forks, pivoted on a transverse beam. A force transducer is employed to connect the wheels at the back and detect the lateral force (Figure 2.4). Tests were performed on dry asphalt road for three tyres. They were inflated at the maximum recommended pressure, and tested with five different vertical loads, ranging from 294 N to 862 N.

Figure 2.4 – Test device developed in [92]. A cart to be towed held two tyres, and a force sensor was placed in between the tyres to measure the lateral force.

The apparatus presented in [92] was further improved by Windes et al. [93]. A small trailer with two tyres mounted on pivoting forks was towed by a commercial bicycle, according to the scheme of Figure 2.5. The development of a proper mechanism located on the fork made possible the adjustment of camber angle, ranging from 0 deg to 20 deg (Figure 2.6). The lateral force was measured by means of a load cell placed at the rear of the fork.

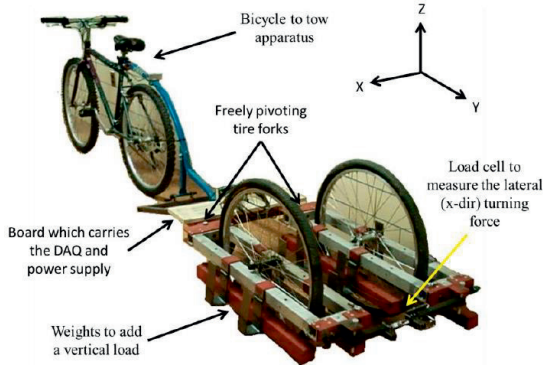

Figure 2.5 – Test apparatus for measuring lateral tyre characteristics exploited in [93]. The cart with the tyres mounted on pivoting forks was conceived to be towed.

Figure 2.6 – Device to adjust the camber angle [93]. Starting from the first concept developed in [92] the authors added the possibility to adjust the camber angle.

They tested four tyres, with vertical loads between 200 N and 800 N, slip angle α in the range 0-1.5 deg and camber angle between 0-15 deg. Maximum cornering stiffnesses were found to ranging from 200 to 250 N/deg, while the camber stiffnesses varied between 2.5 and 4.5 N/deg.

Despite the simple and fairly inexpensive development of such test equipment, the need for accurate tyre parameters to be used for modelling and simulations has forced

the researchers to develop test-rigs for indoor testing. The test-rigs employed to characterise bicycle tyres are described below.

2.3.2 Indoor testing

In this section, the test-rigs for indoor testing of bicycle tyres are presented.

Test-rig at University of Padua

The test-rig at the Department of Industrial engineering of University of Padua was specifically designed for measuring properties of tyres subjected to large camber angles, especially motorcycles and scooters. It was then extended to bicycle tyres (Figure 2.7). The test bench consists of a 3 m diameter rotating disk which allows to test tyres with camber angles up to 54 deg and slip angle up to 10 deg [94]. The disk rotates around a vertical axis, and the wheel under testing rolls on a track covered by high frictional material.

Figure 2.7 – Test-rig at University of Padua specifically configured for bicycle tyres [60]. Tyres were tested on a curved path, with different configurations of slip angle, camber angle and vertical loads.

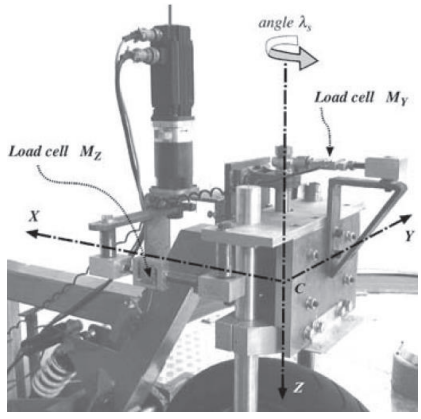

Figure 2.8 – Particular of test-rig at University of Padua, with load cells to measure M_z and M_y enlightened in [94].

A single axis load cell measures the lateral force. A similar load cell is used to evaluate the self-aligning torque M_z, while a third load cell locks the rotation around an axis parallel to the spin axis, measuring the moment M_y (Figure 2.8). Because of curvature of the track, an additional force named ''curvature force'' is introduced. It is directed towards the track outside, added to the lateral force. The measured data must be corrected by less than 4% in order to compensate the curvature effect [60]. First tests were performed by Cossalter et al. [95] on motorcycles tyres, proving the effectiveness of test-rig.

In 2012, Doria et al. [60] tested four bicycle tyres. The speed was set to 4 km/h to prevent detrimental wheel hop vibrations. For the same purpose, camber angles were limited to 24 deg. Tests were carried out with vertical loads of 400 N and 600 N, adding a proper counterweight on the heavy apparatus, this being initially designed for motorcycle tyres typically subjected to higher vertical loads.
Data collected from four tyres designed for commuting bicycles are depicted in Figure 2.9, tested with vertical load of 400 N. Plot (A) in Figure 2.9 shows the normalised lateral force as a function of the slip angle α, while plot (B) shows the normalised self-aligning torque as function of slip angle α. It is worth noticing the different trend of the green curve, being ''tyre 4'' a winter-type tyre specifically conceived for snowy/icy conditions.

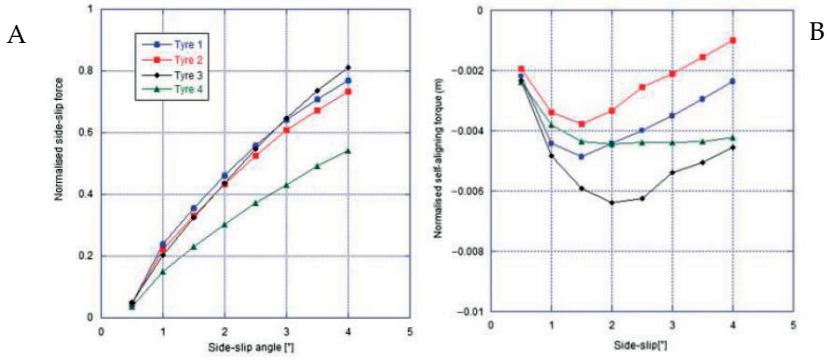

Figure 2.9 – Lines with different colors refer to different tyres tested during the experimental campaign (vertical load: 400 N). Plots (A) shows the normalised lateral force as function of slip angle. Plot (B) reports the normalised self-aligning torque as function of slip angle α (adapted from [60]).

Additional tests were performed by varying inflation pressure (2 bar and 4 bar) and vertical load (400 N and 600 N). As expected, a reduction in inflation pressure led to a decrease in the normalised lateral force. This also affected the self-aligning torque, being strongly dependent on the slip angle.
The limited slip angles of the tests did not allow to reach saturation conditions. Moreover, the authors pointed out the difficulties in measurements of the lateral force for small slip angles (α < 1 deg), for which the presence of curvature force strongly reduces the signal to noise ratio.

Test-rig at University of Wisconsin-Milwaukee

The test-rig at University of Wisconsin-Milwaukee was specifically developed for bicycle tyres [55]. It is the second version of test-rig developed, following the first one made of wood, presented in [96]. The frame is made of welded steel and an aluminium fork is used to hold the wheel on top of a flat track similar to chain [55]. Steel frame is connected to the ground by means of a universal joint, located at a distance of 1.3 m from the bicycle tyre (Figure 2.10). The camber angle can be adjusted by rotating the

universal joint with a crank system, while the slip angle α is set by pivoting the flat track about its vertical axis. The rotation of the fork which defines the steering axis is prevented by a force sensor connected to the rigid frame. In this way, the measurement of the self-aligning torque M_z can be performed. The lateral force F_y is measured by a sensor located close to the flat track and aligned with the tyre-track contact point, so that variations in camber angles do not affect the measurement. Since the lateral force is transmitted both to the universal joint and the lateral force sensor, a static summing of moments with respect to the vertical axis must be evaluated. In this way, the lateral force generated in the contact patch tyre/flat-top chain is provided. The vertical load can be adjusted by adding masses above the fork which defines the steering axis.

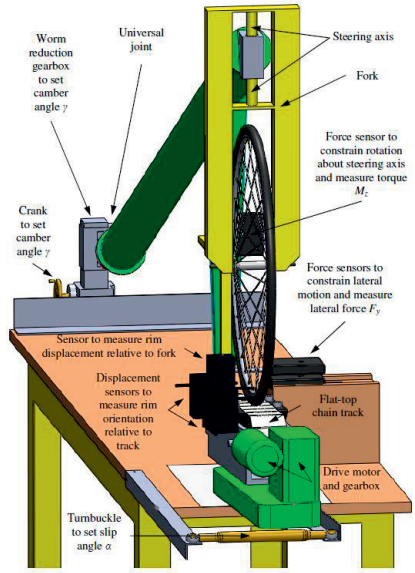

Figure 2.10 – Test-rig developed by Dressel et al. at University of Wisconsin-Milwaukee (figure adapted from [55]). Tyre is held by an aluminium fork on top of flat-top chain, driven by an electric motor.

Experimental tests were performed at a forward speed of 0.15 m/s, due to the maximum power given by the electric motor used to drive the flat track [55].
The described test bench was employed to characterise a number of mountain bike tyres in [86]. The reduced width of the flat-top chain limited the slip angles to +/-2 deg, and camber angles to +15 deg and -25 deg. In Figure 2.11, the normalised and interpolated data are shown. Each colour refers to different tested tyres. Solid line portions are based on the experimental data, while the dashed lines have been extrapolated on the basis of the fit, by exploiting the Pacejka Magic Formula for motorcycles described in [97].

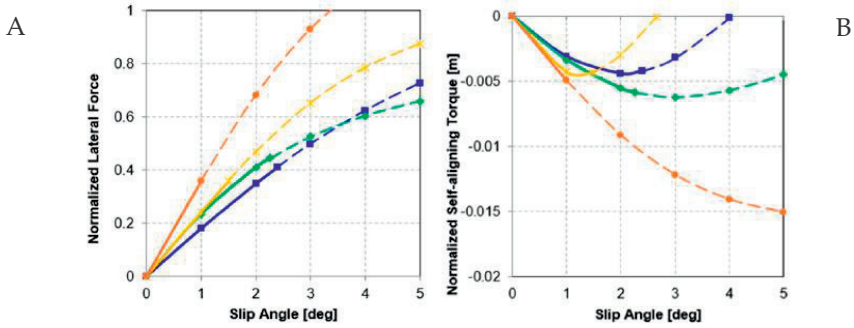

Figure 2.11 – Results obtained in [86] from mountain bike tyres. Plot (A) shows the normalised lateral force as function of slip angle, in plot (B) normalised self-aligning torque is reported as function of slip angle.

The limited range of variation of the slip angle α reduced the possibility to study the complete tyre characteristics curve. The authors concluded their analysis by analyzing the contact area and testing the same tyres after removing the knobs. In this way, an increase in the cornering stiffness was enlightened as the tyre became less treaded, so performing better [86].
The test-rig described above allows testing on flat surface, in order to involve the whole contact patch but limiting the maximum achievable speed to 0.15 m/s. The reduced width of flat track may also limit the range of variation slip angles and/or camber angles of the tests.

Test-rig at Delft University of Technology

The test-rig at Delft University of Technology [55] was designed to test tyres on a rotating drum of 2.5 m diameter. The apparatus consists of a welded steel frame with a fork to hold the bicycle wheel on top of the drum (Figure 2.12). The universal joint is used to fix the frame to the ground. A force sensor placed on the frame prevents the wheel from rotating around the steering axis, thus measuring the self-aligning torque M_z. The lateral displacement is constrained by a force sensor aligned with the centre of the tyre-drum contact patch. The camber angle can be set by rotating the frame with respect to the universal joint. Concerning the slip angle α, it is adjusted by moving the universal joint along a curved path, so as to maintain the tyre contact patch on top of drum. The vertical load can be modified by adding additional masses to the frame.
Tests were performed up to a speed of 2.2 m/s and all the tested tyres were inflated at their target pressure.

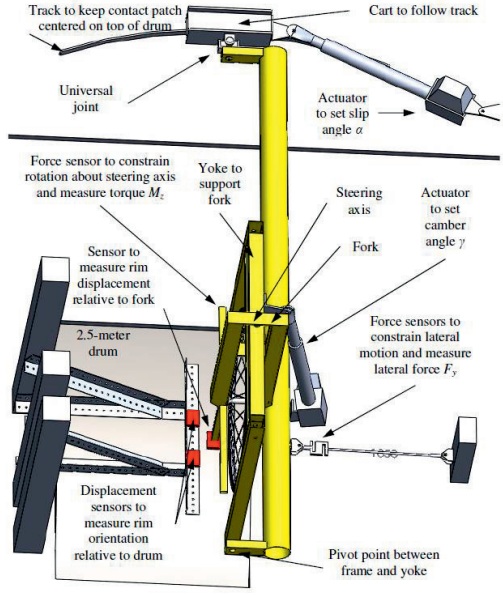

Figure 2.12 – Test-rig developed at Delft University of Technology, adapted from [55]. Steel frame constrains the wheel on top of a drum. Slip and camber angles can be set by acting on the orientation of the universal joint.

Figure 2.13 (A) shows the normalised lateral force as a function of the slip angle α, for the same tyre at different values of vertical load (300 N and 450 N). In Figure 2.13 (B) the self-aligning torque M_z is shown as function of the slip angle α. The authors proved that cornering stiffness is strongly affected by the normal load. Specifically, the cornering stiffness decreases as the normal load increases.
By testing rims of different widths, rim width was related to the normalised lateral stiffness. The latter increases for the same tyre at the same inflation pressure as rim width increases.

A

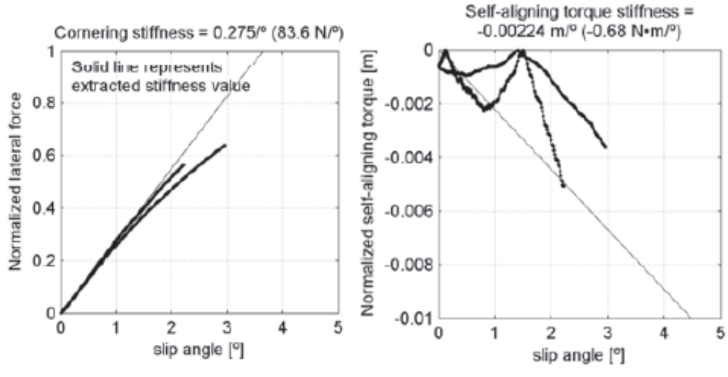

B

Figure 2.13 – The figure shows outcomes for a single tyre. Each diagram shows data for normal load 300 N and 450 N, together with the line of stiffness value. In plot (A) normalised lateral

force as function of slip angle is shown, while in plot (B) the normalised lateral force as function of camber angle is reported. Figure adapted from [55].

As observed by the authors [55], the main drawback of the system was related to the small diameter of the drum with respect to the wheel diameter, which introduced perturbations on the length and width of the contact patch with respect to the flat surface. The slip angle was limited to less than ±3 deg to avoid bias in the lateral force measurement. While the angle was adjusted moving the frame on a curved path, the same was not true for the lateral force sensor.

Test-rig at Karlsruhe Institute of Technology - Vehicle Systems

The test-rig at KIT's - Karlsruhe Institute of Technology – is based on a drum of 3.8 m diameter (Figure 2.14) [56]. Tyre runs on the inside of the drum, which is driven by 310 kW electric motor. It was conceived to test car tyres, but it can be adapted for bicycles tyres. Tested tyre is held by a single-sided fork terminating with an instrumented hub (Figure 2.15). It measures all the six components (three forces and three moments) on a maximum range of 8 kN. Slip angle and camber angle can be simultaneously adjusted. The wheel is connected to a hydraulic motor, which can apply braking/acceleration torque to the rolling tyre.
The surface of the track can be modified applying adhesive surfaces, to simulate different roughness. The inner drum chamber could be cooled up to -15 °C, so as to measure on ice or snow. Moreover, the use of inner part of the drum gives the possibility to create a controlled water film on the track surface.
Experimental campaign was carried out on a trekking bicycle tyre, with ambient temperature of the track equal to 21±2 °C. Tyre was tested with different vertical loads (500 N, 1000 N and 1500 N), inflation pressure (3 bar, 3.5 bar, 4.75 bar and 6 bar) and speeds (10 km/h, 25 km/h, 50 km/h) with the aim of deriving the longitudinal characteristics. Varying one parameter at a time, the curves of longitudinal force as function of the longitudinal slip were obtained. In Figure 2.16, the variation of the speed did not result in a remarkable longitudinal characteristic of tyre. On the contrary, the variation of the inflation pressure led to differences in magnitude of longitudinal force, especially for heavy loads (≥ 1000 N), Figure 2.17. This was mainly attributed to the variation on the area of contact patch.

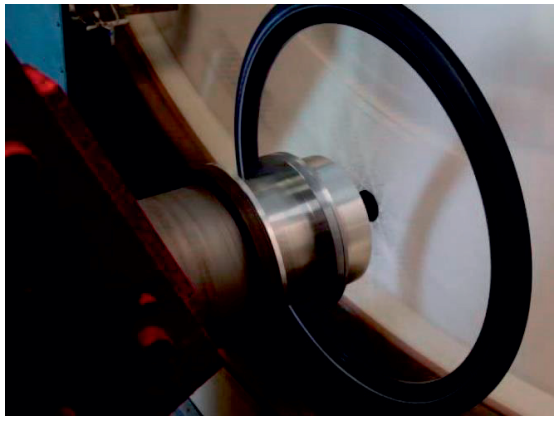

Figure 2.14 – Test-rig at Karlsruhe Institute of Technology. Tyre rolls on the inside of the drum [98].

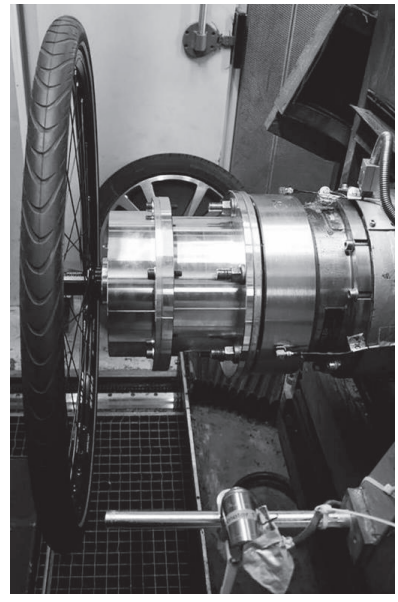

Figure 2.15 – Instrumented hub used to hold the tyre on the internal part of the drum [98].

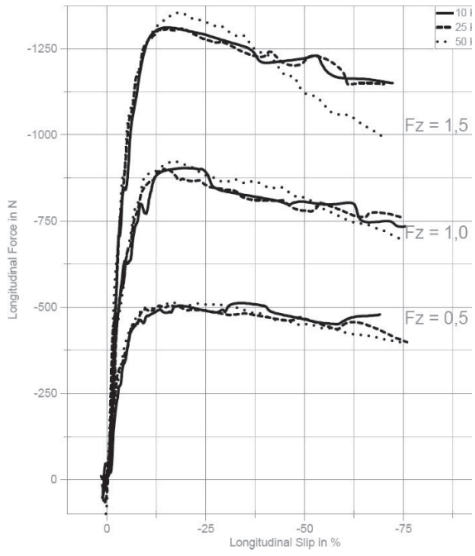

Figure 2.16 – Longitudinal force is depicted as function of longitudinal slip. Test was performed on dry surface, for different speeds (10 km/h, 25 km/h, 50 km/h) at inflation pressure of 4.75 bar [98].

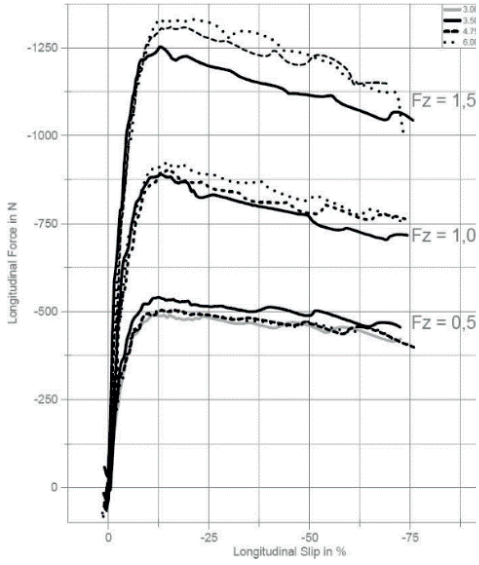

Figure 2.17 – Longitudinal force is depicted as function of longitudinal slip. Test was performed on dry surface, for different inflation pressures (3 bar, 3.5 bar, 4.75 bar, 6.00 bar), speed of 25 km/h [98].

Performing tests on a drum necessarily deforms the contact patch with respect to flat-track simulations. As declared by the researchers, an increase about 8% on cornering stiffness was recorded testing on drum.

Test-rig at Politecnico di Milano

A testing machine specifically conceived for bicycle tyres has been developed at Politecnico di Milano [99]. Known as VeTyT (short of "Velo Tyre Testing"), it has been designed to measure lateral and longitudinal forces and self-aligning torque of a wide range of single-track vehicle tyres, including bicycles, electric scooters and mopeds [100]. Different rim type and sizes can be accommodated, from 16" to 29" (inches).Tyres of widths up to 75 mm can be tested. VeTyT consists of a welded frame made of aluminium 6060 T6 reinforced with plates and steel rods, to ensure lightness and sufficient stiffness (Figure 2.18).

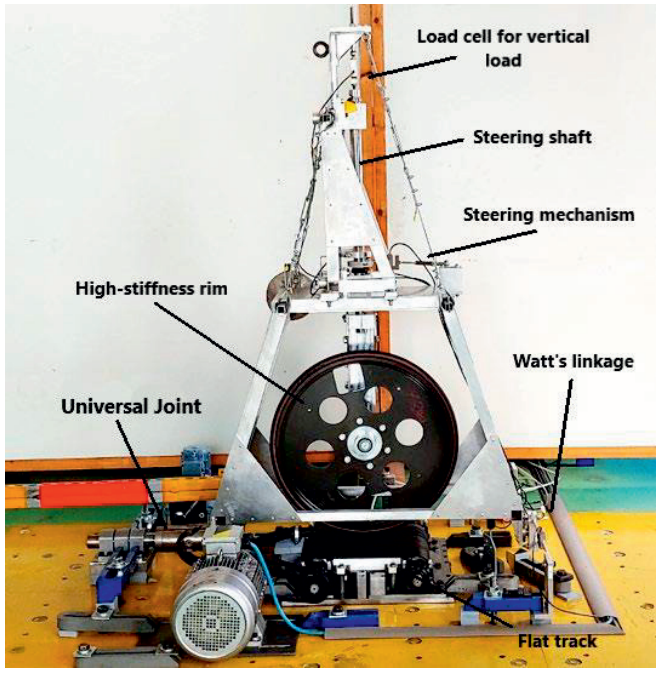

Figure 2.18 – VeTyT test-rig at Politecnico di Milano. The frame holds the bicycle tyre on flat track (adapted from [14]).

The test-rig is connected to the ground by means of Watt's linkage and universal joint. The longitudinal axis passes by the contact point of the tyre, Watt's linkage and universal joint. In this way, by rotating a shaft rigidly connected to the universal joint, the frame can tilt to set the camber angle, with the contact point of the tyre lying along the longitudinal axis. The kinematics of the Watt's linkage allows for a sufficient vertical displacement while it constrains the lateral motion of the structure, as shown in the scheme of Figure 2.19. By mounting two load cells in between rods DC and BA the lateral force F_y can be derived. Thanks to this, lateral forces up to 750 N can be safely measured.

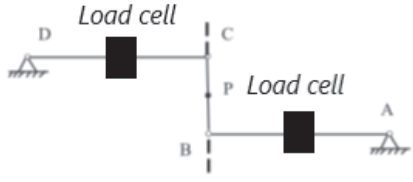

Figure 2.19 – Kinematics of Watt's linkage implemented on VeTyT. It constrains the lateral motion while allowing the vertical one. The load cells for lateral force detection are placed in between rods DC and BA.

The steering shaft holds the wheel and it is connected to the frame so that its axis crosses the longitudinal axis in the contact point of the tyre. The slip angle α can be

adjusted by rotating the steering shaft. A load cell useful for constraining the set slip angle measures the reaction force generated on the steering mechanism, from which the self-alignment moment M_z can be derived.
The vertical load acting on the wheel can be varied by adding masses on the frame. Its magnitude F_z is recorded by a load cell positioned at the top of the steering shaft. It can be adjusted in the range 340 N – 560 N.
The test-rig can be placed both on a drum [101] or on flat track (Figure 2.18). The drum has an outer diameter of 2.6 m and it can reach a peripheral speed of 122.2 m/s. Its surface can be covered with special adhesive papers to simulate different road roughness. The flat track consists of a poly-V rubber belt moved by a 5 kW three-phase asynchronous electric motor. The internal side of the belt is featured by a triangular cross section, complementary to channels manufactured in a supporting aluminium plate. In this way, it is constrained laterally keeping free the rolling in longitudinal direction of motion. To minimise friction and wear of the belt, a pneumatic system has been implemented. An air system inflates a mixture of pressurised air and silicone oil through small holes realised in the aluminium plate. With such a configuration, a maximum speed of 20.8 m/s can be achieved.
In addition to standard commercial rims, the apparatus has been designed to accommodate special high-stiffness laboratory rim, featured by an internal channel width of 22 mm. In this way, the compliance of the rim does not affect the experimental measurements.
Some tests were performed with a road racing tyre 700x25C, mounted on a commercial aluminium rim with an internal channel width of 17 mm. A forward speed of 5 m/s and a vertical force of 490 N were set. Tyre was inflated at 750 kPa. The results for the normalised lateral force and the self-aligning torque as a function of the slip angle α are depicted in Figure 2.20 and Figure 2.21, respectively. The results were obtained at several camber angles ranging from -25 deg to +25 deg. Referring to accuracy, the forces and moments read by VeTyT correspond to the actual applied forces and moments with a mean error less than 0.3%. Referring to precision, the standard deviation of forces and moments is less than 2% with respect to the mean value.

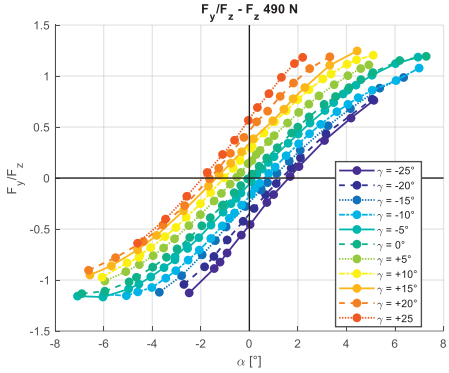

Figure 2.20 – Lateral force F_y as function of slip angle. Curves are obtained at vertical load 490 N, with camber up to 25 deg (adapted from [14]).

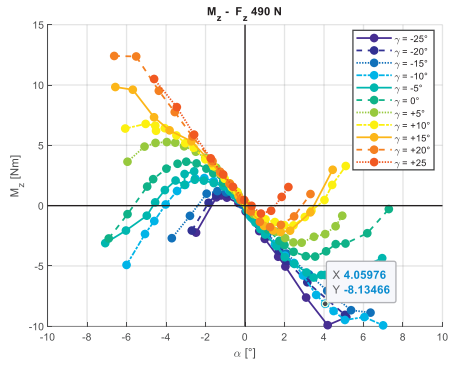

Figure 2.21 – Self-aligning torque M_z as function of slip angle. Curves are obtained at vertical load 490 N, with camber up to 25 deg (adapted from [14]).

The possibility to place the test-rig both on drum and on flat track allows to compare the results obtained with the same tyre in the same conditions. Tests already carried out suggest the use of flat track as the best tool to appreciate the forces exchanged along the entire contact area. A variation of 10% between flat track and drum tests was recorded both on forces and contact patch area, highlighting the large role played by the curvature of drum on the measured quantities [102]. Although flat track is the best option for measurement, the testing procedure requires a special attention. The typical wear of rubber belt is detrimental for testing because it changes the friction coefficient. VeTyT must be replaced to test tyre on different portions of the flat track when wear occurs.

The VeTyT produces data which can be compared with similar test-rigs. The job is in progress. Contacts are being established with other laboratories to start a "round robin" activity to test the same tyre with different test-rigs. At the moment, no comparative analyses are available referring to tyre data characteristics.

2.4 Brief summary on experimental test methods

The main features of the experimental test methods presented in this paper are collected in the Table 2.1. The devices are firstly classified according to the typology of test: field tests, or indoor tests. Then, the possibility to measure different quantities is analysed.

From the Table 2.1, it can be inferred that the complete characterisation of bicycle tyres can be performed nowadays only with indoor testing.

Table 2.1 – Classification of the testing devices based on the possibility to measure different quantities

	Lateral forces	Longitudinal forces	Self-aligning torque	Tested on drum	Tested on flat surface
Field testing References	[57],[89],[92],[93]	/	/	/	/
Indoor testing References	[60],[55],[96], [86],[56], [99],[100],[103],[102]	[56],[99],[100]	[60], [55], [96], [86], [56], [99],[100] [103], [102]	[55], [56], [99],[100] [103], [102]	[60], [96], [86], [99],[100] [103], [102]

All the presented test-rigs have been set to measure lateral forces and self-aligning torque. Only the ones presented in [56] and [99], [100] can be also employed for longitudinal forces. Some of them ([55],[56],[99]) are conceived to test tyres on drum ([55],[56],[99]), the others on flat surface ([60],[86],[99]). The test-rig presented in [99] can be used both on drum and flat surface.

All the references given in this paper are collected and organised in the Table 2.2, according to their main topic.

Table 2.2 – Classification of the references used in this paper.

Transport systems and micromobility	Bicycle dynamics	Vehicle dynamics	Tyre models	Indoor test-rigs	Outdoor test-rigs
[1], [2], [3], [4], [67], [68], [69], [10], [70], [71], [5], [11], [12], [72], [73], [74], [75]	[76], [77], [16], [17], [18], [19], [20], [21], [22], [13], [80], [48], [58], [52], [50], [83], [47], [45], [36], [51], [43], [57]	[21], [78], [24], [30], [32], [83], [24], [28], [95]	[40], [41], [42], [79], [81], [84], [85], [91], [97]	[60], [90], [55], [96], [86], [56], [99], [100] [101], [103], [102]	[57], [89], [92], [93]

2.5 Conclusion

The paper presents a review of the experimental methodologies for the measurements of lateral characteristics of bicycle tyres. The experimental methods have been classified according to two main categories, namely field tests and indoor tests.
Field tests usually feature a relatively simple implementation: a trailer in which the test wheels are constrained by load cells. If on one hand the possibility to test tyres in real environment makes the results close to the effective working conditions, on the other hand this does not allow the tests to be repeatable.
Indoor tests are performed on specific test-rigs. The development of such test-rigs is proven to be difficult and still requires much attention. Although it is complex to replicate real-world conditions, indoor tests allow to measure tyre characteristics with a good level of repeatability.
Synthetizing the analyses presented in the paper, we conclude that

- Many successful attempts have been made to characterise mechanical characteristics of bicycle tyres, nonetheless measurement uncertainties are hardly declared.
- Outdoor measurements have reached a reasonable level of development.
- There is no standardised test-rig or procedure to measure mechanical characteristics of bicycle tyres.
- Often the lateral force has been measured, the self-aligning torque is given with a rather poor accuracy.
- Cornering stiffness has been measured however a standard accurate measurement procedure could be beneficial.
- Ply-steer, conicity, ply-steer residual aligning torque [104] have not generally been measured.
- The characterisation of rolling surface is still to be made for comparing results coming from different test-rigs or outdoor measurements.
- No test-rig presented in the literature allows a quick and automatic measurement of the tyre characteristics (“you push a button, you get the characteristic”)

Despite many attempts, the technology of measuring the lateral characteristics of bicycle tyres is still at its very beginning. In the next years, considerable achievements are expected under the continuous growth of interest in micromobility.

The authors report there are no competing interests to declare.

2.6 Acknowledgements

The authors thank Lorenzo Uslenghi, Lorenzo Vaccari and Gianantonio Magnani for their support during the months of hard work and writing.

Chapter 3

Bicycle tyres - Development of a new test-rig to measure mechanical characteristics

G. Dell'Orto[a,b], F.M. Ballo[a], G. Mastinu[a], M. Gobbi[a]

[a] *Department of Mechanical Engineering, Politecnico di Milano, Via La Masa 1, 20156 Milan, Italy*

[b] *Faculty of Mechanical Engineering ME, Delft University of Technology, Mekelweg 2, 2628 CD, Delft, The Netherlands*

CReditT author statement:
G. Dell'Orto: Software; Formal analysis; Investigation; Methodology; Visualization; Writing – Original Draft. **F.M. Ballo**: Software; Investigation. **G. Mastinu**: Project Administration; Resources; Funding acquisition; Supervision; Writing – Review & Editing. **M. Gobbi**: Supervision; Writing – Review & Editing.

Published in Measurement, Volume 202, 2022, 111813, ISSN 0263-2241,
https://doi.org/10.1016/j.measurement.2022.111813.

3.1 Abstract

Bicycles will be largely exploited in city mobility, as a smart and cheap tool to achieve the goals of reducing air pollution levels and increasing the livability of cities. Their growing popularity requires more knowledge on bicycle dynamics to prevent instability. In this context, tyres may play a crucial role, as already stated in literature. This is why proper test-rigs are needed to obtain reliable tyre parameters.
The paper presents VeTyT, acronym of "Velo Tyre Testing", a new test-rig specifically developed for bicycle tyres at the Department of Mechanical Engineering of Politecnico di Milano. The development procedure is described step by step, enlightening the main goals achieved. VeTyT frame was reinforced to test tyres on flat track, with vertical loads up to 550 N. After that, a new air-cooling system to keep constant the temperature of the rolling surface was added. An uncertainty model was developed on theoretical basis, and a static verification of forces recorded by VeTyT was performed.
At the end, the results coming from a very first experimental campaign are presented. Lateral forces and self-aligning torques are depicted for racing road bicycle tyre, for vertical loads of 400 N and 490 N. The variation of camber angle (tested up to ±10 deg) contributes to the increase in magnitude of the values of lateral force and self-aligning torque.

Keywords: bicycle, test-rig, tyre, uncertainty, lateral force.

3.2 Introduction

Climate change is forcing the governments to drastically reduce the pollutant emissions in the coming years [1] [105]. United Nations Member States signed the "2030 Agenda for Sustainable Development" in 2015, summarizing 17 Sustainable Development Goals ("SDP", [2]) for a better world, also addressing the issue of Sustainable cities and transport (Goal 11). In addition, the European Commission has developed Strategic Transport Research and Innovation Agenda ("STRIA" [106]), to change urban mobility and foster new strategies for sustainable mobility [67]. In this context, we address the challenge of micro-mobility as a cheap and cost-effective means of making cities more liveable and reducing air pollution levels. As a consequence, the number of falls and accidents could increase, forcing the studies of new solutions [11] [68]. With the aim of improving the self-stability and deepening the knowledge on bicycle dynamics, advanced numerical models are required. Furthermore, existing mechanical models of bicycles mostly ignore tyre dynamics and need to be complemented with realistic tyre models.
Tyres are very important element of bicycles [16]. They play a large role in cycling comfort [107] [108], changing the vibration levels perceived by the rider due to their filtering effect [80]. In addition, tyre parameters can also affect both the stability and the handling properties of bicycles [86] [45] [47] [48] [16]. Despite this, only a few

examples of test benches for bicycle tyres are available. Doria et. al [95] presented a test-rig for motorcycle tyres adapted for bicycles [60]. They measured lateral characteristics in the range +-4 deg of slip angle, and camber angle up to 25 deg. Rolling surface was constituted by a disc of 3 m diameter which rotates about a vertical axis. This choice is very helpful for testing tyres with high camber angles, typical of motorcycles, but it introduces a distortion in the shape of contact patch.
Another prototype was conceived at University of Wisconsin-Milwaukee [96]. The first presented version consisted of a wood frame. Then, as a consequence of the limited stiffness of the apparatus, an updated version was manufactured with a steel frame, composed by a fork which held the tyre on top of flat chain. The chain limited however the speed of tests to 0.07 m/s [86] [55].
Another test-rig for bicycle tyres was tested on a drum at Technical University of Delft [55]. It was made of a steel frame, used to set the camber and slip angle while holding the wheel on top of the drum.
A different example of test-rig employed for bicycle tyres was developed at Karlsruhe Institute of Technology [56]. Tyres were tested in the inner part of a 3.8 diameter drum. The wheel was fixed on a single-sided fork, terminating with an instrumented hub to measure the exchanged forces and moments. The main drawback was related to the deformed shape of tyre contact patch, being tested on a drum.
Therefore, an innovative test-rig to fully characterise bicycle tyres and derive useful parameters for modelling has been developed. It is named VeTyT (Velo Tyre Testing), located at the Department of Mechanical Engineering of Politecnico di Milano [99].
A number of previous works on test-rigs for bicycle tyre testing have been presented above. The still existing gaps are as follows. First, the values of uncertainty are generally not declared. Second, there is the request of both accuracy and data production efficiency. Reliable tyre data have to be exploited both by tyre and bicycle manufacturers. VeTyT tries to bridge the gap between accuracy and efficiency.
This paper presents the development and improvement phases on VeTyT. The subsystems of VeTyT are described, and the technical solutions adopted to increase the stiffness and reinforce the VeTyT frame are discussed. Then, an air-cooling system useful to avoid the increase in temperature of the rolling surface is described. It is also presented a new approach to fix the wheel to the frame, improving the accuracy of the positioning at the same time.
In Section 3.5, the uncertainty model developed on theoretical grounds is presented. Finally, the static verification of the VeTyT measurements is shown. By implementing a proper set-up, it was verified the agreement between the applied loads and the forces measured by VeTyT.
In Section 3.6, the static verification of VeTyT is discussed. This procedure aims at verifying the agreement between a given load and the value recorded by the test-rig. Then, the very first experimental results are reported. A road racing bicycle tyre was tested for vertical load of 400 N and 490 N, for camber angles up to 10 deg.

3.3 VeTyT test-rig

The first version of VeTyT test-rig was designed in 2019 [90] (Figure 3.1), then step by step updated. It is possible to measure forces and moments of a wide range of single-track vehicle tyres, including bicycles, electric scooters and mopeds. Different rim type and size can be accommodated, from 16" to 29" (inches), equipped with hubs *QR* – Quick Release skewer [109], or thru-axle system Tyres of widths up to 75 mm can be tested, for any kind of bicycle (road racing bicycles, MTBs, trekking bicycles, etc).
VeTyT consists of a rigid frame made of aluminium 6060 T6, reinforced with plates and steel rods during the last development phase, to ensure lightness and sufficient stiffness (Figure 3.2) [110]. It is connected to the ground by means of Watt's linkage and universal joint. It has been conceived so that the longitudinal axis passes from the universal joint, the contact point tyre/surface and the centre of Watt's linkage. In this way, by rotating a shaft rigidly connected to the universal joint, the camber angle can be set. Furthermore, this solution allows compensating vertical vibrations of the wheel due to unevenness on the rolling surface. The tyre/road contact point can be displayed only in vertical direction, resulting in zero longitudinal speed.
The main axes of VeTyT are shown in Figure 3.3. The kinematics of Watt's linkage allows for a sufficient vertical displacement while it constrains the lateral motion of the structure, as shown in Figure 3.2 and Figure 3.4. By mounting two load cells in between rods, the lateral force F_y can be derived.

Figure 3.1 – First version of VeTyT test-rig. The frame resulted too deformable during the tests.

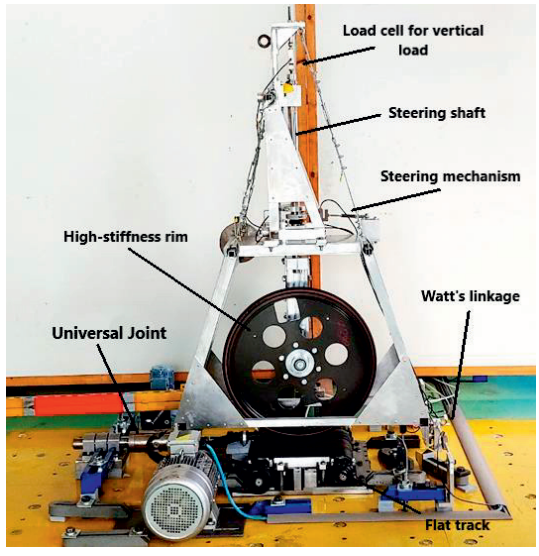

Figure 3.2 – Last version of VeTyT. It is possible to notice the presence of steel rods and aluminium plates at the corners of the frame.

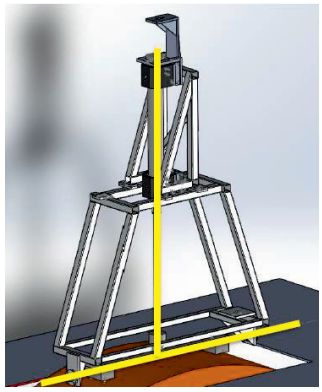

Figure 3.3 – VeTyT main axes are enlightened in yellow. The vertical axis defined by the steering shaft crosses the longitudinal axis in the centre of tyre contact patch.

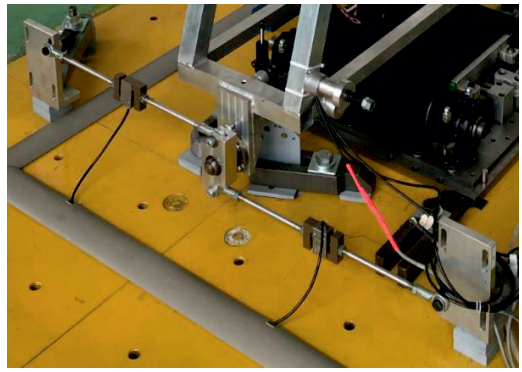

Figure 3.4 - Watt's linkage on VeTyT. The central part is connected to VeTyT, the rods with load cells are fixed to the ground.

A vertical shaft used to hold the wheel represents the vertical axis of VeTyT. It crosses the longitudinal axis in the contact point tyre/surface (Figure 3.3). The slip angle α can be adjusted by rotating the steering shaft. Once the desired slip angle is set, the position can be fixed, and the test can start. An axial load cell used to fix the set slip angle measures the reaction force F_{st} generated by the steered tyre. The self-aligning torque can be derived being the distance between the steering shaft axis and the load cell longitudinal axis (b in formula (3.1)) known. The rod is constrained through uniball joints, which can be schematised as ideal hinges, and so, only axial force is measured.

$$M_z = F_{st} b \tag{3.1}$$

As for the lateral force evaluation, data coming from the load cells S_x (F_{W-S_x}) and D_x (F_{W-D_x}) placed in between the rods of the Watt's linkage (Figure 3.4) must be algebraically added, as shown in (3.2). The sign of the forces will be always different. When the load cell S_x is under traction, the correspondent D_x is under compression. This fact is due to the kinematic properties of the system, as presented in Figure 3.4.

$$F_w = |F_{w-S_x}| + |F_{w-D_x}| \tag{3.2}$$

The lateral force F_y acting at the contact patch can be evaluated by means of equilibrium of moments. A top view of VeTyT is depicted in Figure 3.5 (A). The red line *OF* stands for the longitudinal axis of VeTyT, while the black one *NP* is the wheel, steered of a slip angle α. The acting forces (i.e. F_W and F_y) and the distances for evaluating the equilibrium are shown. L_2 stands for the distance between the centre of the contact patch *E* and the centre of the universal joint *O*, while *L* is the distance between the Watt's linkage and the centre of the universal joint *O*. The lateral force is not applied to the centre of the contact patch *E* but displaced along the longitudinal

axis by a quantity equal to the pneumatic trail t [28]. Considering the universal joint as a kinematic hinge, the equation of equilibrium to be applied for the evaluation of lateral force F_y reads as follows (3.3)

$$F_y(t + L_2 \cos\alpha) = F_W L \tag{3.3}$$

Since $M_z = F_{st} b$ and $t = \frac{F_{st} b}{F_y}$, the formula (3.3) can be rewritten in (3.4).

$$F_y = (F_W L - M_z)/(L_2 \sin\alpha) \tag{3.4}$$

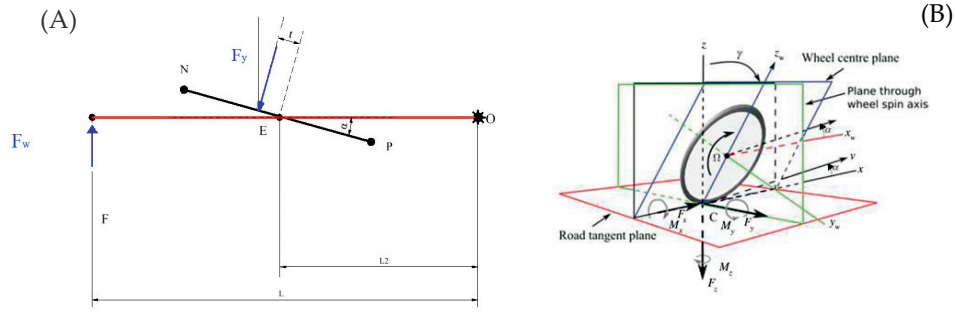

Figure 3.5 – Scheme of top view of VeTyT (A), with the indications of lateral force F_y, the force detected by the Watt's linkage F_W and the distances L and L_2, useful for the evaluation of equilibrium of momentum with respect to the centre of the universal joint O. The latter can be assumed as kinematic hinge [14]. The lateral force F_W is applied in the point F, corresponding to Watt's linkage. Three-axis reference system used to derive forces is depicted on the right (B) [25], with indicated the slip angle α and camber angle γ together with the forces and moments referred to each axis.

The vertical load acting on the wheel can be varied by adding masses on the frame. Its magnitude F_z is recorded by a load cell positioned at the top of the steering shaft. To know the total vertical load acting on the tyre, that value must be added with the weight of the steering shaft and the fork which constrains the wheel. Additional masses can be placed on top of the apparatus to adjust the load at the desired value. In this paper, vertical forces of 400 N and 490 N were considered.

All the forces are reported according to the reference W-axis system [111] [112], where the origin of the system is the road contact-point defined by the intersection of the wheel plane, the road tangent plane and the vertical axis of the tyre (Figure 3.5 (B)).

In this paper, the main improvements made on VeTyT with respect to the first version (Figure 3.1) are presented. The updates on the VeTyT subsystems are discussed in the following sections

- Chassis;
- Running contact surface;
- Steering system and steering shaft.

3.3.1 Chassis

The chassis consists of aluminium 6060 T6 welded frame. It is obtained from extruded beams with hollow square sections 40x40 and 30x30 mm, thickness 2 mm. The lower part (Figure 3.6 (b)) and the upper part (Figure 3.6 (a)) are bolted together for the final assembly (Figure 3.6 (c)). The lower part is connected to the ground by means of one universal joint and a Watt's linkage (Figure 3.4). Their placement defines the longitudinal axis, around which the chassis rolls. The upper part supports the rolling bearings for the steering shaft, which is rigidly linked to the fork which holds the wheel.
Experimental tests revealed insufficient stiffness of the chassis. To understand how and where to modify the existing structure, *FE* analysis were performed (Figure 3.7).

Figure 3.6 Chassis Upper part (a), lower part (b), and the final assembly (c).

Using a commercial software for *FE* analysis, simulations are carried out by applying a lateral load of 500 N to the support of upper roller bearing, so as to replicate the heaviest conditions. In addition, a torque of 10 Nm acting on the steering system was considered (Figure 3.7). The results of numerical analysis showed more criticalities at the interface between the lower and the upper part of chassis. It was decided to use aluminium plates of 3 mm thickness (aluminium 6000 series). Plates are added to the model, and *FE* analysis carried out again, with the same load conditions described above. As it can be seen in Figure 3.8, the deformation can be remarkably reduced. To limit the displacement of the upper part, steel cables have been added.

Once defined where placing the plates, the best fixing method was evaluated.

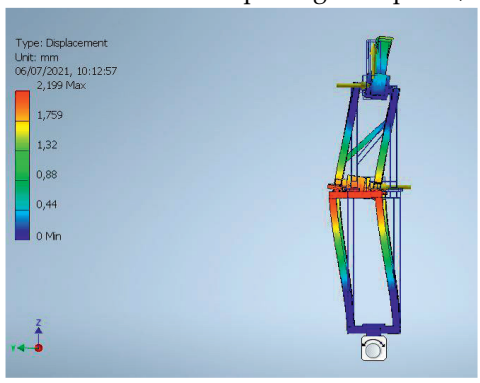

Figure 3.7 – FE analysis of the chassis before the reinforcement. Large displacements are recorded at the interface between lower and upper part of chassis. The maximum displacement of 2.2 mm results in the middle of the test-rig, in between the lower and the upper part of the chassis.

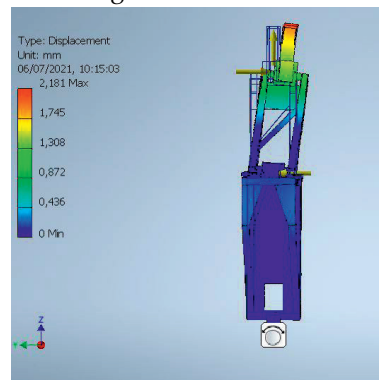

Figure 3.8 – FE analysis after the reinforcements with 3 mm thickness aluminium plates. The displacements are much smaller at the interface between lower and upper part of chassis, but still large at the top.

Discarding the welding due to the technological difficulties in ensuring strict tolerances for low-thickness aluminium bars, the options of rivets and structural epoxy adhesive were considered. To this purpose, tensile tests were carried out on specimens. The latter were manufactured in agreement with the Standard test method D1002 – 10 [113]. The following options were tested:

- Specimen joint with epoxy adhesive only (“Solution 1”);
- Specimen joint with rivet only (“Solution 2”);
- Specimen joint with epoxy adhesive plus rivet (“Solution 3”).

The scheme of different solutions can be seen in Figure 3.9.

The shear strength of the above-mentioned solutions was tested with a testing machine

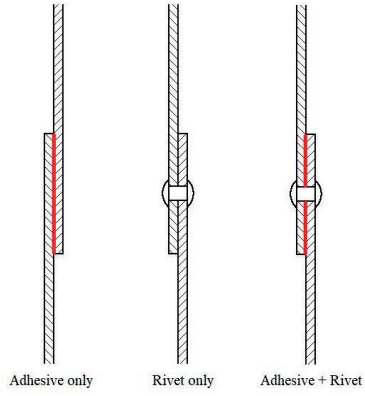

Figure 3.9 – Fixing solutions tested. The red line represents the epoxy adhesive.

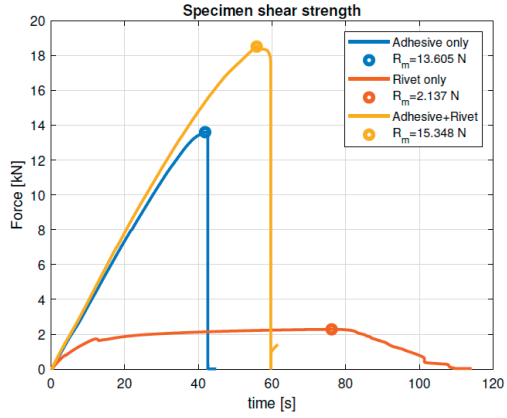

Figure 3.10 – Shear strength test on three different specimens. The force [kN] is shown as function of time of test. The ultimate tensile strength is reported in legenda.

MTS Alliance RT/100 [114]. Specifically, it applies a constant deformation and measures the applied tensile force, until the specimen is broken. The results are collected in Figure 3.10, where the applied force is shown as function of time. The ultimate tensile strength is also presented. "Solution 3" with epoxy adhesive plus rivet resulted to be the best option in terms of tensile strength, with a maximum force measured +13% than the one required for breaking the specimen with adhesive, and seven times higher than the solution with rivet only. In light of this, the solution with epoxy adhesive plus rivet was chosen for fixing aluminium plates to the chassis.

3.3.2 Rolling surface

VeTyT can be placed both on a rolling drum [101] or on flat track [99]. The latter allows appreciating the whole contact patch tyre/surface, being not affected by the curvature of the drum. The flat track at Politecnico di Milano consists of a poly-V belt [115] moved by a 5.5 kW three-phase asynchronous electric motor. The internal side of the belt is featured by a triangular cross section, complementary to channels manufactured in a supporting aluminium plate. In this way, it is constrained laterally keeping free the rolling in longitudinal direction of motion.

To minimise friction and wear of the belt, a pneumatic system has been implemented. An air system inflates a mixture of pressurised air and silicone oil through small holes realised in the aluminium plate. With such a configuration, a maximum speed of 20.8 m/s can be achieved.

Despite these precautions, the temperature of poly-V belt increased after dozens of tests, thus affecting the test repeatability. Therefore, a cooling system was designed to

remove the heat produced by friction. The system was schematised as a flat surface subjected to forced convention [116]. From thermodynamic evaluation, the power to dissipate resulted equal to 153 W. The flow and the speed of air needed were calculated and an available radial fan was adapted to the purpose. To increase the exiting air speed, a proper convergent nozzle for fan was designed and manufactured with additive manufacturing (Figure 3.11).

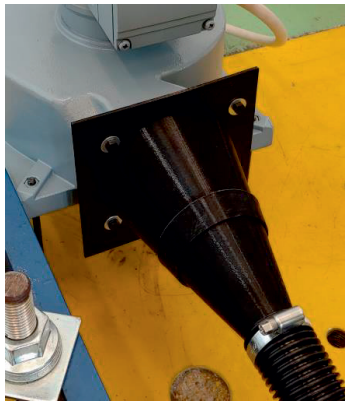

Figure 3.11 – Nozzle applied to the radial electric fan. It was manufactured in PPE through additive manufacturing process.

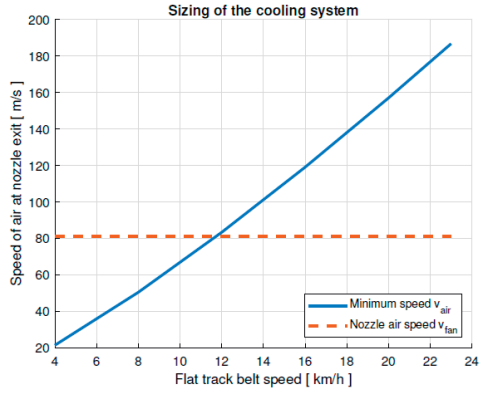

Figure 3.12 – The exiting speed of air at the nozzle is shown as function of the speed of flat track belt. The blue line represents the minimum speed of air necessary to achieve the goal of heat removing, as function of speed of flat track belt. The dashed red line is the actual nozzle air speed. According to this analysis, the speed of flat-track belt must be lower than 12 km/h.

In addition, the speed of the rolling surface should be adapted to reduce the amount of heat generated and improve the efficiency of the fan. For this reason, an optimization analysis is presented in Figure 3.12, where the measured air speed at the outlet of the nozzle is enlightened as threshold together with the minimum air speed needed to dissipate the heat generated, as function of the speed of flat track belt. Reducing the speed to values less than 12 km/h (~ 3.3 m/s), it is possible to dissipate the heat generated during the tests. In this way, the tests can be repeated under the same conditions, without affecting the results. The implemented configuration allows dissipating heat close to the contact area tyre/rolling surface without interfering with the VeTyT chassis in any configurations of camber or load.

3.3.3 Steering system and steering shaft

The steering systems is composed by an instrumented rod fixed on its extremities to the chassis and to the steering shaft through a collar. Steering shaft holds the wheel, and it is connected to the frame so that its axis passes through the centre of the tyre

contact patch. As already mentioned, it crosses the longitudinal axis of the system, generated by the universal joint and the Watt's linkage (Figure 3.4). The instrumented rod is used to constrain the rotation of the steering shaft, so as to measure the reaction force F_{st} generated by the steered tyre. From it, the self-aligning torque can be derived according to (3.1).

Originally, the instrumented rod was connected to a slender aluminium cylinder, bolted to the chassis. The component could be schematised as a cantilever beam with a load applied to the tip (Figure 3.13).

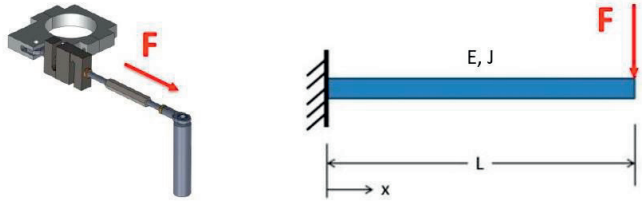

Figure 3.13 – Instrumented rod with collar to hold the steering shaft. The rod is connected to aluminium cylinder, which can be schematised as a slender beam clamped to the chassis. F is the force acting on the collar and transmitted to the rod, L is the length of aluminium cylinder.

Known the moment of inertia J, the Young modulus E, the applied force F and the length of the beam L, the deflection can be analytically evaluated as follows (3.5):

$$\delta = \frac{FL^3}{3EJ} \qquad 3.5$$

With the aim of reducing as much as possible the deflection of the slender beam, detrimental for the accuracy of the measurements, the component was completely redesigned and the benefits in terms of stiffness evaluated.

Firstly, the height of the component was reduced from 90 to 80 mm, in order to minimise the deflection. In doing so, the cubic term L of (3.5) was decreased. Then, the section was changed from circular to rectangular, increasing the moment of inertia J from $1.92 * 10^4\ mm^4$ to $1.93 * 10^6\ mm^4$. The final component is shown in (Figure 3.14).

Figure 3.14 – New component with rectangular section, to replace the aluminium slender beam and ensure more stiffness.

Figure 3.15 – Dial gauge used to measure the deflection of aluminium slender beam.

The modifications were then evaluated measuring the deflection with a proper dial gauge (set-up is shown in Figure 3.15). A force was applied to the instrumented rod and the displacement on the tip measured. In Figure 3.16, the results of the experimental test are shown, distinguishing between traction and compression force applied. As it can be clearly seen, the new configuration allows a remarkable decrease in displacement for the same value of applied force. The resultant stiffnesses are reported in the legenda of Figure 3.16, where "Old" stands for the first version with slender beam, "New" for the updated version with rectangular section.

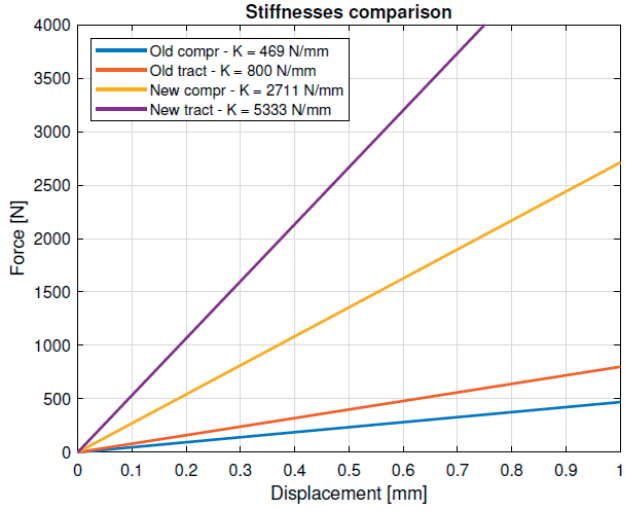

Figure 3.16 – Stiffness comparison between original and updated rod fixing system. The force applied to the rod is reported as function of the displacement of the tip of component. Purple and red lines are obtained applying compressive force, yellow and blue ones result from traction force. The calculated stiffness is reported in legenda.

The stiffness of the updated version is approximately six times higher than the original one. It is worth noticing the different compressive and tensive stiffness. The component results two times stiffer in tension than in compression. This effect can be attributed to the chassis, which reacts differently according how the load is applied.
The wheel is connected to the steering shaft through a fork. Specifically, we can select between two kinds of forks:

- Fork for standard commercial rim (Figure 3.17): designed to accommodate any kind of commercial rim (aluminium alloy or composite materials) equipped with "Quick Release" system or thru-axle hub.
- Single-sided fork: it has been conceived to accommodate a special high-stiffness laboratory rim (Figure 3.18), featured by an internal channel width of 22 mm.

Figure 3.17 – Fork used to hold the commercial rim. It can accommodate different typology of rims commonly mounted on micromobility vehicles.

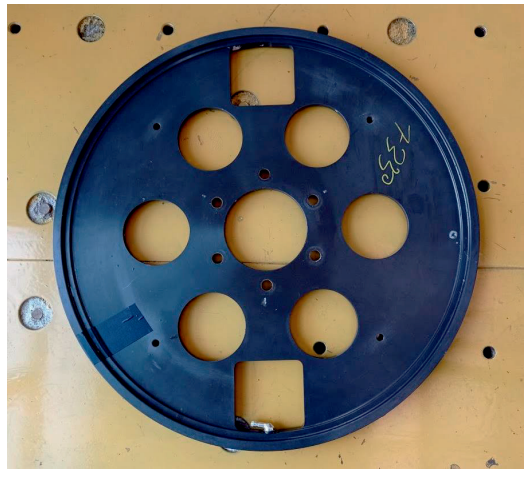

Figure 3.18 – High-stiffness laboratory rim. The weight is equal to 7330 g (courtesy of Pirelli). Internal width of the rim channel is equal to 22 mm.

3.3.4 Standard fork

A new wheel fixing system was introduced for the standard fork. The aim of this improvement is to set the proper camber angle of the tyre avoiding errors from the incorrect rim fixing. The wheel support elements should ensure the fixing for all types of rims with Quick Release system ("QR system") or thru-axle hub independently on the specific tolerances of the manufacturers. To do this, a plate with four holes and single notch "V-shaped" in the lower part was designed and manufactured with tolerances of hundreds of millimetres (Figure 3.19). This can be fixed to the fork, one per each internal side. The external part of the hub is inserted into the "V-shaped"

notch of the plate, so as to create a shape constrain. A steel collar is then placed under the hub to complete the mounting of the wheel (Figure 3.20).

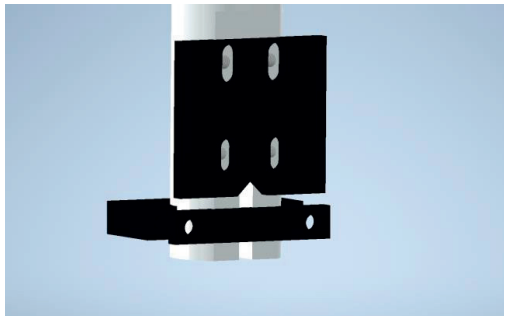

Figure 3.19 – Plate and collar (in black) designed to lock the commercial rims. The notch in the upper plate is useful to create a "shape constrain" for rims.

Figure 3.20 – Final assembly of the commercial rim to the fork.

The alignment of the plates is made by using a proper manufactured jig with tolerances of hundreds of millimetres. It is a steel shaft, crossed in the middle by a steel rod to simulate the wheel hub. It defines the position of aluminium plates in the vertical plane, so that when dismounted and replaced by the wheel, the wheel hub is accurately set.

3.3.5 Single-sided fork

The single-sided fork revealed high deformations when subjected to high loads, affecting the measurements. So, it was necessary to find new solutions to increase the structural stiffness of the component. A *FE* analysis revealed the most effective way to strength the fork without adding to much mass, given that limited oscillations with off-axis masses may induce high dynamic forces. It was decided to use an 8 mm thick 6000 series aluminium plate screwed to the fork (blue circle, Figure 3.21), with threaded bars in the remaining (red circle, Figure 3.21). Welding was avoided because the residual stresses would have compromised the geometric tolerances of the part. The reinforcement reduced stresses and strains in the fork, with an increase in moment of inertia up to +140% with respect to the first version of single-sided fork.

Figure 3.21 - Reinforcement of single-sided fork with 8 mm aluminium plate screws in the upper part (blue circle) and threaded bars (red circle).

3.4 Signal analysis after the reinforcements

Analysis of signal after the improvements has been performed to demonstrate the effectiveness of the work made on VeTyT. The results shown hereafter were obtained during tests on flat track, with the same road racing tyre mounted on commercial rim, vertical load equal to 490 N and inflation pressure 5.5 bar.
The unfiltered signal of the steering force is reported in Figure 3.22 as function of time. The different mean value of the recorded force is due to the fact that the measurements before improvements (in blue) were carried out on a different position of the flat track, where the wear was higher. However, this effect is not relevant for the purpose of the analysis. The remarkable reduction in amplitude of the unfiltered signal can be clearly noticed by zooming Figure 3.22. In particular, the standard deviation of the signals was computed to quantify the benefits. Considering the steady state (so avoiding the initial and final transient phases), the standard deviation passes from 26.05 N to 7.92 N after the improvements, with a reduction of 70%. Excessive vibrations on the wheel may affect the measurements, inducing longitudinal slip and increasing the surface temperature of the belt.

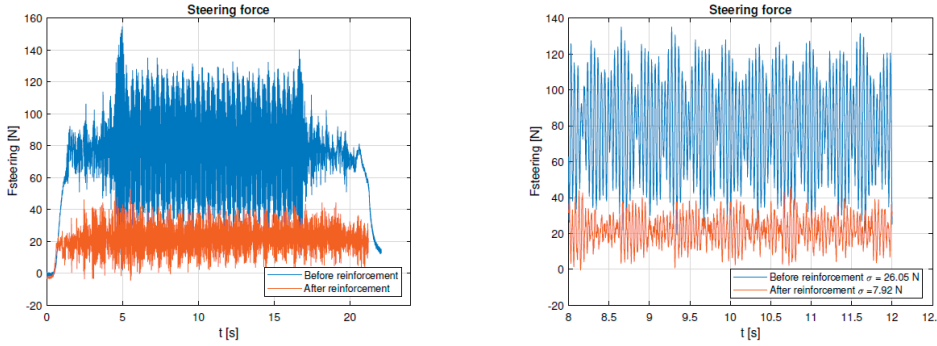

Figure 3.22 – Signals coming from load cell on the rod which locks the steering shaft, after and before the improvements on VeTyT (respectively, red and blue signals). At right, a zoom is useful to see the amplitude of signals. A remarkable decrease in standard deviation of signal after improvements can be noted.

The same behaviour can be appreciated for lateral force, with a reduction in standard deviations in the order of 65-75%.

The torsional stiffness was also evaluated, to demonstrate the effectiveness of improvements on the assembly. It was calculated as the ratio between the recorded self-aligning torque and the actual value of slip angle shown during the test run. It is worth noting that the slip angle set at the beginning differs from the actual one during the test, due to the deformability of the structure during the test. The torsional stiffness K_α as function of the actual slip angle of the test run is shown in

Figure 3.23.

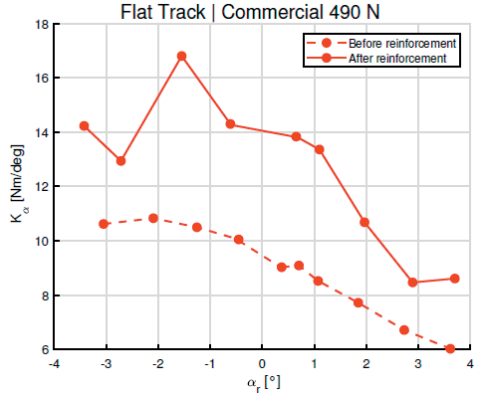

Figure 3.23 – Torsional stiffness as function of the slip angle during the test run.

The torsional stiffness after the structural reinforcement and the update on the steering system is higher than 40% [102]. It is possible to notice the decreasing trend of torsional stiffness at increasing the slip angle. This is due to the stiffness of the chassis, which

reacts differently according how the load is applied, as already stated in Section 3.3.3 for the steering system.

3.5 Uncertainty model

An uncertainty model is needed to proper define the measurements and assess the reliability of the results. It is also requested by certification recognised organizations to assure the quality of the test-rig.
All the measurements performed are affected by uncertainties. The value of uncertainty depends on several factors, mainly related to the chosen measurement methodology and exploited instruments. In case of VeTyT, the uncertainties to estimate are the following:

- i_α [deg]: it is the uncertainty on the value of slip angle of the tyre. The mechanical properties of tyre are strongly related to the slip angle α. It depends on the alignment of the wheel with respect to the reference running surface. In addition, the accuracy of the linear encoder used to read the angular position of the wheel may affect the uncertainty on α.
- i_γ [deg]: it is the uncertainty on the value of camber angle of the tyre. Similarly for what concerns slip angle α, the camber angle γ strongly affects the lateral force and the self-aligning torque of the tyre. Its value depends on uncertainty of inclinometer used to set the camber angle.
- i_{F_y} [N]: it is the uncertainty on the value of lateral force generated by the tyre along the contact patch. Lateral force is calculated through an equilibrium equation, so that the uncertainty of each value of the equation contributes to the total uncertainty of the lateral force.
- i_{M_z} [Nm]: it is the uncertainty on the self-aligning torque generated by the tyre along the contact patch. Its value depends on the uncertainty of load cell used to measure the force on the steering system.
- i_{F_z} [N]: it is the uncertainty on the vertical force. The latter plays an important role in the definition of the mechanical properties of the tyre.

According to [117] [118], the uncertainty can be estimated using available information on measuring instruments (Type B uncertainty).
Most of time the measurand is not directly measured, but it is estimated as function of n uncorrelated variables x_1, x_2, … x_n. In this case, the combined uncertainty of a generic measurand y can be computed through the propagation of uncertainty equation (3.6)

$$y = f(x_1, x_2, x_3 \dots x_n) \tag{3.6}$$

$$i_y = \sqrt{\left(\frac{\delta y}{\delta x_1}\right) i_{x_1}^2 + \left(\frac{\delta y}{\delta x_2}\right)^2 i_{x_2}^2 + \cdots + \left(\frac{\delta y}{\delta x_n}\right)^2 i_{x_n}^2} \quad 3.7$$

The equation (3.7) has been largely used for the theoretical estimation of the uncertainty of measurements, according to Type B uncertainty.
In this section, a model of uncertainty is presented. To do this, the operations to align the device and set the characteristics angles must be defined. The uncertainties on slip angle, camber angle, lateral force, self-aligning torque and vertical force are presented.

3.5.1 Slip angle uncertainty

The evaluation of uncertainty on slip angle α is a direct consequence of the alignment procedure of the VeTyT chassis. Specifically, the longitudinal axis of VeTyT must be aligned to the axis which defines the peripheral speed of the flat track belt. A proper template is used to hold the chassis during the alignment procedure (black template in Figure 3.24).
After that, the wheel mounted on VeTyT can be aligned with respect to the chassis to the define the slip angle α. The operation is made using a rule rigidly fixed to the chassis on which a depth gauge and its holder device is placed. This is useful to define the current angle between the chassis of VeTyT and the wheel mounted on the fork, then the encoder can be set according to the read value. The general configuration of the measuring system is schematised in Figure 3.24.

- Green beams schematise the chassis of VeTyT;
- The rule is fixed to the chassis on points G and H;
- Yellow line IJ stands for the reference axis of the flat track belt;
- Black line represents the wheel, with the slip angle α;
- Points P and N are the extremities of the wheel rim on which the measurements are performed with a depth gauge. Point N' is the projection of N on an axis parallel to the chassis (red line) and passing through point P. It is useful to derive the mathematical relationship for uncertainty;
- Point O coincides with the vertical axis of the universal joint;
- Point F coincides with the centre of Watt's linkage;
- Point E is the centre of the contact patch;
- Red line represents the VeTyT chassis. It is hinged at point O to the universal joint, and θ is the angle between chassis and the reference axis of the flat track belt;
- a, b, c, d are the measurements performed with depth gauge;
- x and y are measured with rule.

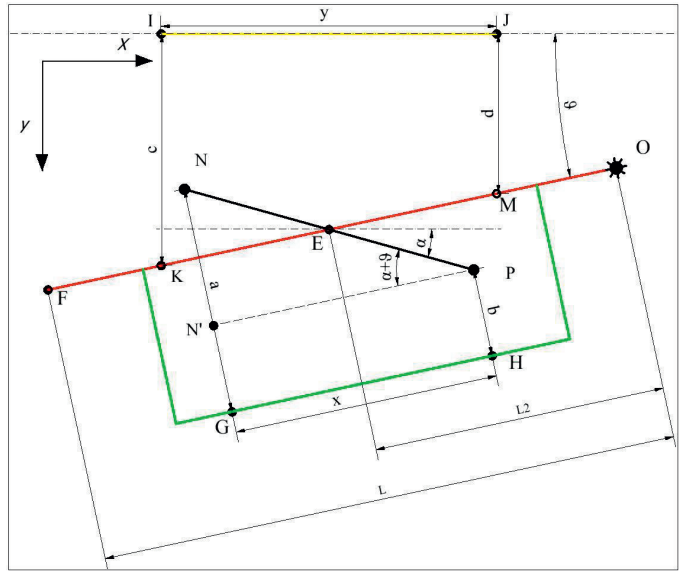

Figure 3.24 – Schematic top-view of VeTyT.

The following trigonometric relationships can be derived (3.8) and (3.9):

$$\theta = \text{atan}\frac{c-d}{y} \tag{3.8}$$

$$\alpha = \text{atan}\frac{a-b}{x} - \theta \tag{3.9}$$

Therefore, the uncertainty on the slip angle α is the following (3.10), according to the uncertainty propagation formula (3.7):

$$i_\alpha = \sqrt{\left(\frac{\delta\alpha}{\delta a}\right) i_a^2 + \left(\frac{\delta\alpha}{\delta b}\right)^2 i_b^2 + \left(\frac{\delta\alpha}{\delta x}\right)^2 i_x^2 + \left(\frac{\delta\alpha}{\delta\theta}\right)^2 i_\theta^2} \tag{3.10}$$

Considering a perfectly aligned chassis, θ would be equal to 0. To better set the angle θ, a new template was designed with tolerances of hundreds of millimetres (red in Figure 3.25). Gauge blocks (green and blue components in Figure 3.25) were machined with tight tolerances on planarity, parallelism and perpendicular.

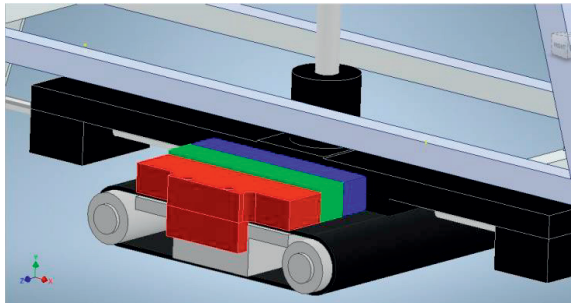

Figure 3.25 – Template and gauge blocks.

The uncertainty on angle θ can be calculated as (3.11):

$$i_\alpha = \sqrt{\left(\frac{\delta\theta}{\delta c}\right)^2 i_c^2 + \left(\frac{\delta\theta}{\delta d}\right)^2 i_d^2 + \left(\frac{\delta\theta}{\delta y}\right)^2 i_y^2} \qquad 3.11$$

Where i_y is due to the uncertainty of the rule (= 0.5 mm), according to DIN 866-A, while the uncertainties on the template i_c and i_d can be evaluated as follows

$$i_\alpha = \sqrt{i_{nts}^2 + i_{gb1}^2 + i_{gb2}^2 + i_{abs}^2 + i_{ts}^2} \qquad 3.12$$

Data used in formula (3.12) are the following (Table 3.1)

Table 3.1 – Data used in formula (3.12)

i	Uncertainty	Value	Unit
i_{nts}	uncertainty of new template straightness	0.03	[mm]
i_{gb1}	uncertainty of gauge block straightness	0.02	[mm]
i_{gb2}	uncertainty of gauge block straightness	0.02	[mm]
i_{abs}	uncertainty of the air bearing surface straightness	0.02	[mm]
i_{ts}	uncertainty of the template straightness	0.02	[mm]

As for the uncertainty on the measurands a and b, the uncertainty can be evaluated as (3.13)

$$i_a = i_b = \sqrt{i_{dg}^2 + i_{rs}^2 + i_{ro}^2 + (2\sigma_{a-b})^2} \qquad 3.13$$

For the sake of accuracy, ten measurements on the extremities of the rim a and b were taken, so that the mean value μa, μb and the standard deviation σ_a, σ_b were calculated. A coverage factor equal to 2 is introduced in (3.13) to consider the expanded uncertainty with a confidence level of 95%. An example of the measurements taken is reported.

$$a = [170.60 \mid 170.60 \mid 170.61 \mid 170.59 \mid 170.61 \mid 170.60 \mid 170.61 \mid 170.62 \mid 170.61 \mid 170.61]$$
$$\mu_a = 170.60\ mm \quad \mid \quad \sigma_a = 0.01\ mm$$

$$b = [171.73 \mid 171.72 \mid 171.70 \mid 171.71 \mid 171.72 \mid 171.73 \mid 171.70 \mid 171.72 \mid 171.71 \mid 171.71]$$
$$\mu_b = 171.71\ mm \quad \mid \quad \sigma_b = 0.01\ mm$$

Data used in (3.13) are reported in Table 3.2.

Table 3.2 – Data used in formula (4.8) for evaluation of uncertainty i_a, i_b

i	Uncertainty	Value	Unit
i_{dg}	uncertainty of depth gauge	0.02	[mm]
i_{rs}	uncertainty of rule straightness (DIN 866-A)	0.04	[mm]
i_{ro}	uncertainty of rim run-out	0.05	[mm]
σ_a	Standard deviation of a measurement	0.01	[mm]
σ_b	Standard deviation of b measurement	0.01	[mm]

The results of uncertainty on the slip angle α are reported in Table 3.3.

Table 3.3 – Results of the evaluation of uncertainties useful to evaluate i_α

i	Uncertainty	Value	Unit
i_c	uncertainty of measurement c	0.05	[mm]
i_d	uncertainty of measurement d	0.05	[mm]
i_a	uncertainty of measurement a	0.08	[mm]
i_b	uncertainty of measurement b	0.08	[mm]
i_θ	uncertainty of measurement θ	0.01	[deg]
i_α	uncertainty of measurement α	0.02	[deg]

The uncertainty related to the magnetic sensor used to read the actual value is an order of magnitude less than the one related to the alignment procedure above described. In light of this, the contribute of encoder can be neglected.

3.5.2 Camber angle uncertainty

Lateral forces of bicycle tyres are strongly dependent on slip angle α and camber angle γ. Different camber angles can be set with VeTyT, by tilting the whole chassis around the camber axis defined by the universal joint and the Watt's linkage. The camber angle is measured through a digital inclinometer fixed to the steering shaft, with a resolution of 0.05 deg. Its uncertainty was found to be 0.1 deg (datasheet from manufacturer).

3.5.3 Lateral force uncertainty

The lateral force is calculated according to (3.4). Therefore, by applying the propagation formula (3.7), the uncertainty of lateral force can be calculated as follows

$$i_{F_y} = \sqrt{\left(\frac{\delta F_y}{\delta F_w}\right)^2 i_{F_w}^2 + \left(\frac{\delta F_y}{\delta L}\right)^2 i_L^2 + \left(\frac{\delta F_y}{\delta F_s}\right)^2 i_{F_s}^2 + \left(\frac{\delta F_y}{\delta b}\right)^2 i_b^2 + \left(\frac{\delta F_y}{\delta L_2}\right)^2 i_{L_2}^2 + \left(\frac{\delta F_y}{\delta \alpha}\right)^2 i_\alpha^2} \quad 3.14$$

Analysing term by term the equation (3.14)

- i_{F_w} is the uncertainty related to the load cells of Watt's linkage, evaluated in (3.15). $i_{F_{w1}}$ and $i_{F_{w2}}$ are declared by the manufacturer of load cells (3.16).

$$i_{F_w} = \sqrt{i_{F_{w1}}^2 + i_{F_{w2}}^2} \quad 3.15$$

$$i_{Fw1} = i_{Fw2} = 0.02\%\ P_1 g \quad 3.16$$

$$P_1 = 100\ kg \quad 3.17$$

- i_L is the uncertainty on the distance between the centre of tyre contact patch and the cross of the universal joint. It was estimated to be 1 mm, since vibrations, deformations and clearances play an important role in the final position of tyre.
- i_{F_s} is the uncertainty of the load cell used to constrain the steered tyre, useful to derive the self-aligning torque (3.18) (3.19).

$$i_{F_s} = 0.02\%\ P_2 g \quad 3.18$$

$$P_2 = 25\ kg \quad 3.19$$

- i_b is the uncertainty on the distance between the axis of steering shaft and the longitudinal axis of the load cell of steering system. It was estimated to be 0.1 mm, due to manufacturing tolerances.
- i_{L_2} is the uncertainty on the distance between the cross of universal joint and the Watt's linkage. For the sake of safety, it was estimated to be 5 mm since vibrations, deformations, slight errors during the alignment process and clearances may play an important role.
- i_α is the uncertainty on the slip angle α, evaluated as in the previous section (Table 3.3).

The uncertainty of the lateral force must be evaluated for each measurement, since it depends on the current values of α, F_W, F_s. Specifically, increasing the measured values the uncertainty of lateral force will increase as well. In Figure 3.26 lateral force is reported as function of slip angle α (at left), the correspondent uncertainty values are shown at right. Starting from value of 0.54 N for slip angle 0 deg, the uncertainty becomes larger than 2 N for slip angles > |5 deg|.

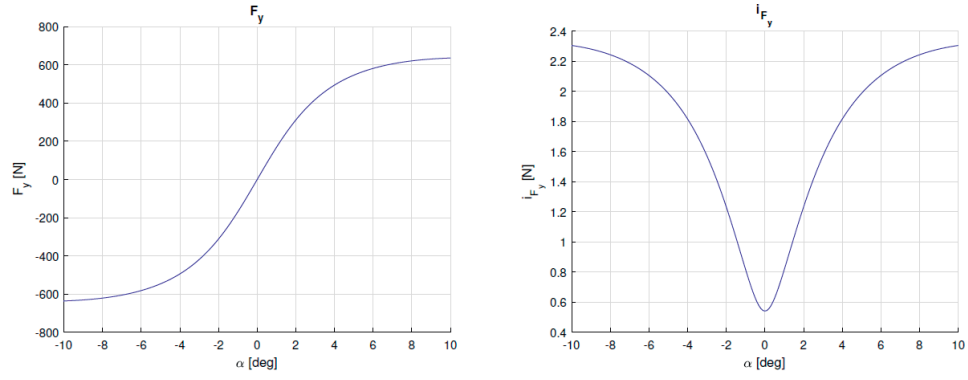

Figure 3.26 – Lateral force F_y as function of slip angle α (at left), uncertainty of F_y as function of slip angle α (at right).

3.5.4 Self-aligning torque uncertainty

The uncertainty on self-aligning torque is computed starting from the formula (3.1) and applying the propagation formula (3.7). The following result is obtained (3.20) (3.21).

$$i_{M_z} = \sqrt{\left(\frac{\delta M_z}{\delta F_s}\right)^2 i_{F_s}^2 + \left(\frac{\delta M_z}{\delta b}\right)^2 i_b^2} \qquad 3.20$$

$$i_{M_z} = \sqrt{b^2 i_{F_s}^2 + F_s^2 i_b^2} \qquad 3.21$$

As already described, i_{F_s} is the uncertainty of the load cell mounted to lock the steered wheel. Its value is defined by manufacturer, as seen in (3.18), (3.19). The value of i_b has been already defined in Table 3.3. The uncertainty on self-aligning torque M_z varies for each measurement, as depicted in Figure 3.27. It reaches a maximum value of 0.0168 Nm, corresponding to the maximum value of measurand.

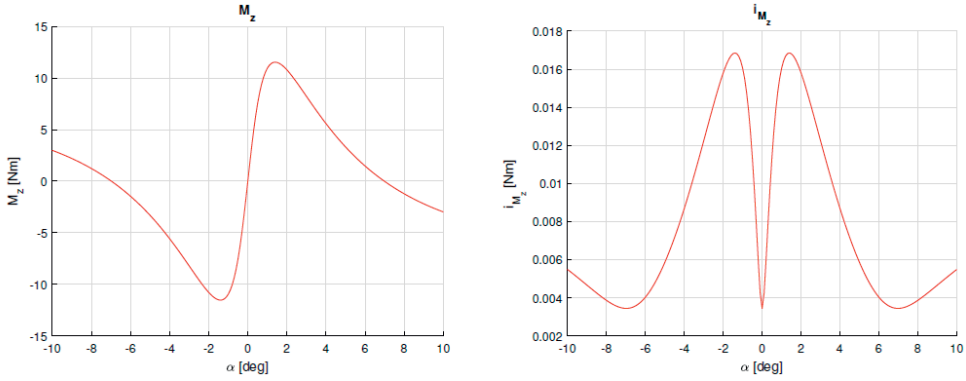

Figure 3.27 – Lateral force M_z as function of slip angle α (at left), uncertainty of M_z as function of slip angle α (at right).

3.5.5 Vertical force uncertainty

The vertical force is computed through equilibrium equation (3.22), as reported below.

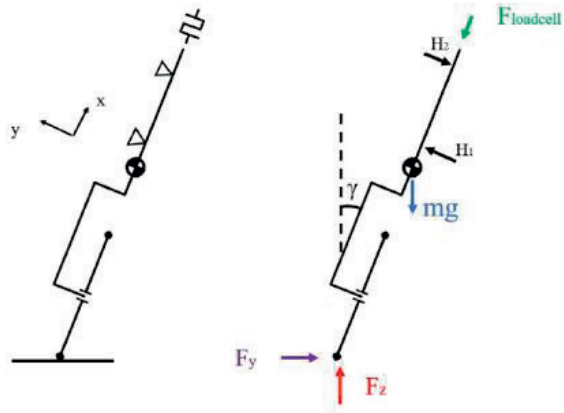

$$\sum F_x = 0$$

$$F_z \cos\gamma + F_y \sin\gamma - mg\cos\gamma - F_{loadcell} = 0$$

$$F_z = \frac{F_{loadcell} + mg\cos\gamma - F_y \sin\gamma}{\cos\gamma} \quad 3.22$$

By applying the propagation of uncertainty formula (3.7), the uncertainty of vertical force F_z can be evaluated as follows (3.23)

$$i_{F_z} = \sqrt{\left(\frac{\delta F_z}{\delta F_{loadcell}}\right)^2 i^2_{F_{loadcell}} + \left(\frac{\delta F_z}{\delta m}\right)^2 i^2_m + \left(\frac{\delta F_z}{\delta g}\right)^2 i^2_g + \left(\frac{\delta F_z}{\delta \gamma}\right)^2 i^2_\gamma + \left(\frac{\delta F_z}{\delta F_y}\right)^2 i^2_{F_y}} \quad 3.23$$

The terms which compose (3.23) are the following

- $i_{F_{loadcell}}$ is the uncertainty related to the load cells placed above the steering shaft. The value of uncertainty is declared by manufacturer (3.24). P_3 is the nominal load of the load cell (3.25).

$$i_{loadcell} = 0.02\%\, P_3 g \quad 3.24$$

$$P_3 = 250\ kg \quad 3.25$$

- i_m is the uncertainty of the total mass of the elements below the load cell for the measurement of F_z. Considering the uncertainty of the balance instrument used to weigh ($i_{balance} = 1\ g$, as declared by the balance manufacturer), given that the number of elements to measure is five, the value of i_m was evaluated as (3.26):

$$i_m = \sqrt{5 i_{balance}} = 2.2\ g \quad 3.26$$

- i_g is the uncertainty of the gravitational acceleration evaluated in Milan. A formula from Italian Institute of Metrology "Gustavo Colonnetti" can be used to this purpose (3.27):

$$g = g_{nom}(1 + C_1 \sin^2 L) \quad 3.27$$

Where $g_{nom} = 9.780318\ m/s^2$, so the gravitation acceleration measured at sea level at the equator line. The coefficients are equal to $C_1 = 5.302410 * 10^{-3}$, $C_3 = 3.085 * 10^{-6}$, $L = 120$, $h = 120\ m$, it is the altitude with respect to sea level. That results in $g = 9.806330\ m/s^2$, similar to the value obtained from direct measurement performed in August 1970 in Milan ($g = 9.805502\ m/s^2$).
Therefore, the uncertainty i_g can be estimated as (3.28)

$$i_g = 9.80633 - 9.80550 = 8.2835 * 10^{-4}\ m/s^2 \quad 3.28$$

- i_γ is the uncertainty of camber angle, defined by digital inclinometer used to perform the angular measurement (see Table 3.2).
- i_{F_y} is the uncertainty of the lateral force, as previously defined (see Table 3.3).

Therefore, according to the test performed, the uncertainty of the vertical force will vary. As an example, Figure 3.28 shows the test with camber angle equal to 25 deg and vertical load set to 600 N. Only positive slip angles are depicted in Figure 3.28, due to symmetry of the results.

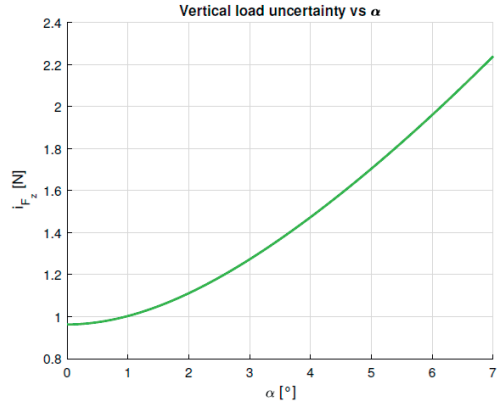

Figure 3.28 – Uncertainty of vertical force as function of slip angle α, depicted only for positive angles.

3.6 Static verification of VeTyT

The aim of this section is to verify that the quantities of lateral force and self-aligning torque can be proper measured.

3.6.1 Lateral force verification

A proper set-up was conceived to verify the effectiveness in the measurements of lateral force, as depicted in Figure 3.29.

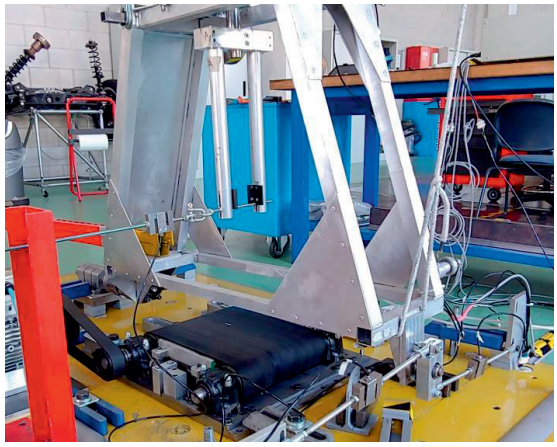

Figure 3.29 – Set-up for the verification of lateral force.

The fork for commercial rim was mounted on the steering shaft. It was loaded with a treaded bar in series with a load cell, proper placed to ensure the perpendicular axis with respect to the longitudinal axis of VeTyT. Once defined the load on the treaded bar, the lateral force F_y was calculated according to (2.4), assuming M_z equal to zero by hypothesis. The measured F_y was compared to the actual value of load applied (F_y''). An increasing force was applied to the treaded bar, and the two signals (F_y'' from the load cell of the treaded bar which measured the actual value of lateral force, F_y derived from VeTyT measurement) were compared in Figure 3.30 as function of acquisition time.

The force measured by VeTyT is slightly higher than the one applied. The difference between signals tends to increase at increasing applied load. The maximum difference is 7.5 N recorded when the load reaches the nominal range of the cell (500 N as declared by manufacturer). Therefore, we can conclude that a mean value of 4.5 N is added to actual applied force. In light of this, the measured lateral force may be reduced of this quantity to improve the quality of the measurements, as shown in Figure 3.31. Referring to accuracy, the lateral force read by VeTyT corresponds to the actual applied force with a mean error less than 0.3%. Referring to precision, the standard deviation is less than 2% with respect to the mean value.

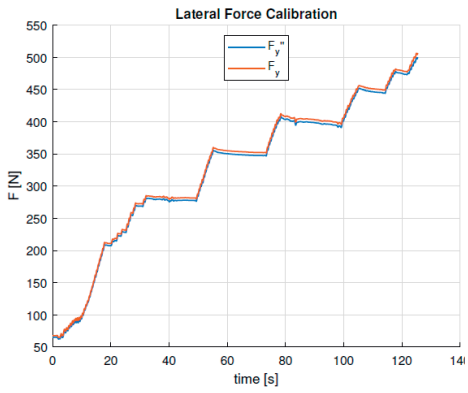

Figure 3.30 – Lateral force verification: comparison between lateral force measured by VeTyT F_y and the one applied to the test-rig (F_y''), as function of acquisition time.

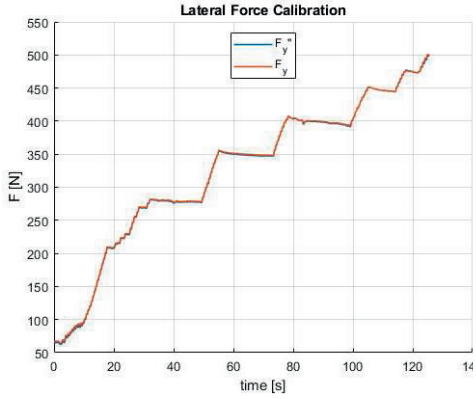

Figure 3.31 – Lateral force verification: a shift of 4.5 N was applied to have the correspondence between the recorded force F_y and the applied one F_y''.

3.6.2 Self-aligning torque verification

To verify the effectiveness of the measurement of self-aligning torque, a proper set-up is required (Figure 3.32). High-stiffness rim was mounted on VeTyT and an instrumented threaded bar was fixed at a given distance a from the hub. A torque can be generated by applying a force F_c to the bar, at a distance a from the axis of the steering shaft. The applied torque M_z'' can be calculated according to (3.29), while the torque measured by VeTyT is evaluated according to (3.1).

$$M_z'' = F_c a \qquad 3.29$$

where a is the lever arm. The presence of bearings which hold the steering shaft may affect the measurements (Figure 3.33, C_1, C_2, C_3). In addition, the friction torque C_4 could be present when the rim is in contact with the ground. In order to minimise as much as possible this effect, a steel plate was placed under the rim and covered with lubricant. A threaded tip was fixed to the high-stiffness rim to have a theoretical "single contact point" between the steel plate and the rim. The set-up is shown in Figure 3.32.

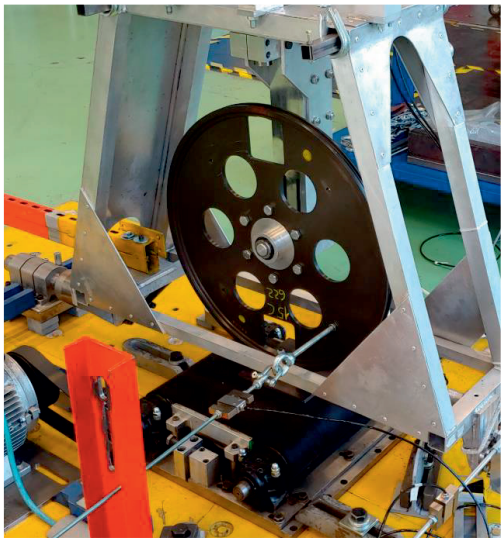

Figure 3.32 – Experimental set-up used to verify the measurement of self-aligning torque. High-stiffness rim is employed, and a threaded bar is fixed to the rim at a known distance from the hub.

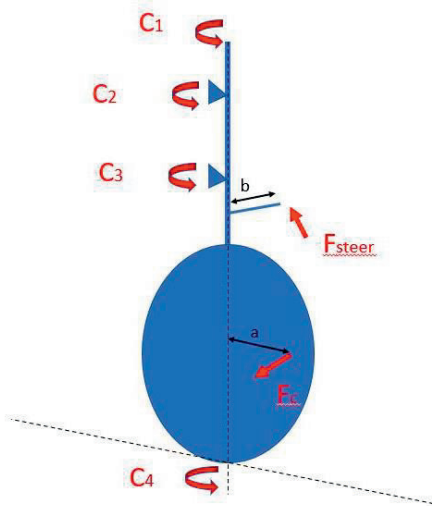

Figure 3.33 – Scheme of rim and steering shaft with the forces and reaction torques of bearings C_1, C_2, C_3. In addition, C_4 represents the moment due to friction rim-ground.

The magnitude of the reaction moment C_4 was evaluated according to formula (3.30)

$$C_4 = T\frac{d}{2} = \mu N\frac{d}{2} \tag{3.30}$$

Friction coefficient μ for lubricated steel on steel contact was estimated to be 0.11 [119] [120]. With a vertical load of 400 N (the load applied during the test) and a maximum arm of 3 mm, according to the diameter of the threaded pin d, we have (3.31):

$$C_4 = 0.11 * 400\ [N] * \frac{0.006\ [m]}{2} = 0.12\ Nm \tag{3.31}$$

The results of the measurements are depicted in Figure 3.34, where M_z is the self-aligning torque measured by VeTyT, and M_z'' is the one applied (5.1).

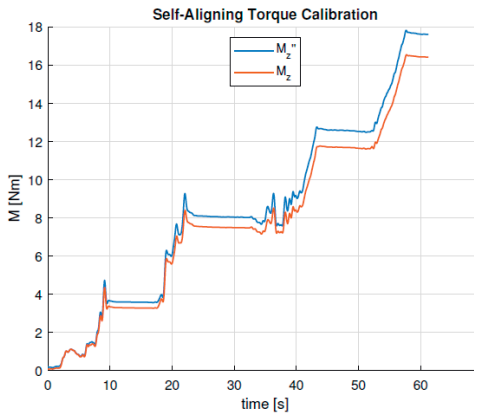

Figure 3.34 – Results of the experimental tests to verify the measurement of self-aligning torque. M_z represents the moment measured by VeTyT, while M_z'' is the one applied.

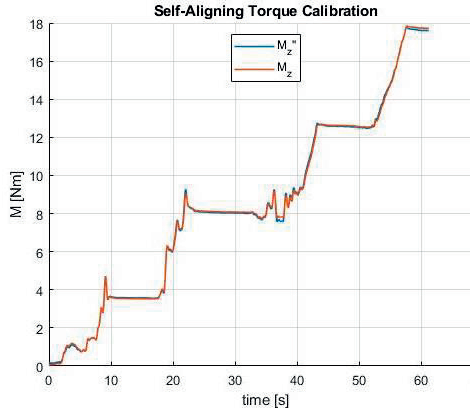

Figure 3.35 – Results of the experimental tests to verify the measurement of self-aligning torque. M_z after the correction of data. Values larger than 8 Nm have been multiplied by 1.1 to have a good agreement between measured and applied loads.

The self-aligning torque measured by VeTyT is underestimated with respect to the actual value applied. As expected, this may be due to the friction of bearings which hold the steering shaft. In addition, the deformation of chassis during the tests may also slightly misalign the bearings, thus increasing the declared friction. The difference increases at increasing the applied torque. During experimental tests, the maximum value of self-aligning torque recorded is around 8 Nm, where the delta between measured and applied moment is equal to 0.55 Nm.
This effect was compensated by multiplying the values larger than 8 Nm by 1.1. This is the result of minimization error procedure between measured and applied loads (Figure 3.35). Referring to accuracy, self-aligning torque measured by VeTyT correspond to the actual applied moment with a mean error less than 1%. As for the precision, the standard deviation was found to be less than 2.5% with respect to the mean value.

3.6.3 Preliminary results

A very first experimental campaign was carried out at the end of the development process. The tests were performed on flat track rolling surface, employing a road racing bicycle tyre of width 25 mm mounted with inner tube on aluminium commercial rim, of internal channel width 17 mm. Lateral force and self-aligning torque were recorded, for tyre inflated at 7.5 bar (value suggested by manufacturer as maximum allowable). Tyre was tested for camber angles up to ±10 deg and slip angles ±7 deg. The vertical loads of 400 N and 490 N were chosen for tests, being compatible with a front bicycle tyre with a rider of 65-75 kg and bicycle 7-10 kg.

Before testing the tyre, alignment procedure must be carried out. As mentioned in Section 3.5.1, chassis is aligned with respect to the rolling surface. Then, the slip angle α is set measuring the actual position of the tyre with respect to the VeTyT chassis. A rule is fixed to the chassis parallel to the longitudinal axis of VeTyT. A depth gauge is placed on the rule, to measure the distance between the axis defined by the rule and the lateral extremities of the rim. The actual slip angle α is obtained as follows (3.32).

$$\alpha = \text{atan}\frac{a-b}{x} \tag{3.32}$$

a and b are the measurements of depth gauge on the left and right side of rim with respect to the wheel hub (according to the scheme of Figure 3.24). x is the distance between the points where the depth gauge is located. After that, the cooling system described in Section 3.3.2 is turned on as well as the motor used to move the rolling surface. Data acquisition can then start.

The results of the tests at vertical load 400 N are presented in Figure 3.36 and Figure 3.37. Different curves stand for different camber angles. The curves are shifted upward or downward according to the value of camber angle, positive or negative respectively (in accordance with the reference system of Figure 3.5 (B)).

Similarly for vertical load 490 N (Figure 3.38 and Figure 3.39), variation of camber angle is the main responsible of the increase in magnitude of lateral force and self-aligning torque, with respect to the test at zero camber angle.

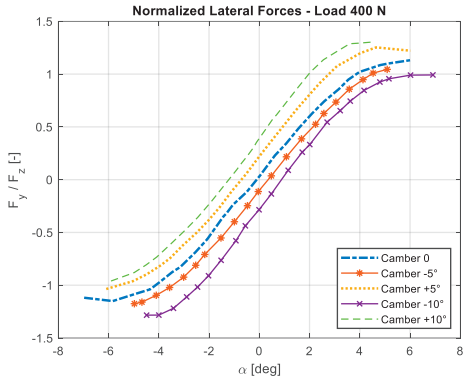

Figure 3.36 – Normalised lateral force F_y as function of side slip angle α. Tyre characteristics were obtained for different camber angles at vertical loads 400 N.

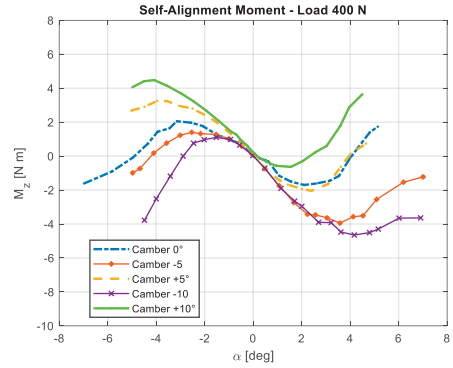

Figure 3.37 – Self-aligning torque as function of side slip angle α for tests performed at vertical load of 400 N.

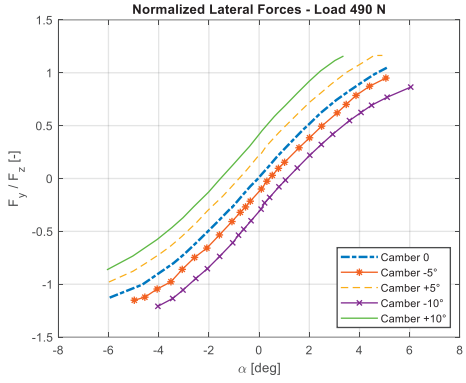

Figure 3.38 – Normalised lateral force F_y as function of side slip angle α. Tyre characteristics were obtained for different camber angles at vertical loads 490 N.

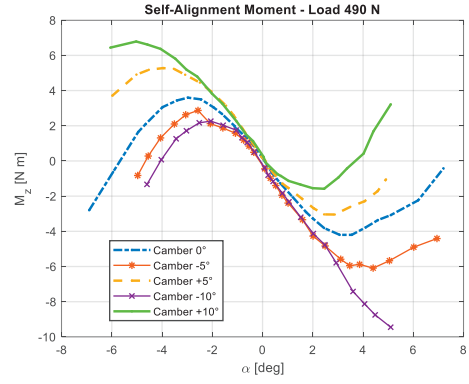

Figure 3.39 – Self-aligning torque as function of side slip angle α for tests performed at vertical load of 490 N.

3.7 Conclusion

This paper presents the development procedure of a new testing machine for bicycle tyre. The device, named VeTyT, is designed to measure the lateral characteristics of bicycle tyres, specifically the lateral force and the self-aligning torque by varying vertical load, inflation pressure, slip angle and camber angle.
Starting from an already manufactured frame, the updates made on VeTyT are described step by step. The main improvements were made to the chassis, with the aim of increasing the stiffness of the device. Aluminium plates of 3 mm thickness were

added using rivets and epoxy adhesive. In addition, steel cables were added to reduce the deformation of the frame as much as possible, as a result of FE analysis.
After that, a signal analysis was performed to verify the effectiveness of the upgrades. The signals before and after the reinforcement were recorded and compared. For the same quantity, a reduction up to 75% in the standard deviation of raw signal was found. At the same time, an increase in about 40% in the torsional stiffness of the system used to hold the tyre steered was appreciated.
The uncertainty model has been then developed on theoretical grounds. The sources of error were considered, to estimate the uncertainties related to the measurement of lateral force, self-aligning torque, vertical force, camber angle and slip angle. The latter was found to have an uncertainty of 0.02 deg, also allowing the effect of ply-steer in the tyre to be evaluated.
An experimental verification of the results was carried out. Given known loads, measurements were performed through VeTyT. It revealed a good agreement between the actual applied loads and those measured. Shifting the recorded lateral force by 4.5 N, the results are essentially overlapped, with an offset less than 1%. As for the self-aligning torque, the measured values must be corrected to ensure good accuracy of the measurements. For values larger than 8 Nm, the results have been multiplied by 1.1 to have a good agreement between measured and applied loads.
In the last section, the results of an experimental campaign were presented. A road racing bicycle tyre mounted on aluminium commercial rim was tested for slip angles ±7 deg and camber angles up to ±10 deg. As expected, large variations in lateral force and self-aligning torque were closely related to the camber angle set.
Summarising the results, we have as follows.

- Test-rig VeTyT allows measuring mechanical characteristics of a wide range of bicycle tyres. Sizes from 16" to 29" (inches) can be tested, as well as width up to 75 mm.
- Rims mounted with "QR system" (Quick Release) or thru-axle can be tested on VeTyT. In addition, tyres can be tested on high-stiffness laboratory rim, to do not affect the results with the deformability of commercial rims.
- A proper uncertainty model was developed for VeTyT measurements. The certification procedure is now in progress.
- Uncertainty of 0.02 deg is ensured for setting the slip angle.
- The verification of lateral force read by VeTyT has allowed to conclude as follows. Referring to the accuracy, the lateral force presents a mean error less than 0.3% with respect to actual applied force. Referring to precision, the standard deviation is less than 2% with respect to the mean value.
- Referring to the accuracy of self-aligning torque, it presents a mean error less than 1% with respect to actual applied moment. Referring to precision, the standard deviation is less than 2.5% with respect to the mean value.

Furthermore, the know-how on bicycle tyres will be important to foster and help in designing new vehicles for micromobility. A deep knowledge of tyre parameters will be crucial to better understand the onset of dynamic instabilities, to improve the safety and the performances of future vehicles.
The test-rig VeTyT has shown very promising results, but still needs some upgrades to decrease the variability, especially in the measurement of self-aligning torque.

The authors report there are no competing interests to declare.

3.8 Acknowledgements

The authors thank Lorenzo Uslenghi, Lorenzo Vaccari and Gianantonio Magnani for their support during the months of hard work and writing. Many thanks to Professor Giorgio Previati, for his advices in the development phase.

Chapter 4

Racing bicycle tyres – Influence on mechanical characteristics of internal pressure, vertical force, speed and temperature

G. Dell'Orto[a,b], F.M. Ballo[a], G. Mastinu[a], M. Gobbi[a], G. Magnani[c]

[a] *Department of Mechanical Engineering, Politecnico di Milano, Via La Masa 1, 20156 Milan, Italy*

[b] *Faculty of Mechanical Engineering ME, Delft University of Technology, Mekelweg 2, 2628 CD, Delft, The Netherlands*

[c] *Department of Electronics, Information and Bioengineering (DEIB), Politecnico di Milano, Via Ponzio 34/5, 20133 Milan, Italy*

CReditT author statement:

G. Dell'Orto: Software; Formal analysis; Investigation; Methodology; Visualization; Writing – Original Draft. **F.M. Ballo**: Software; Investigation. **G. Mastinu**: Project Administration; Resources; Funding acquisition; Supervision; Writing – Review & Editing. **M. Gobbi**: Supervision; Writing – Review & Editing. **G. Magnani**: Supervision.

Published in European Journal of Mechanics - A/Solids, Volume 100, 105010, 2023

ISSN 0997-7538, https://doi.org/10.1016/j.euromechsol.2023.105010

4.1 Abstract

The paper describes how internal pressure, vertical force, speed and rolling surface temperature may affect the mechanical characteristics of a road racing bicycle tyre. The results were obtained from an experimental test campaign performed with VeTyT, a test-rig specifically designed for measuring the mechanical characteristics of bicycle tyres.
The static deflection of tyre for different inflation pressures and vertical loads was measured to determine the static tyre vertical stiffness. Results for tyre rolling on flat track or on a drum were compared. Dynamic analyses were focused on evaluating the effect of inflation pressure and vertical load, for two rims featured by different lateral stiffness. Then, the respective effects of speed and of temperature of the rolling surface on the lateral force were considered.
Stiffer rims can ensure higher values of cornering stiffness. In addition, higher inflation pressure is recommended only for heavy vertical loads. For low vertical loads, too inflated tyre results to be less performant, i.e. to show lower values of cornering stiffness. The speed can affect the mechanical characteristics of bicycle tyres mainly for slip angles less than 1.5 deg, while the temperature of the rolling surface is the most affecting parameter for slip angles larger than 3 deg.

Keywords: flat track; drum; tyre drop; contact patch; inflation pressure; temperature; speed.

4.2 Introduction

After Covid-19 pandemia, many people rediscovered the pleasure of cycling [121]. Cycling is a healthy activity, and it is expected to follow an increasing trend in the upcoming years [5], [71]. To manage and facilitate the transitions through new ways of mobility, it is essential to ensure ride comfort and safety. Some researchers have already dealt with new layouts of road intersections "cycling-friendly" [122], but very few studies are focused on bicycle design [123]. Mathematical models are required to understand bicycle dynamics, but they need to be implemented with realistic tyre parameters [124], [125]. Tyres are very important to ensure safer vehicle handling, since their mechanical characteristics can strongly affect vehicle dynamics [28] [25], [126] This statement is even more important for two wheeled vehicles, such as motorcycles and bicycles, featured by a relatively small contact patch between tyre and road [43] [44]. As well as motorcycle tyres, bicycle tyres are featured by a toroidal cross-section of the carcass [26], [32], but they are completely different in construction and usage, being designed for much smaller loads. In [60], bicycle tyres were tested for different working conditions. A decrease in lateral force was recorded with a decrease in inflation pressure. This phenomenon was explained considering a reduced lateral stiffness when the inflation pressure decreased. In addition, it was noted that

an increase in vertical load resulted in a decreased normalised lateral force. Similar tests were performed in [56], where a set of mountain bike tyres was tested for different vertical loads and inflation pressures. It was found an increase in cornering stiffness with the pressure. Above a certain pressure, all the tyres showed a constant value of cornering stiffness. The latter is useful for modelling, since it may affect vehicle dynamics [48].

It is important to understand how different parameters may affect tyre characteristics. Despite this, very few studies are presented on this topic. Bicycle-rider models often lack information on tyres [36]. Shimmy (or "wobble") is a dynamic instability which may affect bicycles (especially road racing bicycles, running at high speed). Some mathematical models have been presented in the past, trying to understand the phenomenon. Nonetheless, the researchers pointed out the necessity to have measured tyre characteristics to refine the models [51] [47]. This paper tries to close the gap, providing measurements of the mechanical characteristics of road racing bicycle tyre to some extent. Both static and dynamic analysis are carried out on a 26 mm wide road racing bicycle tyre, mounted on aluminium commercial rim and on high-stiffness laboratory rim in order to investigate the effect of rim stiffness on lateral characteristics. The static tests involve tyre not rolling on the contact surface, therefore tyre deflection and contact patch measurements varying inflation pressure and vertical load (Section 4.4). Dynamic contact patches are still hard to measure on such test-rig, as a proper test bench should be implemented to the purpose [127]. The dynamic tests were performed with tyre rolling on the contact surface to measure the lateral force F_y and the self-aligning torque M_z (Section 4.5). Tests were performed both on flat track and on a 2.6 m diameter drum (known as "RuotaVia" [101]). The effect of inflation pressure, vertical load and rim stiffness was evaluated on lateral force and cornering stiffness. After that, the focus is devoted to the effect of the speed on the variation of lateral force. Finally, it is studied how the rolling surface temperature can affect the lateral force F_y.

4.3 Methods

Tests are performed with VeTyT, a testing machine specifically designed for bicycle tyres [100] [62]. The measuring procedure has been certified in accordance with the standard UNI EN ISO 9001-2015.

The aluminium frame carries a bicycle tyre on a flat track or on the top of a drum. The whole chassis can be tilted to set the camber angle in the range ±25 deg, while the slip angle α can be adjusted rotating the steering shaft. The vertical load acting on the wheel can be varied adding masses on the frame. It can measure lateral force, self-aligning torque and vertical force. The complete assembly of the test-rig is shown in Figure 4.1.

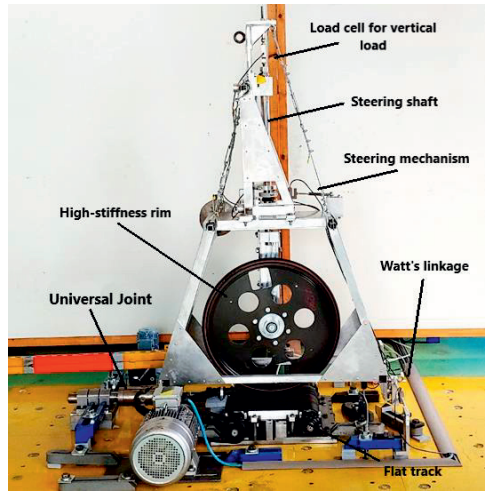

Figure 4.1 – VeTyT test-rig at Politecnico di Milano. In this picture, the frame carries a high-stiffness laboratory rim running on flat track [64].

Tests were performed on a road racing bicycle tyre (26 mm wide), for different inflation pressures, ranging from 3.5 to 7.5 bar, declared by manufacturer as upper limit. The value of 3.5 bar was chosen to simulate a wrong inflation pressure or a flat tyre after punching. The tyre was mounted with inner tube.
Three different vertical loads were tested: 340 N, 400 N and 490 N. The values were chosen being consistent with the mass of common riders and bicycles, as reported in Table 4.1.

Table 4.1 – Rider/bicycle mass, load distribution front/rear, tyre vertical load.

Rider mass	Bicycle mass	Load ratio	Vertical load on tyre
58 kg	10 kg	50/50	≈ 340 N
70 kg	10 kg	50/50	≈ 400 N
88 kg	10 kg	50/50	≈ 490 N

The load ratio represents the load distribution front/rear wheel of the bicycle. The value 50/50 is compatible with road racing bicycles [128], while the bicycle mass of 10 kg is feasible for a carbon frame bicycle equipped with two water bottles and pedals.

4.4 Static analysis

4.4.1 Static tyre deflection

Static tyre deflection (also known as tyre drop) corresponds to the tyre deflection due to the application of a vertical load [129] [130]. It is a quantity of interest since it is

related to the extension of contact patch and can be assumed as a reference for setting the optimal tyre inflation pressure [131]. From the knowledge of static tyre deflection, the normal stiffness can also be derived.
The static tyre deflection (tyre drop) was measured both on a flat track and on the RuotaVia drum [101]. Tyre was mounted on aluminium commercial rim and tested for different inflation pressures and vertical loads.

4.4.2 Methods

VeTyT was used for the measurements of the static tyre deflection. A 26 mm wide road racing bicycle tyre was mounted with inner tube on an aluminium commercial rim. A proper gauge was employed to measure the height. It was placed on the base of the rolling surface (flat track or RuotaVia drum, respectively), so that its probe was in contact with the rim (set-up depicted in Figure 4.2). After the application of vertical load, the difference between the undeformed and deformed height of the tyre was recorded. Three different vertical loads were applied (340 N, 400 N and 490 N), for inflation pressures ranging from 3.5 bar to 7.5 bar. All the experiments were led in laboratory at room temperature (23±4 °C), and tests were repeated three times and averaged.

Figure 4.2 – Set-up for measuring the static tyre deflection with VeTyT, here depicted for RuotaVia drum.

4.4.3 Results

In Figure 4.3, the static tyre deflection is depicted as function of vertical load for different inflation pressure, for the tests on the flat track. The relationship between tyre drop and vertical load results to be almost linear for all the tested inflation pressures. The same can be concluded for the RuotaVia drum (Figure 4.4), since the trend is linearly increasing with the vertical load. As expected, the increase in vertical load causes a larger deflection of the tyre, independently of the inflation pressure. On the RuotaVia drum (Figure 4.4), the maximum values achieved are larger than those measured on the flat track, for all the tested inflation pressure values. This can be

explained considering the shape of the contact patch tyre/rolling surface. The curvature of RuotaVia drum affects the contact patch length, acting on a smaller contact area.

It can be assumed that the contact patch length decreases at increasing curvature of the rolling surface ($\frac{1}{R'}$, where R stands for RuotaVia radius) [132]. When the radius of drum is significantly smaller than the radius of the tyre, the contact patch could be schematised as a single point (Figure 4.7). The area of the contact patch decreases at increasing the curvature of the contact surface. According to this statement, a smaller portion of the tyre should sustain the vertical load, so that a higher value of tyre drop is expected. Therefore, a smaller value of vertical stiffness for the measurements performed on RuotaVia drum is expected.

On average the values of static deflection of tyre measured on RuotaVia are 18% larger than those measured on flat track (see Table 4.2).

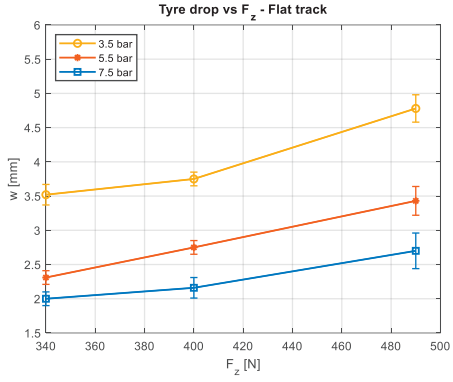

Figure 4.3 – Tyre drop as function of vertical load, for different inflation pressure (see legenda), here depicted for flat track. A 26 mm wide tyre was tested.

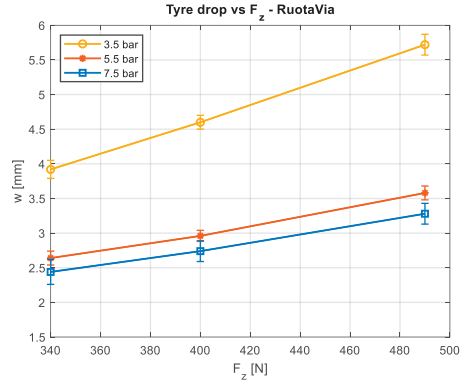

Figure 4.4 – Tyre drop as function of vertical load, for different inflation pressure (see legenda), here depicted for RuotaVia. A 26 mm wide tyre was tested.

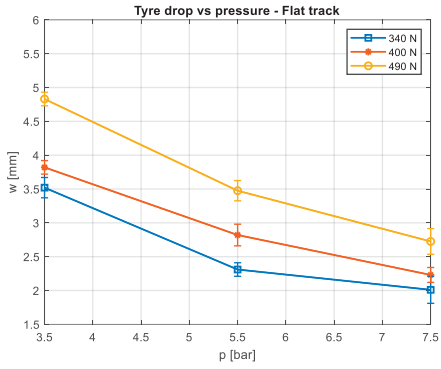

Figure 4.5 – Tyre drop as function of inflation pressure, for different vertical loads (see legenda), here depicted for flat track (26 mm wide tyre).

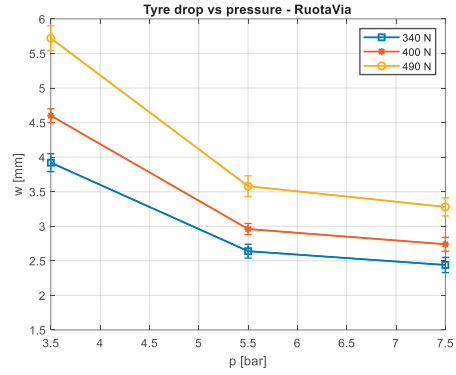

Figure 4.6 – Tyre drop as function of inflation pressure, for different vertical loads (see legenda), here depicted for RuotaVia. A 26 mm wide tyre was tested.

Concerning the tyre drop as function of inflation pressure, the trend is linearly decreasing at increasing the inflation pressure, for tests on the flat track (Figure 4.5). As expected, larger pressures mean higher load capacity, so less static deflection at constant vertical load. The behaviour is slightly different for the RuotaVia drum (Figure 4.6). As already mentioned for Figure 4.3 and Figure 4.4, the deflection values for the RuotaVia drum are larger than those recorded for the flat track.

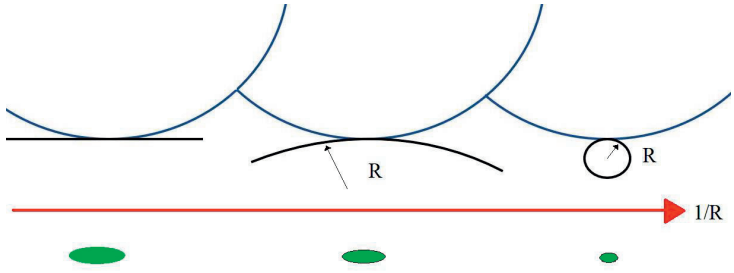

Figure 4.7 – Contact patch variation at increasing the curvature of the rolling surface. In green, the expected contact patch, in blue the tyre, in black the rolling surface. At left, the case of R equal to ∞, i.e. the flat track. At right, the case with R close to zero, so curvature very large.

The values of static deflection of tyre tested on flat track and on RuotaVia drum are summarised in Table 4.2. The results on RuotaVia drum and on flat track are evaluated in the last column. As already mentioned, an average variation of 18% can be appreciated, being the values on RuotaVia drum always larger than those on flat track.

Table 4.2 – Measurement of tyre drop for flat track and RuotaVia drum (2.6 m diameter), and the% variation of results. The values were obtained for a 26 mm wide tyre.

Pressure [*bar*]	**Vertical Load** *[N]*	**Tyre drop** w *[mm]* **– Flat track**	**Tyre drop** w *[mm]* **– RuotaVia drum**	**% Variation RuotaVia drum VS Flat track**
3.5	340	3.52	3.92	11%
	400	3.75	4.60	22%
	490	4.78	5.72	20%
5.5	340	2.31	2.64	14%
	400	2.75	2.96	7%
	490	3.43	3.58	4%
7.5	340	2.00	2.44	22%
	400	2.16	2.74	27%
	490	2.70	3.28	21%

Comparing the results, it is clear the difference in magnitude for the tests on the RuotaVia drum and on the flat track. All the results on flat track are smaller than those on RuotaVia drum, for all the considered vertical loads and inflation pressures.
The evaluation of vertical stiffness was then carried out linearly interpolating the experimental data. The results are shown in Figure 4.8 and Figure 4.9. The vertical stiffness corresponds to the slope of the curves, as reported in the legenda of the Figures below. The vertical stiffness increases as inflation pressures increases, both for RuotaVia and flat track.

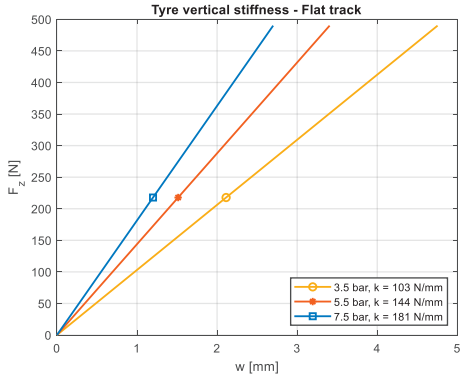

Figure 4.8 – Tyre drop as function of vertical loads, for different inflation pressure. Results obtained on flat track.

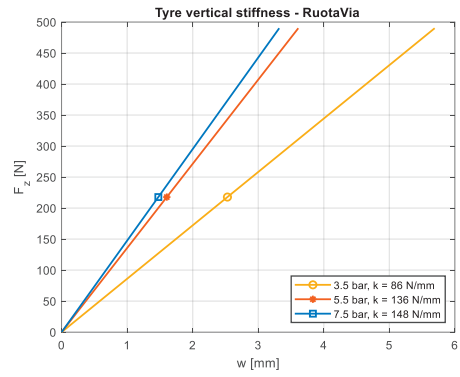

Figure 4.9 – Tyre drop as function of vertical loads, for different inflation pressure. Results obtained on RuotaVia drum.

The comparison of the results is summarised in Table 4.3. Vertical stiffness measured on the RuotaVia drum is always less than that on the flat track. On average, a reduction of 14% was found. A reduction in contact area due to the shape of contact patch tyre/drum may be the main cause of this difference, as explained above.

Table 4.3 –Vertical stiffness, comparison for results from RuotaVia and flat track, tested for different inflation pressures.

Pressure *[bar]*	K_z *[N/mm]* – **Flat track**	K_z *[N/mm]* – **RuotaVia**	**% Variation RuotaVia VS Flat track**
3.5	103.1	86.1	-16%
5.5	143.9	135.7	-6%
7.5	181.5	147.6	-18%

4.4.4 Tyre contact patch

An analysis to evaluate the area and the shape of contact patch on RuotaVia drum or on flat track was carried out. Contact patches were experimentally determined both using pressure sensitive film and chalk dust.

A sensitive pressure film was placed under the tyre, so as to impress on it the shape of the contact patch (Figure 4.11). Then, the film was scanned and post-processed through an ad hoc MATLAB® script. It was possible to measure the total area and the pressure distribution. Tests were performed for different inflation pressures and vertical loads. For the sake of accuracy, measurements were then repeated covering the tyre with chalk powder. A black cardboard was placed under the contact surface (Figure 4.10). As first approximation, the contact patches were assumed to be elliptical. The lengths

of major and minor axis (we refer as a and b, respectively) were measured through a gauge. The area was calculated according to (4.1)

$$Area = a\ b\ \pi \tag{4.1}$$

Contact patches were then scanned and processed by the software IMAGEJ®, usually employed in the field of microbiology [133] [134]. The effectiveness of considering contact patch as an ellipse was confirmed, with a difference less than 5% on the total area measured with (4.1). Results were also confirmed for the pressure sensitive film. The contact patches on flat track are on average 12% larger than those on RuotaVia drum. The difference is related to the curvature of the RuotaVia drum, which affects the shape of the contact. It mainly changes the length of contact patch, with a reduction from RuotaVia drum to flat track in the order of 10%. Increasing the vertical load, the difference in contact patch area decreases.

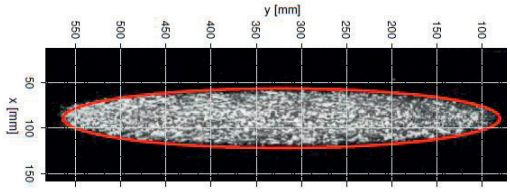

Figure 4.10 – Contact patch obtained with chalk powder and a black cardboard, on flat track. In red, the ellipse approximation of the contact patch.

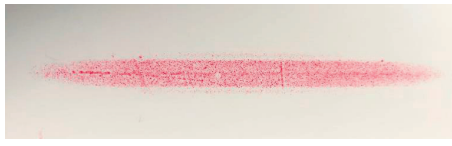

Figure 4.11 – Contact patch obtained with pressure sensitive film.

4.5 Dynamic measurements

4.5.1 Combined effect of inflation pressure and vertical load on cornering stiffness

The dynamic tests on bicycle tyres were performed on flat track, with tyre mounted both on a commercial rim and on a high-stiffness rim. Flat track surface was covered by sand of controlled granulometry (1.2 mm), to simulate the road surface.
The cornering stiffness can be evaluated according to (4.2)

$$C_{F_y} = \frac{\delta F_y}{\delta \alpha}|_{\alpha=0} \tag{4.2}$$

Once measured the lateral force F_y as function of slip angle α, C_{F_y} can be derived. The values of cornering stiffness evaluated according to (4.2) are depicted in Figure 4.12 and Figure 4.13 for standard aluminium rim and high-stiffness laboratory rim, respectively. The values were then interpolated with high-order polynomial, to understand the relationship between cornering stiffness and vertical load applied to the tyre.

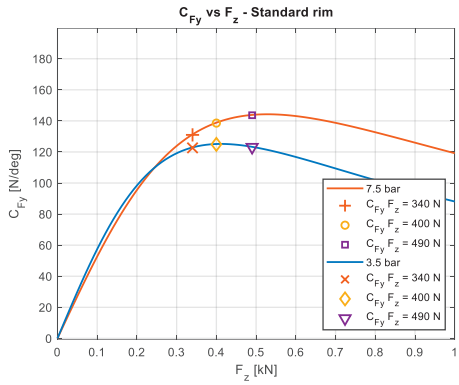

Figure 4.12 – Cornering stiffness C_{F_y} as function of the vertical load F_z. The red curve is for inflation pressure of 7.5 bar, the blue one is for 3.5 bar. Tyre was tested on flat track, mounted on standard commercial rim.

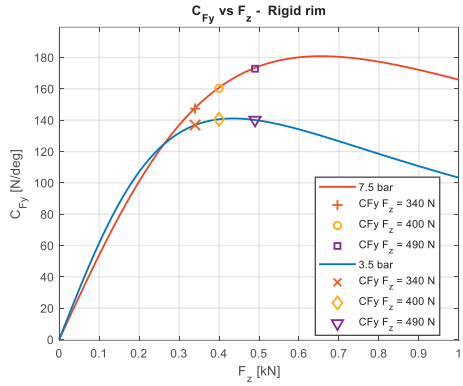

Figure 4.13 – Cornering stiffness C_{F_y} as function of the vertical load F_z. The red curve is for inflation pressure of 7.5 bar, the blue one is for 3.5 bar. Tyre was tested on flat track, mounted on high-stiffness rim.

The value of C_{F_y} largely changes with inflation pressure. As depicted in Figure 4.12, the values for the inflation pressure of 7.5 bar are higher than those for inflation pressure 3.5 bar. The peak of cornering stiffness for inflation pressure 7.5 bar corresponds to the maximum tested vertical load of 490 N. The trend is not confirmed for lower inflation pressures, where the peak of cornering stiffness can be found for lower vertical load. Similar trend was also found for tyre mounted on high-stiffness rim (Figure 4.13), which can strongly affect the tyre performance. The highest values of cornering stiffness are obtained with the stiffest rim (Figure 4.13). The rim used for these tests is approximately five times stiffer than a standard aluminium rim. The results of cornering stiffness for the tested rims are summarised in Table 4.4. Independently on the inflation pressure or on vertical load, the value of C_{F_y} is on average 13% higher for the high-stiffness rim.

Table 4.4 – Cornering stiffness values for tyre mounted on standard aluminium rim and high-stiffness rim, for different inflation pressures and vertical loads. The percentage of variation of the cornering stiffness for different rims (standard or high-stiffness one) is reported in the last column.

$p\ [bar]$	$F_z\ [N]$	$C_{F_y}\ [N/deg]$ (U=1.5%) **Standard rim**	$C_{F_y}\ [N/deg]$ (U=1.5%) **High-stiffness rim**	**Variation High-stiffness rim VS Standard rim**
3.5	**340**	122.6	136.9	+12%
	400	124.9	140.6	+12%
	490	123.1	140.1	+14%
5.5	**340**	131.1	145.3	+11%
	400	137.7	155.2	+13%
	490	141.2	163.2	+16%
7.5	**340**	131.0	147.4	+13%
	400	138.6	160.3	+16%
	490	143.7	172.9	+20%

The effect of inflation pressure is also crucial for ensuring good performance. Both for standard and high-stiffness rim, an increase in inflation pressure means an increase in cornering stiffness. This trend was found only for vertical loads larger than a certain threshold equal to 400 N. Below that value, a tyre less inflated seems to perform better. This can be understood thinking about the need of adjusting pressure according to vertical load [131]. A too inflated tyre shows a small contact patch if the vertical load is not sufficient to push the tyre on the road. Another experimental campaign was carried out on a different model of 26 mm wide road racing bicycle tyre, tested on flat track and mounted on standard rim to validate the hypothesis. Tests were performed with many different inflation pressure and vertical loads (Figure 4.14).

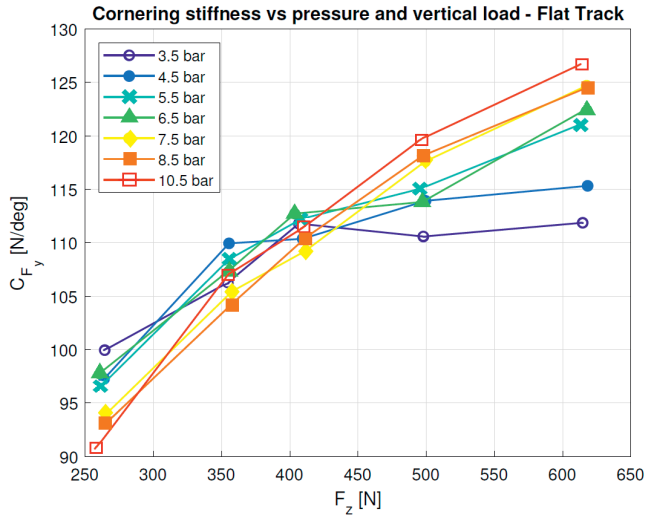

Figure 4.14 – Cornering stiffness for a 26 mm road racing bicycle tyre as function of vertical load. The curves of different colors correspond to different inflation pressures. Tests were carried out on flat track.

Looking at Figure 4.14, we can notice that for a vertical load close to 250 N a lower inflation pressure is required to ensure higher values of cornering stiffness. On the contrary, higher inflation pressures result in high cornering stiffness for large vertical loads (clearly visible for vertical load larger than 600 N).

4.5.2 Effect of the speed

The effect of the rolling speed on the lateral force of bicycle tyre was evaluated. Tests were performed on the flat track by varying the speed of the rolling surface between 4 km/h up to 23 km/h.
A 26 mm wide road racing bicycle tyre was tested for a vertical load equal to 400 N and inflation pressure of 7.5 bar. The results for lateral force are depicted in a carpet plot for positive slip angles only (Figure 4.15). This allows to appreciate the variations of lateral force F_y increasing the speed of the rolling surface.
For slip angles close to zero, the lateral force slightly increases linearly with the speed.

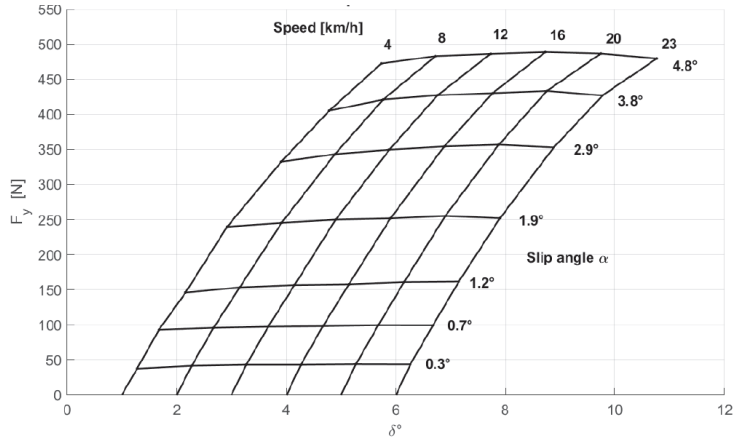

Figure 4.15 – Influence of the speed of rolling surface on the lateral force. In the upper part of the plot, the values of speed are reported. At right, values of slip angles are shown.

Considering slip angles higher than 2 deg, the trend of variation is no more linear. Lateral force achieves a maximum for the speed equal to 16 km/h, then it slightly decreases. This phenomenon may be due to increase in the temperature of the rolling surface. Lateral force is expected to linearly increase with the speed, but for high slip angles the heat generated by the friction between the flat belt and the supporting surface increases as well. The effect of the temperature generates a decrease in the measured lateral force, as discussed in the next section.

Table 4.5 summarises the percentage of variation of the measured lateral force with respect to the lowest speed tested (4 km/h), taken as reference. It can be noticed that the lateral force increases as the speed of the rolling surface increases, almost linearly for slip angles less than 2 deg. The trend changes for high slip angles, for which the effect of the temperature may affect the measurements [64].

Table 4.5 – Percentage variation of the lateral force with respect to the values measured at speed 4 km/h, up to 23 km/h. A 26 mm wide tyre was tested.

Δ_{F_y} %		$Speed\ [km/h]$					
		4	8	**12**	**16**	**20**	**23**
$Slip\ angles[\ deg]$	**0.3**	0	12	16	15	17	16
	0.7	0	3	5	6	7	7
	1.2	0	5	8	8	10	11
	1.9	0	2	4	5	6	5
	2.9	0	3	5	7	7	6
	3.8	0	4	5	6	7	5
	4.8	0	2	3	3	3	1

The values reported in Table 4.5 demonstrate that the effect of the speed variation is almost negligible for slip angles larger than 2 deg. On the contrary, the effect of the temperature must be considered as detrimental for the measurements for high speeds of the rolling surface and high slip angles. VeTyT has been recently updated for compensating this effect. A cooling system was designed and implemented to remove the heat close to the contact patch tyre/flat track [100].

4.5.3 Effect of the temperature

In this Section, the effect of temperature variation on the lateral force of bicycle tyre is studied. A 26 mm wide road racing bicycle tyre was used for the tests, mounted on high-stiffness laboratory rim. Specifically, the main parameter of interest is the temperature of the rolling surface. This is simpler and more accurate to be measured if compared to the tyre external surface [135] [136]. In addition, it may be the independent variable of interest for riders and cycling professional teams. The vertical load was set to 400 N and the inflation pressure to 7.5 bar.
The lateral force was measured and plotted as function of the temperature of the flat track. The latter was measured with an infrared thermometer and a thermocamera in the area close to the contact patch. In Figure 4.16, the lateral force is reported as function of the recorded temperature. The slip angle was set to 3.3 deg.

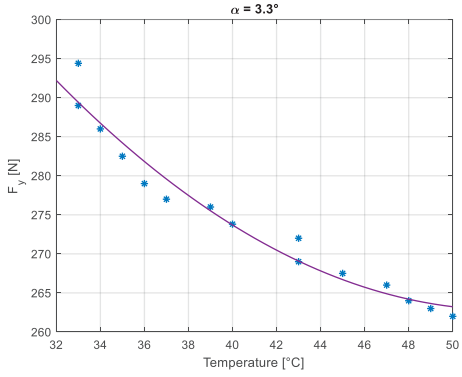

Figure 4.16 – Lateral force as function of recorded temperature of flat track, for slip angle equal to 3.3 deg. In violet the data interpolating line (second order polynomial interpolation).

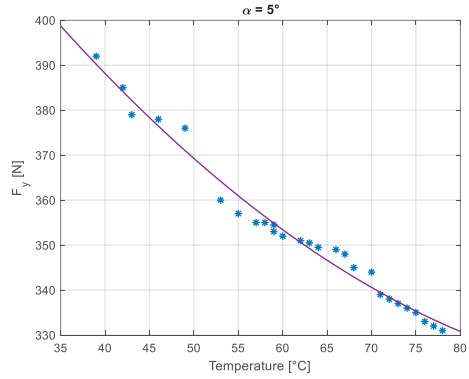

Figure 4.17 - Lateral force as function of recorded temperature of flat track, for slip angle of 5 deg. In violet the data interpolating line (second order polynomial interpolation).

It is possible to note the remarkable correlation between the decrease in the measured values and the increase in temperature. While the temperature increases from 32 °C to 50 °C, the lateral force decreases of 11%, showing a quadratic decreasing trend. Additional tests were performed setting the slip angle at 5 deg. The results are collected in Figure 4.17. We can note that data follow a quadratic decreasing trend, as

well as results for slip angle equal to 3.3 deg. Increasing the temperature, the lateral force decreases 16% for a variation in temperature of 40 °C. The important role played by the temperature is even more evident for large slip angles.
The decreasing trend with the increase in temperature is confirmed for slip angles $|\alpha| > 3\ deg$. Repeating the test for slip angle equal to 1 deg, the results are completely different, as shown in Figure 4.18. The variability is much smaller and limited to less than 1% for lateral force.

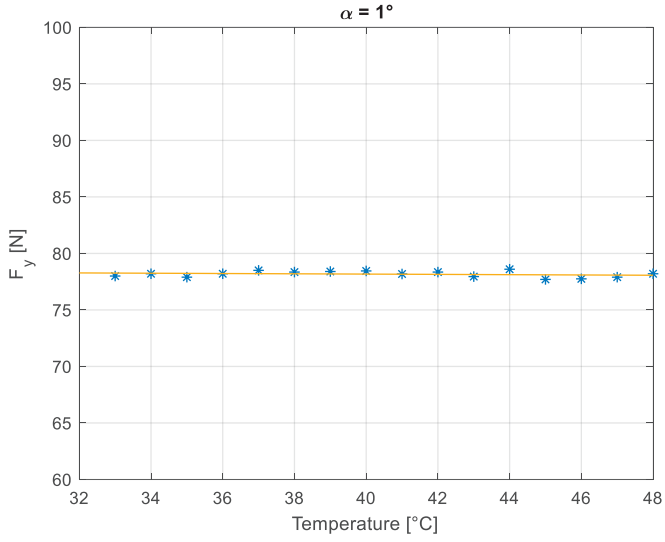

Figure 4.18 - Lateral force as function of recorded temperature of flat track, for slip angle equal to 1 deg. Data can be interpolated by a straight line.

Observing Figure 4.18, values are almost constant and can be interpolated by a straight line (angular coefficient equal to 0.01). Repeating tests for other slip angles $|\alpha| < 3\ deg$ a clear trend cannot be distinguished, but variability remains however lower than 2% for lateral force.
These effects could be relevant considering paved roads during summer, when the presence of shaded corners may cause a sudden increase/decrease in road temperature, thus changing the bicycle handling. This is strictly connected to bicycle dynamics, and it could be relevant for the occurrence of sudden and dangerous dynamic instabilities [45], [47].

4.6 Conclusions

In the paper, the results of some external parameters on the mechanical characteristics of a 26 mm road racing bicycle are presented. Both static and dynamic tests were performed.

Specifically, it was considered the effect of the inflation pressure, vertical load, type of rolling surface (flat track or drum), stiffness of the rim, speed and temperature.
Vertical stiffness was statically measured for different vertical loads and inflation pressure, both on a flat track and the RuotaVia drum (drum of 2.6 m of diameter). Static tyre vertical stiffness is defined as the ratio between the applied load and the static deflection of the tyre. Static deflection is important since manufacturers provide recommended inflation pressure on the basis of the static deflection, also known as "tyre drop".
Summarizing the results obtained from tests, we have:

- The static deflection on RuotaVia was found to be on average 18% higher than one measured on flat track, for all vertical loads and inflation pressures tested. The curvature of RuotaVia drum may affect the contact patch length, acting as a punch in the middle of contact area. As a consequence, the vertical stiffness on the RuotaVia drum was found to be higher than that one on the flat track.
- The curvature of the RuotaVia drum mainly changes the length of contact patch, with a reduction from RuotaVia drum to flat track in the order of 10%. The area of contact tyre/rolling surface that is on average 12% reduced with respect to flat track.
- A correct inflation pressure is hard to recommend. Nowadays, manufacturers consider the static deflection or the feeling of the rider to define an optimal inflation pressure. The latter affects many parameters, so that a deeper study is necessary to define a standardised method useful to define the best inflation pressure.
- The stiffness of the rim largely affects the lateral characteristics of the tyre. It was found that the use of high-stiffness rim can ensure up to 13% higher cornering stiffness for tyres tested under the same working conditions.
- The study of the combined effect of inflation pressure and vertical load may be a good approach to suggest the best set-up for tyres; nonetheless a synthetic index useful for final user is still hard to find since the measurements strongly depend on other variables such as speed and temperature of the rolling surface.
- The effect of the speed on the lateral force does not affect so much the measurement of the lateral force F_y, nonetheless the increase in speed means higher energy to be dissipated to avoid the detrimental effect of the temperature.
- Temperature of the rolling surface can largely affect the measurements. Specifically, an increase in temperature of 40 °C causes a decrease in lateral force about 16%. This aspect may change bicycles dynamics, especially on paved roads featured by the presence of shaded corners during summer days.

In the future, it will be of great interest to test different type of bicycle tyres such as trekking or mountain bike tyres, featured by the presence of knobbles. The focus will

be also devoted to the camber effect. Furthermore, a strong effort is required to provide synthetic indexes useful for final users to proper set tyre parameters.

The authors report there are no competing interests to declare.

4.7 Acknowledgements

The authors thank Lorenzo Uslenghi, Lorenzo Vaccari and Prof. Giorgio Previati for their support during the months of experimental test campaign.

Chapter 5

Racing bicycle tyres – Experimental indoor evaluation of relaxation length

G. Dell'Orto[a,b], F.M. Ballo[a], G. Mastinu[a], M. Gobbi[a], G. Magnani[c]

[a] *Department of Mechanical Engineering, Politecnico di Milano, Via La Masa 1, 20156 Milan, Italy*

[b] *Faculty of Mechanical Engineering ME, Delft University of Technology, Mekelweg 2, 2628 CD, Delft, The Netherlands*

[c] *Department of Electronics, Information and Bioengineering (DEIB), Politecnico di Milano, Via Ponzio 34/5, 20133 Milan, Italy*

CReditT author statement:
G. Dell'Orto: Software; Formal analysis; Investigation; Methodology; Visualization; Writing – Original Draft. **F.M. Ballo**: Software; Investigation. **G. Mastinu**: Project Administration; Resources; Funding acquisition; Supervision; Writing – Review & Editing. **M. Gobbi**: Supervision; Writing – Review & Editing. **G. Magnani**: Supervision.

Published in Meccanica, Volume 58, 1523–1537, 2023

https://doi.org/10.1007/s11012-023-01684-z

5.1 Abstract

The paper presents the measurement of the relaxation length of road racing bicycle tyres. In the paper the relaxation length is given as the ratio between cornering stiffness and lateral stiffness of the tyre. Tests were performed with VeTyT, a test-rig specifically designed for measuring the lateral characteristics of bicycle tyres. The results from road racing bicycle tyres of two different brands are discussed. Then, a comparison is presented between of 26 mm and 28 mm wide racing tyres. The tyres were tested both on a flat track and on a drum of 2.6 m diameter. The relaxation length for tests on flat track resulted to be on average 15% higher than the ones on drum, for the same vertical load and inflation pressure. In addition, the large role played by inflation pressure on the relaxation length was discovered. Since the relaxation length may affect the bicycle dynamics, the study provides the first quantitative information for the further development of safer and more performant bicycles.

Keywords: lateral characteristics; inflation pressure; test-rig; dynamics; wobble

5.2 Introduction

In this paper, the relaxation length has been evaluated for bicycle tyres, by varying vertical load, inflation pressure and rolling surface. The relaxation length related to the lateral force has been exclusively considered since it has the largest effect on the stability of the bicycle [137].

Bicycle dynamics has been studied since the last decade of 19th century [138] [50]. Bicycles are featured by large camber angles when moving along a curvilinear path [40] [139], so that tyre properties are very important for stability and handling. Tyre is the only part of the vehicle conceived to connect the vehicle itself to the ground. The interaction between tyre and ground is therefore crucial for vehicle dynamics [140] [141]. This aspect is even more important for single-track vehicles, for which tyre properties may largely affect the stability and safety [142] [25]. Realistic dynamic simulations need therefore to be updated with accurate tyre parameters [143].

With reasonable approximation, the lateral tyre dynamics can be described by a first order differential equation, where the time constant is given by the relaxation length divided by the speed [13]. The relaxation length is a transient property parameter of tyres which describes the lag of the tyre response when subjected to a sudden variation of slip angle [24].

Despite the large role played by tyres on bicycle dynamics [48], very few studies have been published on this topic. Most of them are focused on car or motorcycle tyres [25]. The role of the tyre relaxation length on the stability of motorcycles has been addressed in [32] [144]. A proper representation of motorcycle dynamic characteristics needs the introduction of tyre relaxation properties [32]. In particular, weave and wobble modes can be considerably affected by variations of tyre parameters. Increasing the value of

relaxation length leads to the destabilization of a single-track vehicle. In [145], the stability of a new motorcycle with four wheels is studied considering linear differential equations for tyres. In [146] an advanced multi-body code for motorcycle modelling takes into account the tyre transient response (i.e. relaxation length).
The relaxation length was estimated for motorcycle and scooter tyres in [147], for inflation pressure ranging from 0.5 to 4 bar. Considering the rigid ring model [148], a modal analysis of the tyre was presented, and the stiffness properties were identified. The results were then compared with those derived from experimental tests performed on test-rig at University of Padua [62] [95], with a difference of 20% for radial tyres inflated at 2 bar. Considering diagonal tyres, the difference was found to be 30-50%, showing the necessity of experimental tests.
Based on the results related to motorcycles, similar behaviour is expected for bicycles. The occurrence of dynamic instabilities like wobble [46] [47] may be affected by tyre parameters [149]. Specifically, relaxation length and cornering stiffness were found to be among the most influential parameters for wobble [43]. Similar conclusions were also drawn in [52]. Cornering stiffness and relaxation length are strictly related to tyre inflation pressure and, according to the simulations on a Carvallo-Whipple bicycle model extended by lateral slipping [50], they might cause the destabilization of wobble mode.
A study on the influence of tyre forces on bicycle stability was also addressed in [58]. The relaxation length was discovered to affect the occurrence of wobble mode. In particular, an increase in relaxation length together with a decrease in cornering stiffness destabilised the wobble mode. Furthermore, the introduction of relaxation length into the tyre model added new high frequencies unstable modes.
A set of simulations was performed in [150] to analyse the influence of geometrical, compliance and tyre parameters on road racing bicycle stability. Using a hands-on bicycle model presented in [149], it was discovered that the stability of wobble model decreased with an increase in relaxation length.
The relaxation length for light scooter tyres was identified in [147], using proper test-rig [142],[60]. They applied harmonic excitations and measured the input motion with a gyro. Lateral force was recorded by load cell of the test-rig. Signals were then fitted with sine functions, and the phase lag was calculated to derive the relaxation length. In [96], cornering stiffness and lateral stiffness were evaluated for bicycle tyres.. Then, the relaxation length was evaluated as the ratio between cornering stiffness and lateral stiffness, as suggested in [25].
Despite the important role played by tyre parameters in bicycle dynamics, only a few studies on the measurement of tyre characteristics can be found in literature [62]. This is mainly due to the difficulties in performing measurements with a low signal-to-noise ratio [62]. The evaluation of relaxation length is even more rarely addressed by researchers, and a set of accepted parameters for each kind of tyre is still not available. This paper aims to provide an accurate measurement of the relaxation length for racing bicycle tyres, trying to close the gap on the lack of data in this field of research. In this

way, we are contributing to build a database to enable parametric analysis of different bicycles, continuing the work of Moore et al. [143].
The measurement of tyre characteristics presented in this paper are performed through VeTyT (Velo Tyre Testing) [14] [102], a test-rig specifically designed for measuring the mechanical characteristics of bicycle tyres, located at the Department of Mechanical Engineering of Politecnico di Milano. Tests were performed on 26 mm and 28 mm wide road racing bicycle tyres from two different market leader brands. In addition, a comparison between results on flat track and on RuotaVia (a 2.6 m diameter drum [151]) was performed.
The measurement of the relaxation length was made in this paper resorting to the lumped parameter model by Von Schlippe-Dietrich [25], [152]. In such a model the tyre contact is a point, and the lateral compliance is given by a simple spring. In this case the relaxation length is simply the ratio between the cornering stiffness and the lateral stiffness. For sake of simplicity, we do not perform the measurement in the time domain of the rising lateral force due to a slip step. This limits our investigation to constant tyre forces and small lateral slips, the latter condition being generally the case for road racing bicycle tyres.
The paper is structured as follows. An introduction to the theory related to relaxation length is given in paragraph 5.2.1. After that, the methods and instruments used for this study are presented in Section 5.3. The test-rig VeTyT exploited for measurements is presented as well as the implemented set-up and the fitting methods for modelling experimental data. In Section 5.4, the results of measurements of lateral stiffness and cornering stiffness are summarised. Finally, Section 5.5 collects the results of relaxation length and the discussion.

5.2.1 Relaxation length

The relaxation length is an important parameter that characterises the dynamic response of pneumatic tyres. It affects bicycle handling and its stability. It is defined as the distance a tyre covers before reaching 63% of the steady state value of the lateral force, after a step variation in the slip angle [24].
In case the vertical force F_z is constant, the transient lateral force generated by a tyre can be estimated by resorting to a simple lumped parameter model [24], [25], [152]. The model is described by the following first order differential equation (5.1).

$$\frac{\lambda}{v}\frac{dF_y}{dt} + F_y = \bar{F} \tag{5.1}$$

where F_y [N] is the lateral force, $\bar{F}$ [N] is the steady state value of lateral force, λ [m] is the relaxation length, v [m/s] is the forward velocity and $\frac{\lambda}{v}$ [s] (also defined τ) is the time constant. Equation (5.1) can be solved by obtaining (5.2).

$$F_y = \bar{F}(1 - e^{-\frac{\lambda}{\bar{v}}t}) \qquad 5.2$$

The solution can be plotted, as in Figure 5.1. The lines with different colours refer to different tyres. The tyre presented by red line performs better than the others, since at the same speed the time constant τ is smaller, so that tyre reaches faster the steady state conditions.

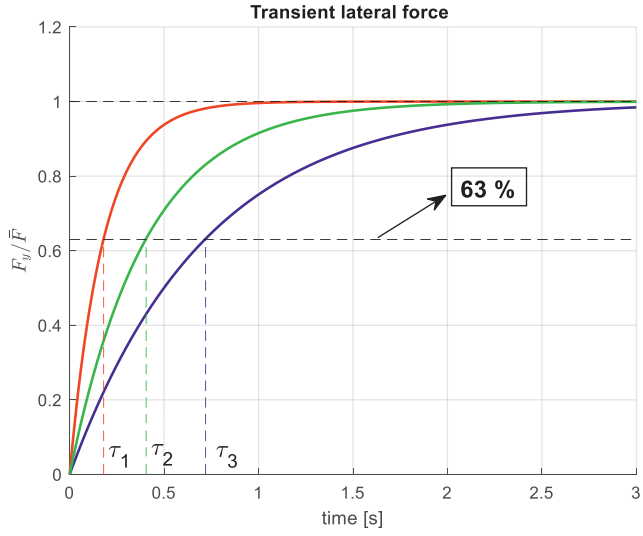

Figure 5.1 – Graphical solution of equation (5.1). The ratio $\frac{F_y}{\bar{F}}$ is depicted as function of time. Three lines represent three different tyres. When the ratio $\frac{F_y}{\bar{F}}$ reaches 63% of the steady state value, the relaxation length can be derived from abscissa axis.

The relaxation length can be directly measured by recording the time required for reaching the 63% of steady state value of lateral force, then dividing it by the actual speed of tyre. Alternatively, λ is derived as the ratio between cornering stiffness C_{F_y} [N/rad] and lateral stiffness of tyre K_y [N/mm], as proposed in [25] (5.3). (1.3

$$\lambda = \frac{C_{F_y}}{K_y} \qquad 5.3$$

In this paper the indirect evaluation of relaxation length is presented. Specifically, the role played by inflation pressure, vertical load and tyre width on the relaxation length is investigated.

The direct method is complex to implement accurately, since it requires that the stiffness of test-rig is sufficient to sustain high loads without deforming. In addition, it is necessary to have an electric motor able to perform in milliseconds the step variation of slip angle. These aspects may cause a low signal-to-noise ratio, compromising the

quality of the measurement. Considering this, it was chosen to evaluate the relaxation length through an easier but still accurate indirect method, as described in (5.3).

5.3 Methods and Instruments

5.3.1 VeTyT test-rig

The evaluation of relaxation length through the indirect method requires the measurement of two parameters, specifically the tyre cornering stiffness and the lateral stiffness.

In this study, the measurement of the lateral force and lateral stiffness were performed through VeTyT, a testing machine specifically designed for measuring the mechanical characteristics of bicycle tyres [14]. It is the first test-rig for bicycle tyres in compliance with the standard ISO 9001-2015.

VeTyT consists of a rigid frame made from aluminium 6060 T6, reinforced with plates and steel rods to ensure lightness and sufficient stiffness (Figure 5.2). It is connected to the ground by means of Watt's linkage and universal joint. It has been conceived so that the longitudinal axis passes through the universal joint, the contact point tyre/surface and the centre of Watt's linkage. In this way, by rotating a shaft rigidly connected to the universal joint, the camber angle can be set. Furthermore, this solution allows compensating vertical vibrations of the wheel due to unevenness on the rolling surface. The tyre/road contact point can be displaced only in vertical direction, resulting in zero longitudinal slip.

The whole chassis can be tilted to set the camber angle in the range ±25 deg, while the slip angle α can be adjusted by rotating the steering shaft. The vertical load acting on the wheel can be varied by adding masses on the frame. Its magnitude F_z is recorded by a load cell on the top of the steering shaft. The complete assembly of the test-rig is shown in Figure 5.2.

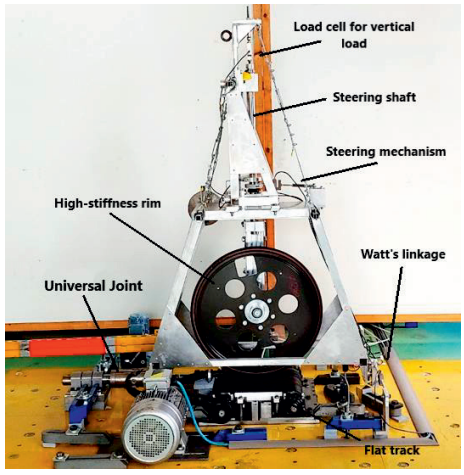

Figure 5.2 – VeTyT test-rig at Politecnico di Milano. The frame carries the bicycle tyre running on flat track. In this picture, tyre is mounted on high-stiffness laboratory rim [14].

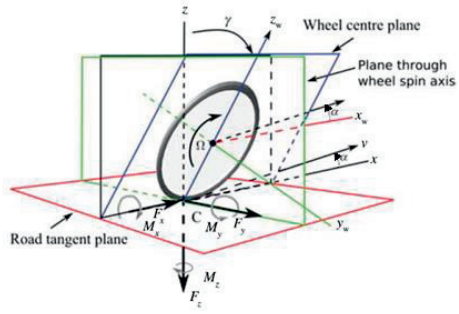

Figure 5.3 – Three-axis reference system used to derive forces, adapted from [60], with indicated the slip angle α and camber angle γ, the lateral force F_y, the longitudinal force F_x, the vertical force F_z and self aligning torque M_z.

As mentioned, the test-rig can be placed both on a drum, named "RuotaVia" [151], or on a flat track (Figure 5.2). The drum has an outer diameter of 2.6 m, and it can reach a peripheral speed of 122 m/s. The flat track consists of a poly-V belt [115] moved by a 5 kW three-phase asynchronous electric motor. A maximum speed of 21 m/s can be achieved. An aluminium plate supports the flat track belt in the contact region. Pressured air mixed with silicone oil is blown between the plate and the flat track belt to reduce the friction.

In addition to standard commercial rims, the apparatus has been designed to accommodate special high-stiffness laboratory rim (the one mounted on in Figure 5.2). In this way, the compliance of the rim does not affect the experimental measurements. Loads acting on tyre are presented in Figure 5.3, adapted from [25].

The cornering stiffness can be derived from post-processed data, as described in Section 5.3. Then, a proper set-up must be implemented for the static measurement of the lateral stiffness.

5.3.2 Fitting of experimental data

The experimental data collected during the tests were fitted by means of interpolating curves from Pacejka Magic Formula [153] [91] as reported in (5.4). Data of lateral force F_y were firstly normalised with respect to the vertical load F_z.

$$\frac{F_y}{F_z} = D\sin\{C\text{atan}[B\alpha - E(B\alpha - \text{atan}(B\alpha)]\} + S_v \tag{5.4}$$

It is necessary to find the set of parameters which guarantee the best fitting between the experimental curves and the Pacejka's Magic Formula. For this purpose, an iterative best-fitting method was exploited. The parameter S_v locates the centre point of the curve with respect to the origin. D represents the peak value, B is the stiffness factor. C is the shape factor, while E has been introduced to determine the curvature at the peak [25]. The cornering stiffness (C_α, which corresponds to the slope at the origin of axis [25]) can be obtained by multiplying the parameters B, C and D as it follows (5.5)

$$C_\alpha = BCD \tag{5.5}$$

The cornering stiffness C_α allows to know the angular coefficient of the interpolating curve evaluated in $\alpha = 0\ deg$. Cornering stiffness is crucial to study the tyre response when subjected to different operative conditions such as inflation pressure or vertical load. Moreover, in [47] [45] the authors concluded the remarkable effect of tyre cornering stiffness C_α in the onset of dangerous dynamical instabilities.
The quality of the fitting method should be quantitively assessed. Therefore, the correlation coefficient R^2 of the fitting of n experimental data was calculated in accordance with the following formula (5.6) [60] [154].

$$R^2 = 1 - \frac{\sum_i^n (y_i - f(x_i))^2}{\sum_i^n (y_i - \bar{y})^2} \tag{5.6}$$

The term $\bar{y}$ is the mean value of the measured force, while $f(x_i)$ is the resulting value from the fitting formula (5.4). The correlation coefficient R^2 can vary between 0 and 1, according to the fitting quality. Higher values of R^2 mean a better fitting between the experimental data and the modelled ones.

5.3.3 Measurement of the lateral stiffness

The lateral stiffness per unit length K_y [N/mm] [137] is defined as the ratio between the lateral force F_y and the lateral displacement of the carcass δ_{tyre}, according to (5.7).

$$K_y = \frac{F_y}{\delta_{tyre}} \tag{5.7}$$

VeTyT can be used also to measure the lateral displacement of the carcass (δ_{tyre}).
The tyre was mounted on high-stiffness laboratory rim while the slip and camber angles were set to zero. An aluminium plate covered with adhesive sandpaper was placed on the flat track, under the tyre to test.
The plate was pulled laterally, and its displacement was recorded by dial gauge (δ_p). Also, the displacement of the wheel rim was measured (δ_{rim}). Lateral displacement of the tyre only (δ_{tyre}) can be then evaluated as follows (5.8).

$$\delta_{tyre} = \delta_p - \delta_{rim} \tag{5.8}$$

The lateral force F_y responsible of the displacement δ_{tyre} was measured by VeTyT.
The whole set-up was arranged to reduce as much as possible the presence of undesired friction sources.
As for RuotaVia drum, a similar arrangement was implemented. Results were very similar but featured by a higher level of uncertainty since measuring the lateral stiffness on RuotaVia drum is a big challenge. Specifically, the results were affected by similar average values but large standard deviation. This forced us to rely only on lateral stiffness results measured on flat track. The current technological limitations of our set-up (designed primarily for flat track) make still do not allow us to obtain reliable lateral stiffness results on RuotaVia drum.

5.4 Measurements

The measurements were performed on three different premium tyres, mounted on high-stiffness laboratory rim with inner tube (Table 5.1). During the experimental campaign, different configurations of inflation pressure and vertical load were tested. First, the results of lateral stiffness measurement as well as a comparison between tyres are presented in Section 5.4.1. Then, the measurements of lateral force and the evaluation of cornering stiffness are discussed in Section 5.4.2.
We tested tyres at three different vertical loads: 340 N, 400 N and 490 N. They are representative of common loads for a racing bicycle, considering the mass of common riders and bicycles. No standards for such bicycle tyre tests have been set so far.
Three different inflation pressures were tested, specifically 3.5 bar, 5.5 bar, and 7.5 bar. They were chosen to simulate an incorrect inflation pressure (or after punch), an intermediate pressure and the maximum recommended pressure. To have a benchmark for further analysis, a 26 mm wide tyre was tested both on flat track and RuotaVia drum [101]. The latter was used because cleat tests are made preferably on drums [155]. Therefore, it may be of interest also to test on drum and set benchmarks for further analysis, even if we know that the drum curvature affects the tyre contact patch shape.

Table 5.1 – Tyres used for tests.

	Width [mm]	ETRTO	Brand
Tyre1	26	700x26c	Brand #1
Tyre2	26	700x26c	Brand #2
Tyre3	28	700x28c	Brand #2

5.4.1 Lateral stiffness

The lateral stiffness was measured according to the set-up presented in Section 5.3.3.

The measured lateral force F_y applied to the tyre is plotted as function of the lateral displacement δ_{tyre} in Figure 5.4, for vertical load equal to 340 N (results for Tyre1 are shown).

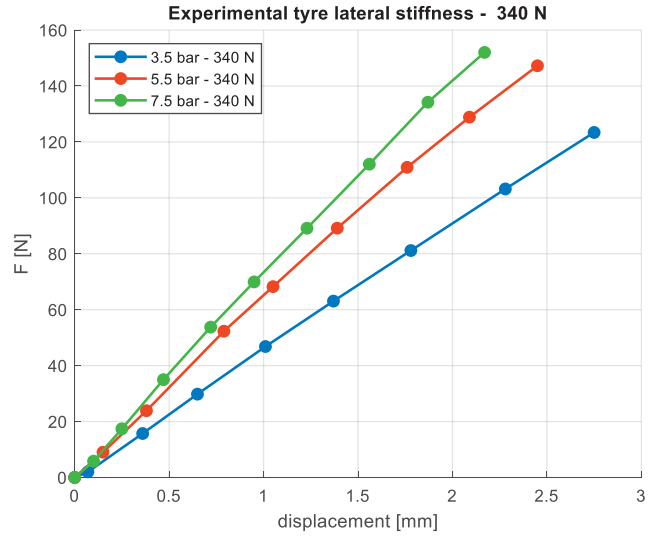

Figure 5.4 – Applied lateral force as function of displacement, recorded through dial gauges. The results for Tyre1 (26 mm wide tyre) are shown.

The relationship shown in Figure 5.4 is linear for all the tested inflation pressures. As expected, large force is required to obtain the same displacement if the tyre is inflated more.

Since the relationship between lateral force and displacement is linear, the lateral stiffness can be directly derived as the slope of the curves evaluated in the origin of axis. Similar behaviour was found for the other tested tyres.

The tests were repeated for vertical loads equal to 400 N and 490 N. The results of lateral stiffness as function of vertical load for Tyre1 and Tyre2 are plotted in Figure 5.5, for different inflation pressures.

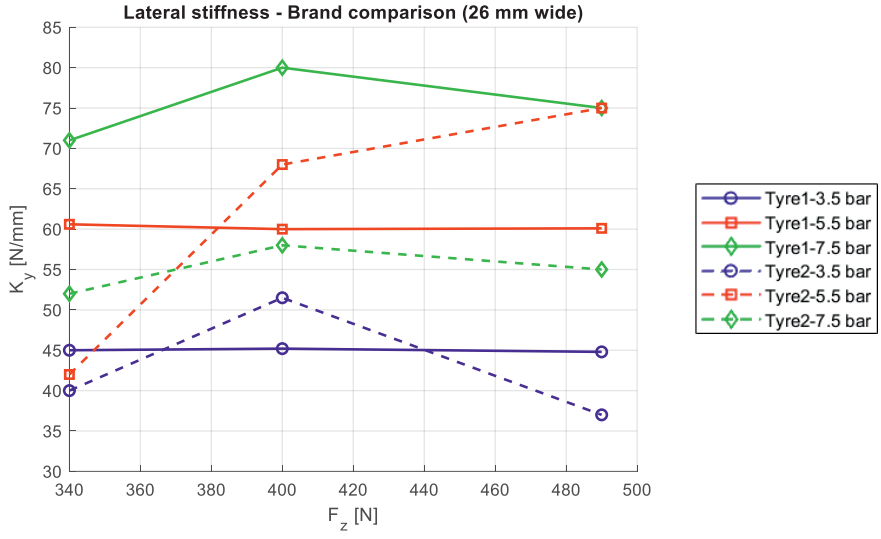

Figure 5.5 – Lateral stiffness as function of vertical load. Three different inflation pressures were tested, for three vertical loads. Results from tyres of different brands but equal wide (26 mm) are depicted.

The results in Figure 5.5 prove that the lateral stiffness K_y largely depends on inflation pressure. As for Tyre1, the variation of vertical load does not appear to have a great influence on lateral stiffness, especially for low pressures (3.5 bar and 5.5 bar, the blue and red line respectively). A limited influence of vertical load on lateral stiffness seems to occur only for pressure equal to 7.5 bar, where a variation in the order of 10% is recorded changing the vertical load. On the contrary, Tyre2 is affected by the variation in vertical load as well as pressure variations. Lateral stiffness for low inflation pressure (3.5 bar) is almost the same for the tested tyres; nonetheless, Tyre2 (blue dashed line) seems to increase up to 20% when the vertical load passes from 340 N to 400 N. A large difference was found between Tyre1 and Tyre2 inflated at 5.5 bar. While the lateral stiffness for Tyre1 at 5.5 bar is basically independent of vertical load, Tyre2 is affected a lot by variation in F_z. At 5.5 bar, it shows an increasing trend with the vertical load, reaching higher values than the ones measured for the same tyre at 7.5 bar. On the contrary for what observed at 5.5 bar, the lateral stiffness for Tyre2 resulted to be 25% lower than the outcome for Tyre1 for inflation pressure equal to 7.5 bar. This may be explained by the different tyre manufacturing process. While Tyre1 is obtained from a single compound, Tyre2 is featured by the superimposition of different compounds layers added with graphene and silica, glued and pressed together. This may result in a tyre more sensitive to pressure variation, narrowing the optimal inflation pressure range.

These features may be of strong practical and computational interest since they are related to realistic scenarios. It could be a feasible riding case when the cyclist

approaches a downhill or it moves forward the chest for sprinting (referring to a front wheel). It means that tyres may show different behaviour in different circumstances. A comparison between tyres of the same brand but different wide was then carried out, for different inflation pressures and vertical loads (Figure 5.6).

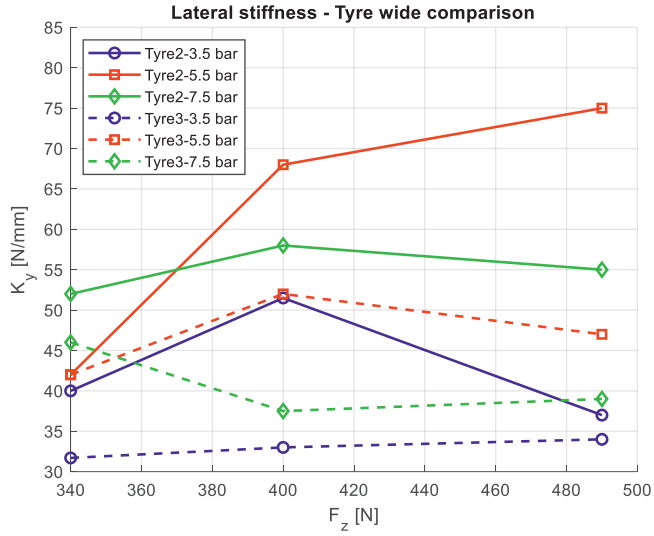

Figure 5.6 – Lateral stiffness as function of vertical load. Three different inflation pressures were tested, for three vertical loads. Results of different wide tyres are depicted (Tyre2: 26 mm wide; Tyre3: 28 mm wide).

Tyre2 (26 mm wide) showed larger lateral stiffness if compared to Tyre3 (28 mm wide), for the same inflation pressure. Similarly to what already pointed out for Tyre2 in Figure 5.5, the lateral stiffness for Tyre3 at 5.5 bar resulted to be higher than the one measured at 7.5 bar, for the same tyre at vertical loads larger than 400 N. It is worth noticing that Tyre2 and Tyre3 are featured by the same manufacturing process, so that the results in Figure 5.6 are confirming the outcomes discussed in Figure 5.5.

5.4.2 Cornering stiffness

VeTyT was used to measure the lateral force of the tested tyre, varying slip angle, inflation pressure and vertical load. The cornering stiffness C_{F_y} was then derived from the model described in Section 5.3, according to (5.5). The tests were performed on flat track and on RuotaVia drum for Tyre1, on flat track only for Tyre 2 and Tyre3. The rolling speed of the test was set at 9.3 km/h, as a result of an iterative process to reduce as much as possible the detrimental increase in temperature of the rolling surface [64]. To study the combined effect of inflation pressure and vertical load variation, data are plotted in form of carpet plot. It is possible to observe the curves of lateral force exerted by the tyre as function of different vertical loads, inflation pressures and slip angles.

The analysis was carried out on slip angles α up to 4 deg, since the aim of this work is to evaluate of the cornering stiffness.
The results in Figure 5.7 come from tests on flat track, for tyre mounted on high-stiffness laboratory rim. The curves for inflation pressure equal to 3.5 bar (yellow curves in Figure 5.7) result in a lower cornering stiffness, for each vertical load tested. The same behaviour cannot be observed for tests on RuotaVia drum (Figure 5.8), where for vertical load equal to 340 N the trend is completely inverted with respect to that shown in Figure 5.7. The reason of this phenomenon may be related to the different contact patch geometry. The contact patch area is smaller for RuotaVia drum [101], due to the geometrical characteristics of the contact surface.

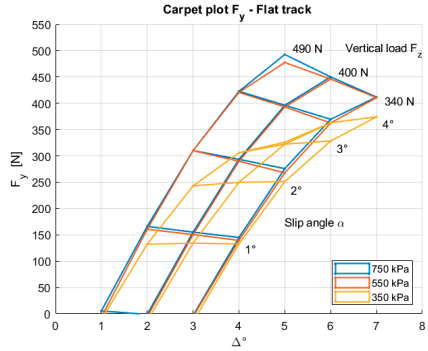

Figure 5.7 – Carpet plot showing the lateral force for a combination of inflation pressures and vertical loads. Tests were performed with tyre mounted on high-stiffness rim, on flat track. Tyre1 (26 mm wide) was tested.

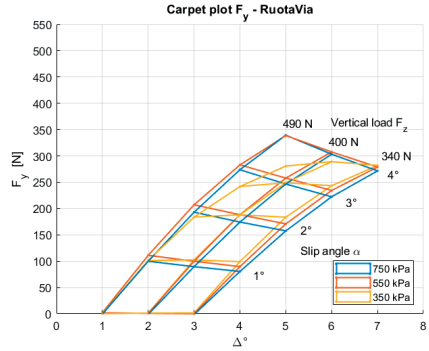

Figure 5.8 – Carpet plot showing the lateral force for a combination of inflation pressures and vertical loads. Tests were performed with tyre mounted on high-stiffness rim, on RuotaVia drum. Tyre1 (26 mm wide) was tested.

The cornering stiffnesses of the analysed cases in Figure 5.7 and Figure 5.8 were then evaluated, according to (5.5). The results are shown in Figure 5.9 both for flat track and RuotaVia tests.

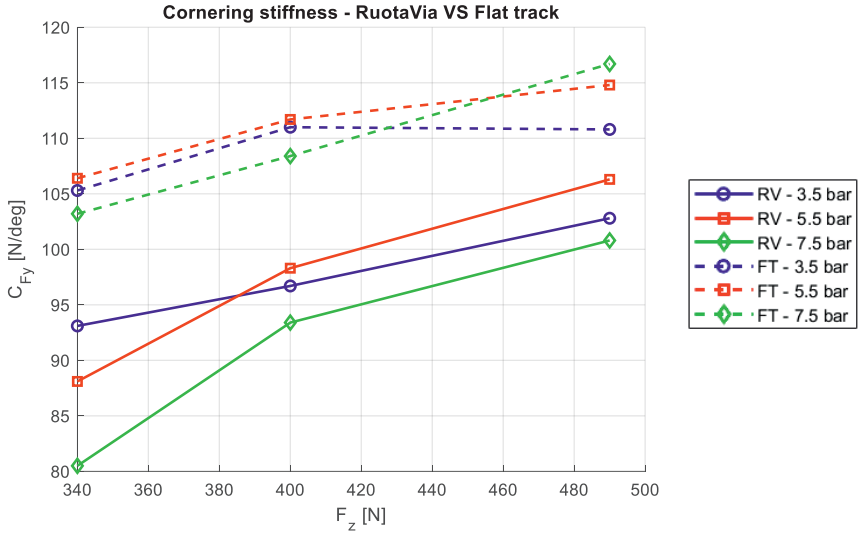

Figure 5.9 – Cornering stiffness for different inflation pressures, as function of vertical load. Comparison between tests on flat track (FT) and on RuotaVia drum (RV) (Tyre1, 26 mm wide).

Cornering stiffness measured on flat track is on average 15% higher than the one measured on RuotaVia, since it may be affected by different shape of contact patch [101].

Referring to flat track, cornering stiffness C_{F_y} increases with vertical load, for pressures equal to 5.5 bar and 7.5 bar. Considering inflation pressure of 3.5 bar, C_{F_y} slightly decreases for vertical loads higher than 400 N. For pressure equal to 7.5 bar and vertical load 340 N it is smaller than for other inflation pressures.

The peak value of cornering stiffness for high vertical load (490 N) was found for larger inflation pressure, i.e., 7.5 bar. It is worth noticing that this behaviour corresponds to the expected one, since higher pressures are needed to ensure better performances for higher vertical loads. On the contrary, reduced inflation pressures are advised for smaller vertical loads.

As for tests on RuotaVia drum, they show a different trend of cornering stiffness with respect to the flat track. The cornering stiffness appears to increase with the vertical load. At lower values of vertical load, C_{F_y} is higher for low inflation pressures. For F_z equal to 340 N, the cornering stiffness at 3.5 bar is 15% higher than at 7.5 bar. The peak of cornering stiffness at 490 N was found for inflation pressure of 5.5 bar.

The influence of vertical load on cornering stiffness is smaller on flat track than on RuotaVia [101]. The trend of C_{F_y} on RuotaVia and the difference in magnitude with respect to the flat track may be due to the smaller contact patch area, as mentioned before.

The cornering stiffnesses depicted in Figure 5.9 are summarised in Table 5.2 and Table 5.3 for flat track and RuotaVia, respectively.

Table 5.2 – Cornering stiffness values at different inflation pressures and vertical loads, for tests on flat track. A 26 mm wide tyre was tested (Tyre1).

C_{F_y} $[N/deg]$ Tyre1 – Flat track		p $[bar]$		
		3.5	**5.5**	**7.5**
F_z $[N]$	**340**	105.3	106.4	103.2
	400	111.1	111.7	108.4
	490	110.7	114.8	116.7

Table 5.3 – Cornering stiffness values at different inflation pressures and vertical loads, for tests on RuotaVia drum. A 26 mm wide tyre was tested (Tyre1).

C_{F_y} $[N/deg]$ Tyre1 - RuotaVia		p $[bar]$		
		3.5	**5.5**	**7.5**
F_z $[N]$	**340**	93.1	88.1	80.5
	400	96.7	98.3	93.4
	490	102.8	106.3	100.8

The comparison between same wide tyres (26 mm) but different brands was then carried out. As aforementioned, they are featured by different manufacturing processes, layers and compounds.
The tyres were tested on flat track, mounted on high stiffness rim with the same inner tube. The measured cornering stiffness is depicted in Figure 5.10.

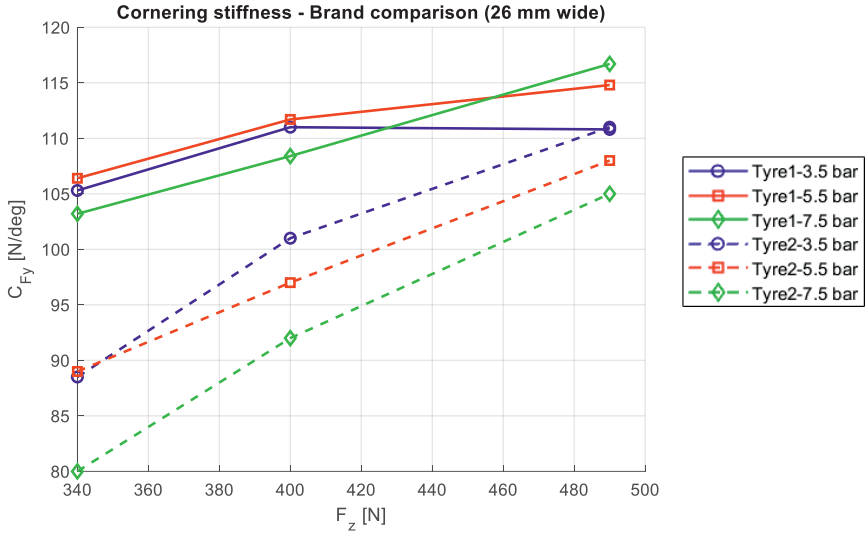

Figure 5.10 – Cornering stiffness for different inflation pressures, as function of vertical load. Comparison between tests with Tyre1 and Tyre2 (26 mm wide, different brand).

The cornering stiffnesses of Tyre1 are higher than those of Tyre2 for each value of inflation pressure and vertical load. The peak value for vertical load 490 N is obtained for pressure equal to 7.5 bar for Tyre1, while for pressure 3.5 bar for Tyre2.
The cornering stiffness for Tyre2 follows an increasing trend with vertical load, for each value of internal pressure. For F_z equal to 490 N, C_{F_y} for Tyre2 is equal to the corresponding one for Tyre1. The latter has already reached its saturation limit since it shows a decrease in C_{F_y}. Contrarily, Tyre2 seems to sustain higher vertical load before reaching the saturation limit.
The results of cornering stiffness for Tyre1 (measured on flat track) and Tyre2 are reported in Table 5.2 and Table 5.4, respectively.

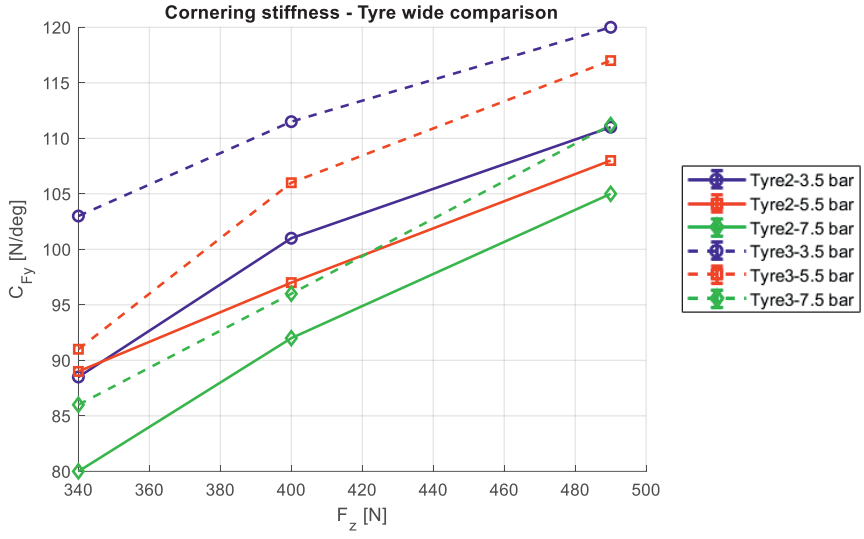

Figure 5.11 – Cornering stiffness for different inflation pressures, as function of vertical load. Comparison between Tyre2 (26 mm wide) and Tyre3 (28 mm wide).

Observing Figure 5.11, larger tyre (Tyre3) is able to generate higher cornering stiffness for each value of inflation pressure and vertical load. Results for Tyres 2 and 3 depicted in Figure 5.11 follow an increasing trend, without reaching the saturation limit even for the largest vertical load (490 N). The mean difference between cornering stiffness for Tyre2 and Tyre3 is on average 8 N/deg (~6%).
The results of cornering stiffness for Tyre2 and Tyre3 are reported in Table 5.4 and Table 5.5, respectively.

Table 5.4 – Cornering stiffness values at different inflation pressures and vertical loads. A 26 mm wide tyre was tested on flat track (Tyre2).

C_{F_y} $[N/deg]$ Tyre2 – Flat track		p $[bar]$		
		3.5	**5.5**	**7.5**
F_z $[N]$	**340**	88.5	88.8	80.1
	400	101.0	97.2	92.0
	490	110.7	107.9	105.0

Table 5.5 – Cornering stiffness values at different inflation pressures and vertical loads. A 28 mm wide tyre was tested on flat track (Tyre3).

C_{F_y} $[N/deg]$ Tyre3 – Flat track		p $[bar]$		
		3.5	**5.5**	**7.5**
F_z $[N]$	**340**	103.6	91.0	86.2
	400	111.5	105.8	95.6
	490	120.0	117.2	111.2

5.5 Evaluation of Relaxation length

The relaxation length can be computed according to (5.3). Firstly, a comparison between results on flat track and RuotaVia drum is presented.

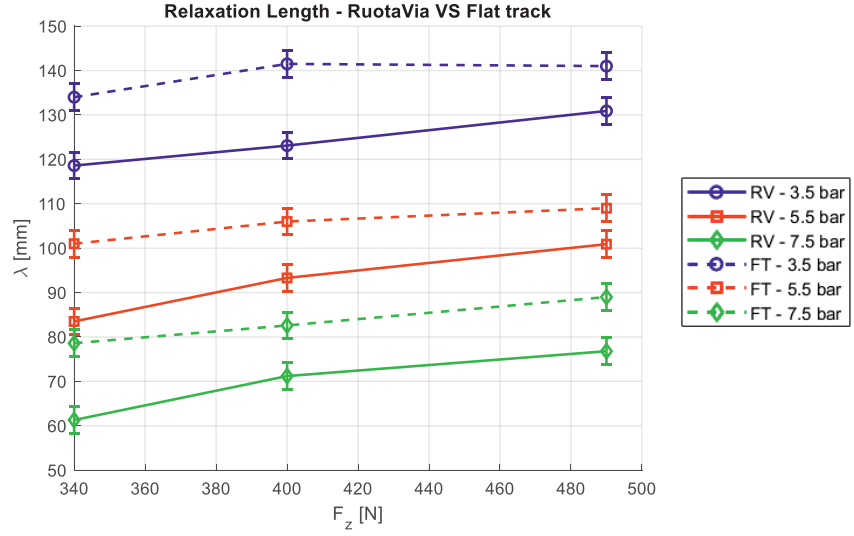

Figure 5.12 – Relaxation length evaluated for different pressure values and vertical loads, for Tyre1 (26 mm wide). Dashed lines represent the measurements on Flat track (FT), while continuous lines are for tests on RuotaVia (RV).

According to Figure 5.12, relaxation length tends to increase with the increase in vertical load. Moreover, it also increases while pressure decreases, meaning that the tyre becomes less responsive for low pressure values. Data of each measurement are summarised in Table 5.6 and Table 5.7. An uncertainty of 3 mm was introduced for relaxation length values, according to the analysis presented in [14].
We found that the relaxation length is generally lower for RuotaVia drum, due to the smaller value of cornering stiffness, as stated before in Section 5.4.2.

It was discovered the large variation in relaxation length due to inflation pressure. Relaxation length is almost doubled when passing from inflation pressure of 3.5 bar to 7.5 bar, both for RuotaVia and flat track for the same vertical load. This proves the large role played by inflation pressure on the relaxation length, therefore on the responsiveness of the tyre.

Table 5.6 – Relaxation length values, for a combination of inflation pressures and vertical loads. This is referred to measurements on RuotaVia drum. A 26 mm wide tyre was tested (Tyre1).

$\lambda_{RuotaVia}\ [mm]$ Tyre1		$p\ [bar]$		
		3.5	**5.5**	**7.5**
$F_z\ [N]$	**340**	118.6	83.5	61.3
	400	123.1	93.3	71.2
	490	130.9	100.9	76.8

Table 5.7 – Relaxation length values, for a combination of inflation pressures and vertical loads. This is referred to measurements on flat track. A 26 mm wide tyre was tested (Tyre1).

$\lambda_{Flat\ track}\ [mm]$ Tyre1		$p\ [bar]$		
		3.5	**5.5**	**7.5**
$F_z\ [N]$	**340**	134.0	100.9	78.6
	400	141.5	106.0	82.6
	490	140.9	108.9	88.9

Relaxation length for same wide tyres (26 mm) but from different brands were then analysed. For a direct comparison, the results are plotted in Figure 5.13.

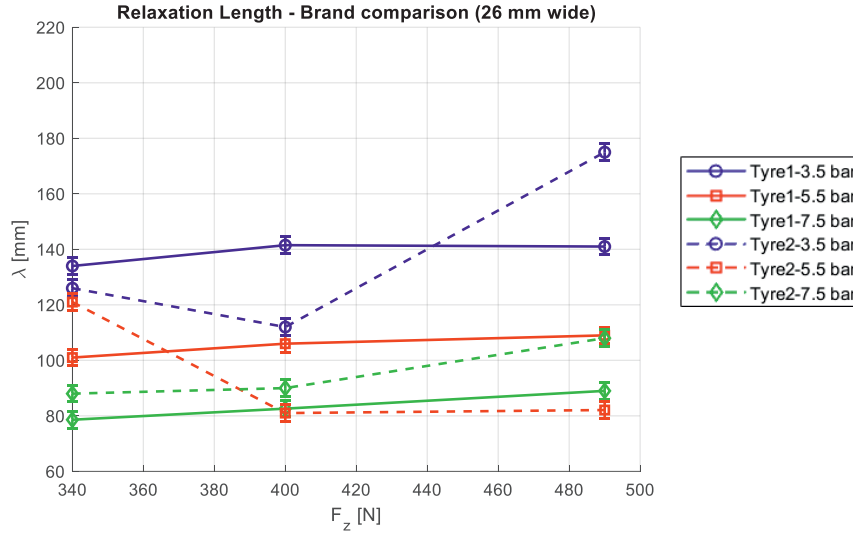

Figure 5.13 – Relaxation length evaluated for different pressure values and vertical loads, for Tyre1 and Tyre2 (26 mm wide). Tests performed on flat track.

Observing Figure 5.13, the relaxation length of Tyre2 appears more sensitive to variation in vertical load than for Tyre1.
Considering inflation pressure of 7.5 bar, the trend of Tyre1 and Tyre2 is very similar but shifted on average by 13%. Tyre2 at pressure of 3.5 bar reaches the peak of relaxation length for vertical load 490 N, with a difference of +24% with respect to Tyre1.
The lowest relaxation length can be found for Tyre2 at vertical load 490 N and inflation pressure of 5.5 bar.

Table 5.8 – Relaxation length values, for a combination of inflation pressures and vertical loads. This is referred to measurements on flat track. Tyre2 (26 mm wide) was tested.

$\lambda_{Tyre2}\ [mm]$		$p\ [bar]$		
		3.5	**5.5**	**7.5**
$F_z\ [N]$	**340**	126.7	121.1	88.3
	400	112.0	81.7	90.5
	490	175.8	82.1	108.9

Table 5.9 – Relaxation length values, for a combination of inflation pressures and vertical loads. This is referred to measurements on flat track. Tyre3 (28 mm wide) was tested.

λ_{Tyre3} $[mm]$		p $[bar]$		
		3.5	**5.5**	**7.5**
F_z $[N]$	**340**	187.3	123.2	107.4
	400	192.2	115.5	145.8
	490	198.5	143.3	163.3

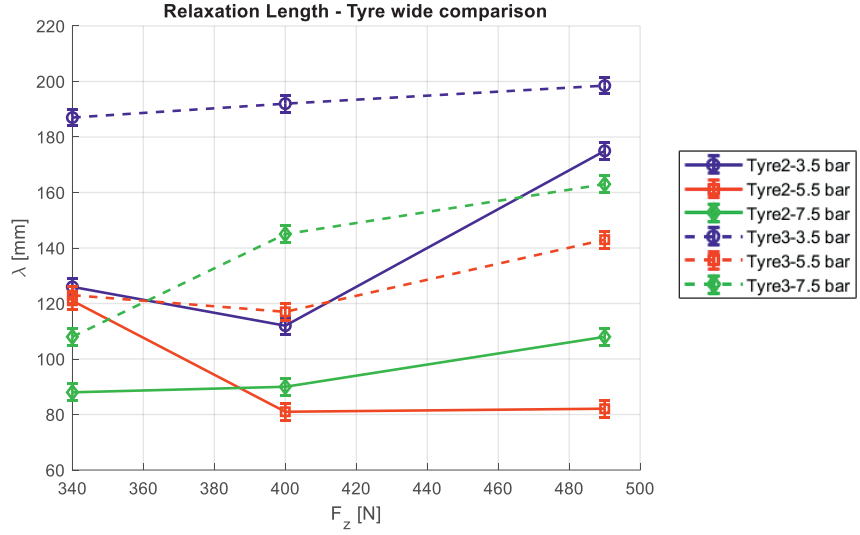

Figure 5.14 – Relaxation length evaluated for different pressure values and vertical loads, for Tyre2 and Tyre3 (respectively, 26 mm and 28 mm wide tyres of the same brand). Results derive from tests on flat track.

According to the results presented in Figure 5.14, a 28 mm wide tyre (Tyre3) has higher relaxation length if compared to 26 mm wide one (Tyre2). We can conclude that 28 mm wide racing tyre is less responsive in turning manoeuvrers with respect to the tighter one. Nonetheless, 28 mm wide tyre (Tyre3) can carry higher vertical and lateral loads (Figure 5.11).

The relaxation length of both Tyre2 and Tyre3 is higher for pressure 7.5 bar than for pressure 5.5 bar. As already observed for lateral stiffness in Figure 5.6, this may be due to the manufacturing process featured by the superimposition of different compound layers. We hypothesise that at high pressure a kind of micro slippage between the layers may appear, leading to a decrease in relaxation length.

A comparison of the results presented in this paper with the ones obtained by other researchers cannot be carried out since there is a lack of information on how the tests

were performed. Moreover, they tested different kind of tyres, not for racing bicycles so that a direct comparison may be useless and meaningless.
In [96], the relaxation length was evaluated on flat track for different bicycle tyres, applying a vertical load of 430 N and inflating at the suggested pressure (not declared). The values were in the range of 40-60 mm, less than those obtained in this paper. The authors highlighted some flexibility in the frame which carried the tyres that might have affected the measurements.
In [147], tests were performed on scooter tyres, for different inflation pressures and tyre sizes. Values in the range 54-96 mm were found for relaxation length, much closer to those presented in this paper. Again, this is not a reasonable comparison, as scooter tyres are designed for greater loads.

5.6 Conclusions

The paper presents the results of the relaxation length related to the lateral force for road racing bicycle tyres. It has been derived as the ratio between cornering stiffness C_{F_y} [N/rad] and lateral stiffness K_y of the tyre.
A 26 mm wide tyre was tested both on flat track and drum of 2.6 m of diameter (named "RuotaVia drum"). The curvature of the drum may affect the length and the shape of contact tyre/ground. Considering this, the cornering stiffness on flat track resulted in 15% higher values. Consequently, relaxation length on flat track is on average 11% larger than the outcomes from RuotaVia drum, for inflation pressure of 7.5 bar.
A comparison was then performed on same wide tyres (26 mm) but different brands, tested on flat track. Differences were found both on lateral stiffness and cornering stiffness. The relaxation length was very sensitive to the variation in inflation pressure. It almost doubled when passing from inflation pressure of 3.5 bar to 7.5 bar, for the same vertical load. Conversely, the tyre of the second brand was affected both by inflation pressure and vertical load (same wide tyres).
A 28 mm wide tyre was then tested, so as to compare the outcomes with the corresponding 26 mm wide one (same brand). Both the cornering stiffness and relaxation length of 28 mm wide tyre was higher than the 26 mm wide one.
Summarizing the analyses presented in the paper, the following conclusions may be drawn.

- There are no protocols to evaluate relaxation length for bicycle tyres. Moreover, no studies on racing bicycle tyres seem to exist. This paper provides a preliminary result to try to close the gap.
- Some attempts to measure bicycle tyre characteristics have been made, nonetheless a reliable evaluation of relaxation length is hard to find. We try to foster the development of a database of bicycle tyre parameters through accurate measurements.

- The relaxation length increases with the vertical load. In addition, we noted that the relaxation length is much more sensitive to variation of inflation pressure than of vertical load for a tyre of a specific brand. Conversely, the tyre of second brand was affected both by inflation pressure and vertical load.
- The differences revealed between the same wide tyres but different brands may be due to some peculiarities in manufacturing process.

A 28 mm wide tyre is less responsive than 26 mm wide one, of the same brand, since it showed higher values of relaxation length. Nonetheless, it is able to carry higher vertical loads, and the cornering stiffness resulted on average 6% higher than for 26 mm wide tyre. In the future, the evaluation of relaxation length will be performed for different type of tyres (trekking bicycle tyres, cargo-bike tyres, etc.), with the method derived in this paper. These data may help the advancement in the field of bicycle dynamics, with the aim of improving safety and performances.

The authors report there are no competing interests to declare.

5.7 Acknowledgements

The authors thank Isabel Pollini, Vincenzo Tartaglione and Prof. Giorgio Previati for their support during the months of experimental test campaign. Many thanks to Mario Pennati, always willing to help us.

Chapter 6

Twisting torque – A simplified theoretical model for bicycle tyres

G. Dell'Orto[a,b], F.M. Ballo[a], M. Gobbi[a], G. Mastinu[a]

[a] *Department of Mechanical Engineering, Politecnico di Milano, Via La Masa 1, 20156 Milan, Italy*

[b] *Faculty of Mechanical Engineering ME, Delft University of Technology, Mekelweg 2, 2628 CD, Delft, The Netherlands*

CReditT author statement:
G. Dell'Orto: Software; Formal analysis; Investigation; Methodology; Visualization; Writing – Original Draft. **F.M. Ballo**: Software; Investigation. **M. Gobbi**: Supervision; Writing – Review & Editing. **G. Mastinu**: Resources; Funding acquisition; Supervision; Writing – Review & Editing.

Published in Measurement, Volume 221, 113460, 2023

ISSN 0263-2241, https://doi.org/10.1016/j.measurement.2023.113460

6.1 Abstract

In this paper, the twisting torque of bicycle tyres is studied. The twisting torque is just the self-aligning torque for null lateral slip and non-null camber. The relationship between twisting torque and contact patch area has been analysed. As the latter increases, twisting torque increases as well. A theoretical model to evaluate twisting torque has been implemented. Since twisting torque is mainly due to longitudinal slip in cambered wheel, increasing the contact patch area the stresses are located at a larger distance from the median plane of the contact patch. The resulting torque will be higher in magnitude.
Finally, the model has been validated comparing the outcomes with the experimental data, with a mean error less than 3% for camber angles less than 10 deg.

Keywords: self-aligning torque; lateral characteristics; modelling; mobility; sustainability

6.2 Introduction

Climate-change requires governments to take action to reduce pollutant emissions. In this context, transportation sector is a relevant source of pollution. It is responsible of one-third of all energy in EU and accounts for more than one-quarter of total EU greenhouse gas emissions [1]. We need alternative and low-impact ways of mobility, and cycling may be a simple and cost-effective solution [3] [4]. In addition, the current increasing cost of carbon fossil fuels [156] is forcing to reduce their use, so speeding up the process of conversion throw a more sustainable mobility.
An increase in the use of bicycles is expected in the close future [5] [71], so that concerns about road safety are growing as well [11] [12]. This aspect will force designers to find new feasible solutions for improving safety, performances [157] and comfort [158] [108]. Advanced numerical models are required to study bicycle dynamics, nonetheless they usually ignore tyre dynamics and need to be complemented with realistic tyre models [62], [159].
Tyres are important for bicycle handling [16], [48], [86]. Despite this, very few studies were focused on bicycle tyre characterisation [62] [88] and only few researchers have presented test-rigs for bicycle tyres [62]. In [60], they use a test-rig for motorcycle tyres adapted to accommodate bicycle tyres. Three different prototypes were also presented in [55]. Using one of them, it was possible to characterise mountain-bike tyres [86].
The dynamics of two-wheeled vehicles is featured by large camber angles, useful to generate lateral forces even with slip angle equal to zero [62] [60]. The influence of camber angle on the mechanical characteristics must be properly addressed to fully characterise tyres. Nonetheless, no studies on twisting torque for bicycle tyres seem to have been carried out, being the research mainly focused on motorcycle tyres [30], [94], [160], [161]. According to Pacejka [25], the self-aligning torque is different from zero when slip angle set to zero degrees, just for the camber effect. The relationship between

the contact patch and twisting properties was stated in [162]. It was discovered the increase in magnitude of the twisting torque with the increase in contact patch area. This was also confirmed in [142]. They measured motorcycle tyre properties for different inflation pressures, also concluding the almost linear relationship between twisting torque and camber angle. An increase in inflation pressure led to decrease in twisting torque, since it changed the contact patch [163]. Self-aligning torque and twisting torque are the main responsible of yaw moment [164]. Furthermore, twisting torque has a relevant effect on steering torque, decreasing the effort required to driver leaning into a curve [165].
We would like to know if the same conclusions are valid also for bicycle tyres. The latter share with motorcycle tyres the toroidal shape of cross section [164], but they differ a lot in terms of compound, layers and manufacturing process. These aspects may affect considerably the tyre behaviour, so that a deep study is necessary. Twisting torque tends to reduce the radius of curvature during the turning manoeuvre [24]. It is relevant to predict this behaviour because it may affect the manoeuvrability [165] and the feeling of riders when approaching a curve. They perceive a sort of "autosteer" as they are leaning into a curve [86]. Twisting torque depends on vertical load and inflation pressure, which, together, may strongly affect the area of contact patch [162]. In this paper, a simplified theoretical model for predicting the twisting torque of bicycle tyres is presented. The self-aligning torque was measured through the test-rig VeTyT [62] [14], [102] developed at the Department of Mechanical Engineering of Politecnico di Milano. The twisting torque was experimentally evaluated for camber angles up to 25 deg (Section 6.3). Then, a simplified model to predict the twisting torque for different vertical loads and inflation pressure was implemented in Section 6.4. The effectiveness of the model was verified comparing the outcomes with the experimental results (Section 6.5).

6.3 Experimental tests – Contact patch and Twisting torque

In this Section, the device to measure the lateral characteristics of the tyre is presented. Then, the evaluation of contact patch and twisting torque is discussed.

6.3.1 VeTyT test-rig

In this study, the measurement of the lateral characteristics of the tyre was performed through VeTyT, a test-rig specifically designed to measure the mechanical characteristics of bicycle tyres [14]. The measuring procedure is now certified in accordance with the standard defined by ISO 9001-2015.
VeTyT consists of a rigid frame made of aluminium 6060 T6, reinforced with plates and steel rods to ensure lightness and adequate stiffness (Figure 6.1). It holds the tyre on top of a flat track, moved by a 5 kW three-phase asynchronous electric motor. The

frame is connected to the ground by means of Watt's linkage (Figure 6.2) and universal joint. Two load cells can measure the lateral force exchanged along the contact patch tyre/rolling surface, while a third load cell is used to constrain the rotation of the steered wheel during the dynamic test. It measures the reaction force given by the tyre, from which the self-aligning torque can be derived.
The whole chassis can be tilted to set the camber angle in the range ±25 deg, while the slip angle α can be adjusted by rotating the steering shaft. Longitudinal axis, defined by the centre of Watt's linkage and centre of universal joint, crosses the vertical axis (defined by steering shaft) in the contact tyre/rolling surface. In this way, we can set the camber angle while the contact patch always lying along the longitudinal axis. This allows both compensating the unevenness of rolling surface and ensuring zero longitudinal velocity of the contact point tyre/rolling surface. The vertical load acting on the wheel can be varied by adding masses on the frame. Its magnitude F_z is recorded by a load cell on the top of the steering shaft. The design solutions also allow changing the centre of mass location due to added masses without affecting the measurements. The complete assembly of the test-rig is shown in Figure 6.1.

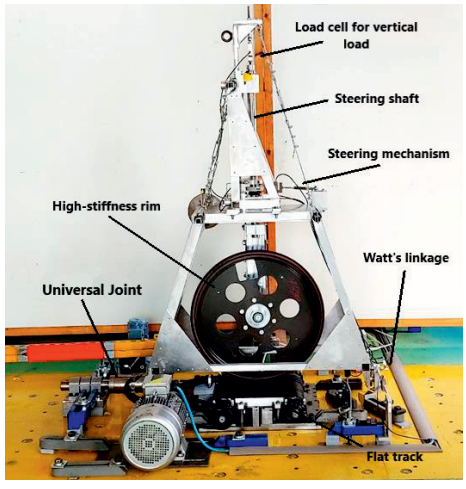

Figure 6.1 – VeTyT test-rig at Politecnico di Milano. The frame carries the bicycle tyre on flat track. Here you can see the tyre mounted on high-stiffness laboratory rim.

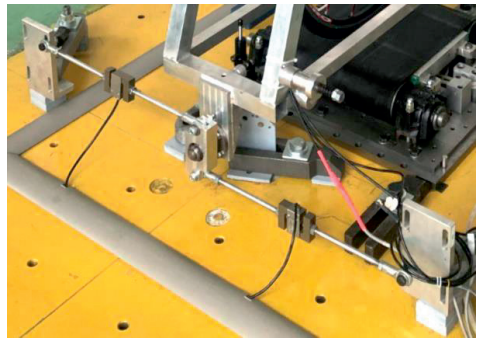

Figure 6.2 – Watt's linkage used on VeTyT. The central part is connected to VeTyT, the rods with load cells are fixed to the ground. (adapted from [128]). It constrains the lateral motion, while it allows a limited vertical motion.

In this study, tests were performed on flat track covered with coarse sand (1.2 mm of granulometry). The speed was set to 9.3 km/h, found as optimal value to avoid the increase in temperature of the rolling surface.
The tyre was mounted on high-stiffness laboratory rim. In this way, the compliance of the rim does not affect the experimental measurements, being the lateral and radial

stiffness of the rim much larger than the ones of the tyre. The lateral force was measured so as to derive the cornering stiffness. Twisting torque was derived from the measurement of self-aligning torque, setting the slip angle to 0 deg and varying the camber angle up to 25 deg.

6.3.2 Contact patch and twisting torque

Contact patch area may strongly affect the twisting torque [162], [163], as stated in next Section 6.2. This is why it is necessary to evaluate the area and the shape of contact patch.
Contact patches were determined statically using sensitive pressure films. A 26 mm wide road bicycle tyre was tested for different inflation pressures and vertical loads. The dynamic measurement of contact patch is still really hard to implement to such a device designed for bicycle tyres. Systems based on image processing [166] [167] or optical measuring system [127] have been recently presented but they still require large modifications on VeTyT.
Sensitive pressure films were scanned, and the area was calculated through the software ImageJ®. It is typically employed in the field of microbiology [133][134], but it can be also used to measure contact patches, with a proper calibration of input images.
It is possible to note the increase in area as the vertical load increases, for the same inflation pressure. Similarly, contact patch area becomes larger with the increase in vertical load, keeping constant the inflation pressure.
Twisting torque was derived from the measurement of self-aligning torque through VeTyT. It corresponds to the self-aligning torque when slip angle is equal to 0 deg and camber angle varies [24].
The tyre was mounted on high-stiffness rim and tested for different camber angles, inflation pressures and vertical loads. The results of an experimental campaign led with inflation pressure of 7.5 bar and vertical load equal to 490 N are depicted in Figure 6.3 Each test was repeated three times, then averaged, resulting with a standard deviation of 2.5%. Because of the technical limitations to set exact null slip angle, the tests were repeated several times in then slip angle range ±0.5 deg. Results were then linear interpolated in that range, to compensate for any detrimental errors which may occur when the forces to be measured are very small.

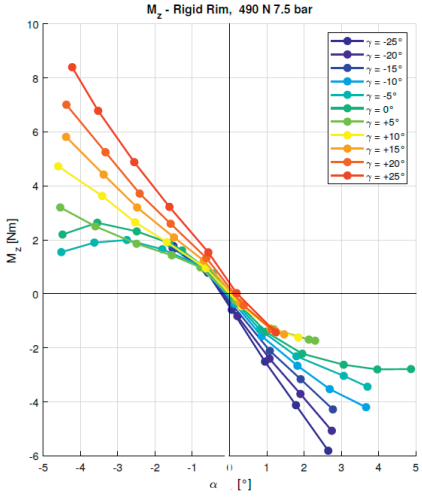

Figure 6.3 – Self-aligning torque as function of slip angle. Results come from a test performed on 26 mm wide road racing tyre inflated at 7.5 bar and mounted on high-stiffness rim. A vertical load of 490 N was applied. Values were recorded for camber angles in the range -25 deg up to +25 deg.

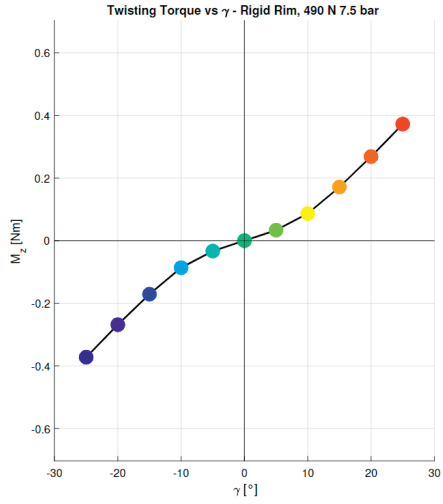

Figure 6.4 – Twisting torque obtained from the test shown in Figure 6.3. Values were recorded for camber angles in the range -25 deg up to +25 deg. Colors are referred to the ones reported in Figure 6.3.

Self-aligning torque varies as function of slip and camber angle. In particular, when slip angle α is set to 0 deg the self-aligning torque is equal to the twisting torque. Practically, it means that the rider may feel a slight torque on the handlebar due to the camber effect. The twisting torque is depicted in Figure 6.4 as function of camber angle γ.

Comparing the results with the ones for motorcycle tyres found in [25], the magnitude of the twisting torque is definitively smaller for bicycle tyres. We can note that twisting torque is one order of magnitude lower than the peak of self-aligning torque for the same camber angle. Remarkably, for motorcycle tyres it resulted of the same order of magnitude [148]. This may be due to the peculiar shape of contact patch for bicycle tyres, featured by large tyre diameter if compared to the width.

It was found a correlation between the twisting torque and the contact patch area. Larger contact patches imply higher difference in peripheral tyre speed, so locally different longitudinal slip values can be found within the contact patch. In Figure 6.5 it is possible to observe the twisting torque measured for camber angle equal to 25 deg, for different contact patch areas (on x-axis). They were obtained varying inflation pressures (3.5, 5.5 and 7.5 bar) and vertical loads (400 N and 490 N). As the contact patch area increases also the twisting torque follows the same increasing trend. Experimental data have been fitted by a quadratic curve, as shown in Figure 6.5 (dotted blue line).

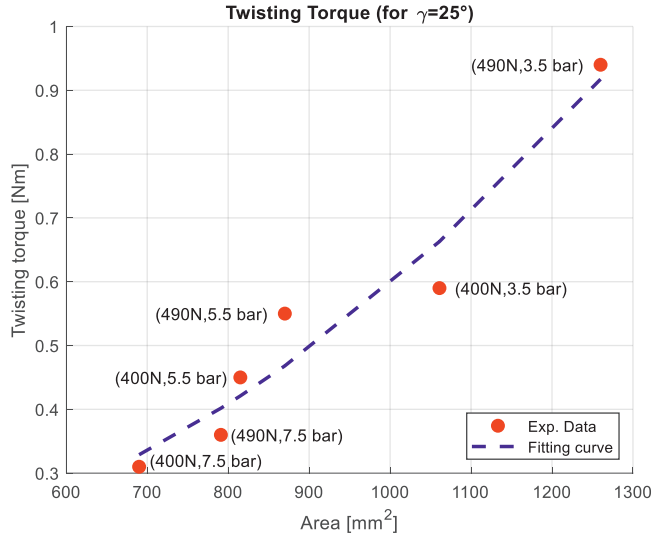

Figure 6.5 – Twisting torque obtained for camber angle of 25 deg (y-axis), from tests on 26 mm wide road tyre. Different inflation pressures (3.5, 5.5 and 7.5 bar) and vertical loads (400 N and 490 N) were tested. It is depicted as function of contact patch area. Quadratic fitting curve is shown (blue dotted line, mathematical expression is: $y = 6.634(*10^{-7})x^2 - 0.0002613x + 0.1933$).

6.4 Model for twisting torque

In [24], the presence of longitudinal slip in the contact patch was found to be one of the causes of the twisting torque. The latter could be strongly affected by the contact patch area since it varies with the pressure and vertical load [162] [168].
The peripheral speed of a cambered free rolling tyre is not equal to the forward velocity at each location in the contact patch. Considering the wheel of Figure 6.6 with an angular velocity ω, two different areas of stress level can be distinguished, featured by opposite stress levels and distance from the spin axis equal to r_A and r_B respectively ($r_A < r_B$). If r_0 is taken as the radius of the wheel along the median plane, we can consider a portion of the contact patch in which $r > r_0$ and a portion in which $r < r_0$ for the cambered wheel. Specifically, the longitudinal slip is positive where $r > r_0$, so that $\omega_r > \omega_{r_0}$. On the contrary, it is negative where $r < r_0$ (i.e. $\omega_r > \omega_{r_0}$). The longitudinal slip is responsible for the generation of longitudinal forces and a torque is generated around the centre of the contact patch.

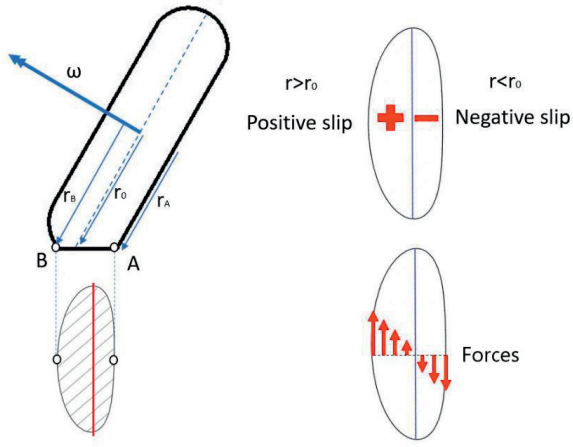

Figure 6.6 – Cambered wheel with the distances between axis of rotation and the contact patch tyre/ground. The wheel is rotating at angular velocity ω. We can distinguish the points A and B on the lateral extremities of contact patch, featured by distances r_A and r_B from the spin axis of the wheel. r_0 is the radius of the wheel along the median plane.

In this paper, some assumptions have been made. The contact patch was considered elliptical even without varying in shape as camber angle increases. Then, longitudinal slip ε was assumed to vary linearly along transversal direction (y direction in Figure 6.7). In this way, we can subdivide the contact patch into slices, and assume that a slice dy at a distance of y from the centreline of ellipse generates a force dF [25]. Similarly to the work presented by Pacejka in [25] for car tyres, we tried to evaluate the twisting torque as the integral of the infinitesimal force dF times the distance y, computed over the area (6.1). Reference system x-y was placed in the plane of the contact patch, where the *x-axis* defines the longitudinal direction and the *y-axis* the transversal one.

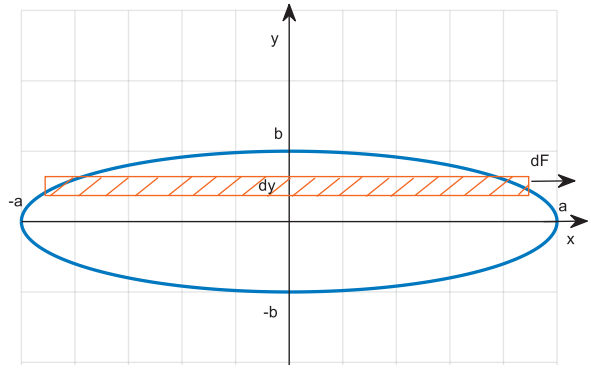

Figure 6.7 – Top-view representation of the contact patch, with the reference system x-y with the origin in the centre of the ellipse. The slice of wide dy is at a distance y from the origin of axes.

$$T = \int_A dF\ |y| \tag{6.1}$$

The radial distance between a generic point P belonging to the contact patch and the wheel spin axis can be expressed as follows (6.2) (also refer to Figure 6.8)

$$r(y) = r_0 + y\ \sin\gamma \tag{6.2}$$

Where γ is the wheel camber angle. The radial distance r is function of the coordinate y since we are considering the cambered wheel.

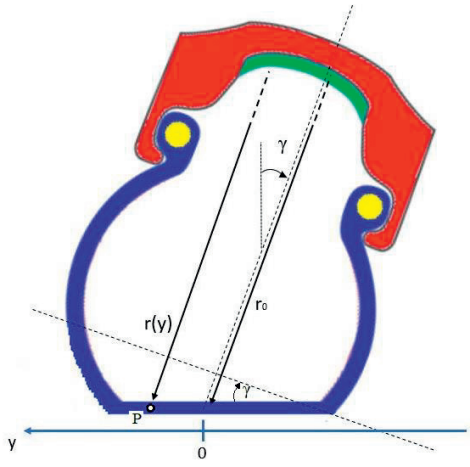

Figure 6.8 – Schematic view of the cross section of cambered tyre. The angle γ is the wheel camber angle, while $r(y)$ is the generic distance between a generic point P and the wheel spin axis. r_0 is the radius of the wheel along the median plane, which crosses the contact patch along the major axis of ellipse. The reference system x-y lays in the plane of the contact patch.

The longitudinal slip ε is positive for $y > 0$ and negative for $y < 0$ (Figure 6.8), from which the longitudinal stress τ can be derived. It is defined according to (6.3).

$$\varepsilon = \frac{\omega\, r(y) - \omega\, r_0}{\omega\, r_0} = \frac{r(y) - r_0}{r_0} = \frac{r_0 + y\sin\gamma - r_0}{r_0} = \frac{y}{r_0}\sin\gamma \tag{6.3}$$

Since for limited values of slip (adhesion zone [169]) the longitudinal force F_x is linearly proportional to the longitudinal slip itself, we have (6.4)

$$F_x = C_{F_x}\,\varepsilon \tag{6.4}$$

As first approximation, the longitudinal slip stiffness is assumed to be equal to the cornering stiffness [28] (6.5).

$$C_{F_x} = C_{F_y} \tag{6.5}$$

The stresses τ can be expressed according to (6.6)

$$\tau = K_\varepsilon \, \varepsilon = K_\varepsilon \frac{y}{r_0} \sin\gamma \tag{6.6}$$

Where we have introduced the proportionality coefficient K_ε [N/mm²]. It has been initially estimated as follows (terms a and b define the semi-major and semi-minor axis of the ellipse contact patch, see Figure 6.7) (6.7)

$$K_\varepsilon = \frac{C_{F_x}}{ab\pi} \tag{6.7}$$

The infinitesimal force dF is defined as the stress τ multiplied by the infinitesimal area $dA = 2x \, dy$, where dy is the width of the considered slice and $2x$ is the length (the slice is assumed to be a rectangle). In this way, we have (6.8)

$$dF = \tau \, dA = \tau \, 2x \, dy \tag{6.8}$$

The term x can be written as function of y, since the contact patch was assumed to be elliptical by hypothesis (6.9).

$$x = a\sqrt{1 - \left(\frac{y}{b}\right)^2} \tag{6.9}$$

The infinitesimal force dF can be expressed as follows (6.10)

$$dF = 2\tau a\sqrt{1 - \left(\frac{y}{b}\right)^2} \, dy \tag{6.10}$$

Because of the symmetry of the problem, the expression of twisting torque (6.3) can now be simplified in (6.11).

$$T = \int_{-b}^{b} dF \, |y| = 2\int_{0}^{b} dF \, |y| \tag{6.11}$$

$$T = 2\int_{0}^{b} 2\tau a|y|\sqrt{1 - \left(\frac{y}{b}\right)^2} \, dy \tag{6.12}$$

$$T = 2\int_{0}^{b} 2K_\varepsilon \frac{y}{r_0} \sin\gamma \, a|y|\sqrt{1 - \left(\frac{y}{b}\right)^2} \, dy \tag{6.13}$$

Then, substituting with the expression found above (6.12) (6.13), we have

$$T = \frac{4a}{r_0} \sin\gamma \int_0^b y^2 \sqrt{1 - \left(\frac{y}{b}\right)^2}\, dy \qquad 6.14$$

Solving the integral (6.14), the result is as follows (6.15)

$$T = \frac{K_\varepsilon}{4r_0} \pi \sin\gamma\, ab^3 \qquad 6.15$$

The equation (6.15) has been derived referring to the contact patch. Analysing the terms of (6.15), it can be stated that:

- The twisting torque T increases with the dimensions of the contact patch. The parameters a and b correspond to the semi-major and semi-minor axis of the ellipse which approximates the contact patch. Specifically, T increases linearly with respect to the length of contact patch (i.e. a), while it increases by a cubic factor with the width of contact (i.e. b).
- Twisting torque increases at increasing the camber angle γ (according to the term $\sin\gamma$).
- It is proportional to the longitudinal characteristics of the tyre through the term K_ε. A tyre with larger longitudinal slip stiffness will be featured by higher twisting torque.
- The twisting torque increases with the decrease in radius of the tyre r_0 [mm]. A tyre with reduced diameter will produce higher twisting torque with respect to a bigger one, if contact patch dimensions and longitudinal tyre properties are kept constant.

6.5 Model validation

Equation (6.15) was used to predict the twisting torque, then the results of the model can be compared with experimental data. The latter were derived from tests on test-rig VeTyT, for a 26 mm road racing tyre, mounted on high-stiffness rim with inner tube. It was tested for vertical load of 400 N and 490 N, for different inflation pressures (range from 3.5 to 7.5 bar). In this way, it is possible to have different contact patch areas and longitudinal stiffness. The contact patch areas were also measured for different conditions, as described in Section 6.3.2. The coefficient K_ε may vary with inflation pressure and vertical load, since tyre lateral characteristics and contact patch area change.

The model requires as input a single value of K_ε, so that it is necessary to develop a strategy to define a synthetic index, to simplify as much as possible the model. It was assumed a reference value of cornering stiffness $\overline{C_{F_y}} = 100\ N/deg$ coming from the mean value of many tests conducted on the same tyre with different vertical load and inflation pressure. Concerning the contact patch area, $\bar{A} = 906\ mm^2$ was considered as

mean value of several measurements under different conditions of vertical load and inflation pressure. The coefficient K_ε resulted as follows (6.16)

$$K_\varepsilon = \frac{\overline{C_{F_y}}}{\bar{A}} = 6.3\ N/mm^2 \qquad 6.16$$

Looking at the results, it was noticed that the amplitude of twisting torque was always underestimated. To solve it, a least square method was used to define a factor to multiply the proportionality coefficient K_ε. A value of 6 was found to improve the matching between theoretical model and experimental data, as shown in Figure 6.9 and Figure 6.10 (obtained using a proportionality coefficient equal to $6K_\varepsilon$).

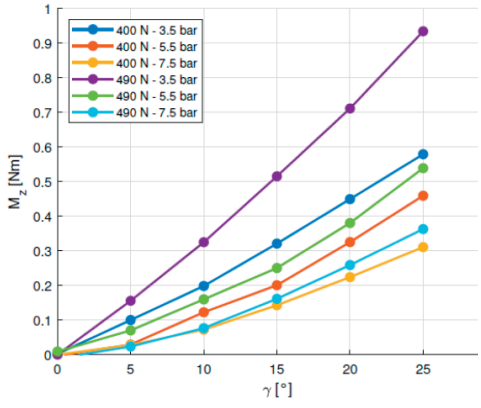

Figure 6.9 – Experimental results of twisting torque obtained for a tyre of width 26 mm, inflated at 750 kPa. A vertical load of 490 N was applied. Values were recorded for camber angles in the range 0-25 deg.

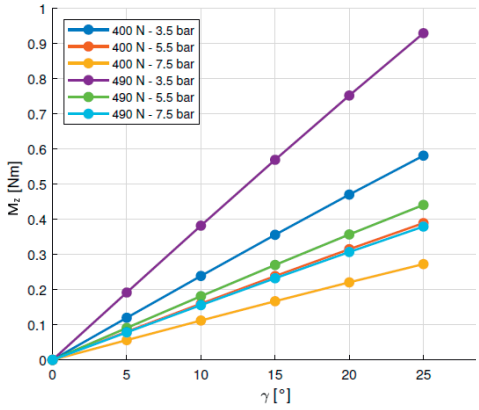

Figure 6.10 – Twisting torque obtained from theoretical model. It was derived for different vertical loads (400 N and 490 N) and inflation pressures (range 3.5 -7.5 bar).

The theoretical model is able to provide curves sorted in very similar way. Referring to accuracy, the twisting torque estimated by the theoretical model corresponds to the measured one with a mean error less than 3% for low camber angles (< 10 deg). The main difference is represented by the slope variation of the curves. The derivative of the measured twisting torque (Figure 6.9) increases as the camber angle increases, while the derivative of estimated curves decreases with the increase in camber angle. This effect can affect the results for camber angles in the range 10-20 deg, since measured values present an increasing quadratic trend.

The difference in results may be explained by the approximations introduced in the model, such as the assumptions made on the shape of contact patch, the linear relationship between stress and slip and the possible slippage which may occur increasing the camber angle.

6.6 Conclusions

Twisting torque is relevant also for bicycle tyres, but significantly reduced in magnitude with respect to motorcycle tyres. Nonetheless, it may contribute to bicycle dynamics, so that it is very important to measure it.
Contact patch areas were measured for different inflation pressure and vertical load on a reference road tyre, 26 mm wide. Tests were carried out with VeTyT to measure the self-aligning torque by varying the camber angle and evaluate the twisting torque experimentally. The measured twisting torque was found to increase with increasing contact patch area, for the same value of camber angle.
A simplified model to predict the twisting torque was introduced. It was found to provide satisfying results in terms of accuracy. Nonetheless, it presents some limitations:

- It cannot be used for large camber angles. The elliptical approximation of the contact patch is not valid anymore.
- The model requires to know the dimensions of contact patch that have to be measured.
- A model able to predict the dimensions of contact patch specific for bicycle tyres has not been implemented yet. A study on the correlation between the contact patch area and the influence of parameters such as inflation pressure and vertical load has been carried out, and it could be a first step through the definition of a larger database.
- The longitudinal stiffness was assumed to be equal to the cornering stiffness, since we worked with limited slip angles. In addition, the longitudinal slips were assumed to be equal along the entire contact patch wide (i.e. constant in x direction, as defined in Figure 6.7).
- The proportionality coefficient K_ε was assumed to be constant despite it may vary with inflation pressure and vertical load. Nonetheless, this approximation may provide a ready-to-use value for future analysis on road racing bicycle tyre. In this way, we are contributing to develop a database to enable parametric analysis of different bicycle tyres, complementing the work of Moore et al. [143], [170].

The model presented in this paper was found to predict the trend and magnitude of the twisting torque for the most exploited range of camber angles (0-10 deg). Self-aligning torque and twisting torque for bicycle tyres are among the toughest characteristics to measure, since they are commonly featured by high uncertainty and poor signal-to-noise ratio. This simplified model tries to provide a rather simple way to predict twisting torque starting from the knowledge of cornering stiffness and contact patch area, usually easier to measure. It requires additional efforts to be refined, and in the future we may try to introduce smarter synthetic indexes.

The authors report there are no competing interests to declare.

6.7 Acknowledgements

The authors thank Lorenzo Uslenghi, Lorenzo Vaccari, Prof. Gianantonio Magnani and Dr. Mario Pennati for their support during the months of hard work and test.

Chapter 7

Measurement of the lateral characteristics and identification of the Magic Formula parameters of city and cargo bicycle tyres

G. Dell'Orto[a,b], G. Mastinu[a], R. Happee[b], J.K. Moore[b]

[a] *Department of Mechanical Engineering, Politecnico di Milano, Via La Masa 1, 20156 Milan, Italy*
[b] *Faculty of Mechanical Engineering 3mE, Delft University of Technology, Mekelweg 2, 2628 CD, Delft, The Netherlands*

CReditT author statement:
G. Dell'Orto: Software; Formal analysis; Investigation; Methodology; Visualization; Writing – Original Draft. **G. Mastinu**: Resources; Funding acquisition; Supervision; Writing – Review & Editing. **R. Happee**: Supervision; Writing – Review & Editing. **J.K. Moore**: Resources; Supervision; Writing – Review & Editing; Funding acquisition.

Published in Vehicle System Dynamics, 1-25, 2024

https://doi.org/10.1080/00423114.2024.2338143

7.1 Abstract

The paper presents measurements of the lateral force and self-aligning torque from cargo and city bicycle tyres. Based on the experimental data, we have determined the parameters for the Magic Formula model, both for lateral force and self-aligning torque. We performed tests with VeTyT, an indoor test-rig specific for bicycle tyres, under different vertical loads (ranging from 343 N to 526 N), camber angles (-5, 0, 5) deg, and inflation pressure (from 300 kPa to 500 kPa). For each condition, we evaluated the cornering stiffness and we found that it generally decreases with the increase in inflation pressure for the tour/city bicycle tyres. However, the cargo tyre we tested showed an opposite trend, with an increase in the cornering stiffness as the inflation pressure increased from 300 kPa to 400 kPa.

Keywords: lateral characteristics; inflation pressure; test-rig; dynamics; cargo bicycle

7.2 Introduction

Tyres play a large role in vehicle dynamics [28] [171]. Therefore, a lot of effort is devoted to tyre development and modelling for cars [172] [173] and motorcycles [30] [139]. By way of analogy, we expect that the tyres are also relevant in bicycle dynamics. As indicated in [45], [46] [174], understanding the tyre characteristics may be essential for investigating the wobble (or shimmy) phenomenon [52] [51]. However, tyres contribution has often been neglected in bicycle models both due to implementation complexities and lack of data on bicycle tyres [55]. The measurements are usually challenging and featured by a low signal-to-noise ratio. In the last decade, proper methods and testing machines have been developed to characterise bicycle tyres with reasonable accuracy [60] [86]. Even if outdoor tests can be performed in real environment, test-rigs for indoor testing seem to provide repeatable and accurate tests [62].

There is an increase in the use of bicycles, particularly after the Covid-19 pandemic [5]. Also cargo bikes are growing in use. Leading delivery companies are updating their fleets with cargo bicycles for "last mile" deliveries [175] [176], as environmentally friendly and efficient means of transportation in urban areas. The cargo bicycles are mostly two-wheeled vehicles with an extended wheelbase to carry loads in front of the rider (known as "front-loader" bicycles), or behind the rider (models known as "longtail") [177]. There are also three-wheeled cargo bicycles, with a large basket for goods or children usually in front of the rider. These vehicles are usually designed so that they cannot tilt in curve (with a few exceptions, as [178]). These peculiarities require the development of specific tyres, capable of handling high vertical loads and high accelerations (usually conceived for pedal-assisted bicycles).

In this context, we tested both cargo and tour/city bicycle tyres. The data have been measured with the indoor test-rig VeTyT (acronym of Velo Tyre Testing), located in the facilities of the Department of Mechanical Engineering of Politecnico di Milano [62]

[14]. According to the knowledge of the authors, the VeTyT is currently the only bicycle tyre test-rig which has been certified ISO 9001-2015. Results have been then compared and discussed (Section 7.4.3). After that, we fitted our experimental data to the "Magic Tyre Formula" (MF) [61] for modelling the tyres (Section 7.5). Data, code, and results are made publicly available [179].
The paper tries to close a still existing gap in the availability of bicycle tyre data. These results may be of great interest for enhancing the understanding of bicycle dynamics, updating existing models with tyre contributions or providing a dataset of measurements on bicycle tyres.

7.3 Methods

The experimental tests were performed with the VeTyT, a test-rig specifically designed for bicycle tyres [14] (Figure 7.1 (A)). An aluminium frame carries the wheel on top of a flat track, while measuring lateral force and self-aligning torque. The VeTyT is laterally constrained by a universal joint (acting as hinge) and a Watt's linkage (Figure 7.1 (B)). This combination allows a pure vertical motion at the tyre/ground contact point. The vertical displacement occurs without any longitudinal component if the displacement is limited. The vertical displacement must be allowed to filter out the effect of possible wheel or flat track unevenness. By means of two instrumented bars (two bars, one load cell per each bar), we can measure the lateral force at the contact patch between the tyre and the ground. First, we need to calculate the force F_W measured on the Watt's linkage (Figure 7.1 (B)), as follows (7.1).

$$F_W = F_{W-S_x} - F_{W-D_x} \tag{7.1}$$

where F_{W-S_x} and F_{W-D_x} are the forces from the load cells (we define S_x and D_x to distinguish the load cells). The sign of the forces F_{W-S_x} and F_{W-D_x} will be always different. When the load cell S_x is under traction, the correspondent D_x is under compression. This is due to the kinematic properties of the system. The lateral force F_y can be evaluated as follows (7.2).

$$F_y = (F_W L_2 - M_z)/(L_1 \cos \alpha) \tag{7.2}$$

The distances L_1 and L_2 are known (Figure 7.2 (A)), M_z is the self-aligning torque (measured), α is the slip angle.

(A)

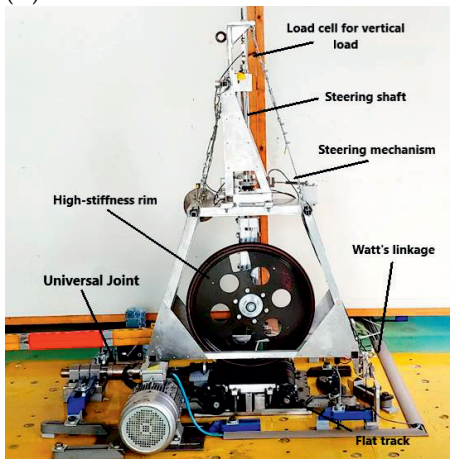

(B)

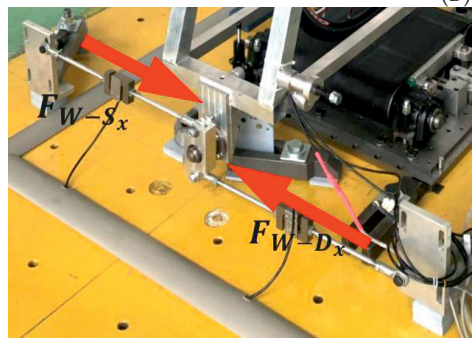

Figure 7.1 – Test-rig VeTyT. In (A), you can see the main subsystems of the testing device. It carries a bicycle tyre running on flat track. In this picture, the tyre is mounted on high-stiffness laboratory rim (adapted from [14] [180]). In (B), the Watt's linkage. It constrains the lateral motion, while it allows a limited vertical motion.

The vertical load acting on the tyre can be varied by simply adding masses to the frame. We measure the actual vertical force with a load cell on top of the steering shaft. The latter is mounted so that its axis corresponds to the vertical axis of the testing machine. Such an axis crosses the longitudinal axis of the VeTyT in the contact patch (Figure 7.2 (B)).

The forces acting on the VeTyT were recorded at 1612 Hz sample rate. Raw data were filtered by means of a 4th order low-pass band Butterworth filter, implemented in the commercial software MATLAB® R2021a (MathWorks, Natick, USA) [181]. With the aim of avoiding detrimental high frequency components, the cut-off frequency of the filter was set to 2 Hz. Signals with high frequency components coming from Watt's linkage load cells and from the load cell for the self-aligning torque are depicted in Figure 7.2 (C). The final results come from averaging of multiple tests. However, before averaging, different test runs need to be realigned with respect to time (x-axis in Figure 7.2 (D)) using an appropriate implemented algorithm.

Tests were performed on the flat track [99]. It consists of a poly-V belt supported by a specifically manufactured aluminium plate. To minimise friction and wear of the belt, an air system inflates a mixture of pressurised air and silicone oil between the belt and the aluminium plate.

During this experimental campaign, we tested bicycle tyres under different vertical loads, camber angles and inflation pressures. An overview of the tyres we tested is collected in Table 7.1. In Section 7.4, we present all the tests performed, clarifying the test conditions. For better clarity, we assign three-digit codes to the tyres alongside the full name of the tyre model.

Table 7.1 – Tyres tested with VeTyT. Tyre brand, commercial series label, dimensions and ETRTO standards (European Tyre and Rim Technical Organisation) are reported alongside the rim used for each tyre we tested. In the last column, you can find the three digit codes used to identify the tyres in the paper.

Brand	Series	Size	ETRTO	Rim	ID code
Schwalbe	Balloon, Big Ben Plus	20" x 2.15	55 - 406	Mach1 Kargo (Disc) 20" (406 - 25c)	T01
CST	Brooklyn	20" x 2.15	55 - 406	Mach1 Kargo (Disc) 20" (406 - 25c)	T02
Schwalbe	50km Energizer, Plus G-Guard 5/Addix-E	28" x 1.75	47 - 622	Shimano Deore (HB-M525A), 28" (622)	T03
Schwalbe	50km Energizer, Active Plus P-Guard 5	28" x 1.75	47 - 622	Shimano Deore (HB-M525A), 28" (622)	T04
Scalato	Mondano	28" x 2.15	55 - 622	Shimano Deore (HB-M525A), 28" (622)	T05

(A) (B)

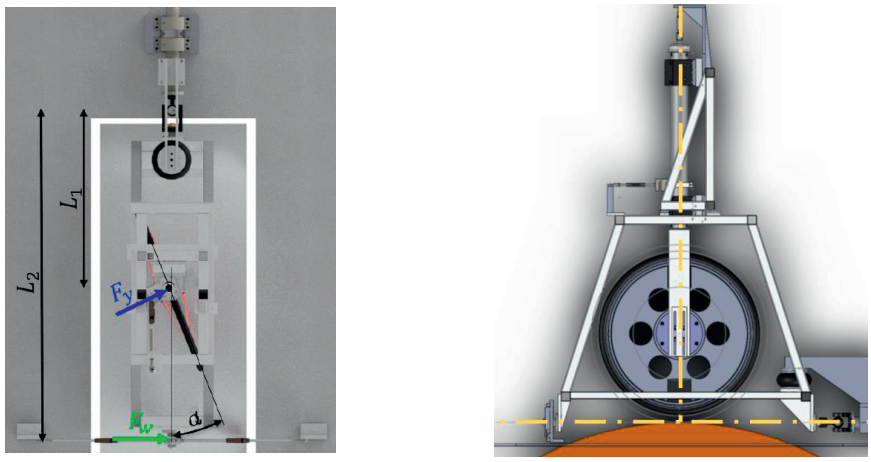

(C) (D)

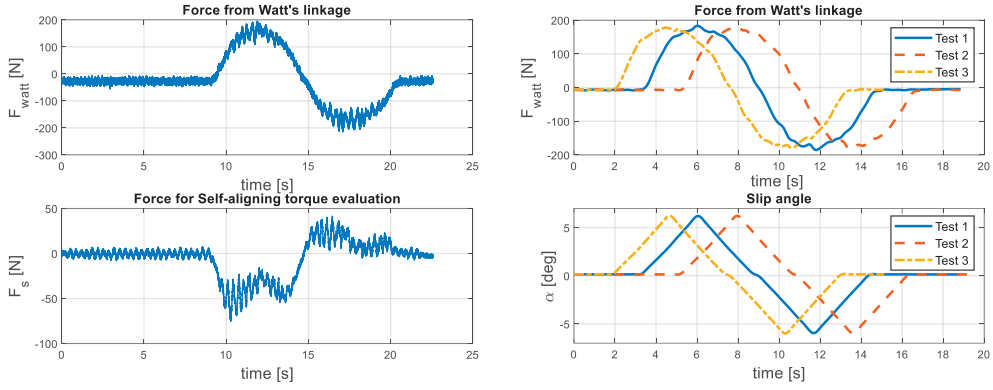

Figure 7.2 – Some VeTyT features: (A) is a top view of the VeTyT, with the indications of lateral force F_y, the force measured by the Watt's linkage F_W and the distances L1 and L2, useful for the evaluation of equilibrium of momentum with respect to the centre of the universal joint. The latter can be assumed as kinematic hinge. Picture adapted from [61]. (B) VeTyT frame and construction axes. The vertical axis crosses the longitudinal one in the contact point tyre ground. Here you can see a schematic lateral view of VeTyT mounted on top of a drum. (C) Signals from VeTyT: raw data from load cells in Watt's linkage as function of acquisition time, before the filtering procedure (first plot). In the plot below, the non-filtered force for the evaluation of self-aligning torque is depicted as function of acquisition time. (tyre CST Brooklyn (T02), camber 0 deg, vertical load 411 N, inflation pressure 300 kPa). (D) Data from three repeated tests (tyre CST Brooklyn, camber -5 deg, vertical load 449 N, inflation pressure 400 kPa). In the first plot, we can see the force measured by Watt's linkage as function of acquisition time. In the plot below, the slip angle α is depicted as function of acquisition time, for three repeated tests.

7.4 Tyre testing

In this section, we present the measurement results referring to the tyres listed in Table 7.1. Each tyre is discussed in a subsection, providing details on the configuration and the peculiarities of test. To collect the test results, tables are largely used. The data linked to the results presented hereafter are publicly available [179].
We limited the tested camber angle to ± 5° to avoid detrimental resonance of the test-rig, which may affects the measurements. In addition, it is worth noticing that this paper presents the results of a batch of bicycle tyres commonly used on tour/city bicycles, primarily conceived for work, commuting or leisure activities. Therefore, we do not expect significant variations in camber angle.
All the tests were performed at a rolling speed of 9.3 km/h, to ensure result repeatability while avoiding detrimental increase in the temperature of the rolling surface [64]. The latter was constantly monitored with thermal camera and/or pyrometer, to be in the admissible range for tests (22 – 30 °C) [63]. We measured both the lateral force and the self-aligning torque, varying working parameters (vertical force, inflation pressure, camber angle). The cornering stiffness can be evaluated from the lateral force as function of the slip angle, according to (7.3).

$$C_{F_y} = \frac{\delta F_y}{\delta \alpha}|_{\alpha=0} \tag{7.3}$$

The cornering stiffness estimates have a 1.5% uncertainty and self-aligning torque 2.5% based on the procedure described in [14].

7.4.1 Cargo bicycle tyres

We tested two cargo bicycle tyres, with the same overall dimensions but manufactured by different companies. Due to the smaller size of the tyres (20″), it was necessary to design a special steel fork to carry the wheel on top of the flat track (Figure 7.3 (A)). In addition, we manufactured steel plates to attach the wheel to the fork, with tight tolerances to ensure proper alignment of the tyre with respect to the rolling surface (Figure 7.3 (B)).

(A) (B)

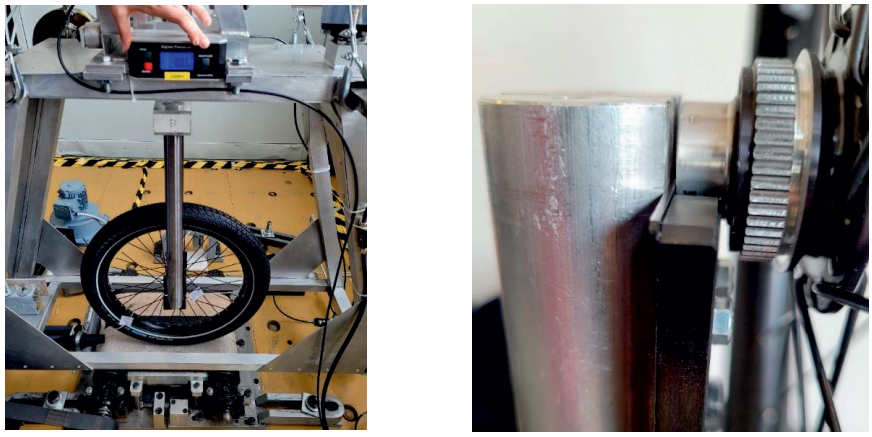

Figure 7.3 – Test-rig VeTyT with the cargo bicycle tyre mounted. You can notice the long steel fork used to accommodate the cargo bicycle tyre. In (B), the steel plates used to mount the wheel on the steel fork. Pictures adapted from [177].

7.4.1.1 Schwalbe Balloon (Big Ben Plus) – T01

The Schwalbe Balloon tyre (labelled as T01), series "Big Ben Plus", has been specifically designed for e-bikes and cargo bikes. It features by 3 mm puncture protection layer and reinforced sidewalls, enabling to carry heavy loads (according to the Schwalbe website [182]). We tested the 20" x 2,15 tyre, applying vertical loads of 411 and 526 N, inflation pressure of 400 kPa, camber angle (-5, 0, 5) deg. With this load configuration we simulated the scenarios of cargo bicycle without any additional load and medium load case with a package in the front basket. Testing at higher vertical loads is still not possible due to the technical limitations of the test-rig and the existing set-up [177].
The results for vertical load of 411 N, varying the camber angle, are shown in Figure 7.4 (A) and (B), for lateral force and self-aligning torque, respectively. As for camber angle equal to 0 deg, with variations in vertical load, the results are depicted in Figure 7.4 (C) and (D). Given the large number of Figures, we decided to provide an overview of the most significant plots and collect all the relevant findings into tables.

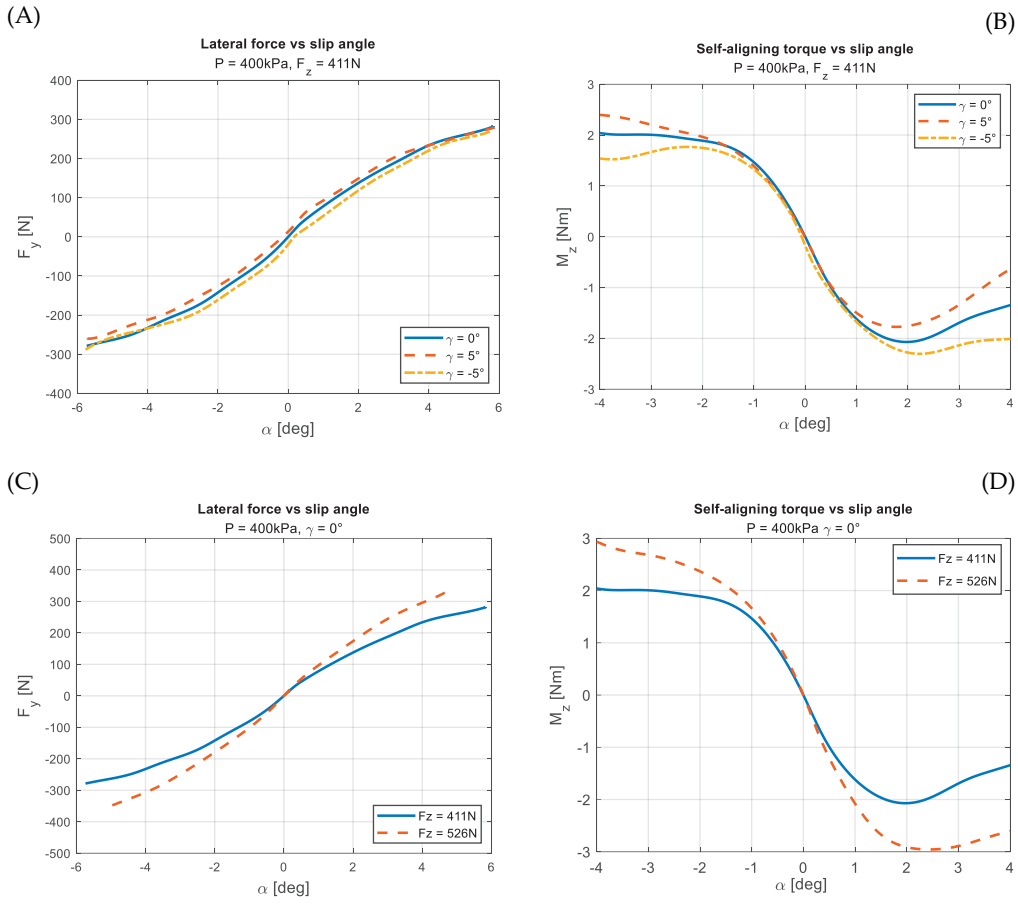

Figure 7.4 – Lateral force F_y [N] and self-aligning torque M_z [Nm] (B) as function of slip angle α [deg], tyre Schwalbe Balloon (T01). In (A) and (B), results for inflation pressure of 400 kPa, vertical load of 411 N, camber angle equal (-5, 0, 5) deg. In (C) and (D), results for inflation pressure of 400 kPa and camber angle equal to 0 deg (pictures adapted from [177]).

As the vertical load increases, both the lateral force and the self-aligning torque increase in magnitude (Figure 7.4 (C) and (D)). The tyre can generate higher forces with higher vertical load. The peak value of the lateral force will be reached for very large slip angles (> |6| degrees, the maximum value tested in this study), as shown in Figure 7.4 (A) and (C). Tyres for cargo bicycles are designed to carry large loads, therefore we expect to reach saturation conditions for higher vertical forces. Cornering stiffness values evaluated according to (7.3) are collected in Table 7.2, for different vertical loads and camber angles. Then, the variation of cornering stiffness C_{F_y} due to vertical load is expressed in % in the last column, for the same camber angle. Cornering stiffness values C_{F_y} for the same vertical load but different camber angles are expected

to be similar [97], as observed in Table 7.2. Conversely, remarkable variations in C_{F_y} are reported due to vertical load increase. With an addition vertical load 115 N or so, we found a variation of 24% in cornering stiffness for camber angle equal to 0 deg, which could result in different bicycle handling.

Table 7.2 – Cornering stiffness under different vertical loads (third and fourth columns), for the same inflation pressure (400 kPa), tyre Schwalbe Balloon (T01) . In the last column, the variation (in percentage) of cornering stiffness due to increasing vertical, referring to the lowest vertical load tested (here 411 N).

Inflation pressure	**Camber angle**	**C_{F_y} [N/deg] ($F_z = 411\ N$)**	**C_{F_y} [N/deg] ($F_z = 526\ N$)**	**% Variation C_{F_y} F_z [N]: 526 vs 411**
400 kPa	-5°	83.5	107.3	+28%
	0°	85.1	105.5	+24%
	5°	84.2	103.8	+23%

7.4.1.2 CST Brooklyn – T02

Similar to what described for the Schwalbe Balloon, the CST Brooklyn (T02) is featured by a carcass designed to handle heavy loads, stiff sidewalls and anti-puncture layer [183].

The results of lateral force and self-aligning torque for different working conditions are depicted in Figure 7.5 (inflation pressure 400 kPa, F_z = 411 N, camber angle (-5, 0, 5) deg in (A) and (B); inflation pressure 300 kPa, F_z (411, 449, 526) N, camber angle 0 deg in (C) and (D)).

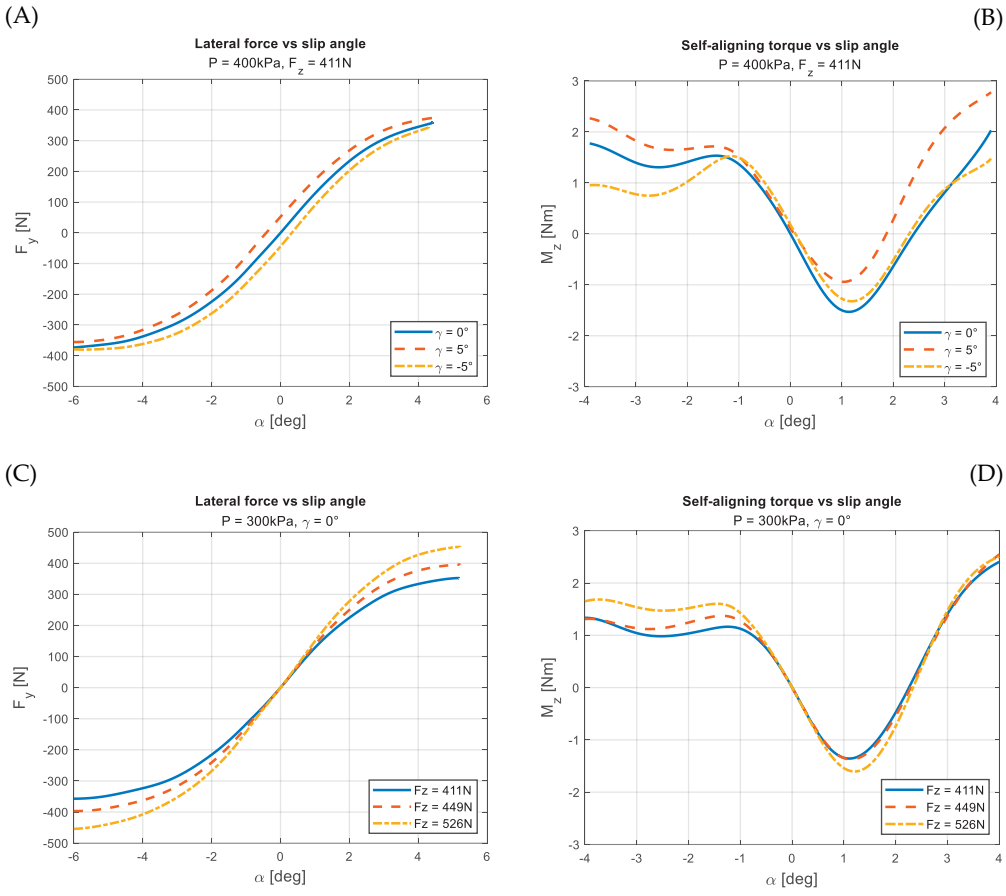

Figure 7.5 – Lateral force F_y [N] and self-aligning torque M_z [Nm] as function of slip angle α [deg], tyre CST Brooklyn (T02). In (A) and (B), results for inflation pressure of 400 kPa, vertical load 411 N, camber angle equal to (-5, 0, 5) deg. In (C) and (D), results for inflation pressure of 300 kPa, camber angle 0 deg, vertical load of (411, 449, 526) N.

The cornering stiffness increases with the vertical load while keeping the pressure constant (Table 7.3). Similar observations may be drawn for inflation pressure. C_{F_y} has a limited increase as the inflation pressure increases from 300 to 400 kPa. However, we cannot clearly define a trend, as we only have data for two different pressures.

The self-aligning torque as function of the slip angle (Figure 7.5 (B) and (D)) is clearly asymmetrical with respect to the origin of axis, leading to unexpected results. To ensure the accuracy of data acquisition process, we repeated multiple tests in different days, coming to similar outputs. We analysed the contact patches using a pressure sensitive film and we found a remarkable asymmetry in the contact pressure distribution (Figure 7.6. Blue dash-dot line represents the median plane line). The varying intensity of the colour in the film corresponds to a different pressure level,

where more intense colour means higher pressure. A visual inspection of the tyre external surface also revealed a "step" between the left and right side of the tyre, with respect to the median plane line. This may account for some unexpected results. The misalignment left-right sides is not constant over the entire tyre (Figure 7.6 (B)). Furthermore, this feature only affects self-aligning torque, as we do not find any specific peculiarities in lateral force measurement (Figure 7.5 (A) and (C)).

(A) (B)

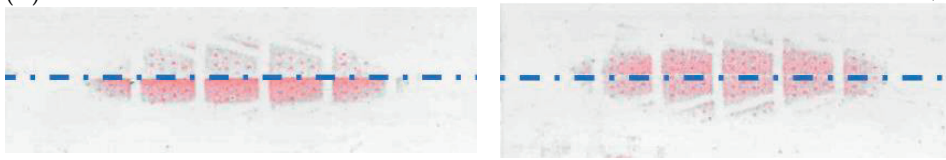

Figure 7.6 – Contact patch on pressure sensitive film for inflation pressure 400 kPa, vertical load 449 N (contrast set to -40% to increase readability), tyre CST Brooklyn (T02). Dash-dot lines represent the median plane lines. In (A) and (B) we can see the results from the same tyre, but different locations on the tyre itself.

Table 7.3 – Cornering stiffness [N/deg] under different vertical loads, inflation pressures (300-400) kPa, tyre CST Brooklyn (T02). In the last column, the variation (in percentage) of cornering stiffness due to increasing vertical load, referring to the lowest vertical load tested (here 411 N).

Inflation pressure	**Camber angle**	**C_{F_y} [N/deg] ($F_z = 411\ N$)**	**C_{F_y} [N/deg] ($F_z = 449\ N$)**	**C_{F_y} [N/deg] ($F_z = 526\ N$)**	**% Variation C_{F_y} F_z [N]: 449 vs 411 (F_z [N]: 526 vs 411)**
300 kPa	-5°	110.7	122.9	139.8	+11% (+26%)
	0°	117.2	127.4	140.7	+8% (+20%)
	5°	121.9	136.1	148.5	+11% (+22%)
400 kPa	-5°	121.0	132.2	140.7	+9% (+16%)
	0°	124.0	136.3	143.1	+10% (+15%)
	5°	130.0	144.0	148.2	+10% (+14%)

In Figure 7.7, the cornering stiffness values are depicted as function of the vertical force F_z. The values of C_{F_y} are higher for the highest tested inflation pressure (in this case 400 kPa). This peculiar trend was not found for the other tyres we tested. This behavior may be due to the specific properties of the carcass of cargo bicycle tyres, which may account for these unexpected results. Also consider that cargo tyres are conceived to carry high vertical loads. Therefore, an increase in inflation pressure may lead to a further increase in tyre's lateral characteristics, as we are still far from the saturation

limit. Unfortunately, we could not test under higher vertical loads, due to the technical limitations of the test-rig.

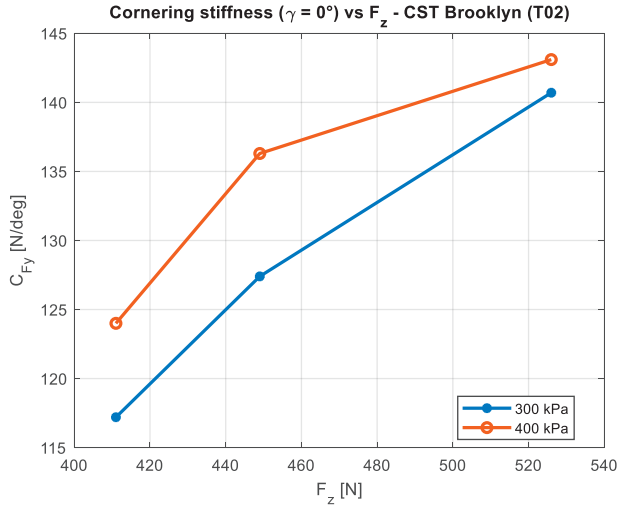

Figure 7.7 – Cornering stiffness C_{F_y} [N/deg] as function of vertical force F_z [N], tyre CST Brooklyn (T02). Results for inflation pressure of 300 and 400 kPa, camber angle equal to 0 deg.

7.4.2 Tour/city bicycle tyres

We tested four tyres commonly used on bicycles for commuting and/or leisure. Cornering stiffness values C_{F_y} are collected into tables. We set the inflation pressure to (300, 400, 500) kPa, camber angle (-5, 0, 5) deg, vertical load (343, 404, 488) N. The Scalato Mondano tyre was tested only for inflation pressures (300, 400) kPa.

7.4.2.1 Schwalbe 50km Energizer (Plus G-Guard 5/Addix-E) – T03

According to the manufacture specs, this tyre was specifically designed for e-bikes. It is certified ECE-R75, making it suitable for fast e-bikes (over 25 km/h motor assist bicycles) (information available on Schwalbe website [182]).
Lateral force and self-aligning torque are presented for different working conditions (Figure 7.8).

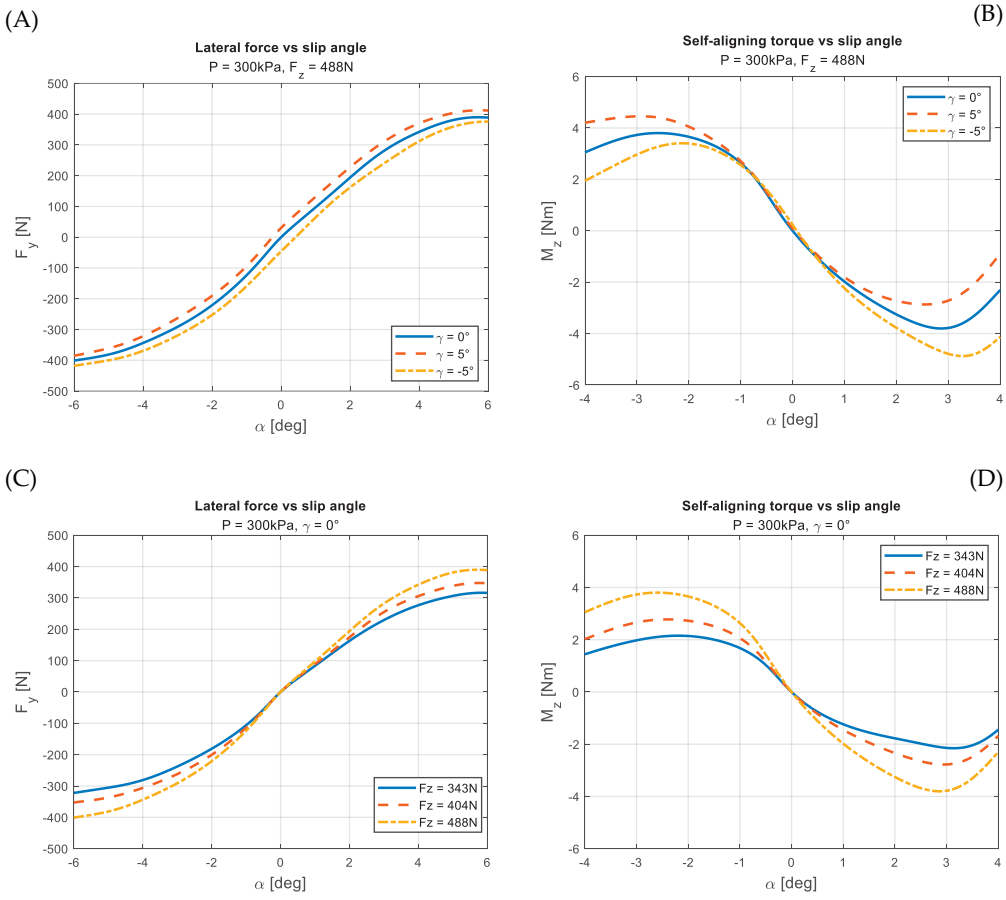

Figure 7.8 – Lateral force F_y [N] and self-aligning torque M_z [Nm] as function of slip angle α [deg], tyre Schwalbe Plus (T03). In (A) and (B), results for inflation pressure of 300 kPa, vertical load 488 N, camber angle equal to(-5, 0, 5) deg. In (C) and (D), results for inflation pressure of 300 kPa, camber angle 0 deg, vertical load of (343, 404, 488) N.

The variation of camber angle for constant inflation pressure and vertical load causes a shift in the curve of lateral force relative to the reference camber angle 0 deg. The shift is downward for negative camber angles and upward for positive camber angles (according to standard Pacejka's adapted SAE reference system – see Appendix 1 of [25]).

As for the self-aligning torque, a nonlinear behaviour is observed for slip angles > |1,5| deg. Furthermore, an increase in the vertical load results in an increase in the self-aligning torque as the lateral force also increases. The influence of camber angle on the self-aligning torque is similar to its effect on the lateral force, however with a reduced impact at lower slip angles. It is difficult to notice a clear trend for twisting torque,

which is defined as the self-aligning torque for slip angles equal to 0 deg at different camber angles [60] [65]. The cornering stiffness values are collected in Table 7.4.

Table 7.4 – Cornering stiffness for different vertical loads, inflation pressures (300, 400, 500) kPa. In the last column, the variation (in percentage) of cornering stiffness due to increasing vertical load, referring to the lowest vertical load tested.

Inflation pressure	Camber angle	C_{F_y} [N/deg] ($F_z = 343\ N$)	C_{F_y} [N/deg] ($F_z = 404\ N$)	C_{F_y} [N/deg] ($F_z = 488\ N$)	% Variation C_{F_y} F_z [N]: 404 vs 343 (F_z [N]: 488 vs 343)
300 kPa	-5°	107.9	111.7	113.2	+3% (+5%)
	0°	105.2	113.6	123.5	+8% (+17%)
	5°	102.0	112.5	124.5	+10% (+22%)
400 kPa	-5°	92.6	112.0	120.2	+21% (+30%)
	0°	98.2	108.1	124.4	+10% (+26%)
	5°	99.3	107.8	119.7	+8% (+20%)
500 kPa	-5°	87.7	97.0	109.6	+10.6% (+25%)
	0°	86.6	90.1	111.6	+4% (+28%)
	5°	83.7	85.3	115.3	+2% (+38%)

Figure 7.9 presents a comparison of C_{F_y} for different inflation pressures. The lowest inflation pressure tested (300 kPa) provided the largest cornering stiffness. As the inflation pressure increases, the cornering stiffness decreases. C_{F_y} also increases along with the vertical load, for all the pressures tested.

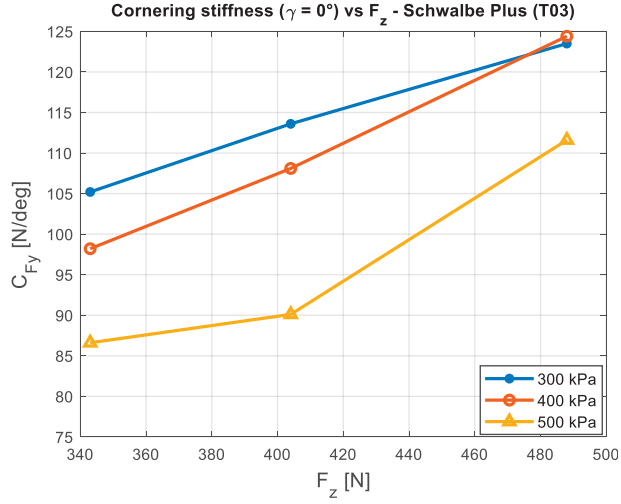

Figure 7.9 – Cornering stiffness C_{F_y} [N/deg] as function of vertical force F_z [N], tyre Schwalbe (T03). Results for inflation pressure of (300, 400, 500) kPa, camber angle equal to 0 deg.

7.4.2.2 Schwalbe 50km Energizer (Active Plus P-Guard 5) – T04

Similar to the tyre presented in 3.2.1, this tyre shares the same tread patterns and layers, but it is featured by a different compound.
The results for different camber angles and vertical loads are presented in Figure 7.10. Although the lateral force does not show any unexpected behaviour, the self-aligning torque has not a clear peak when the inflation pressure is equal to 500 kPa. It is hard to observe a defined curve trend, for all the camber angles we tested. Excessive inflation pressure may elicit unpredictable results.

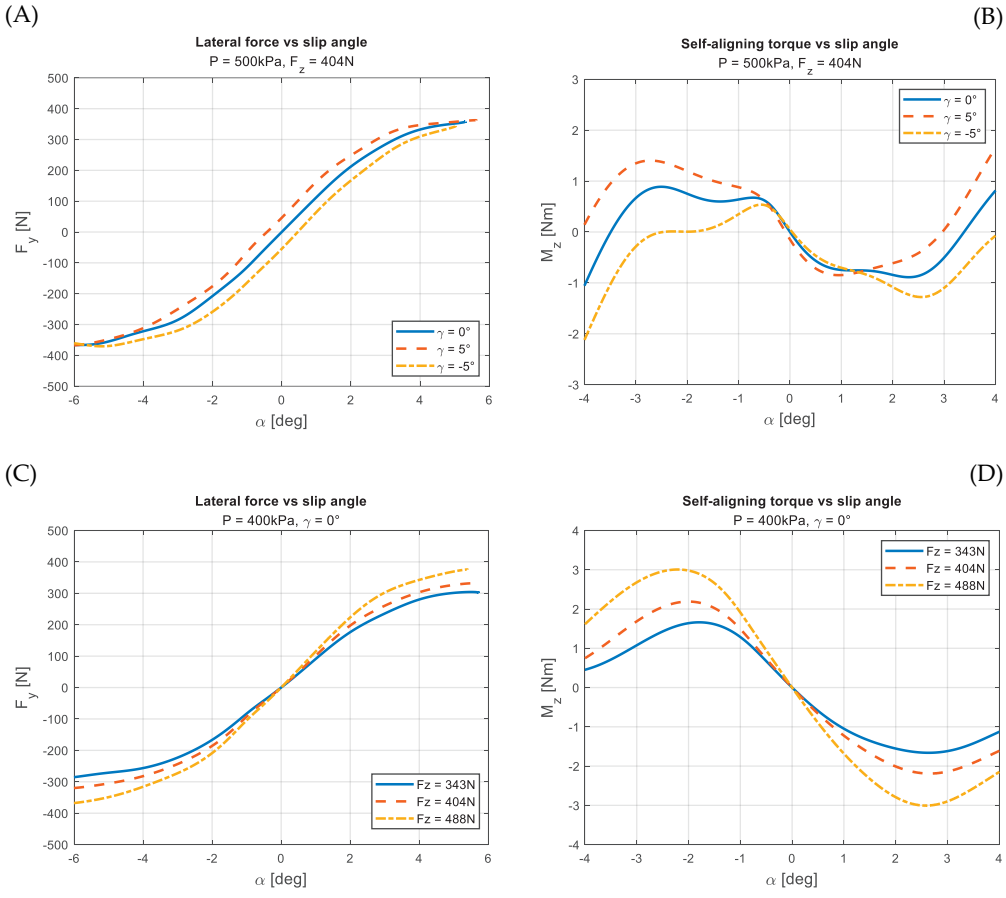

Figure 7.10 – Lateral force F_y [N] and self-aligning torque M_z [Nm] as function of slip angle α [deg]. In (A) and (B), results for inflation pressure of 500 kPa, vertical load 404 N, camber angle equal to (-5, 0, 5) deg. In (C) and (D), results for inflation pressure of 400 kPa, camber angle 0 deg, vertical load of 343, 404, 488 N.

The results for cornering stiffness C_{F_y} obtained for different tests are collected in Table 7.5.

Table 7.5 – Cornering stiffness for different vertical loads, inflation pressures (300, 400, 500 kPa). In the last column, the variation (in percentage) of cornering stiffness due to increasing vertical load, referring to the lowest vertical load tested (here 343 N).

Inflation pressure	Camber angle	C_{F_y} [N/deg] ($F_z = 343\ N$)	C_{F_y} [N/deg] ($F_z = 404\ N$)	C_{F_y} [N/deg] ($F_z = 488\ N$)	% Variation C_{F_y} F_z [N]: 404 vs 343 (F_z [N]: 488 vs 343)
300 kPa	-5°	96.9	102.9	115.8	+6% (+19%)
	0°	100.1	107.0	123.4	+7% (+23%)
	5°	89.8	104.8	121.2	+16% (+35%)
400 kPa	-5°	75.8	89.7	97.8	+18% (+29%)
	0°	81.7	89.6	101.7	+9% (+24%)
	5°	79.5	87.3	104.2	+10% (+31%)
500 kPa	-5°	76.5	108.4	124.6	+41% (+62%)
	0°	79.1	114.4	120.3	+44% (+52%)
	5°	81.7	108.5	132.7	+32% (+62%)

Both the lateral force and the cornering stiffness increase with the vertical load, at constant inflation pressure (Figure 7.11). However, a peculiar behaviour was observed at inflation pressure equal to 500 kPa. Similar to the self-aligning torque, the unexpected trend could be attributed to very high inflation pressure, overtaking the values the manufacturer's recommended values.

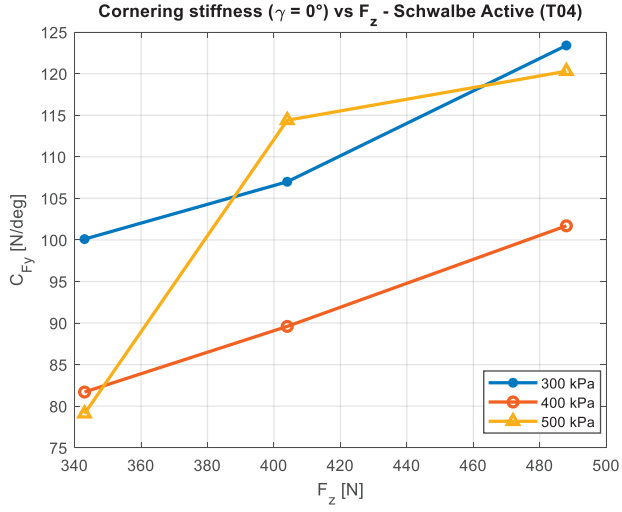

Figure 7.11 – Cornering stiffness C_{F_y} [N/deg] as function of vertical force F_z [N], tyre Schwalbe Active (T04). Results for inflation pressure of (300, 400, 500) kPa, camber angle equal to 0 deg.

7.4.2.3 Scalato Mondano – T05

The tyre "Scalato Mondano" is designed for city bikes, especially for e-bikes (usually heavier than muscular bicycles). As mentioned before, this tyre was tested only for inflation pressures of (300, 400) kPa.
The results from tests are depicted in Figure 7.12, for different camber angles (in (A) and (B)), and different vertical loads (in (C) and (D)).
When maintaining a constant inflation pressure, the camber angle is responsible for the increase in the lateral force (Figure 7.12 (A)). The same can be stated for the self-aligning torque, for high side slip angles (Figure 7.12 (B)). The cornering stiffness increases with the vertical load, keeping the inflation pressure constant (Figure 7.12 (C)). Conversely, the cornering stiffness decreases with the increase in the inflation pressure when the vertical load is kept constant (Figure 7.13).
Regarding the self-aligning torque, the peak values increase in magnitude as the vertical load increases. This is particularly visible for high slip angles ($> |1{,}5|$ deg) (Figure 7.12 (D)).

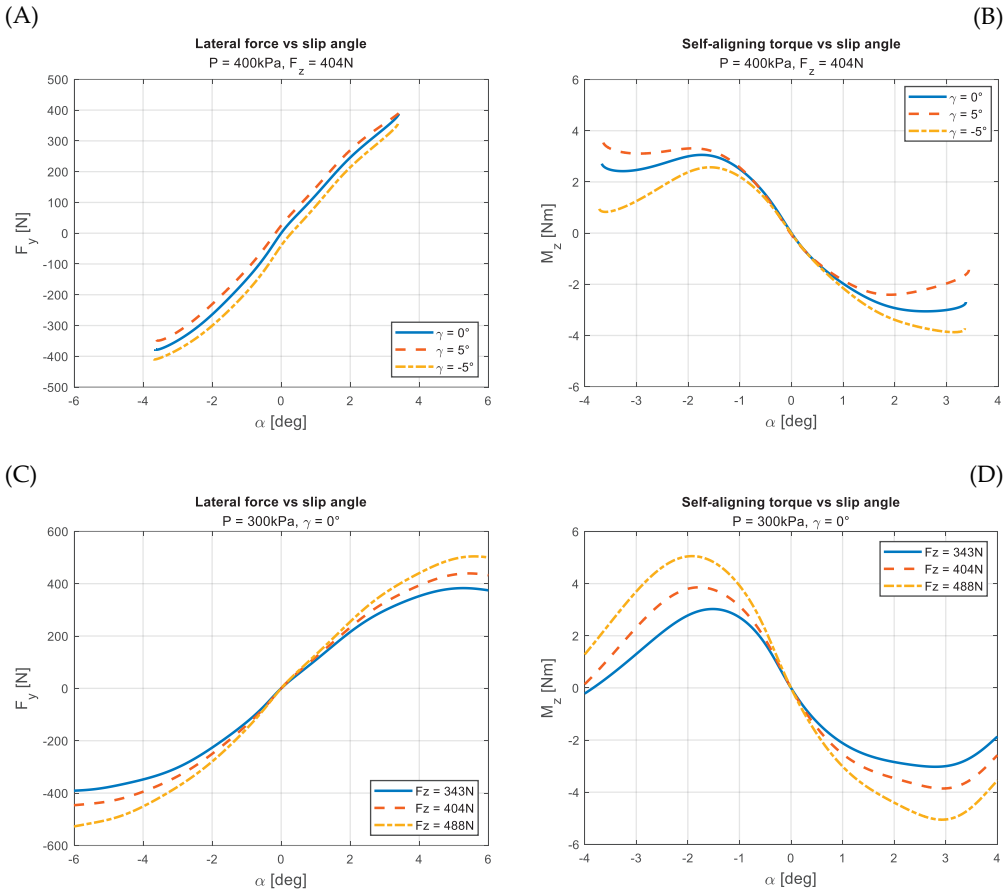

Figure 7.12 – Lateral force F_y [N] and self-aligning torque M_z [Nm] as function of slip angle α [deg], tyre Scalato Mondano (T05). In (A) and (B), results for inflation pressure of 400 kPa, vertical load 404 N, camber angle equal to (-5, 0, 5) deg. In (C) and (D), results for inflation pressure of 300 kPa, camber angle 0 deg, vertical load of 343, 404, 488 N.

Numerical results from tests are summarised in Table 7.6.

Table 7.6 – Cornering stiffness for different vertical loads, inflation pressures (300, 400 kPa), tyre Scalato Mondano (T05). In the last column, the variation (in percentage) of cornering stiffness due to increasing vertical load, referring to the lowest vertical load tested (here 343 N).

Inflation pressure	**Camber angle**	**C_{F_y} [N/deg] ($F_z = 343\ N$)**	**C_{F_y} [N/deg] ($F_z = 404\ N$)**	**C_{F_y} [N/deg] ($F_z = 488\ N$)**	**% Variation C_{F_y} F_z [N]: 404 vs 343 (F_z [N]: 488 vs 343)**
300 kPa	-5°	140.9	144.3	163.2	+2% (+15%)
	0°	132.0	145.0	158.5	+10% (+20%)
	5°	129.4	139.6	147.5	+8% (+14%)
400 kPa	-5°	125.1	140.6	153.0	+12% (+22%)
	0°	121.1	136.8	149.8	+13% (+23%)
	5°	120.6	132.5	148.2	+10% (+23%)

When the pressure increases the cornering stiffness C_{F_y} decreases (Figure 7.13). The trend exhibits an increase with vertical load, and the curves appear to be shifted by a magnitude of approximately 10 N/deg.

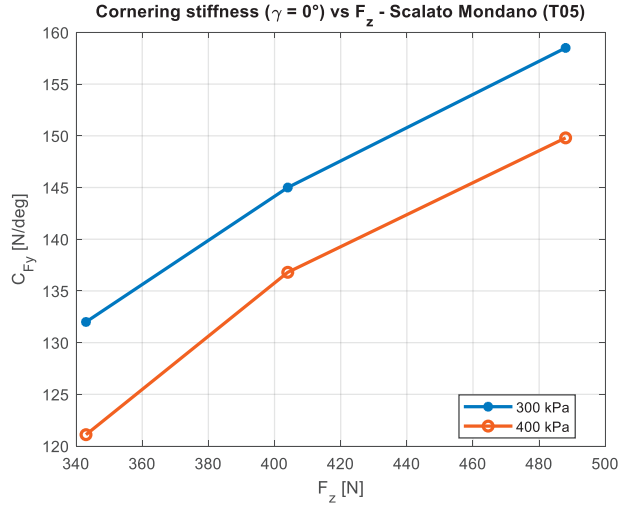

Figure 7.13 – Cornering stiffness C_{F_y} [N/deg] as function of vertical force F_z [N], tyre Scalato Mondano (T05). Results for inflation pressure of (300, 400) kPa, camber angle equal to 0 deg.

7.4.3 Comparisons

Comparing the results obtained for the Schwalbe Balloon (Big Ben Plus - T01) and the CST Brooklyn T02 (same wide tyres), we notice that the cornering stiffness C_{F_y} of the CST tyre T02 is remarkably higher than that of Schwalbe Balloon T01, for the same

inflation pressure (400 kPa) and vertical load (411 and 526 N) (Figure 7.15 (A)). Specifically, C_{F_y} is on average +47% for a vertical load of 411 N, and +36% for F_z = 526 N. We guess that this may be due to differences in sidewalls stiffness, hard compound and tread pattern geometry. While the Schwalbe Balloon T01 is featured by 2.3 mm tread pattern depth, the CST Brooklyn T02 tread pattern is smoother and just 1.9 mm depth (-17%) (see Figure 7.14), therefore to some extent closer to a slick tyre. These features may justify the remarkable difference in cornering stiffness. Note that the tyres were mounted on the same rim (Mach1 Kargo) for the tests.

(A) (B)

Figure 7.14 – Detail of tread pattern. In (A), Schwalbe Balloon (Big Ben Plus – T01) 20" x 2,15. In (B), CST Brooklyn (T02) 20" x 2,15.

The CST Brooklyn (T02) C_{F_y} results are similar to the ones of the Scalato Mondano (T05) (Figure 7.15 (C)), under the same working conditions (inflation pressure 400 kPa, camber angle 0 deg). Among the tested tyres, the Schwalbe Balloon (T01) has the lowest value of cornering stiffness.

In [59], a Schwalbe cargo bicycle tyre was tested employing a truck for outdoor testing. Unfortunately, a direct comparison of the results cannot be carried out, since they tested under higher vertical loads (for 625 N to 765 N, camber angle equal to 0 deg). They pointed out a decrease in cornering stiffness as the inflation pressure increases (from 300 to 400 kPa), contrarily on what observed for the CST Brooklyn (T02) we tested. This may be due to the differences in vertical loads (100 N higher in [59]). Regarding the vertical load of 625 N, the cornering stiffness found in [59] was about 180-190 N/deg, resulting in 35% higher than the value measured for CST Brooklyn (T02) at 526 N.

As for tour/city bicycle tyres, the Scalato Mondano (T05) exhibits the highest cornering stiffness, both for inflation pressure 300 and 400 kPa. The tyre T05 indeed shows a

stiffer and smoother tread pattern. As stated before for CST Brooklyn T02, this may justify larger cornering stiffness. The Schwalbe tyres (T03 and T04) are featured by very similar tread pattern and C_{F_y} at inflation pressure of 300 kPa (Figure 7.15 (B)), with an average difference of 4%. Then, the C_{F_y} of the Schwalbe Plus (T03) results to be higher than the Schwalbe Active (T04)at inflation pressure of 400 kPa (maximum pressure recommended by manufacturer). Surprisingly, the T03 C_{F_y} at inflation pressure of 500 kPa is higher than Schwalbe Plus (T03), as vertical load increases (Figure 7.15 (D)). Schwalbe Plus (T03) is featured by an additional anti-puncture layer. This may partially justify the differences in the measured C_{F_y}.

As already stated for road racing bicycle tyres featured by the superimposition of different layers (as anti-puncture protection) [53] this may cause a remarkable deviation in tyre characteristics as function of working parameters. The interaction between different compound layers is hard to predict, resulting in unclear trend. On the contrary, for tyres with few layers (without specific anti-puncture protection) it seems to be easier to find a specific trend [63].

The inflation pressure also plays a relevant role in tyre cornering stiffness, as depicted in Figure 7.15 (E) and (F). In (E), we report the C_{F_y} as function of the inflation pressure, for the cargo bike tyre CST Brooklyn T02. We have not data for different inflation pressure for tyre Schwalbe Balloon T01, indeed. As we only have results for two different inflation pressures (300 and 400 kPa), we can see the increase in C_{F_y} for all the tested vertical loads. Whether we focus only on pressure 300 and 400 kPa, this is exactly the contrary of what happens for the tour/city bicycle tyres T03, T04, T05. This may be explained considering that the cargo tyre T02 can carry vertical loads higher than the tested ones, therefore we are still far from the saturation limit. An increase in the inflation pressure may still allow carrying higher vertical loads without impacting negatively the lateral characteristics. Contrarily for the tyres T03, T04, T05 (Figure 7.15 (F)), higher inflation pressure mean a decrease in the C_{F_y} (from 300 to 400 kPa). They are actually conceived to carry lower vertical loads than cargo bike tyres, thus justifying the decreasing trend. Although this applies for inflation pressure up to 400 kPa, the tyre T04 increases in C_{F_y} for higher pressures (we cannot state anything for pressure higher than 500 kPa, as we constrained the research to the range of pressures recommended by the manufacturer – 300 to 500 kPa). The T04 mainly differs from the T03 for the presence of an anti-puncture protection layer. As mentioned before referring to (D), the addition of multiple layers during the manufacturing process may affect the tyres' characteristics. To some extent, in [53] we also found that the cornering stiffness of racing bicycle tyres obtained from multiple layers of different compound are more sensitive to pressure variation, sometimes leading to unexpected results.

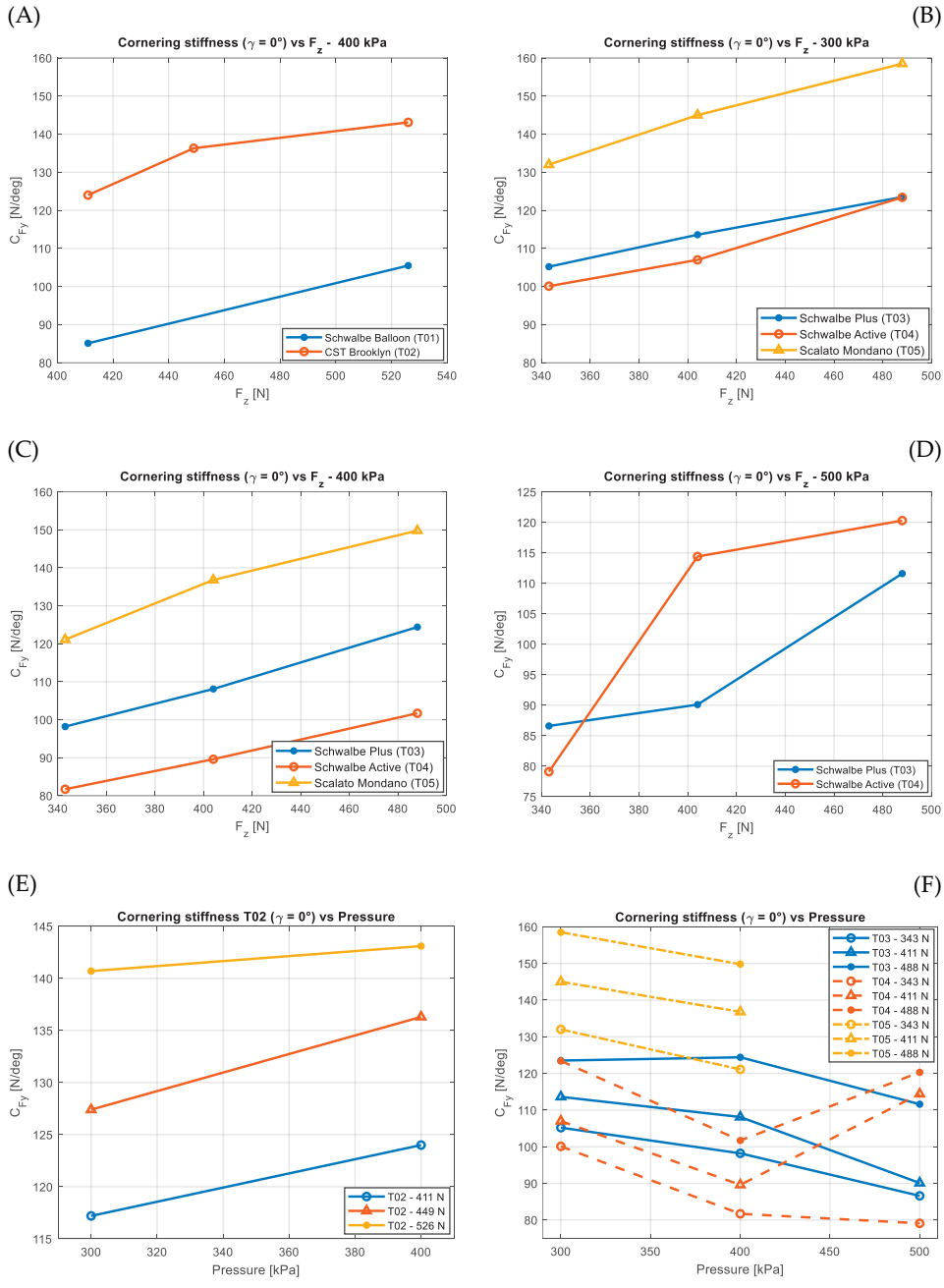

Figure 7.15 – Cornering stiffness comparison for different tyres. (A) cargo bicycle tyres T01 and T02, for camber angle equal to 0 deg and inflation pressure 400 kPa. (B) tour/city bicycle tyres, for camber angle equal to 0 deg and inflation pressure 300 kPa. (C) tour/city bicycle tyres, for camber angle equal to 0 deg and inflation pressure 400 kPa. (D) tour/city bicycle

tyres, for camber angle equal to 0 deg and inflation pressure 500 kPa. We do not have data for inflation pressure of 500 kPa for Scalato Mondano (T05) tyre, so we can only compare results from two tyres (respectively, T03 and T04). (E) shows the cornering stiffness as function of the inflation pressure, depicted for different vertical loads (411 N, 449 N, 526 N), for CST Brooklyn (T02). (F) is equivalent to (E), but reporting the results for the tyres T03, T04 and T05.

C_{F_y} of tour/city tyres are collected in Table 7.7, and the percentage variation between tyres C_{F_y} is reported in the last column.

Table 7.7 – Comparison of cornering stiffness for different for the tour/city tyres Schwalbe Plus (T03), Schwalbe Active (T04), Scalato Mondano (T05). In the last column, the variation (in percentage) for different tyres, with the same working conditions (same inflation pressure and vertical load).

Inflation pressure	Vertical load F_z	C_{F_y} [N/deg] Schwalbe Plus – T03	C_{F_y} [N/deg] Schwalbe Active – T04	C_{F_y} [N/deg] Scalato Mondano – T05	% Variation C_{F_y} T04 vs T03 (T05 vs T03)
300 kPa	343 N	105.2	100.1	132.0	5% (25%)
	404 N	113.6	107.0	145.0	6% (27%)
	488 N	123.5	123.4	158.5	0% (28%)
400 kPa	343 N	98.2	81.7	121.1	16.5% (23%)
	404 N	108.1	89.6	136.8	17% (26%)
	488 N	124.4	101.7	149.8	18% (20%)
500 kPa	343 N	86.6	79.1	/	8%
	404 N	90.1	114.4	/	27%
	488 N	111.6	120.3	/	7%

As expected, all the tyres show an increase in cornering stiffness as the vertical load F_z increased, with all the inflation pressures tested [63] [184].

7.5 Modelling

After collecting the experimental data, we fit Pacejka Magic Formula [25] [81] to the data. The current study refers to steady-state working conditions, neglecting the transient effects [185]. We investigate the use of simplified semi-empirical Magic Formula (4.1) [153], which is easy to manage and still suitable for our purposes. It requires the identification of 14 parameters for lateral force and 18 parameters for self-aligning torque, by means of an iterative optimization process. More complex Magic Formula models can also take into account the effect of pressure variation; nonetheless they need to be integrated with more parameters, which are currently hard to measure with our experimental set-up. The literature on bicycle tyre modelling is still poor, and

technological limitations of the experimental apparatus used for testing do not allow the measurement of large part of parameters needed for more complex tyre modelling (for example, acceleration/braking situations, real-time inflation pressure measurement). Furthermore, as for simulations we are mostly interested in linear range of curves (slip angles in the range ±4 deg), for which simplified Magic Formula models still work well.

The lateral force F_y and the self-aligning torque M_z can be predicted according to the following model (y is a generic term to be replaced with F_y or M_z) (7.4)

$$y = D\sin\{C\text{atan}[B\alpha - E(B\alpha - \text{atan}(B\alpha))]\} + S_v \qquad 7.4$$

An iterative best-fitting method was implemented in MATLAB® R2021a (MathWorks, Natick, USA) [181] to find the best set of parameters. S_v locates the centre point of the curve with respect to the origin. B is the stiffness factor while D is estimated from the maximum peak value of the curve. C is known as shape factor, E determines the curvature at the peak.

We identified all the optimal parameters, for each tyre we tested. Optimal parameters and scripts for processing are made publicly available [186] [187]. The set of coefficients B, C, D, E are collected into Table 7.8, for each tested tyre and inflation pressure. The constitutive parameters are listed in Table 7.9 (see Appendix 7.8).

Magic Formula was initially conceived for car/truck tyres, designed to carry much higher vertical loads than bicycle tyres. This made somehow challenging the identification of the optimal parameters for our batch of bicycle tyres, especially the strategy to identify the initial parameters. To cope with it, at the very beginning we used a set of initial parameters from ADAMS/Tire [81] to fit a single set of bicycle tyre data. Afterwards, we deployed the optimal parameters for the first tyre we processed as initial parameters for the next set of data.

The order of magnitude of the coefficients for the same tyre are consistent throughout the different inflation pressure and vertical loads. The results for tyre Schwalbe Active, tested at inflation pressure of 300 kPa, under different vertical loads and camber angles are shown in Figure 7.16. Experimental data (blue circles) have been down-sampled only for enhanced plot visualization. Then, the fitting lines are the results of Magic Formula model (7.4). Optimal parameters have been calculated for each tyre, one set per each inflation pressure [186].

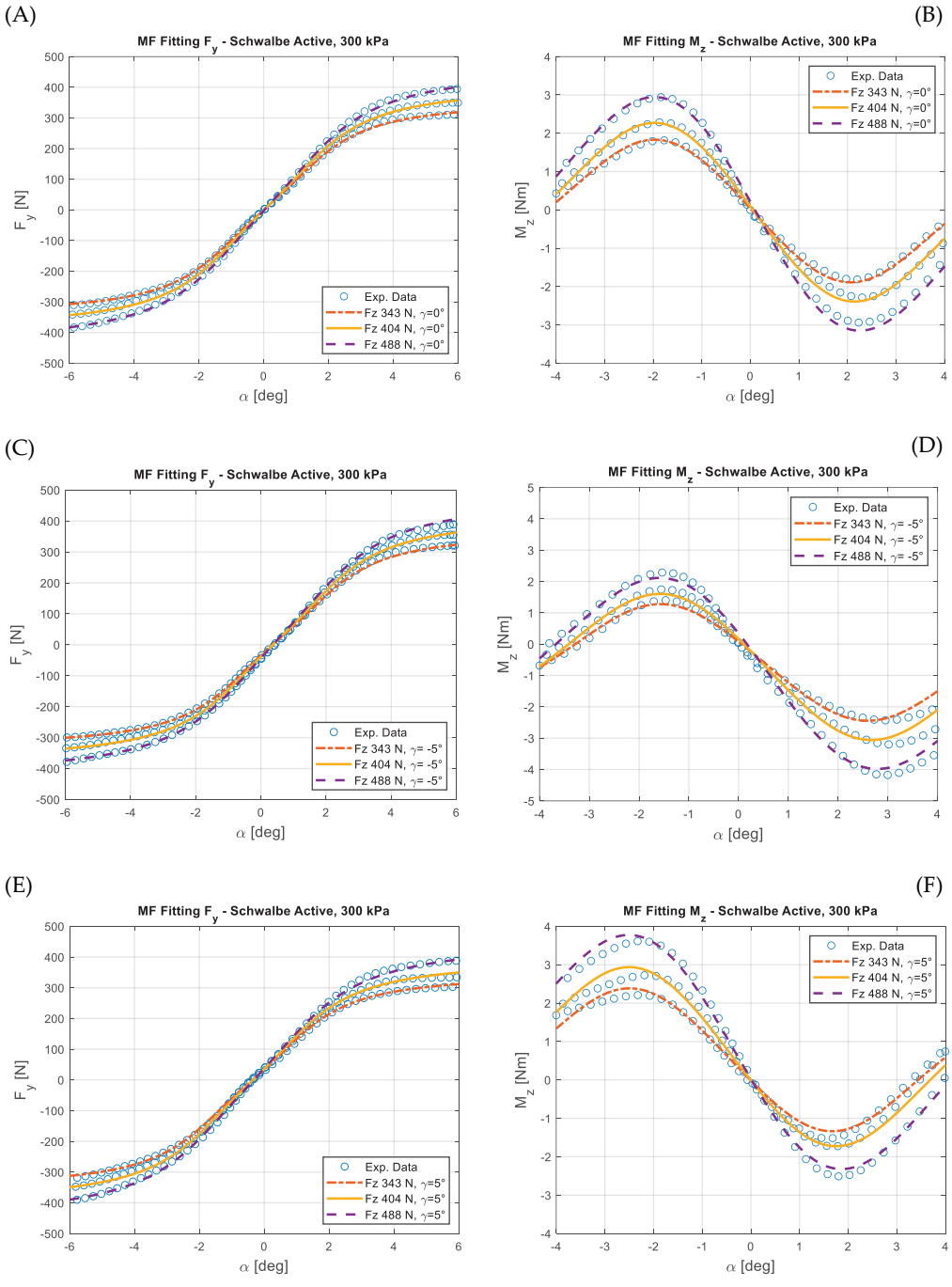

Figure 7.16 – Lateral force [N] and self-aligning torque [Nm] for Schwalbe Active, inflation pressure of 300 kPa. Experimental data from VeTyT are depicted as blue circles. Lines are the

fitting curves from Magic Formula (7.4). In (A) and (B), results results for camber angle 0 deg. In (C) and (D), results for camber angle -5 deg. In (E) and (F), results for camber angle 5 deg.

Visual inspection of the results gave positive feedback for the majority of the tested tyres. However, some difficulties were found for the self-aligning torque of the CST Brooklyn tyre (Section 7.4.1.2, Figure 7.5 (B) and (D)). The unexpected trend observed in M_z may result from misalignments in the tyre itself, supposed to come from the manufacturing process (as discussed in Section 7.4.3). Despite our attempts to address the issue, Magic Formula model could not fit well the experimental results. We think that this discrepancy was mainly due to the unique features of the tyre we tested.

Table 7.8 – Coefficients of fitting for all the tested tyres, under different inflation pressures and vertical loads. **These results have been obtained after applying boundary constraints $1 \leq C \leq 1.6000$ an and $E \leq 1$. Results differs from Table 8 presented in the paper** [66]**. We will inform the editor to publish a corrigendum to that paper.**

Tyre	Inflation pressure	F_z [N]	B $[1/rad]$	C [-]	D [N]	E [-]
Schwalbe Balloon (T01)	400 kPa	411	11.108	1.0000	398.230	0.5213
		526	10.114	1.0000	546.033	0.4988
CST Brooklyn (T02)	300 kPa	343	12.844	1.5640	361.232	-0.2421
		404	12.552	1.5640	394.985	-0.2587
		488	11.931	1.5640	463.564	-0.2921
	400 kPa	343	17.243	1.0646	430.122	0.1254
		404	16.941	1.0646	443.489	-0.6534
		488	16.509	1.0646	456.876	-2.2314
Schwalbe Plus (T03)	300 kPa	343	10.6331	1.5625	321.118	-0.3820
		404	10.3936	1.5625	360.252	-0.4420
		488	10.0234	1.5625	405.258	-0.5246
	400 kPa	343	9.9666	1.6000	316.789	-0.4213
		404	9.7117	1.6000	365.284	-0.4486
		488	9.3031	1.6000	428.186	-0.4861
	500 kPa	343	13.8482	1.0244	348.391	-0.7466
		404	13.3350	1.0244	393.777	-0.7026
		488	12.5839	1.0244	448.085	-0.6421
Schwalbe Active (T04)	300 kPa	343	17.0600	1.0000	330.315	-1.6132
		404	16.6914	1.0000	373.278	-1.3917
		488	16.1005	1.0000	424.641	-1.0866
	400 kPa	343	10.8962	1.6000	310.432	0.3024

		404	10.7549	1.6000	353.128	0.4336
		488	10.4996	1.6000	405.738	0.6143
	500 kPa	343	15.3858	1.0000	370.962	0.5264
		404	15.0201	1.0000	399.133	-1.3455
		488	14.6632	1.0000	419.242	-3.9231
Scalato Mondano (T05)	300 kPa	343	11.3790	1.5541	385.168	-0.8070
		404	10.7231	1.5541	448.247	-0.7371
		488	9.7935	1.5541	532.432	-0.641
	400 kPa	343	10.6008	1.6000	426.654	0.3200
		404	10.8454	1.6000	455.165	-0.5092
		488	11.2969	1.6000	471.015	-1.6511

7.6 Conclusion

The paper presents the measurements of the lateral characteristics for cargo and tour/city bicycles. The tests were performed with the VeTyT, a test-rig specifically designed for bicycle tyres. Then, based on experimental data, we found the optimal parameters for the Magic Formula model, both for the lateral force and the self-aligning torque. It was observed a strong relationship between the cornering stiffness and the vertical load, with the latter being the main parameter affecting the results. Also, inflation pressure played a large role, as it changed the tyre stiffness both in radial and lateral direction.
The main findings are as follows.

- Cargo bicycle tyres usually reach saturation conditions for high vertical loads and/or large slip angles. However, due to the limitations of our experimental set-up we could test up to F_z 526 N, and the saturation limit was not yet pointed out.
- Significant variations in both cornering stiffness and self-aligning torque were observed among cargo bicycle tyres of different brands. The cornering stiffness of the CST Brooklyn was on average 40% higher than the Schwalbe Balloon one. We supposed that this difference may be due to compound, sidewalls stiffness, tread pattern (smother and less depth for the CST Brooklyn). Concerning the self-aligning torque, unexpected results were measured for the CST Brooklyn, without a symmetric trend with respect to slip angle of 0 deg. We also found a biased contact patch, with a step left/right side of the tyre, with respect to the median plane line. This might result from manufacturing process.

- As for tour/city bicycle tyre, Scalato Mondano was found to have higher values of cornering stiffness than the Schwalbe tyres (on average 25% larger than the Schwalbe tour/city tyres), at the tested inflation pressures (300 and 400 kPa).
- The CST Brooklyn (cargo bicycle tyres) had an increase in cornering stiffness as the inflation pressure increased. On the contrary, the other tested tyres displayed the opposite trend. Regarding tour/city bicycle tyres, an increase in inflation pressure usually means a decrease in cornering stiffness. We may explain this unexpected result considering the strong and hard carcass of cargo tyres, specifically designed to carry high loads.
- Tests were constrained to +- 5 deg of camber angle, to minimise excessive tread pattern wear. In this way, it was possible to test different vertical loads and inflation pressures.
- Simpler Magic Formula models can still provide valuable results for bicycle tyres. However, advanced models should be considered for modelling inflation pressure variations.
- The data and the code used in this publication have been made publicly available to enhance advancements in the research fields of bicycle tyres and bicycle dynamics.

In the future, we will try to test different tyres, with a special focus on cargo bicycle tyres, under different vertical loads and camber angles. Then, the use of more complex Magic Formula models will be investigated. In the meanwhile, we will continue in the improvement of VeTyT test-rig, to ensure both accuracy and efficiency in testing procedure. Then, it will be of our interest to further investigate the contact patch, with the aim of finding insights and relationships between contact patch features and the lateral characteristics of bicycle tyres.

7.7 Acknowledgements

The authors thank Prof. G. Magnani and Prof. Giorgio Previati for their contribution to the construction of the VeTyT. Isabel Pollini, Vincenzo Tartaglione and Federico Maria Ballo are acknowledged for their support during the months of experimental tests. Special thanks to Mario Pennati, who was always willing to help us. Sometimes it was difficult to perform the tests, but we also had a lot of fun together.
We thank Prof. Barys Shyrokau, who helped us with tyre modelling. Last but not least, we thank Sierd Heida and Royal Dutch Gazelle, for providing the tyres we tested.

The authors report there are no competing interests to declare.

The project was partially financed and supported by the TKI/ClickNL 'De Fiets van de Toekomst' grant, Royal Dutch Gazelle and Wittenstein Italia SpA.

Authors' disclaimer

The data produced in this paper are not -and cannot be- related in any way on the quality of the products that have been tested. Actually, only one single tyre per type has been tested and the data have been acquired in a laboratory, which is not the real environment. Relevant factors defining the quality of tyres are not -and cannot be- addressed in this paper.

List of abbreviations

List of abbreviations used in this paper.

- VeTyT: acronym of Velo Tyre Testing, a test-rig specifically designed for bicycle tyres. It is currently located at the Department of Mechanical Engineering of Politecnico di Milano (Italy) [14].
- MF: Magic Formula, semi-empirical model used to fit the model curve to the experimental measured data from tyres [25].
- ETRTO: European Tyre and Rim Technical Organisation [188].

7.8 Appendix

The 14 parameters from which we derived the Magic Formula coefficients for the lateral force are listed in Table 7.9, per each tyre and pressure. Each list of parameters associated to a tyre and inflation pressure can be used to fit results for different vertical loads F_z.

Table 7.9 - Parameters used to generate the Magic Formula coefficients presented in Table 7.8

Tyre	Inf. Pressure	x(1)	x(2)	x(3)	x(4)	x(5)	x(6)	x(7)	x(8)	x(9)	x(10)	x(11)	x(12)	x(13)	x(14)
Schwalbe Balloon (T01)	400 kPa	1.000	601.362	721.769	199.363	2.02829	0.000518	-0.19541	0.60160	0.03115	0.50526	-0.18807	7.3034	-55.0172	20.9567
CST Brooklyn (T02)	300 kPa	1.5640	20.7855	870.3673	199.2216	1.1379	0.0005179	-0.4348	-0.0634	0.0311	-0.3204	0.1323	7.3034	41.9707	-13.2932
	400 kPa	1.0646	-1547.3	1682.5	141.0859	0.4981	0.0005179	-20.4940	8.5484	0.0311	0.3812	-0.2251	7.3034	-26.7101	21.0629
Schwalbe Plus (T03)	300 kPa	1.5625	-729.3696	1186.4	118.9888	0.7052	0.0005179	-0.9832	-0.0448	0.0311	0.0160	-0.0526	7.3034	-4.3386	-1.5400
	400 kPa	1.6000	-318.3103	1032.8	134.1451	0.9089	0.0005179	-0.4471	-0.2679	0.0311	-0.2969	0.1134	7.3034	-33.9058	6.2881
	500 kPa	1.0244	-672.4780	1246.4	106.0367	0.6609	0.0005179	0.7201	-0.9935	0.0311	0.2673	-0.0094	7.3034	92.9838	-38.9464
Schwalbe Active (T04)	300 kPa	1.0000	-640.3693	1182.7	132.0338	0.7617	0.0005179	3.6314	-2.8588	0.0311	-0.3454	0.0755	7.3034	41.1567	-8.8786
	400 kPa	1.6000	-507.7110	1079.2	142.7687	0.9009	0.0005179	2.1511	-0.4354	0.0311	0.2834	-0.2155	7.3034	3.2777	12.3458
	500 kPa	1.000	-1533.9	1607.7	107.9347	0.5077	0.0005179	-30.6863	11.0518	0.0311	0.5585	-0.2550	7.3034	-106.4741	45.7536
Scalato Mondano (T05)	300 kPa	1.5541	-219.9363	1198.4	151.9244	0.7054	0.0005179	1.1458	-1.2000	0.0311	0.2153	-0.0902	7.3034	-47.7652	13.3318
	400 kPa	1.6000	-1922.0	1903.2	157.4179	0.6767	0.0005179	-13.5935	4.9825	0.0311	-0.4973	0.1052	7.3034	77.5374	-27.1839

Chapter 8

Effect of tyre inflation pressure and vertical load on bicycle dynamics following lateral perturbation with a kickplate

G. Dell'Orto[a,b], L. Alizadehsaravi[b], R. Happee[b], J.K. Moore[b]

[a] *Department of Mechanical Engineering, Politecnico di Milano, Via La Masa 1, 20156 Milan, Italy*

[b] *Faculty of Mechanical Engineering ME, Delft University of Technology, Mekelweg 2, 2628 CD, Delft, The Netherlands*

CReditT author statement:
G. Dell'Orto: Data Curation; Formal analysis; Investigation; Methodology; Software; Visualization; Writing – Original Draft. **L. Alizadehsaravi**: Investigation. **R. Happee**: Supervision; Writing – Review & Editing. **J.K. Moore**: Data Curation; Resources; Software; Supervision; Writing – Review & Editing; Funding acquisition.

8.1 Abstract

The paper aims to quantify the impact of tyre characteristics on bicycle dynamics, both numerically and experimentally. We simulated the nonlinear Carvallo-Whipple bicycle-rider model by adding a nonlinear tyre model (Magic Formula) and a human rider model. We studied the effects of tyre inflation pressure and vertical load using the Magic Formula parameters derived experimentally from tests with an indoor test-rig. Simulations show a variation in yaw rate and roll rate as a consequence of different tyre characteristics. Based on that, we conducted an experimental campaign to validate the findings of numerical simulations. We present a novel tool to laterally perturb the bicycle by kicking the bicycle rear wheel at the tyre-ground contact point. The experiment, known as kickplate test, was performed using an instrumented bicycle, changing the tyre inflation pressure (300, 400, 500 kPa), and the vertical load (rider weight 50, 61, 72 kg, namely 570 N, 635 N, 701 N on the rear tyre – considering also the bicycle weight). The results confirm that the inflation pressure affects the bicycle dynamics, in particular roll rate and yaw rate. The model matched the experimental data in terms of magnitude however with different dynamics and we aim to address discrepancies before further publications. Experimental results indicate that per each value of vertical load applied there is an optimal inflation pressure which facilitates a faster recovery after a perturbation and better energy dissipation. Looking at the yaw rate signal, the recovery from the disturbance is 43% faster for the heavier rider (701 N on the rear tyre) when the tyres are inflated at the highest inflation pressure (500 kPa). With the lighter rider (570 N on the rear tyre), a change of inflation pressure from 500 kPa to 300 kPa results in 16% faster recovery, meaning that the inflation pressure has a remarkable impact on bicycle dynamics.

Keywords: pressure, dynamics, Magic Formula, bicycle-rider model, kickplate

8.2 Introduction

Bicycle dynamics has been a subject of studies for more than one century, and it is still being investigated today to improve both the safety, the performance and the handling of bicycles [45] [189] [138] [83] [15]. In this paper we aim to address some concerns arising from unexpected but realistic situations you may encounter riding a bicycle in daily life. Specifically, we want to investigate if changes in tyre inflation pressure can make bicycles safer when dealing with unexpected lateral disturbances. Even if we spent most of the time riding straight ahead, some of the most dangerous situations arise from lateral disturbances, making them an important field of research [31].
We know from literature that the tyres have a role in bicycle dynamics [32] [43] [46], being the unique interface between the vehicle (i.e. the bicycle in our case) and the road. For example, when hit by a gust of crosswind or a road pothole, or slipping on an icy road, tyres affect the bicycle dynamics. A different tyre width [53], compound or inflation pressure may change the kinematic response over time [48]. We tested

several tyres with indoor test-rig VeTyT (acronym for Velo Tyre Tester) [14] [62] to derive the cornering stiffness and Magic Formula's coefficients [25] [186] while varying inflation pressures and vertical loads. We know that inflation pressures affect tyre characteristics and cornering stiffness [66], commonly used to assess tyre lateral characteristics [53]. With this study, we aim to prove that they also impact the bicycle-rider dynamics. We try to close the gap between tyre testing and actual bicycle dynamics, to show that the tyre characteristics we measured indoor also affect daily rides.

To simulate disturbances in a measurable and reproducible way, we designed and developed an experimental setup based on a novel kickplate device. Similar to training methods for car drivers to face loss of vehicle handling [190], we perturbed the straight motion by applying a lateral disturbance to the rear tyre of the bicycle to elicit the nonlinear effects on the tyres and quantify their actual role in bicycle-rider dynamics. To investigate the actual contribution of bicycle tyre parameters (vertical load and inflation pressure) in bicycle dynamics, we asked three different volunteers with varying weights to ride over the kickplate with an e-bike equipped with an IMU, and repeat the test under different inflation pressures. The tyre chosen for tests is among the most popular tyres for e-bikes and trekking/tour bicycles. It was experimentally characterised on the indoor test-rig VeTyT and the results have been presented in [66] [179].

Experimental lateral perturbation on bicycle dynamics is quite an uncommon topic to find in academic literature. In [34], the researchers simulated the effect of crosswind for different forward speeds. They used the Carvallo-Whipple bicycle model, adding a rider control model implemented as a linear steer torque controller with full state feedback. Feedback gains were obtained experimentally riding a bicycle on a treadmill. Uncontrolled bicycles tend to steer into the wind, requiring a constant steer torque action from the rider to control the bicycle. Riding in the wind requires higher skills and it is usually more dangerous as it may compromise the bicycle stability. In [35], they aimed to identify the rider control parameters. They measured the rider steering response after perturbing the lateral balance with impulsive forces to the seat post, on a steer-by-wire bicycle. Similarly in [36] [37], the bicycle was laterally perturbed from the seat post, with impulsive forces. The researchers attached a stick in series with a load cell and applied pulling/pushing forces to a bicycle riding on a treadmill.

As mentioned before and stated in the literature [13] [25] [24], the tyres play an important role in two-wheeled vehicles. However, there are only a few studies on bicycles, and none of them seems to really investigate the tyre effect on lateral dynamics in a real environment. A kickplate for bicycles has never been tested before, therefore there was a lack of literature to support us during the experiment design.

Researchers mostly focused on the modelling of bicycle dynamics [36] [50] [52] [191]. For example, bicycle design was investigated and optimised for lateral handling in [33]. They started from the Carvallo-Whipple bicycle model and they estimated the bicycle parameters for four different design speeds. A study on the effect of tyres on

bicycle dynamics has been presented in [48], using a multibody model implemented in commercial software ADAMS® [82]. Before simulations, they experimentally measured tyres' data on a test-rig [60]. The effect of each tyre parameter was investigated by changing one tyre parameter at a time while keeping the others constant. They gave a lateral disturbance to the model, to monitor the response of the system following the perturbation (0.1 N lateral force input for 0.1 s, at the centre of mass of the bicycle rear frame). They demonstrated that the vertical load affected the weave speed (e.g. the lowest speed at which the weave mode of the bicycle model is stable), while cornering stiffness had a very limited influence on weave mode, which is mainly destabilised by the twisting torque [65]. In [43] the researchers investigated the influence of tyre properties on the stability of bicycles. The tyre cornering stiffness as well as front-assembly stiffness and twisting torque stiffness are among the most influential parameters for weave mode, while for wobble mode we should also take into account the tyre relaxation length.

The use of a kickplate aims to go beyond the already addressed topic of bicycle-rider lateral perturbation. It allows altering the tyre-ground interface by acting directly at the contact patch. The device provides a lateral perturbation at road level, which directly affects the tyre response. It also makes possible the study of the rider's reaction (not the main topic of this paper) and tyre properties following a perturbation event. In doing so, it is possible to elicit large slip angles (>5 deg) and experience the tyre nonlinear effects.

This paper is organised as follows. In Section 8.3 we describe the methods, including constructive features of the kickplate, the experimental setup, tyre used for testing, and the experiment protocol. Section 8.4 presents the simulations conducted on extended Carvallo-Whipple bicycle-rider model, updated to simulate the kickplate test with the addition of nonlinear tyre contribution. Afterwards, Section 8.5 reports the results of the experimental campaign using the kickplate device.

8.3 Methods

Kickplate device

The experiment is based on the use of a kickplate device specifically designed for bicycle testing [54]. It consists of a moving platform, able to apply a sudden lateral perturbation to the bicycle wheel (150 mm displacement, in less than half a second), therefore it elicits slip angles larger than 5 degrees on the rear tyre (Figure 8.1 (A) and (B)). The platform is an 8 mm thickness aluminium plate, 500x500 mm, fully covered by P100 grade sandpaper to minimise relative slippage tyre-plate. It is rigidly fastened to a pneumatic cylinder (FESTO Normcilinder DNC-63-250-PPV-A-EX4) able to provide up to 2000 N of pushing force. The latter is pressurised by an air compressor connected to the cylinder. The pressure was set in the range 4500 – 5000 kPa for our test (or, as commonly referred, 4.5 to 5 bar). The cylinder is put under pressure and the plate held in position by a stopper cylinder (FESTO Stoppercilinder DFSP-50-20-DS-

PA), whose timing is governed through electro valves. As the bicycle rides over the kickplate, the front wheel is detected by an ultrasonic sensor placed forward with respect to the device at a distance approximately equal to the bicycle wheelbase. The stopper cylinder is retained and the platform moves in a very short time span. In this way, we kick the bicycle rear wheel which is on top of the kickplate, and the rider has to steer to retain balance and the desired direction. Once the kickplate has been fully displaced, the plate motion is damped by a pair of shock absorbers (Model: ACE Shock Absorber MA 3325EUM, 83mm Body Length). Afterwards, the kickplate was manually returned to its initial position, ready to pressurise the system again. The device is equipped with an accelerometer and a pressure sensor (both at 100 Hz of sampling frequency), from which we derive the force applied to the plate. To relate the pressure within the cylinder and the force that it provides, we performed preliminary static calibrations. A load cell was placed in between the rod of the cylinder and the plate fixing system, applying an increasing pressure each time. Both the values of pressure and force from the load cell were recorded and plotted. We fitted a curve to the measured data and obtained a good linear relationship featured by $R^2 = 0.98$ between the pressure measured by the pressure sensor (connected very close to the air-entrance side of the pneumatic cylinder, to avoid losses due to pipes and tubes) and the force. We can derive the applied force according to the equation (8.1), where y represents the resultant force (in N), and x is the pressure from the pressure sensor (in kPa).

$$y = 2.47x + 146 \tag{8.1}$$

Instrumented bicycle

Tests have been performed using an instrumented Gazelle® Arroyo C8 e-bike [192]. The bicycle is equipped with a wheel speed sensor on the rear wheel. Additionally, a steering angle sensor is positioned at the steering tube to measure the steer angle and steer angular rate, at a sampling rate of 100 Hz. An inertial measurement unit (IMU) was mounted on the rear frame, to measure the roll and lean angular rates (sampling rate 100 Hz). The apparatus is powered by the internal battery of the e-bike. Data was logged on a micro SD flash memory card.

We equipped the bicycle with Schwalbe trekking tyres 50km Energizer, Plus G-Guard 5/Addix-E (both front and rear wheels, on the rim provided as standard by the manufacturer). We tested under different inflation pressures and vertical loads (all details in Table 8.1). This tyre is often chosen as the first equipment of several e-bikes, and was previously characterised with VeTyT, an indoor test-rig conceived for measuring the lateral characteristics of bicycle tyres (lateral force and self-aligning torque) [99] [14]. Furthermore, when tested with VeTyT the tyre showed 15% difference in cornering stiffness between different inflation pressures (on average), making it the ideal choice for our outdoor test.

As we can see in Table 8.2, the cornering stiffness C_{F_y} increases with the vertical load and decreases with inflation pressures. The variation among the cornering stiffnesses measured at 300 kPa and 500 kPa is about 18% for vertical loads of 343 N and 404 N, nearly 9% for the highest load tested (488 N). Due to technical limitations of our VeTyT test-rig, we could not test under higher vertical loads, like the ones actually used during the kickplate experiment. Nevertheless, this fact does not impact the presented test nor the results, as our aim is to understand if a change in tyre inflation pressure might result in a different bicycle response. We demonstrate with the indoor test-rig that both the inflation pressure and vertical load have an impact on tyre lateral characteristics.

Participants

Three participants took part in the experiment (2 males, 1 female; weights: 52 kg, 61 kg, 70 kg; age: 27±3 years old); see Table 8.3. They were all familiar with riding bicycles for commuting, they did not report any injury or disturbance at the moment of the experiment. They were selected among the researchers' university network according to their availability.

Procedure

We instructed the participants to keep the same bicycle setup for the test, riding at a speed between 1.92 and 2 m/s in eco-mode (the cycling mode with the lowest propulsion assist), found as optimal for the kick action. Higher or lower speeds made the wheel detection too difficult with the current experimental set-up, forcing us to this choice. Additionally, the effect of the riding speed on the tyre characteristics is negligible for limited variation (<5 km/h in terms of difference) [63]. The riders got familiar with the bicycle for a few minutes before the experiment.

Participants started the ride 13-15 meter away from the kickplate, following a straight trajectory towards the device to let them stabilise and feel safe on the bicycle. No external disturbances were applied at that time. The bicycle approached the kickplate and the front wheel passed over it. As the passage of the front wheel was detected by the ultrasonic sensor placed in front of the kickplate (approximately 1 m in front of the kickplate itself), the microcontroller activated the stopper cylinder valve allowing the plate to move and kick the rear wheel. Riders had to control the bicycle to not fall and continue the ride. All the tests ended with riders in total control of the bicycles. None of the tests resulted in fallings or dangerous situations for either the researchers or the participants. Before data acquisition, the participants rode over the kickplate at least a couple of times to familiarise themselves with the protocols. All the tests were conducted setting the pressure of the air compressor at 4.5-5 bar, to apply a lateral acceleration of about 30-35 m/s^2 (about 12 tests per each pressure, three different series per each participant).

To negotiate the device and avoid any detrimental bump which may affect the bicycle dynamics, the device was installed into the ground, so that the moving plate was at

the road level (Figure 8.1 (B)). Before the experimental campaign, the device was inspected and approved by a safety inspector of the Delft University of Technology. The entire test procedure was discussed and approved by the Human Research Ethic Committee of the Delft University of Technology (application #3334).

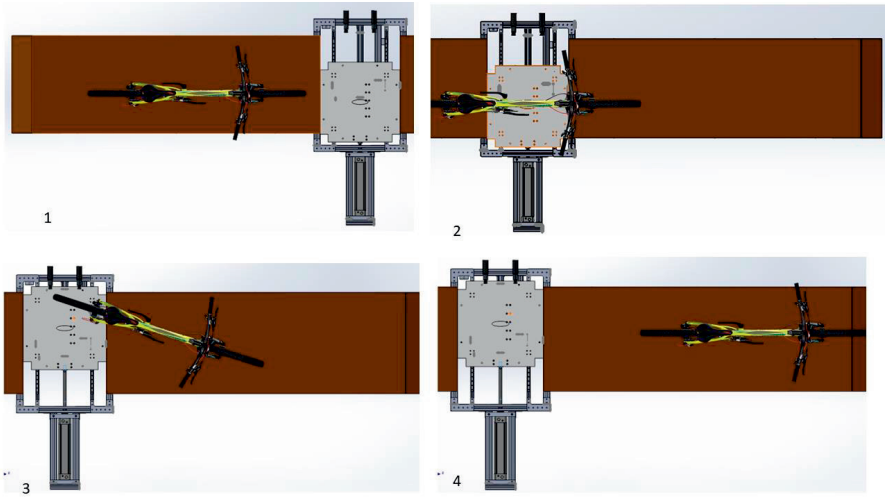

(A)

(B)

Figure 8.1 – (A) Kickplate schematic top-view. When the bicycle (in yellow) is on top, the device kicks the rear wheel laterally. Please note that the plate displacement here depicted is exaggerated to enhance a better understanding of the test procedure. (1) The bicycle is going to approach the kickplate. (2) Bicycle front wheel passes over the device before being detected by the ultrasonic sensor. (3) When the rear wheel is on top of the kickplate, the aluminium platform moves kicking the wheel, while the bicycle continues its riding (4). In (B), the kickplate device into the ground, after removing the brick tiles and levelling the underneath surface. You can also see the instrumented e-bike used for tests.

Table 8.1 – Tyre tested mounted on the bicycle, and also tested with indoor test-rig VeTyT. Tyre brand, commercial series label, size and ETRTO standards are reported. We tested for different inflation pressures and vertical loads. F_z on rear tyre is our variable of interest, as the lateral disturbance was directly applied to the rear wheel.

Brand	**Serie**	**Size**	**ETRTO**	**Inflation Pressures [kPa]**	**F_z (on rear tyre) [N]**
Schwalbe	50km Energizer, Plus G-Guard 5/Addix-E	28" x 1.75	47 - 622	300 – 400 - 500	570 – 635 – 701

Table 8.2 – (Adapted from [66]) Cornering stiffness for different vertical loads and inflation pressures (300, 400, 500 kPa). In the last column, the variation (in percentage) of cornering stiffness due to increasing vertical load, referring to the lowest vertical load tested (here 343 N). Similarly in the last row, but the variation is now reported relative to the inflation pressure.

Inflation pressure	**Camber angle [deg]**	**C_{F_y} [N/deg] (F_z 343 N)**	**C_{F_y} [N/deg] (F_z 404 N)**	**C_{F_y} [N/deg] (F_z 488 N)**	**% Variation C_{F_y} F_z [N]: 404 vs 343 (F_z [N]: 488 vs 343)**
300 kPa	0	105.2	113.6	123.5	+8% (+17%)
400 kPa	0	98.2	108.1	124.4	+10% (+26%)
500 kPa	0	86.6	90.1	111.6	+4% (+28%)
% Variation C_{F_y} Pressure [kPa]: 400 vs 300 (500 vs 300)		-7% (-17%)	-5% (-20%)	+ 0.7% (-9%)	/

Table 8.3 – Riders' weights, bicycle weight and the total vertical load F_z applied on the rear tyre (the one we kicked during the test). Note that the values reported in the column "Load ratio front/rear wheel %" are based on an estimate based on common weight distribution for such bicycle models. Slight differences may arise from actual riders' posture during the test.

# Riders	**Weight [kg]**	**Load ratio front/rear wheel %**	**Weight (Total | Rear wheel) [kg]**	**Total F_z on front tyre [N]**	**Total F_z on rear tyre [N]**
Rider A	52	25 / 75	33 | 19	265	570
Rider B	61	25 / 75	33 | 19	287	635
Rider C	70	25 / 75	33 | 19	309	701

Data analysis

Data from the accelerometer fixed to the moving plate and the pressure sensor were gathered via cable connection to an Arduino UNO microcontroller placed next to the kickplate itself, at a sampling frequency of 100 Hz. We wrote a dedicated C++ script and we ran it using Visual Studio Code (Microsoft Corporation). It collected data organised in columns into .txt files. We filtered raw data using a low-pass filter with a cut-off frequency of 20 Hz. Before starting the experimental rides, we switched on the data acquisition system on the instrumented bicycle. To ensure the synchronisation between the data from the load cell and the ones from the bicycle, we hit the plate laterally when the rear wheel bicycle was statically on top of the plate itself (we held the bicycle in standstill, without rider), in order to have a trigger on bicycle lateral acceleration and kickplate acceleration to realign signals during post-processing.
To reduce the variability and uncertainty given by the rider response, the results presented in the following sections are the average of three different trials. This was possible as the signals showed good repeatability among successive tests. In Figure 8.2, we depict three different time histories before averaging for bicycle yaw rate and roll rate, taken from the same rider under the same inflation pressure.
The time histories were then averaged and we statistically estimated the uncertainty around the estimate of the mean measurement through the standard error (referred to as "SE" in figures) [193]. It is defined as the ratio between the standard deviation and the square root of the sample size (in our case, sample size is equal to 3).

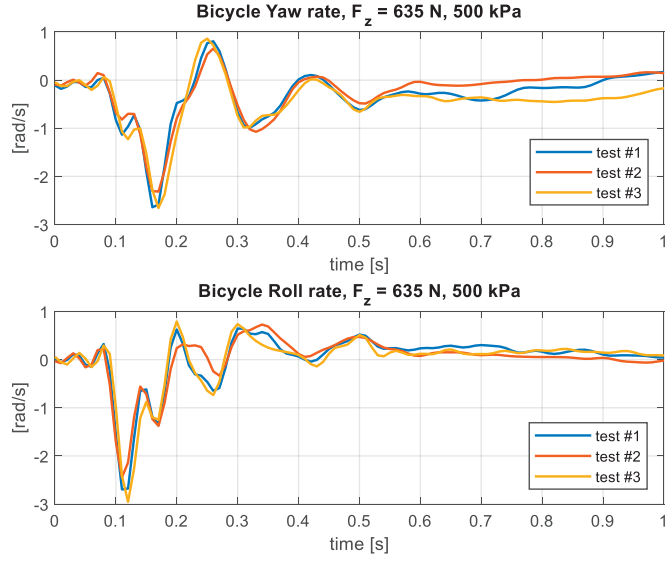

Figure 8.2 – Bicycle yaw rate and roll rate for three different tests following the kickplate experiment, under the same vertical load (635 N on the rear tyre) and inflation pressure (500 kPa). Time histories have been filtered out of high frequency components (cut-off frequency 20 Hz). No average was applied here.

Based on the cornering stiffnesses evaluated in [63] under different inflation pressures as function of vertical loads, we expect that lower inflation pressures are more suitable for lighter riders. On the other hand, we can assume that heavier riders need higher tyre inflation pressures.
One method to assess this can be the analysis of peaks' decay time. The first one can be derived by observing the time histories of bicycle IMU signals. In particular, we exploited the bicycle yaw rate signal as it was the most involved signal according to the applied disturbance. Furthermore, it also pointed out a good repeatability among different tests, making it an ideal choice for our analysis. We observed the yaw rate peaks over the time and reported those on a plot. We stopped the peak detection when the peaks' magnitude was lower than 8% of the first peak (the highest in magnitude), as we found it to be a good threshold to mark the end of the disturbance effect.
We also investigated the yaw rate logarithmic decrement δ [194]. It is defined as the rate at which the amplitude of a signal decreases, being the natural logarithm of the ratio of any two successive amplitudes U_0 and U_n, where n is the number of periods between the selected peaks (equation 8.2) [194]. It refers to damped free oscillation by definition. Our system is actually controlled, as we have the rider in the loop. Nonetheless, we evaluated it as it can give us a synthetic index to assess the effect of tyre pressure on the bicycle yaw rate alongside the damping ratio ζ found from logarithmic decrement, according to equation (8.3). Analysis were conducted on successive peaks (first peak, marked as #1, and third peak, marked as #3. Likewise for peaks #2 and #4, then peaks #3 and #5). This is due to the fact that we are dealing with a controlled system, therefore logarithmic decrement of successive peaks after a period may differ considerably.

$$\delta = \frac{1}{n} \ln \left[\frac{U_0}{U_n}\right] \tag{8.2}$$

$$\zeta = \frac{\delta}{\sqrt{4\pi^2 + \delta^2}} \tag{8.3}$$

We also performed an analysis in the frequency domain. We plotted the amplitude of the yaw rate and roll rate signals over the frequencies up to 25 Hz, as no relevant contributions are present above it.

Model implementation

The numerical modelling of the kickplate test is based on the nonlinear Carvallo-Whipple bicycle-rider model [36] [49] (Figure 8.3 shows the bicycle in a general configuration, with the definitions of the coordinate systems), which includes nonholonomic constraints and thereby ignores tyre slip. Originally featuring three velocity degrees of freedom (namely, roll rate, steer angular rate and rear wheel rotation rate) [50], we extended this model by adding a nonlinear tyre model [25] [66]

which includes tyre slipping and relaxation length. Specifically, tyre-ground nonholonomic constraints have been replaced by Magic Formulas [25] for the tyre lateral force and self-aligning torque as functions of the slip and camber angle of the wheels. We kept the nonholonomic constraints for longitudinal motion to impose rolling without any longitudinal slip. We introduced the tyre vertical stiffness and tyre damping to allow an easier calculation of the instantaneous vertical force to be used in the nonlinear tyre model. Although a linear tyre model would be simpler to use and provide good results for simulations with small lateral perturbations, the use of a nonlinear tyre model is preferred when dealing with large slip angles (i.e. >5 deg), as it allows taking into account the lateral force and self-aligning torque saturation [45].

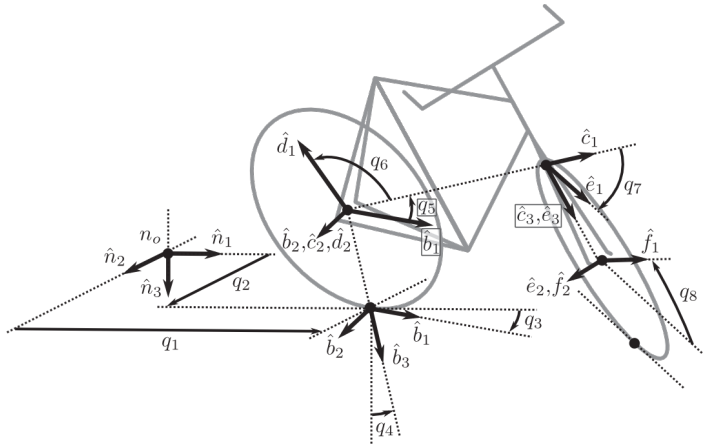

Figure 8.3 - Definition of the coordinate systems and generalised coordinates for the bicycle in a generic configuration (adapted from [36]).

We added a basic human-like closed loop controller without delay, to apply steering torque and stabilise the bicycle following the perturbation. From the linearised Carvallo-Whipple model (model linearised before adding the Pacejka's Magic Formula tyre model), we derived the Linear Quadratic Regulator (LQR) gains at simulation speed of 3 m/s [195]. We built the controller using the signals of frame roll angle (q_4), steering rotation angle (q_7), frame roll angular rate (u_4), and steering rotation angular rate (u_7), with the associated four gains (kq_4, kq_7, ku_4, ku_7, respectively) listed in Table 8.4. The nomenclature comes from [196]. We adopted different parameters for each rider according to their different height and weight, therefore we obtained different gains for each rider. The controller output T_δ is calculated as follows (8.4).

$$T_\delta = kq_4 * q_4 + kq_7 * q_7 + ku_4 * u_4 + ku_7 * u_7 \qquad 8.4$$

We also conducted simulations of the kickplate test without a human-like controller, in order to see how the tyres alone could affect the results.

The mathematical tyre model, based on Pacejka's Magic Formula [25], was built from the experimental data obtained from the indoor test-rig VeTyT [66]. As the friction coefficient of the flat track used for tyre indoor testing differed from that of the kickplate one (moving plate was covered by coarse sandpaper), we applied a corrective coefficient CF_c to the tyre data from indoor testing, in order to take into account the actual friction coefficient we had during outdoor tests. The corrective coefficient is given by (8.5):

$$CF_c = \mu_{kickplate}/\mu_{VeTyT} \quad 8.5$$

Where $\mu_{kickplate}$ and μ_{VeTyT} are the friction coefficients directly measured on kickplate moving plate and VeTyT flat track, respectively. In our study, CF_c was equal to 1.31 (adimensional) (see Table 8.5). The μ_{VeTyT} comes from the analysis of the plot of the measured lateral force as function of the slip angle. The ratio between the maximum peak value of the lateral force and the applied vertical load gives μ_{VeTyT} Regarding $\mu_{kickplate}$, we placed the bicycle with the rear wheel on the moving plate of the kickplate device. While a person sat on the bicycle, we used a lever with two digital load cells to pull at the base of the rim until the tyre slid. Given the knowledge of the applied lateral force and the vertical load on the wheel, we derived the $\mu_{kickplate}$.

For each inflation pressure we have a different set of Magic Formula parameters to be used in the simulations. This allows simulating the tyre lateral force F_y and self-aligning torque M_z for different vertical loads and camber angles, as function of the slip angle. To take into account the variation of tyre vertical stiffness with inflation pressure, we referred to the literature to estimate values for our test [63] [98] [197]. In particular, we used the same vertical stiffness coefficients K_z both for front and rear tyres, as they were inflated at the same pressure. Values used in the study are collected in Table 8.5. An example of the nonlinear tyre model results is depicted in Figure 8.4 (A) and (B), for the Schwalbe trekking tyre 50km Energizer, Plus G-Guard 5/Addix-E (the tyre which equipped the instrumented bicycle during tests, see Table 8.1) at an inflation pressure of 500 kPa, for different vertical loads and camber angles.

The Carvallo-Whipple bicycle-rider model also included rider body inertia assuming a rigid connection of the body to the frame. The rider characteristics were built on Yeadon human inertia model [198], therefore we scaled the inertia of each body segment according to the specific rider's weight and height.

The model aimed to simulate the kickplate action on the rear wheel to show the bicycle-rider dynamics under different tyre inflation pressures. We perturbed the model by applying a lateral acceleration at the contact point tyre-ground for a period of 0.15 s (lateral displacement of 150 mm, Figure 8.5). After this the position was held constant reflecting that the wheel drove from the plate. However, the model stands on some assumptions which can affect the predicted signals. Furthermore, we miss some information from the experimental test that makes it challenging to achieve an ideal mapping between the experiment and the model. For instance, we do not know the actual lateral forces at the tyre contact patch achieved during the test, as well as the

exact position of the bicycle rear wheel at the moment of the kick (whether it was in the middle, towards the trailing or the leading edge of the plate). We implemented a basic human-like controller, but we do not have any information to ensure that this aligns with the control strategy actually used by the participants. In addition, we did not implement any heading tracking control loop that the human rider could have used to stay in a straight direction. The model also assumes a rigid connection between the rider (upper body and legs) and the bicycle, which is not true in real world. This assumption may affect the predicted signals in response to strong perturbations like those induced by the kickplate. To address this limitation, we conducted additional simulations with reduced bicycle-rider rear frame rotational inertia (50% reduction in the initial values of $I_{B,xx}, I_{B,yy}, I_{B,zz}, I_{B,xz}$, based on a rider of 61 kg, in reference to the parameters proposed by Meijaard in [50]). We also reduced the height of the centre of gravity of the rear body by 50% (parameter z_B). The input disturbance profile does not precisely match what happened in reality. We perturbed the model with a 13.3 m/s^2 acceleration peak, lasting 0.15 s (Figure 8.5), while in real experiment we measured accelerations' peaks up to 40 m/s^2. The model simulations failed with such a large acceleration, thus constraining us to limit the acceleration peak value. We aim to address these uncertainties before further publication.

All the simulations were performed using scripts written in Python language, and Visual Studio Code version 1.93.1 (VSC, Microsoft Corporation) with the addition of a Python interpreter version 3.12.7 (also including SymPy 1.13.3, Matplotlib 3.9.2, SciPy 1.14.1, PyDy 0.7.3, NumPy 2.1.2). We decided to use the SciPy's function `solve_ivp` to numerically integrate ODEs, setting the numerical method LSODA (relative tolerance `rtol` for the solver set to 1e-12). This enabled the automatic switch of ODE solvers to handle both stiff and non-stiff systems. To generate the equations of motion of the mechanical system, we used the Kane's method, and the Cramer's rule to solve constraints. We performed all the calculations and data acquisition with a laptop Dell Latitude 7310, with Operation System (OS) Microsoft 10.

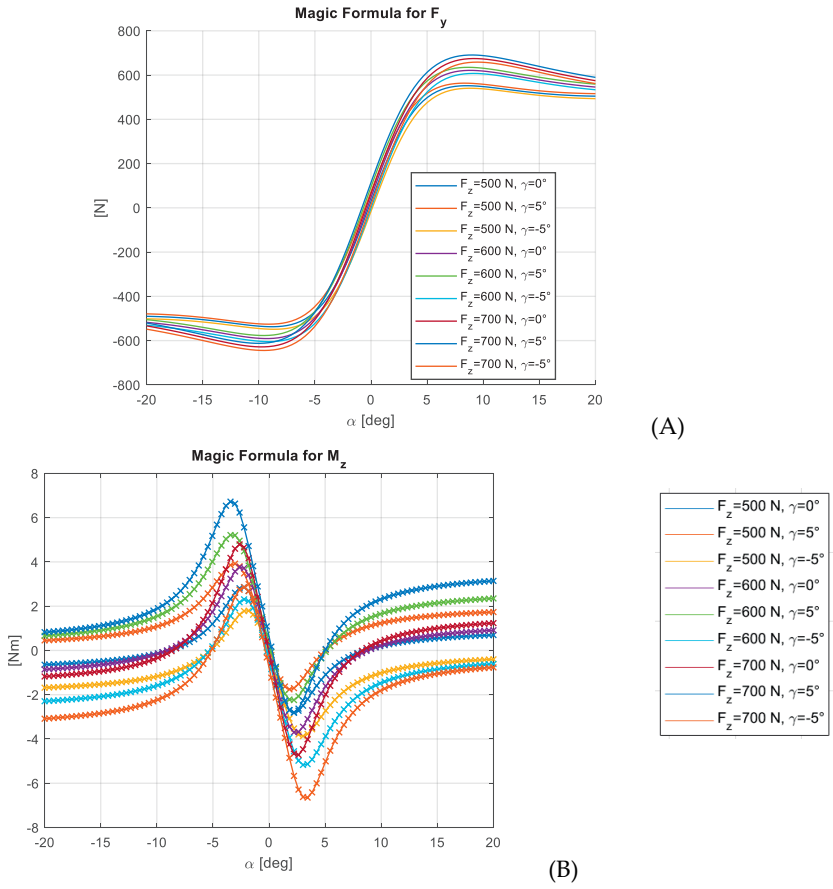

Figure 8.4 – Lateral force (A) and self-aligning torque (B) for Schwalbe trekking tyre 50km Energizer, Plus G-Guard 5/Addix-E cycle, for the tyre inflated at 500 kPa. Curves are from Magic Formula tyre model, simulated for different vertical loads (500, 600, 700N) and camber angles (0, ±5 deg).

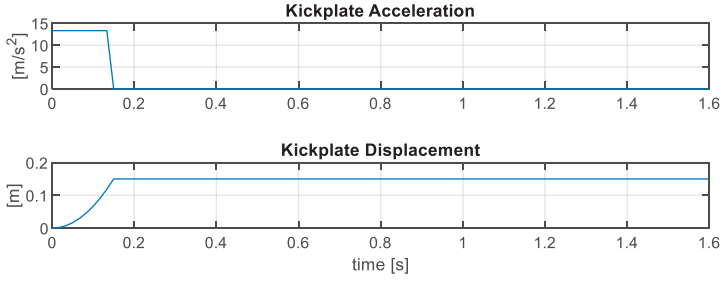

Figure 8.5 –Kickplate acceleration and displacement used in simulations, as a function of time.

Table 8.4 – LQR gains used to build the human like steering torque controller. Each column is for a different vertical load applied to the rear wheel (namely, different rider parameters). kq_4, kq_7, ku_4, ku_7 stand for the LQR gains related to frame roll angle, steering rotation angle, frame roll angular rate, steering rotation angular rate, respectively.

	F_z= 570 N	F_z= 635 N	F_z= 701 N
kq_4	-18.619	-19.5679	-20.5164
kq_7	14.721	15.4934	16.2624
ku_4	-6.2915	-6.7665	-7.3074
ku_7	1.5647	1.5876	1.600

Table 8.5 – Values of the coefficients used in tyre mathematical modelling to simulate kickplate test.

	Values	Units
$\mu_{kickplate}$	1.03	[-]
μ_{VeTyT}	0.79	[-]
CF_c	1.31	[-]
K_z at pressure 300 kPa	80	[N/mm]
K_z at pressure 400 kPa	106	[N/mm]
K_z at pressure 500 kPa	133	[N/mm]

8.4 Modelling the kickplate test

We simulated the activation of the kickplate on the rear wheel with a 150 mm displacement at the time 0 s, resulting in a lateral acceleration of 13.3 m/s^2 (Figure 8.5) and we showed the response of the bicycle under different tyre inflation pressures. In Figure 8.6, we show the results of the model simulations with a basic human-like steering torque controller, for a vertical load applied to the rear wheel equal to 635 N. The initial speed was set to 3 m/s, to match the real conditions of the experiment. We focus on the yaw rate, roll rate, steer rate, and lateral force F_y on the rear wheel. As the kickplate disturbance is applied to the rear wheel, it is indeed of interest to investigate the simulated lateral force at the tyre following the perturbation.

Despite the inflation pressure difference, the first peak of the yaw rate signal is very similar among the curves (#1 in the top plot of Figure 8.6). Variations appear from subsequent peaks. In particular, we see that the red curve (obtained for inflation pressure of 400 kPa) diverges from the others, with a different peaks timing. The blue and yellow curve (obtained under inflation pressures of 300 and 500 kPa, respectively) are almost superimposable, all over the timeline. All the curves return to their initial steady state condition (~0 rad/s) 2 seconds after the kickplate disturbance.

Regarding the roll rate signal, the red curve (400 kPa) deviates from the other ones at abscissa 0.2 s, just after the first peak. For the steer angular rate, the trend of the curve at 400 kPa changes after 0.2 s. Similar for the lateral force F_y on the rear wheel, which shows a difference for the curve at 400 kPa starting from the peak at 0.2 s.

We also simulated the kickplate test without any human-like steering torque controller. The comparison of the outcomes with the rider's controller switched on and off is depicted in Figure 8.7, alongside the condition with the LQR gains set to 50% of their original values (red curve in Figure 8.7). We depict the results for an inflation pressure of 400 kPa and vertical load on the rear wheel equal to 635 N. The controlled bicycle-rider model can deal with the lateral perturbation and return quickly to its steady state (in about 1 s, if we look at the steer angular rate and roll rate signals). Also the bicycle-rider model with the LQR gains set to 50% is able to recover from the perturbation, following a trend similar to the reference controlled bicycle-rider, even though in longer time (about 1.25 s). On the contrary, the uncontrolled bicycle-rider model cannot cope with the kickplate disturbance, as we see the bicycle falling at abscissa 0.9 s after the disturbance. The same conclusions can be drawn for all the pressures tested, as the absence of control is not able to ensure the return to the steady state conditions (Figure 8.8), for all the pressures tested. The simulations end with the bicycle falling in less than 1 s. The human-like controller is therefore crucial to keep the bicycle under control in a straight trajectory when dealing with such a strong lateral perturbation. Figure 8.8 also highlights the significant role of the tyres in bicycle dynamics. Even though we recognise the role of the controller, the way the bicycle handles the disturbance is different, simply by changing the tyre characteristics (i.e. the inflation pressure in our case).

The simulated results with the addition of the human-like controller provided the best overall results, as the controller allows the return of the bicycle-rider model to the steady state and it prevented the bicycle from falling. However, it is hard to draw definite conclusions on what the optimal pressure is as we do not see major differences among the curves. Even though it is clear that the curves are not identical due to the effect of the tyre characteristics, we conclude that the tyre inflation pressure does not seem to appreciably affect the overall bicycle dynamics according to the simulations.

The model discussed so far assumed the rider body rigidly connected to the bicycle frame, by adding the rider inertia to the bicycle frame inertia. Figure 8.9 quantifies the effect of this assumption in an approximate manner, by presenting the results of the model with reduced inertia and a lower centre of gravity for the rear frame body "B" (-50% in the rear frame rotational inertia parameters and centre of gravity height, red curve in Figure 8.9). The blue curve, already presented in Figure 8.6, represents the test simulation with rider inertia added to the bicycle frame inertia. As we may expect, the red curve exhibits larger motion compared to the blue one ("Original" condition). In particular, the peaks' magnitude is larger as we can see at time instants 0.18 s and 0.4 s for the roll rate. Similarly, the steer angular rate indicates that a reduction in inertia leads to a motion increase.

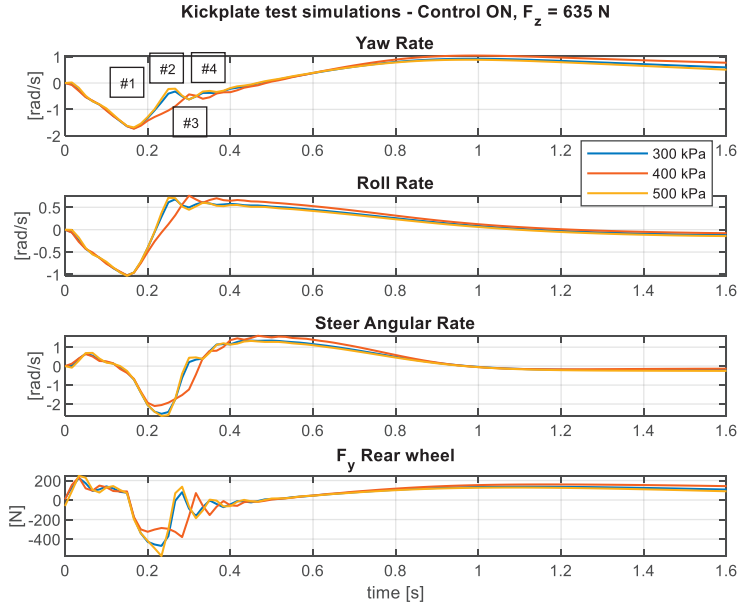

Figure 8.6 – Nonlinear simulations of Carvallo-Whipple bicycle-rider model varying tyre characteristics (namely, tyre inflation pressure), following the kickplate perturbation to the rear wheel. We focus on the simulated yaw rate, roll rate and steer rate. It is also of interest to see the time history of the lateral force on the rear wheel, where the kickplate action takes place. The labels in the top plot refer to the detected peaks in the signal.

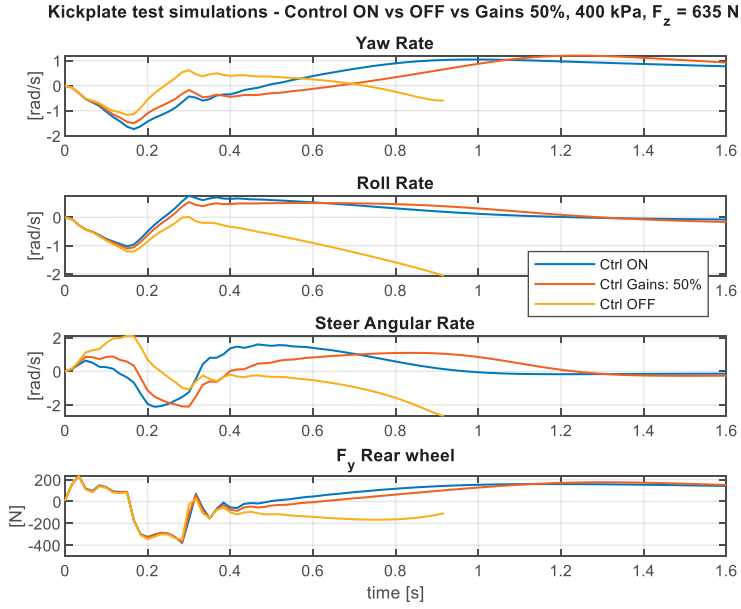

Figure 8.7– Nonlinear simulations of Carvallo-Whipple bicycle-rider model, with human-like rider control ON (blue curves), with LQR gains set to 50% of their original (red curves) and control OFF (yellow curves), for vertical load on the rear wheel equal to 635 N and inflation pressure 400 kPa.

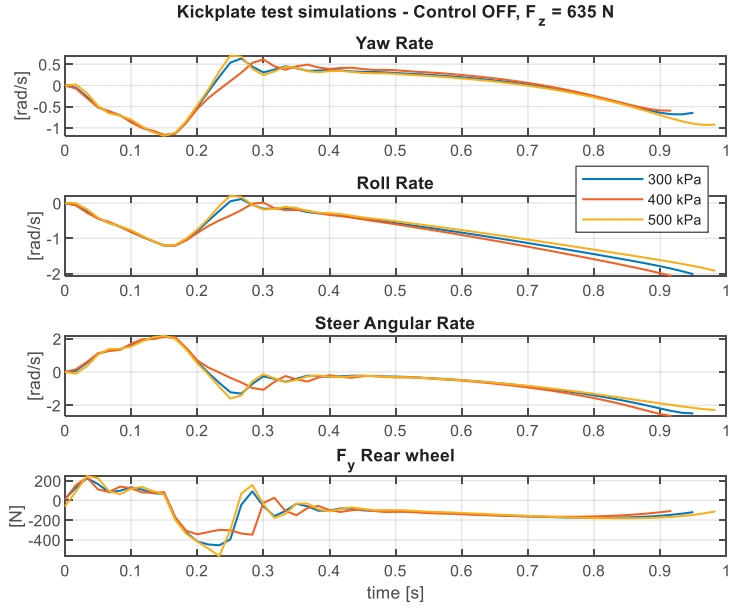

Figure 8.8 – Nonlinear simulations of Carvallo-Whipple bicycle-rider model, with human-like rider control disabled, for vertical load on the rear wheel equal to 635 N. Each curve corresponds to a different inflation pressure, as described in the legenda.

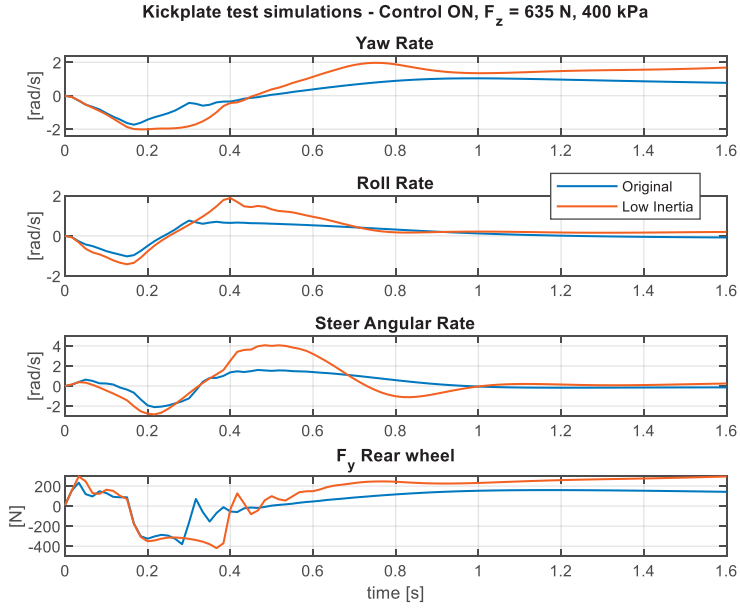

Figure 8.9 – Simulations of Carvallo-Whipple bicycle-rider model, with human-like rider control enabled, for vertical load on the rear wheel equal to 635 N and inflation pressure of 400 kPa. The blue curve ("Original" in legenda) is the same one already presented in Figure 8.6, with rider inertia added to the bicycle frame inertia and controller enabled. The red curve ("Low Inertia" in legenda) is obtained from the model with - 50% inertia of rigid body *B* and - 50% centre of gravity height of body *B*.

8.5 Experimental results

In this section, we present the experimental results of the kickplate test. Each subsection focuses on a different vertical load applied to the rear tyre, for three variations of the inflation pressure.

We plot the yaw rate, the roll rate, and the steer angular rate. We also plot the kickplate acceleration from the accelerometer fixed to the moving plate. This is useful to determine the exact kicking moment, enlightened by a vertical dot green line in the plots. As the bicycle was travelling at 1.92–2 m/s, and the disturbance was applied when the wheel was in the first half of the moving plate (closer to the entrance side, the plate is 0.5 m long), it is reasonable to assume that the rear wheel left the kickplate in about 0.2 – 0.22 s after the kicking instant, thus the bicycle fully experienced the kick (about 0.15 s). All the results are plotted with their standard error (referred to as "SE" in the legenda of the plot), as described in Section 8.3 ("Procedure" subsection).

8.5.1 F_z on the rear tyre: 570 N

Figure 8.10 (A) depicts the results under a vertical load of 570 N on the rear tyre. The variability of the averaged results over three different runs is very limited, as we can see from the SE that features Figure 8.10 (A).

The time instant of kickplate force application was derived from the accelerometer fixed to the moving plate. We are not particularly interested in the time history of the kickplate acceleration except for detecting the release instant, as it turned out to be the most reliable way to detect the kicking time. Following the disturbance application, the bicycle-rider was destabilised, as we see from the roll rate and yaw rate signals. The rider was able to recover from the disturbance in less than a second, thus covering an approximate distance of 1.7 meters (travelling speed in the range 1.92 – 2 m/s).

The rider did not react instantaneously to the disturbance. If we assume the steer angular rate to be the actual rider reaction on the handlebar, we see that it occurs ~0.04 seconds after the force application (indicated by the green vertical line). This reaction time is too short and not feasible for visual stimuli for humans according to the literature, which sets it around 0.2 seconds [29] [199]. Therefore, the delay found during this experiment must be related to the involuntary reaction of the rider, including vestibular and muscle feedback, but can also result from passive body and bicycle dynamics.

The analysis of yaw rate peaks is shown in Figure 8.10 (B). Peaks have been selected from the yaw rate time history shown in the top plot of Figure 8.10 (A) (#number labels refer to the identified peaks). The oscillation disappears in less than 0.5 seconds, so we limited our analysis to the first visible peaks (six different peaks can be identified). They are reported with their standard errors (SE), resulting from the average of three different time histories (Section 8.3 – *Data analysis*). The last peak (#6) of yaw rate under an inflation pressure of 300 kPa (blue curve) appears 0.04 seconds before the peak #6 at an inflation pressure of 400 kPa (red curve) and 0.05 seconds before the one at pressure of 500 kPa (yellow curve). In Table 8.6, we report the abscissa values of the last peaks #6 and compare them, showing the percentage variation. This suggests that the rider was able to recover faster from the disturbance when the tyres were inflated at 300 kPa.

The analysis of logarithmic decrement of yaw rate signal (according to equation 8.2) was conducted on successive periods (corresponding to first peak, marked as #1, and third peak, marked as #3. Then for peaks #2 and #4, followed by analysis on peaks #3 and #5). The values and percentage variations are collected in Table 8.6. According to the results from Figure 8.10 (B), where we saw that oscillations disappeared earlier for the inflation pressure of 300 kPa, we would expect the signals at 300 kPa to have the largest logarithmic decrement. This is not actually true, given that the inflation pressure of 400 kPa ensured the highest logarithmic decrement between successive peaks (#1 and #3) over one period. Likewise, the damping ratio, as directly calculated from logarithmic decrement (equation 8.3), indicated that the tests were strongly

underdamped in the beginning, with all the calculated damping ratios $\zeta << 1$ (Table 8.6, peaks #1 and #3). Conversely, for the peaks #2 and #4, the system was strongly overdamped (damping ratio >> 1, Table 8.6). We attribute this strong variation to the involuntary control action of the rider. While the damping ratios for pressures of 300 and 400 kPa are very similar (variation of 2%), the results differ significantly when we set the pressure at 500 kPa, with a 59% variation with respect to a pressure of 300 kPa. Repeating the analysis on peaks #3 and #5 we do not notice any relevant difference in logarithmic decrement for different inflation pressure, and the system is slightly overdamped ($\zeta > 1$).

The tyre inflated at 300 kPa gave the shortest signal period compared to other pressures. In other words, the bicycle with tyres inflated at 300 kPa allows the bicycle to recover faster from the disturbance as seen in Figure 8.10 (B). Nonetheless, we cannot draw any conclusion by only looking at the logarithmic decrement or damping ratio. Logarithmic decrement rule may provide us with some information on the difference in amplitude between successive peaks, but it does not fully apply if we look at the great picture of the yaw rate signal. This may be due to the fact that the signal only appears periodic, but we cannot neglect the nonlinear effects of the tyres and even more the rider control action on the bicycle dynamics.

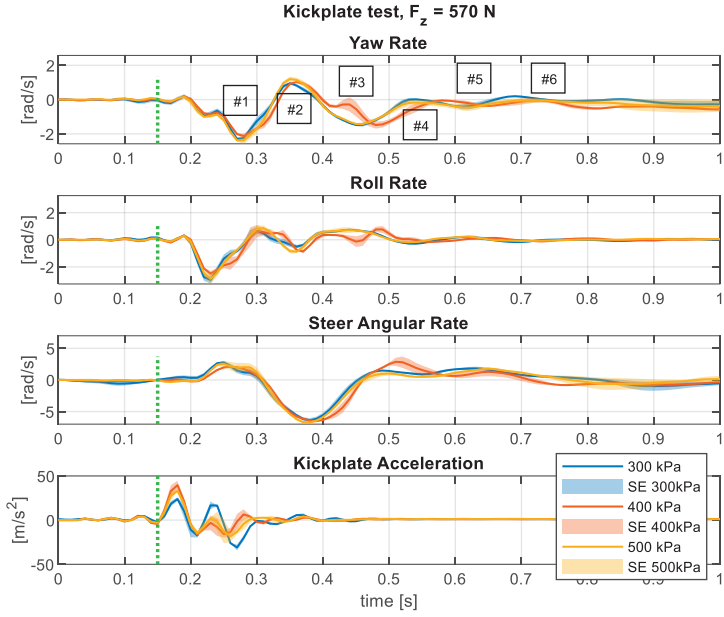

(A)

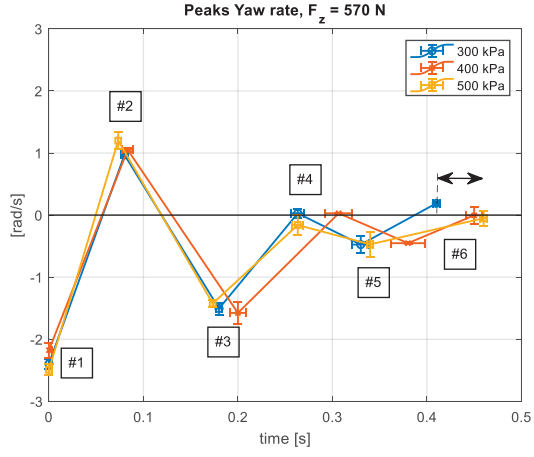

(B)

Figure 8.10 – (A) Bicycle kinematics at the moment of the kick, under vertical load of 570 N on the rear tyre. We focus on 1 second of time history to enlighten the bicycle yaw rate, roll rate, steer angular rate before and after the kickplate action. The kickplate acceleration is useful to derive the exact kick instant and relate that to the bicycle response. The results for three different pressures are depicted (300, 400, and 500 kPa), alongside the standard errors "SE". The vertical green line represents the kick moment (vertical dot green line). The labels in the top plot refer to the detected peaks in the signal. (B) Time history of the peak values for the yaw rate, from the top plot of figure (A). Each line represents a different inflation pressure, as reported in the legenda. The double arrow line indicates the (qualitative) difference in time between the results at 300 kPa (blue line) and the other ones. Note that

here we only depict 0.5 seconds of time history, as the peaks become then negligible and very close to 0. Each value is plotted along with the uncertainty interval (evaluated as standard error). The #number labels refer to the yaw rate peaks identified in the top plot of (A).

Table 8.6 – Yaw rate peaks timing for F_z = 570 N. First row: time values at which we have the last peaks of the yaw rate signal before the disturbance is recovered, when the vertical load applied to the rear tyre is equal to 570 N. Time values correspond to the abscissa values from Figure 8.10 (B), under different inflation pressures. Second row: logarithmic decrement, evaluated over one period (among peaks #1 and #3). Third row: damping ratio from equation (8.3), evaluated from the logarithmic decrement of the second row. Fourth and fifth rows are equivalent to second and third ones, but now referred to the peaks #2 and #4. The procedure has been repeated for peaks #3 and #5 (sixth and seventh rows). The last column reports the variation (in percentage) of values reported in the first three columns, for different inflation pressure. In the last row, we report the period of the signal for different inflation pressures.

Yaw rate (F_z = 570 N)	**300 kPa**	**400 kPa**	**500 kPa**	**% Variation Inf. Pressure [kPa]: 300 vs 400 (300 vs 500)**
Last peaks' time [s] (peaks #6)	0.41	0.45	0.46	-9% (-11%)
Log decrement δ Peaks #1 and #3	0.46	0.32	0.56	+44% (-17%)
Damping ratio ζ Peaks #1 and #3	0.07	0.05	0.09	+43% (-17%)
Log decrement δ Peaks #2 and #4	3.49	3.59	0.83	-3% (+73%)
Damping ratio ζ Peaks #2 and #4	0.49	0.50	0.30	-2% (+59%)
Log decrement δ Peaks #3 and #5	1.16	1.25	1.11	-7% (+4%)
Damping ratio ζ Peaks #3 and #5	0.18	0.20	0.17	-7% (+4%)
Period of the signal	0.18	0.22	0.19	-18% (-6%)

The results in the frequency domain are shown in Figure 8.11. Most of the signals split over the first 10 Hz. At 3 Hz, there is a peak in the roll rate amplitude, corresponding

to a local minimum in the yaw rate. Conversely, at 5 Hz the yaw rate PSD reveals a local maximum while the roll rate is at a minimum.
The tests at 300 kPa and 500 kPa (blue and yellow lines) have the local maxima at frequencies of 3 Hz (where they show very similar amplitude) and 12 Hz. Roll rate signal at 400 kPa shows the local maxima at 3 Hz and 6 Hz. Besides that, the differences among the tests under different pressure are basically negligible and they do not allow us to draw any valuable conclusions from the frequency domain analysis.

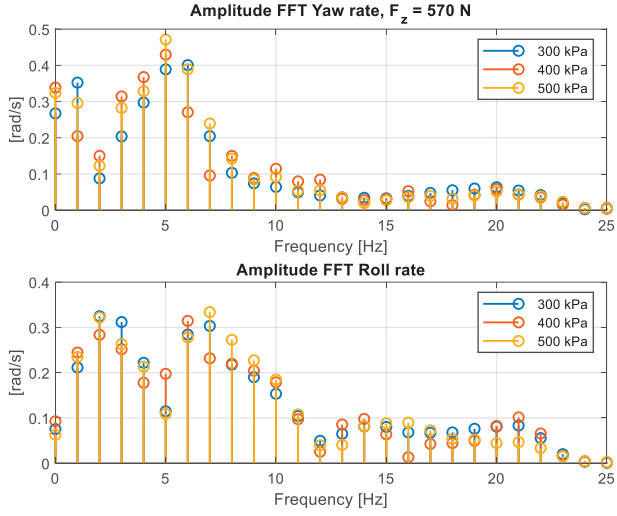

Figure 8.11 – Frequency domain analysis of the results depicted in Figure 8.10, obtained through the Fast Fourier Transform (FFT), for vertical load on the rear tyre equal to 570 N. Specifically, we study the frequency domains for the signals yaw rate and roll rate.

8.5.2 F_z on the rear tyre: 635 N

With an applied vertical load on the rear tyre equal to 635 N, the time histories of the recorded bicycle dynamics before and after the kickplate action are shown in Figure 8.12 (A). The yaw rate and roll rate follow a similar trend, while tests at 400 kPa exhibit slight differences (red curve), as the first positive peak (#2) for the yaw rate is reached earlier, with higher magnitude. Furthermore, the roll rate signal at 400 kPa does not show any valley at the time instant of 0.23 s, unlike the other tests.
The first significant variation in the signal occurs 0.05 seconds after the kickplate force application. The analysis of the steer angular rate reveals that the rider's reaction time at 500 kPa occurs slightly before the others (0.01 seconds earlier). This time must be related to the involuntary rider reaction. As for the steer angular rate, time histories are pretty similar among different inflation pressures.
Oscillations in the signals disappear in 0.6 seconds, allowing us to detect six distinguishable peaks in the yaw rate signal, depicted in Figure 8.12 (B) with standard error. The oscillation of the yaw rate signal vanishes on average 15% earlier for the

inflation pressure of 400 kPa compared to the other pressures tested (Table 8.7, first row "Last peaks' time"). We limited the analysis to 0.5 seconds, as the peaks are then negligible. This means that the oscillations disappear in about 0.5 meters, considering a travelling speed in the range 1.92–2 m/s.

Logarithmic decrements of yaw rate signal (equation 8.2) on successive periods are collected in Table 8.7. The results over the peaks #1 and #3 show that the lowest value is for a pressure of 300 kPa, then it increases to the maximum at a pressure of 500 kPa. Similar conclusions can be drawn for the damping ratio, as it directly depends on the logarithmic decrement (equation 8.3). The results show that the system is highly underdamped (damping ratio $\zeta << 1$), pointing out an increase in damping ratio when we consider the successive peaks #2 and #4. Here the bicycle with tyres inflated at 400 kPa shows the lowest damping among the others. When the tyre was inflated at 400 kPa we also had the longest signal period compared to other pressures. Contrarily for peaks #3 and #5, the system is overdamped only under inflation pressure of 400 kPa, while it turns out to be underdamped under the other tested pressures (damping ratio $\zeta < 1$). In this case we have a huge percentage difference in logarithmic decrement (thus in damping ratios) among tests at pressure 400 kPa and the others (larger than 100% difference, Table 8.7, sixth and seventh rows).

As mentioned before for tests with vertical load on rear tyre equal to 570 N (Section 8.5.1), the logarithmic rule does not apply to describe the signal recovery from oscillations over the time, as we found major differences among logarithmic decrements for successive peaks.

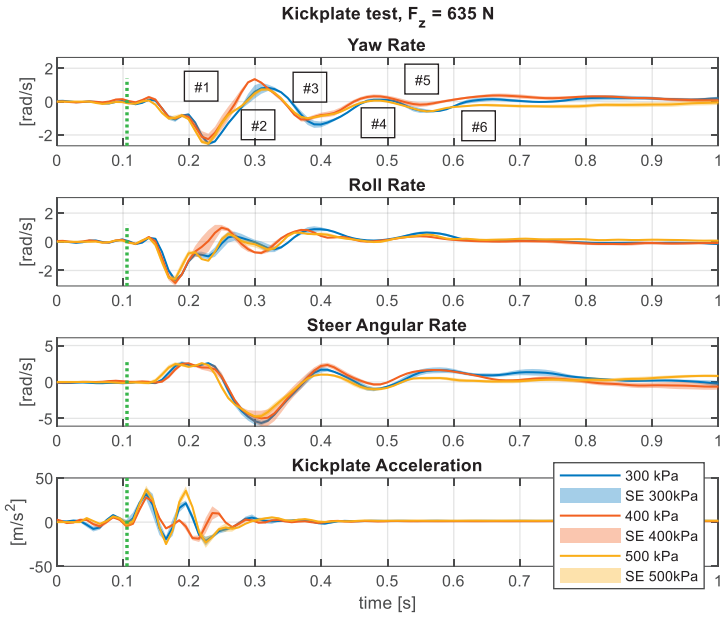

(A)

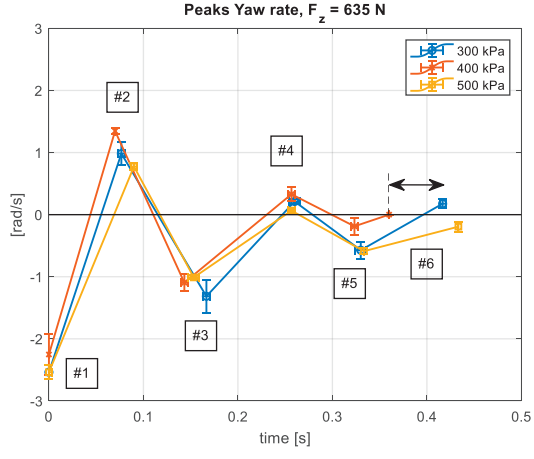

(B)

Figure 8.12 – (A) Bicycle kinematics at the moment of the kick, under vertical load of 635 N on the rear tyre. We focus on 1 second of time history to enlighten the bicycle yaw rate, roll rate, steer angular rate before and after the kickplate action. The kickplate acceleration is useful to derive the exact kick instant and relate that to the bicycle response. The results for three different pressures are depicted (300, 400, and 500 kPa), alongside the standard errors "SE". The vertical green line represents the kick moment (vertical dot green line). The labels in the top plot refer to the detected peaks in the signal. (B) Time history of the peak values for the yaw rate, from the top plot of figure (A). Each line represents a different inflation pressure, as reported in the legenda. The double arrow line indicates the (qualitative)

difference in time between the results at 300 kPa (blue line) and the other ones. Note that here we only depict 0.5 seconds of time history, as the peak values become then negligible and very close to 0. Each value is plotted along with the uncertainty interval (evaluated as standard error). The # number labels refer to the yaw rate peaks identified in the top plot of (A).

Table 8.7 – Yaw rate peaks timing for F_z = 635 N. First row: time values at which we have the last peaks of the yaw rate signal before the disturbance is recovered, when the vertical load applied to the rear tyre is equal to 635 N. Time values correspond to the abscissa values from Figure 8.12 (B), under different inflation pressures. Second row: logarithmic decrement, evaluated over one period (among peaks #1 and #3). Third row: damping ratio from equation (8.3), evaluated from the logarithmic decrement of the second row. Fourth and fifth rows are equivalent to second and third ones, but now referred to the peaks #2 and #4. The procedure has been repeated for peaks #3 and #5 (sixth and seventh rows). The last column reports the variation (in percentage) of values reported in the first three columns, for different inflation pressure. In the last row, we report the period of the signal for different inflation pressures.

Yaw rate (F_z = 635 N)	**300 kPa**	**400 kPa**	**500 kPa**	**% Variation Inf. Pressure [kPa]: 400 vs 300 (400 vs 500)**
Last peaks' time [s] (peaks #6)	0.42	0.36	0.43	-14% (-16%)
Log decrement δ Peaks #1 and #3	0.66	0.72	0.92	+10% (-22%)
Damping ratio ζ Peaks #1 and #3	0.10	0.11	0.15	+10% (-28%)
Log decrement δ Peaks #2 and #4	1.54	1.41	2.47	-8% (-40%)
Damping ratio ζ Peaks #2 and #4	0.24	0.22	0.37	-7% (-40%)
Log decrement δ Peaks #3 and #5	0.83	1.76	0.54	+112% (+215%)
Damping ratio ζ Peaks #3 and #5	0.13	0.27	0.09	+106% (+214%)
Period of the signal	0.18	0.19	0.17	+2% (+12%)

The frequency domain analysis reveals that the largest variability among the tests is in the range of 0–10 Hz (Figure 8.13). For frequencies larger than 10 Hz, we cannot

distinguish any notable difference in the amplitudes of the yaw rate and roll rate, similar to what found in Figure 8.12 when the vertical load applied to the rear tyre was 570 N. In particular, the local maxima for the yaw rate are at 0 and 6 Hz, for the roll rate they are at 1 and 7 Hz. While the yaw rate FFT amplitude for the tests at 300 and 400 kPa are almost superimposable, this does not occur for the roll rate. The amplitude at the first local maximum (1 Hz) for yaw rate at inflation pressure 400 kPa is half of the tests at 300 and 500 kPa. Contrarily, roll rate FFT amplitude at 400 kPa shows the largest amplitude among the others, for the frequency 7 Hz.

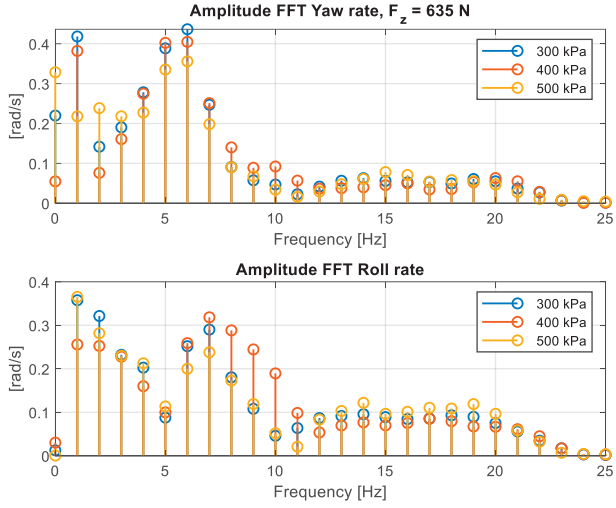

Figure 8.13 – Frequency domain analysis of the results depicted in Figure 8.12 (A), obtained through the Fast Fourier Transform (FFT), for 635 N of vertical load on the rear tyre. Specifically, we study the frequency domains for the signals yaw rate and roll rate.

8.5.3 F_z on the rear tyre: 701 N

As already stated, the time histories analysis has been limited to 1 second, to enlighten the bicycle dynamics before and after the kickplate disturbance. The rider was able to completely recover from the disturbance in less than a second, for all the tested inflation pressures.

The observation of the yaw rate time histories (Figure 8.14 (A)) puts in evidence the differences among the curve under a pressure of 500 kPa (yellow curve) and the other ones. Similarly for the roll rate, when the tyres are inflated at 500 kPa the bicycle dynamics differ from the other test and the curves do not look superimposable. The standard errors (SE) are very limited around the averaged curves, showing a good test repeatability over different tests.

Differences in human reaction time are observed in the steer angular rate varying the inflation pressures. The promptest reaction is for tests at 400 kPa, followed by 500 and 300 kPa, to be quantified in 0.01 seconds of difference (Figure 8.14 (A)). Although the

rider involuntarily reacts earlier to balance the bicycle after the disturbance, the oscillations in the yaw rate signal disappear before for the tests at inflation pressure of 500 kPa, for which we only distinguish four peaks in yaw rate signal. The signals at 500 kPa reach higher peak values (yellow curves), both for yaw rate, roll rate and steer angular rate, despite the applied force is pretty similar (kickplate acceleration signals are superimposable, kickplate force was in the range 1600 ± 50 N). The yaw rate peaks' analysis reveals that the oscillations end before for tests under inflation pressure of 500 kPa (Table 8.8), as we can only distinguish four peaks, instead of six for other pressures. This means that the rider was able to recover from the disturbance 43% earlier than the other tests at different inflation pressures. The yaw rate peaks over time for pressures of 300 kPa and 400 kPa are very similar both in time and amplitude, showing a longer decay time. The yaw rate signal period is larger at 500 kPa, and the logarithmic decrement is larger by far for that pressure, both for peaks #1-#3 and peaks #2-#4. Although the system resulted to be underdamped for all the inflation pressures, there is a huge difference among tests at 500 kPa and the others, with an increase in the order of 500% if we consider the second oscillation period (peaks #2 and #4). Here we do not analyse peaks #3 and #5, as we did in Section 8.5.1 and 8.5.2, because we do not have more peak #4 for inflation pressure 500 kPa.

In short, if on one hand we recorded the largest oscillation amplitudes of yaw rate, on the other hand we also had an extremely larger logarithmic decrement and damping ratios at inflation pressure of 500 kPa compared to other pressures. The rider was able to recover faster from the disturbance with tyres inflated at 500 kPa.

The increase in vertical load applied to the rear tyre also makes more evident the effect of inflation pressure on bicycle dynamics. If for lower vertical loads the yaw rate decay among tests at different pressures was more limited, here the variation is much larger.

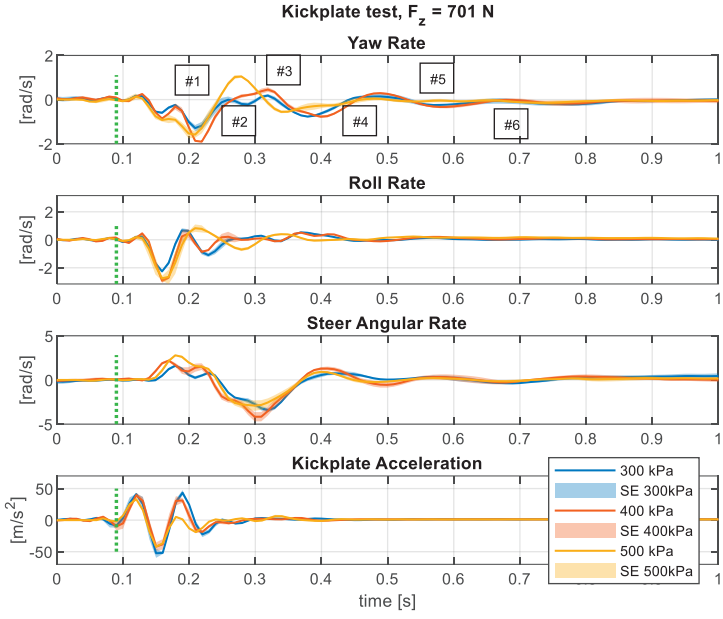

(A)

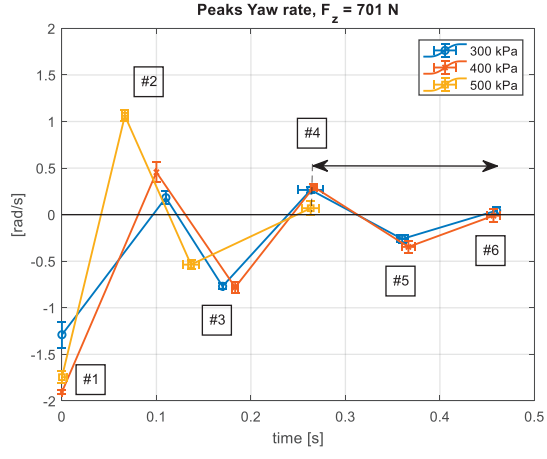

(B)

Figure 8.14 – (A) Bicycle kinematics at the moment of the kick, under vertical load of 701 N on the rear tyre. We focus on 1 second of time history to enlighten the bicycle yaw rate, roll rate, steer angular rate before and after the kickplate action. The kickplate acceleration is useful to derive the exact kick instant and relate that to the bicycle response. The results for three different pressures are depicted (300, 400, and 500 kPa), alongside the standard errors "SE". The vertical green line represents the kick moment (vertical dot green line). The labels in the top plot refer to the detected peaks in the signal. (B) Time history of the peak values for the yaw rate, from the top plot of figure (A). Each line represents a different inflation pressure, as reported in the legenda. The double arrow line indicates the (qualitative)

difference in time between the results at 300 kPa (blue line) and the other ones. Note that here we only depict 0.5 seconds of time history, as the peak values become then negligible and very close to 0. Each value is plotted along with the uncertainty interval (evaluated as standard error). The #number labels refer to the yaw rate peaks identified in the top plot of (A).

Table 8.8 – Yaw rate peaks timing for F_z = 701 N. First row: time values at which we have the last peaks of the yaw rate signal before the disturbance is recovered, when the vertical load applied to the rear tyre is equal to 701 N. Time values correspond to the abscissa values from Figure 8.14 (B), under different inflation pressures. Second row: logarithmic decrement, evaluated over one period (among peaks #1 and #3). Third row: damping ratio from equation (8.3), evaluated from the logarithmic decrement of the second row. Fourth and fifth rows are equivalent to second and third ones, but now referred to the peaks #2 and #4. The procedure has been repeated for peaks #3 and #5 (sixth and seventh rows). The last column reports the variation (in percentage) of values reported in the first three columns, for different inflation pressure. In the last row, we report the period of the signal for different inflation pressures.

Yaw rate (F_z = 701 N)	**300 kPa**	**400 kPa**	**500 kPa**	**% Variation Inf. Pressure [kPa]: 500 vs 300 (500 vs 400)**
Last peaks' time [s] (peaks #4 and #6)	0.46	0.46	0.26	-43% (-43%)
Log decrement δ Peaks #1 and #3	0.52	0.89	1.18	+128% (+32%)
Damping ratio ζ Peaks #1 and #3	0.08	0.14	0.18	+125% (+31%)
Log decrement δ Peaks #2 and #4	0.38	0.43	2.73	+627% (+538%)
Damping ratio ζ Peaks #2 and #4	0.06	0.07	0.40	+568% (+487%)
Period of the signal	0.15	0.17	0.20	+28% (+18%)

In this case, we cannot perform the logarithmic decrement analysis on peaks #3 and #5 because we cannot distinguish the fifth peak for the signal at inflation pressure 500 kPa. As for the other pressures, the fifth peaks are both equal to 0, therefore we encounter numerical errors when we evaluate the logarithmic decrement as ratio between the third and the fifth peak.

Frequency analysis of the yaw rate (Figure 8.15) reveals a maximum at 5 Hz. The lowest inflation pressure tested (300 kPa) also has the lowest amplitude over all the

frequencies. As stated before in Figure 8.11 and Figure 8.13, the local maxima for the yaw rate correspond to local minima for the roll rate (here at 5 Hz). Similarly to what is seen for the yaw rate, the amplitude of the roll rate signal under inflation pressure 300 kPa is the lowest one (except for only a couple of frequencies – 11 and 12 Hz). The roll rate amplitude has a peak at 8 Hz for the inflation pressure of 500 kPa, then it diminishes for higher frequencies, up to 0 for frequencies higher than 20 Hz.

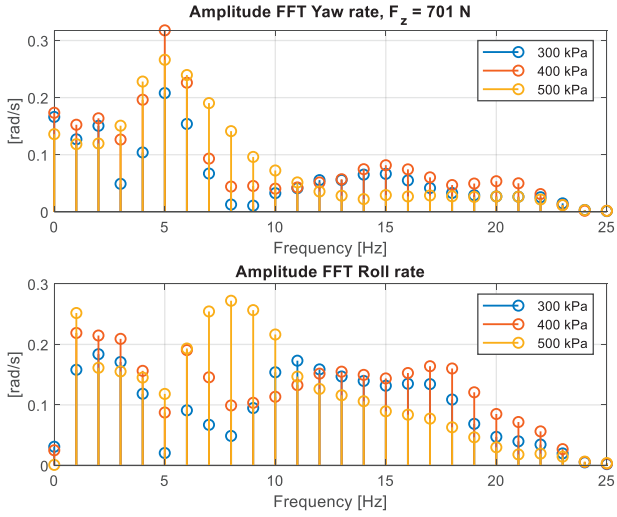

Figure 8.15 – Frequency domain analysis of the results depicted in Figure 8.14, obtained through the Fast Fourier Transform (FFT), for 701 N of vertical load on the rear tyre. Specifically, we study the response in frequency for the signals yaw rate and roll rate.

8.6 Conclusion

Bicycle tyres can affect the dynamic response of bicycle-rider models. In this study, we demonstrated how different tyre inflation pressure and vertical force impact bicycle dynamics. To investigate it, we performed numerical simulations using an extended Carvallo-Whipple bicycle-rider model, updated to include a disturbance from the kickplate motion and nonlinear tyre dynamics. A basic human-like steering torque controller was necessary to prevent the bicycle from falling and restore the initial steady state condition. We obtained a different set of Magic Formula parameters according to tyre inflation pressures (we tested 300-400-500 kPa), and we used them in simulations. Although tyre characteristics had an effect on the predicted bicycle dynamics, the variations seemed relatively limited among the different inflation pressures tested, in the order of only a few percent. The simulations also revealed the necessity of introducing a tyre model which includes slip.

To further investigate these findings, we conducted an experimental campaign using a kickplate device, capable of applying a sudden lateral perturbation to the bicycle rear

wheel. We used an e-bike equipped with Schwalbe tyres, under three different inflation pressures (300-400-500 kPa) within the range recommended by the manufacturer. We mostly focused on the yaw rate signal and its decay helped determine the proper inflation pressure relative to the vertical load applied to the wheels. The oscillation following a strong lateral disturbance dissipated more quickly when the pressure was set according to the applied vertical load, i.e. the rider's weight. Concerning the lower vertical load applied to the rear tyre (570 N), the use of a 300 kPa inflation pressure allowed an 8% faster recovery from the perturbed yaw rate compared to higher inflation pressures. We also noticed that an increase in the applied vertical load (635 N on the rear tyre) had even more significant impact on the choice of inflation pressure. In particular, the tests revealed that the yaw rate recovered 15% faster from the kickplate lateral disturbance when the inflation pressure was set to 400 kPa. For the heaviest vertical load tested (701 N), the inflation pressure of 500 kPa was the most suitable among the others as it allowed a 43% reduction in yaw rate recovery time following the kickplate lateral disturbance.

We also explored the possibility of using synthetic indexes like logarithmic decrement and damping ratio to analyse the yaw rate signal and provide information about the difference in amplitude between successive peaks. Nonetheless, this approach did not fully apply when considering the larger picture. The results varied widely over the time histories due to significant impact of the rider control action. The frequency domain analysis for the yaw rate signal revealed the presence of local maxima in the 5-6 Hz frequency range, consistent across different riders. Conversely, the same analysis for the roll rate signal pointed out the local minima in the 5-6 Hz frequency range.

The comparison between the predicted and the experimental results (Figure 8.6 and Figure 8.12 (A), respectively) for the same inflation pressure of 400 kPa and vertical load on the rear wheel is depicted in Figure 8.16, where we focus on the yaw rate and roll rate. The outcomes are in the same order of magnitude however with different dynamics. The simulations are not able to catch the oscillations in the signals following the lateral perturbation. This is more evident for the yaw rate. The assumptions about the forces at the tyre-ground contact point, such as the estimated friction coefficient and the use of a basic human-like controller without delays, may partially explain the discrepancies. In addition, the occurrence of sliding phenomena at the tyre-kickplate interface during the outdoor tests may also have affected the data. The kickplate test elicits large slip angles for which unpredictable phenomena may arise.

There is also to consider that the model assumes the rider body rigidly connected to the bicycle frame, which is not true in reality. The low inertia model variation in Figure 8.9 shows that the rider inertia influences the response rather strongly. While the use of simple models can provide an indication of the expected results, this is insufficient to accurately predict the dynamics. To achieve that, we will likely need more complex human-like models, which also account for body segment motion following the disturbance, as is done in crash modelling.

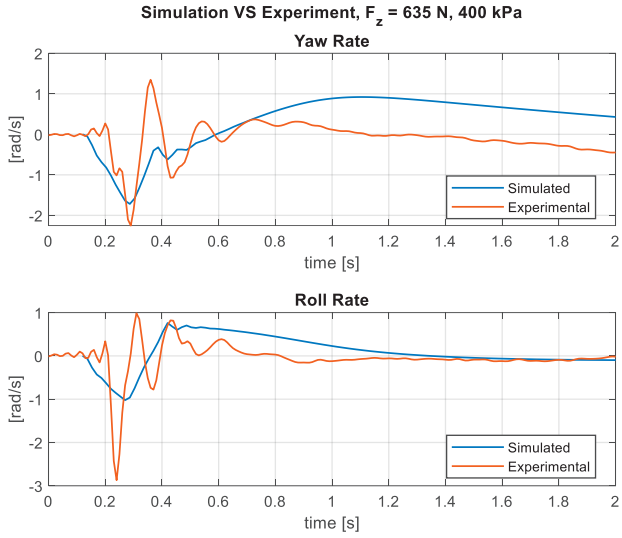

Figure 8.16 – Comparison between simulated results from Carvallo-Whipple bicycle-rider model (Section 8.4) and experimental results (Section 8.5.2), for yaw rate and roll rate. Results for inflation pressure 400 kPa, vertical load on the rear wheel 635 N.

In Table 8.9, we have collected the best pressures for each rider (among the tested pressures of 300-400-500 kPa), according to the yaw rate signal recovery time from the applied disturbance, collected during the experimental campaign. The last column reports the average reduction in time during which we assume that the bicycle-rider has completely recovered from the disturbance.

Tyre inflation pressure plays a significant role in ensuring ride safety, as it changes the tyre characteristics and the rider response to likely perturbation events. This effect becomes even more evident for larger vertical loads, i.e. heavier riders or e-bikes with significant weights, suggesting that future research could focus on cargo bicycles. Therefore, tyre characteristics cannot be neglected when dealing with such strong lateral perturbations, as they affect both the bicycle's response and the rider's reaction. The experiment was conducted by setting the same inflation pressure for both tyres. In light of the results presented in this paper, it will be of interest to test bicycles under different inflation pressures on front and rear tyre according to the actual vertical load. To further study the effect of vertical load on bicycle dynamics, we can also perform experiments with the same rider by adding weights to the bicycle. In this way, we reduce the degree of uncertainty in the results caused by different riders.

In the future, we will further develop the kickplate device to enable testing at higher speeds and extend the research to other light vehicles for micromobility.

We have demonstrated the possibility of introducing a nonlinear tyre model in the Carvallo-Whipple bicycle-rider model. It is of high interest to further investigate this, with the aim to improve both the safety (self-stabilising bicycles) and performance.

The study also proves that investigating bicycle dynamics with varying tyre characteristics is of interest to develop new tyre inflation pressure calculators based on scientific evidence, thus ensuring safer and more comfortable rides.

Table 8.9 – Best pressure for each rider (namely, different vertical loads, first column), among the tested inflation pressures. In the last column, the average reduction in time using the optimal tyre pressure. Results are referred to yaw rate signal. We report the average of the last peaks' times variation with respect to the tests at the best tyre inflation pressure (first column of Table 8.6, Table 8.7, Table 8.8).

F_z on the rear tyre	**Best pressure (among the tested ones)**	**% Recovery time reduction (for yaw rate, on average)**
520 N	300 kPa	-10%
635 N	400 kPa	-15%
701 N	500 kPa	-43%

8.7 Online additional material

GitHub repository with the bicycle-rider model used in this paper: https://github.com/mechmotum/bicycle-kickplate-model

Poster presented at the International Cycling and Safety Conference (ICSC 2023, Den Haag, The Netherlands): http://dx.doi.org/10.13140/RG.2.2.32143.36004

Additional pictures from the experiment: https://doi.org/10.5281/zenodo.13890635

8.8 Acknowledgments

I want to thank all my colleagues from TU Delft Bicycle lab. They actively helped me in setting up and running the experiment. It was also nice to joke with my friend Teddy Vijfvinkel during the long days in Office 1. Many thanks to Adam Kewley, an amazing guy who helped me find the key to several coding troubles we faced along this paper journey.
I would also like to thank Prof. G. Mastinu and Prof. G. Magnani for their invaluable support, even from abroad, throughout the research period.

We are grateful to Mr L.A. Engel, from Festo GmbH, for providing us the pneumatic cylinder and stopper we have used for the kickplate device. Many thanks to Ir. Jan van Frankenhuijzen, Ir. Cornel Weststeijn and Jacques Brenkman for their valuable hints. We would also like to thank Jasper Van Aernsbergen, Jip Smalbroek, Lieve McGee, Luc Roosmalen, and Nick Verhoeks, who actively cooperated to realise the kickplate test, as part of their thesis project. Thanks a lot to Sierd Heida and his team from Royal Dutch Gazelle for providing us the tyre for testing.

The authors report there are no competing interests to declare.

The project was partially financed and supported by the TKI/ClickNL 'De Fiets van de Toekomst' grant and Royal Dutch Gazelle.

Chapter 9

Discussion

In the quest to deepen the knowledge on bicycle tyres and bicycle dynamics, this dissertation aimed to address the following research objective.

1. To develop a new test bench to measure bicycle tyre lateral characteristics, in order to provide a tyre dataset to be used in bicycle dynamics studies.
2. To provide a robust tyre mathematical model that can be added to bicycle-rider models.
3. To quantify the effect of tyres on bicycle-rider dynamics, both experimentally and numerically.

Navigating through the chapters of this dissertation, I have tried to push the boundaries of knowledge about bicycle tyres and their effect on bicycle dynamics. Starting from the literature review of the experimental methodologies for the measurement of the lateral characteristics of bicycle tyres, it was clear the need to further develop indoor testing techniques (**Chapter 2**). Indoor tests are performed on specific test-rigs and they allow measuring tyre characteristics with a good level of repeatability, in controlled environments. Therefore, I focused on the development of a novel test-rig (VeTyT, acronym of Velo Tyre Testing), specifically designed for bicycle tyres (**Chapter 3**). I described the development procedure alongside an uncertainty model to proper define the measurements and assess the reliability of the results on theoretical grounds, then experimentally verified. All these steps allowed meeting the ISO 9001-2015 standards, thus making VeTyT the very first certified testing machine for bicycle tyres. Even though VeTyT has showed very promising results during experimental campaigns, there are of course drawbacks still to solve. First, the test-rig is limited by construction to vertical loads up to 550 N. This constrains the range of testing especially for cargo bike tyres, that should be tested under higher vertical loads. Moreover, the current fork can only accommodate front wheels (both rim and disk brakes), as there is insufficient room for rear wheels with cassette. I have not had the necessity to test rear wheels so far, however in the future I could do that by designing a new fork. I also thought to automatise the way to set and vary camber angle by adding an electric actuator to the rig, making tests faster. However, the idea never found applicability due to budget constraints. To make the test-rig a truly unique piece able to perform not only lateral but also longitudinal characterisation, we

may explore the possibility to add a set of triaxial load cells alongside a braking system and rotary encoders to measure longitudinal forces.

In this dissertation, I mostly conducted experimental campaigns on road racing bicycle tyres, whose setup is featured by relatively low vertical load (for front wheel, we can assume that the load is about 340 N to 500 N). In particular, I quantified the effect of rim stiffness, rolling speed and temperature on the lateral force, self-aligning torque, contact patches, lateral and vertical stiffness (**Chapter 4**), for a 26 mm wide road racing tyre. I found that the use of a high-stiffness rim ensures up to 13% higher cornering stiffness for tests under the same working conditions. While the rolling speed does not affect too much the measurement of the lateral force F_y (variation lower than 3% changing the speed from 8 km/h to 23 km/h), the temperature of the rolling surface largely impacts the measurements. Specifically, an increase in temperature from 35 °C to 70 °C causes a decrease in lateral force about 16% and self-aligning torque about 50%, considering slip angles $|\alpha| > 3\ deg$.. This aspect may change bicycles dynamics, especially on paved roads featured by the presence of shaded corners during summer days (**Chapter 4**). To measure the temperature of the rolling surface, I employed a thermocamera and a pyrometer, but I was not able to set constant temperature of the tyre carcass. This would require much more sophisticated testing machines, with controlled-temperature chambers. Moreover, the lower thermal inertia of a road bicycle tyre made it genuinely impossible to keep the temperature of the carcass within a narrow range. Given that, I focus my attention on the control of the rolling surface temperature, which is much easier to manage. Considering that most of the results of the study on temperature would find applicability in the racing field, I think that it is more of interest to predict the tyre behaviour given the temperature of the road. In a practical application, I would say that cycling team managers might know the road temperature in advance, and inform the riders about the appropriate speed to keep when cornering downhill, for instance. Pushing to the limits without taking unnecessary risks is often the winning strategy.

Among the tests performed on a 26 mm wide racing tyre, I also measured the twisting torque, which is the self-aligning torque at slip angle 0 deg, varying the camber angles only. I found that the twisting torque increased with the contact patch area. Based on that and on the assumption of elliptical approximation of the contact patch, I proposed a simplified theoretical model to predict the twisting torque (**Chapter 6**). It provided satisfying results in terms of accuracy, for camber angles up to 10 deg. The model assumed the longitudinal stiffness to be equal to the cornering stiffness and the longitudinal slip to be constant along the entire contact patch width, acceptable as long as we worked with small slip angles. These assumptions made the model simpler, however they constrained the range of applicability up to 10 deg of camber angle. What is still missing is the measurement of the contact patch during rolling. I can only guess and make hypothesis on the shape and extension of that, as it is not possible to measure contact patch dynamically with VeTyT. This procedure would require to

redesign the flat track treadmill, with a considerable allocation of time and money resources.

Remaining in the track of road racing tyres, I evaluated the relaxation length, as the ratio between cornering stiffness and lateral stiffness (**Chapter 5**). Relaxation length is an indicator of tyre promptness when dealing with turns or sudden maneuverers. The recent interest in using wider tyres in professional cycling pushed me to compare the relaxation length of a 26 mm and 28 mm wide road racing tyre varying vertical loads and inflation pressure. While the 28 mm wide tyre could carry higher vertical loads before reaching saturation limit, the 26 mm wide one had shorter relaxation length, meaning that it was more responsive in handling turns. I concluded stating that the higher the vertical load the longer the relaxation length. A direct measurement of the relaxation length is also possible, but I did not deal with that due to technical limitations of the test-rig. It would require to steeply switch slip angle from 0 to about 1.5 deg in few milliseconds, to catch the transient effects. The experimental setup did not allow that, therefore the indirect evaluation of relaxation length as ratio between cornering and lateral stiffness was the only viable way.

I had the opportunity to also test a batch of city/trekking and cargo bicycle tyres provided by a bicycle manufacturer. I used the measured data to develop a bicycle tyre model based on the Magic Formula, routinely used for 4-wheels vehicles. Although the Magic Formula was originally conceived for tyres subjected to much larger loads, it provided valuable results also applied to bicycle tyres (**Chapter 7**).

The study on city/trekking tyres and the development of tyre mathematical model opened the doors to the investigation of the effect of tyres on bicycle-rider dynamics. To quantify that, I developed the "kickplate" setup, capable of applying a sudden lateral perturbation to the bicycle rear wheel. The kickplate tests elicited large slip angles (>5 deg), thus it allowed catching the saturation limit and the nonlinear regime. I performed numerical simulations on the extended Carvallo-Whipple bicycle-rider model, updated to introduce the kickplate test with the addition of nonlinear tyre model with slipping. Then, I validated the numerical simulations through an experimental campaign using the kickplate device and an e-bike instrumented with IMU, changing repetitively the inflation pressure of both the front and rear tyre. The mathematical model matched the experimental data in terms of magnitude however with different dynamics. This is more evident for the yaw rate. The assumptions about the forces at the tyre-ground contact point, such as the estimated friction coefficient and the use of a basic human-like controller without delays, may partially explain the discrepancies. In addition, the occurrence of sliding phenomena at the tyre-kickplate interface during the outdoor tests may also have affected the data. Experimental results indicated that the pressure variation had a role on bicycle-rider dynamics, especially on the variation of yaw rate (the most affected variable) and roll rate. In particular, there was an optimal tyre pressure for which I observed a faster decay of signals oscillations following the lateral disturbance, different for each rider (namely, different vertical loads). I focused on the yaw rate decay to determine the best inflation

pressure relative to the vertical load applied to the wheels, i.e. the rider's weight. While for tests under vertical load of 570 N, the use of 300 kPa inflation pressure allowed an 8% faster recovery from the perturbed yaw rate compared to higher pressures. Inflation pressure was even more impactful for larger vertical loads. Applying 701 N to the rear wheel, the inflation pressure of 500 kPa allowed a 43% faster yaw rate recovery following the kickplate lateral disturbance. The use of kickplate test can therefore be a viable solution to develop new tyre pressure recommendations according to rider's weight, so as to ensure better bicycle handling following a lateral perturbation (**Chapter 8**). Nonetheless, I did not notice any significant difference in the amplitude of yaw rate and roll rate peaks, as I had expected when changing the inflation pressure.
Even though the results come from the average of three different tests and featured by limited standard error, I cannot neglect the influence of the rider's action. I never repeated the same inflation pressure sequence among different riders (it was random choice, never always scaled up or scaled down pressures). However, the humans can adapt to different situations, and this can also be an example.

I am at the conclusion of this long journey throw the "Magic" world of bicycles, with special focus on tyres.
Literature stated the important role of tyres on bicycle dynamics, as suggested by bicycle models. It was clear since the beginning the need to develop a new testing machine to experimentally measure the tyre lateral characteristics. VeTyT test-rig saw the light in this context. I used VeTyT to measure the lateral characteristics of road racing, city/trekking and cargo bicycle tyres. Experimental data allowed me to develop a tyre mathematical model based on the Pacejka's Magic Formula. At that point, I was wondering about the actual effect of bicycle tyres on bicycle dynamics. I gained experience and know-how from indoor testing, but I was still ignoring the role of tyre lateral characteristics in the real world. I came up with the idea of kickplate, a testing device used to laterally perturb the rear bicycle wheel at the contact point tyre-ground. As with any prototype, I faced several issues, especially in the beginning. But in the end I was able to conduct the experimental campaign I had planned with kickplate, using an instrumented bicycle and changing tyre inflation pressure each time. I quantified the effect of tyre lateral characteristics with the kickplate, both experimentally and numerically. The experiment was indeed simulated using the extended Carvallo-Whipple bicycle-rider model, updated to introduce the kickplate test with the addition of nonlinear tyre model.
So, to wrap up, we must consider the role of tyres in order to enhance handling for safer rides, especially when dealing with extreme situations. I wish that this dissertation can help to raise awareness on the importance of tyres on bicycle-rider dynamics.

Future research

The development of a novel test-rig to measure the lateral characteristics of bicycle tyres has represented a great achievement for my research project and, hopefully, for the entire research community. However, it still needs some improvements, to make the measurement procedure easier and faster. It would be interesting to add load cells to also measure the longitudinal characteristics, thus making the test-rig able to provide a full tyre characterisation. I would also suggest upgrading the indoor test-rig VeTyT for accurate measurements at slip angles larger than 10 deg, under higher vertical loads (now limited to 550 N).

As avid rider and cycling races fan, I am aware of the crucial role of the weather conditions on races. Rainy days make very large selection based on riders' ability and chosen tyre setup. High speed cornering is often among the most dangerous situations to deal with during rainy race days. I have not explored yet the tyre lateral characteristics on wet surface. I started to investigate the possibility to make VeTyT ready for simulating rainy conditions by applying water spray nozzles close to the flat track, alongside proper vacuum cleaners around the treadmill. I had no time to do everything, and the idea remained on paper only. I would recommend to investigate it in future experimental campaigns.

Studies on bicycle tyres should also be further advanced to enhance a full understanding of the phenomena related to cornering force and camber thrust, especially at large slip angles (> 15 deg). Future studies can address the topic to close a still existing gap in the bicycle tyres full characterisation.

The use of the kickplate setup gave very promising outcomes. Based on that, it will be of interest to study the effect of different inflation pressure combinations front/rear wheels, and tests at higher riding speeds. In addition, tests with self-balancing bicycle will provide important information while bypassing the rider's effect. I would also recommend to further develop the kickplate study, both numerically and experimentally, to extend it to other light vehicles for micromobility, like cargo bicycles.

As the tests pointed out the relevant role of the inflation pressure in tyre characteristics, a further investigation on its effect is essential to set new benchmarks for a new tyre pressure calculator and provide a ready-to-use tool based on scientific evidence instead of the riders' feeling. This would mark an important achievement to actually address safety issues related to bicycle dynamics.

Bibliography

[1] European Environment Agency, "Annual Report 2019, EU policies - Energy," pp. 1–5, 2019, [Online]. Available: http://europa.eu/pol/ener/index_en.htm

[2] ONU, "Sustainable Development Goals: Guidelines for the Use of the SDG," *United Nations Department of Global Communications*, no. May, pp. 1–68, 2020.

[3] E. Union and C. I. Europe, "The state of national cycling strategies in Europe (2021)," 2021.

[4] EU Ministers for Transport, "Declaration on Cycling as a Climate Friendly Transport Mode," p. 5, 2015, [Online]. Available: www.gouvernement.lu

[5] S. Corwin, R. Zarif, A. Berdichevskiy, and D. Pankratz, "The futures of mobility after COVID-19. Scenarios for transportation in a postcoronavirus world," *Deloitte Development LLC*, pp. 1–21, 2020.

[6] BEUC, "Mobility habits following COVID-19," *The European Consumer Organisation*, no. October, 2020, [Online]. Available: https://www.beuc.eu/publications/mobility-habits-following-covid-19-snapshot-study-and-beuc-policy-recommendations

[7] EU Parliament resolution B9-0102/2023, "European Parliament - Developing an EU Cycling Strategy," 2023.

[8] H. Abdullah, *Urban Mobility after COVID-19 Long-term strategies for the sustainable mobility transition*.

[9] L. Schwarz, A. Keler, and J. M. Krisp, "Improving urban bicycle infrastructure-an exploratory study based on the effects from the COVID-19 Lockdown," *Journal of Urban Mobility*, vol. 2, p. 100013, Dec. 2022, doi: 10.1016/j.urbmob.2022.100013.

[10] World Economic Forum, "Riding out the pandemic: How COVID-19 turned Europe into a cycle superpower," p. 2020, 2020.

[11] World Health Organization 2020, *Cyclist Safety: An Information Resource for Decision-Makers and Practitioners*, no. October. 2017.

[12] L. E. V. M. de Guerre, S. Sadiqi, L. P. H. Leenen, C. F. Oner, and S. M. van Gaalen, "Injuries related to bicycle accidents: an epidemiological study in The Netherlands," *European Journal of Trauma and Emergency Surgery*, vol. 46, no. 2, pp. 413–418, 2020, doi: 10.1007/s00068-018-1033-5.

[13] R. S. Sharp, "On the stability and control of the bicycle," *Appl Mech Rev*, vol. 61, no. 1–6, pp. 0608031–06080324, 2008, doi: 10.1115/1.2983014.

[14] G. Dell'Orto, F. M. Ballo, G. Mastinu, and M. Gobbi, "Bicycle tyres – Development of a new test-rig to measure mechanical characteristics," *Measurement (Lond)*, vol. 202, Oct. 2022, doi: 10.1016/j.measurement.2022.111813.

[15] J. Ronné, L. Dubuis, and T. Robert, "Assessing the handling quality of bicycles: a review of current theoretical approaches," 2024, *Taylor and Francis Ltd.* doi: 10.1080/00423114.2024.2387043.

[16] D. Gordon Wilson, T. Schmidt, and J. M. Papadopoulos, *Bicycle Science*, 4th ed. MIT Press, 2020.

[17] J.W.L. Glaisher, "The Quarterly Journal of Pure and Applied Mathematics," 1899, *Longmans, Green, and Co*.

[18] J. M. Papadopoulos, "Bike Tech," 1988, ch. Vol. 7, is, pp. 13–15.

[19] J. W. L. Glaisher, "The Messenger of Mathematics," 1969, *Swets & Zeitliger N.V.*

[20] E. Dohring, "Stability of Single-Track Vehicles," Forschung., 1955.

[21] R. N. Collins, "A Mathematical Analysis of the Stability of Two Wheeled Vehicles," 1963.

[22] R. Scott Hand, "Comparisons and Stability Analysis of Linearized Equations of Motion for a Basic Bicycle Model," MSc. thesis, Cornell University, 1988.

[23] J. P. Meijaard, J. M. Papadopoulos, A. Ruina, and A. L. Schwab, "Linearized dynamics equations for the balance and steer of a bicycle: a benchmark and review - ESM Supplementary Appendices," 2007.

[24] V. Cossalter, *Motorcycle Dynamics*. 2006.

[25] H. B. Pacejka, *Tire and Vehicle Dynamics*. 2006. doi: 10.1016/B978-0-7506-6918-4.X5000-X.

[26] R. S. Sharp, *Tyre Models for Vehicle Dynamics Analysis*, vol. 21, no. SUPPL. 1993. doi: 10.1115/1.2895925.

[27] E. Bakker, L. Nyborg, and H. B. Pacejka, "Tyre modelling for use in vehicle dynamics studies," *SAE Technical Papers*, vol. 96, pp. 190–204, 1987, doi: 10.4271/870421.

[28] G. Mastinu and M. Ploechl, *Road and off-Road Vehicle System dynamics Handbook*. Taylor & Francis Group, LLC, 2014.

[29] G. Mastinu, F. Della Rossa, G. Previati, M. Gobbi, and M. Fainello, "Global stability of road vehicle motion with driver control," *Nonlinear Dyn*, vol. 111, no. 19, pp. 18043–18059, Oct. 2023, doi: 10.1007/s11071-023-08794-z.

[30] V. Cossalter, A. Doria, M. Formentini, and M. Peretto, "Experimental and numerical analysis of the influence of tyres properties on the straight running

stability of a sport-touring motorcycle," *Vehicle System Dynamics*, vol. 50, no. 3, pp. 357–375, 2012, doi: 10.1080/00423114.2011.587520.

[31] F. Della Rossa and G. Mastinu, "Analysis of the lateral dynamics of a vehicle and driver model running straight ahead," *Nonlinear Dyn*, vol. 92, pp. 97–106, Apr. 2018, doi: https://doi.org/10.1007/s11071-017-3478-1.

[32] R. S. Sharp, "The stability and Control of Motorcycles," vol. I, no. 5, pp. 316–329, 1971.

[33] J. K. Moore, M. Hubbard, and J. K. Moore, "Expanded Optimization for Discovering Optimal Lateral Handling Bicycles," vol. 9, 2019, doi: 10.6084/m9.figshare.9942938.v1.

[34] A. L. Schwab, G. Dialynas, and R. Happee, "Some Effects of Crosswind on the Lateral Dynamics of a Bicycle," MDPI AG, Feb. 2018, p. 218. doi: 10.3390/proceedings2060218.

[35] G. Dialynas, C. Christoforidis, R. Happee, and A. L. Schwab, "Rider control identification in cycling taking into account steering torque feedback and sensory delays," *Vehicle System Dynamics*, 2022, doi: 10.1080/00423114.2022.2048865.

[36] J. K. Moore, "Human Control of a Bicycle," PhD Thesis, University of California, 2012. [Online]. Available: http://moorepants.github.com/dissertation

[37] P. D. L. de Lange, "Rider Control Identification in Bicycling," Delft University of Technology, Delft, 2011.

[38] "Statista Search Department - Market Insights Bicycles - Worldwide." Accessed: Sep. 10, 2024. [Online]. Available: https://www.statista.com/outlook/mmo/bicycles/worldwide

[39] "Statista Search Department - Market Insights Passenger Cars - Worldwide." Accessed: Sep. 10, 2024. [Online]. Available: https://www.statista.com/outlook/mmo/passenger-cars/worldwide

[40] L. Romano, F. Bruzelius, and B. Jacobson, "Brush tyre models for large camber angles and steering speeds," 2020, *Vehicle System Dynamics*. doi: 10.1080/00423114.2020.1854320.

[41] T. Fujioca and K. Goda, "Discrete Brush Tire Model for Calculating Tire Forces with Large Camber Angle," *Vehicle System Dynamics*, vol. 25, no. sup1, pp. 200–216, Jan. 1996, doi: 10.1080/00423119608969196.

[42] J. Svendenius and B. Wittenmark, "Brush tire model with increased flexibility," *European Control Conference, ECC 2003*, no. December, pp. 1863–1868, 2003, doi: 10.23919/ecc.2003.7085237.

[43] A. Doria and S. D. Roa Melo, "On the influence of tyre and structural properties on the stability of bicycles," *Vehicle System Dynamics*, vol. 56, no. 6, pp. 947–966, Jun. 2018, doi: 10.1080/00423114.2017.1403032.

[44] D. Takács, G. Orosz, and G. Stépán, "Delay effects in shimmy dynamics of wheels with stretched string-like tyres," *European Journal of Mechanics, A/Solids*, vol. 28, no. 3, pp. 516–525, May 2009, doi: 10.1016/j.euromechsol.2008.11.007.

[45] N. Tomiati, A. Colombo, and G. Magnani, "A nonlinear model of bicycle shimmy," *Vehicle System Dynamics*, vol. 57, no. 3, pp. 315–335, Mar. 2019, doi: 10.1080/00423114.2018.1465574.

[46] G. Previati, G. Magnani, and G. Mastinu, "Analysis of Bicycle Shimmy and Relevant Bicycle Compliances," *Proceedings, Bicycle and Motorcycle Dynamics 2019 Symposium on the Dynamics and Control of Single Track Vehicles*, 2019, Accessed: Jan. 05, 2023. [Online]. Available: https://bmd2019.figshare.com/articles/conference_contribution/Analysis_of_Bicycle_Shimmy_and_Relevant_Bicycle_Compliances/12363707

[47] N. Tomiati, G. Magnani, B. Scaglioni, and G. Ferretti, "Model Based Analysis of Shimmy in a Racing Bicycle," in *Proceedings of the 12th International Modelica Conference, Prague, Czech Republic, May 15-17, 2017*, Linköping University Electronic Press, Jul. 2017, pp. 441–447. doi: 10.3384/ecp17132441.

[48] V. E. Bulsink, A. Doria, D. Van De Belt, and B. Koopman, "The effect of tyre and rider properties on the stability of a bicycle," *Advances in Mechanical Engineering*, vol. 7, no. 12, Dec. 2015, doi: 10.1177/1687814015622596.

[49] F. J. W. Whipple, "Stability of the motion of a bicycle," *Quarterly Pure Applied Mathematics*, vol. 30, pp. 312–384, 1899.

[50] J. P. Meijaard, J. M. Papadopoulos, A. Ruina, and A. L. Schwab, "Linearized dynamics equations for the balance and steer of a bicycle: A benchmark and review," Aug. 08, 2007, *Royal Society*. doi: 10.1098/rspa.2007.1857.

[51] F. Klinger, J. Nusime, J. Edelmann, and M. Plöchl, "Wobble of a racing bicycle with a rider hands on and hands off the handlebar," *Vehicle System Dynamics*, vol. 52, no. SUPPL. 1, pp. 51–68, 2014, doi: 10.1080/00423114.2013.877592.

[52] M. Plöchl, J. Edelmann, B. Angrosch, and C. Ott, "On the wobble mode of a bicycle," *Vehicle System Dynamics*, vol. 50, no. 3, pp. 415–429, Mar. 2012, doi: 10.1080/00423114.2011.594164.

[53] G. Dell'Orto, F. M. Ballo, G. Mastinu, M. Gobbi, and G. Magnani, "Racing bicycle tyres: experimental indoor evaluation of relaxation length," *Meccanica*, 2023, doi: 10.1007/s11012-023-01684-z.

[54] G. Dell'Orto, L. Alizadehsaravi, R. Happee, and J. K. Moore, "Kick-plate test for assessing bicycle dynamics and tyre effect," in *11th International Cycling Safety*

Conference, The Hague, The Netherlands: SWOV Institute for Road Safety Research, Nov. 2023.

[55] A. E. Dressel, "Measuring and Modeling the Mechanical Properties of Bicycle Tires," PhD Thesis, University of Wisconsin-Milwaukee, 2013. [Online]. Available: https://dc.uwm.edu/etd/386

[56] O. Maier, S. Hillenbrand, J. Wrede, A. Freund, and F. Gauterin, "Vertical and Longitudinal Characteristics of a Bicycle Tire," 2018.

[57] R. Douglas Roland and James P. Lynch, "Bicycle Dynamics Tire Characteristics and Rider Modeling," 1972.

[58] B. Souh, "Influence of tire side forces on bicycle self-stability," *Journal of Mechanical Science and Technology*, vol. 29, no. 8, pp. 3131–3140, 2015, doi: 10.1007/s12206-015-0711-z.

[59] M. Miller, M. Pfeil, B. Reick, R. Murri, R. Stetter, and R. Kennel, "Measurement and Modeling of a Cargo Bicycle Tire for Vehicle Dynamics Simulation," *Applied Sciences*, vol. 13, no. 4, p. 2542, Feb. 2023, doi: 10.3390/app13042542.

[60] A. Doria, M. Tognazzo, G. Cusimano, V. Bulsink, A. Cooke, and B. Koopman, "Identification of the mechanical properties of bicycle tyres for modelling of bicycle dynamics," *Vehicle System Dynamics*, vol. 51, no. 3, pp. 405–420, Mar. 2013, doi: 10.1080/00423114.2012.754048.

[61] H. B. Pacejka and E. Bakker, "The magic formula tyre model," *Vehicle System Dynamics*, vol. 21, no. sup1, pp. 1–18, Jan. 1992, doi: 10.1080/00423119208969994.

[62] G. Dell'Orto, F. M. Ballo, and G. Mastinu, "Experimental methods to measure the lateral characteristics of bicycle tyres – a review," *Vehicle System Dynamics*, pp. 1–23, Nov. 2022, doi: 10.1080/00423114.2022.2144388.

[63] G. Dell'Orto, F. M. Ballo, G. Mastinu, M. Gobbi, and G. Magnani, "Racing bicycle tyres – Influence on mechanical characteristics of internal pressure, vertical force, speed and temperature," *European Journal of Mechanics, A/Solids*, vol. 100, Jul. 2023, doi: 10.1016/j.euromechsol.2023.105010.

[64] G. Dell'Orto and G. Mastinu, "Effect of temperature on the mechanical characteristics of bicycle tyres," in *International Cycling Safety Conference 2022*, Dresden, 2022.

[65] G. Dell'Orto, F. M. Ballo, M. Gobbi, and G. Mastinu, "Twisting torque – A simplified theoretical model for bicycle tyres," *Measurement*, vol. 221, p. 113460, Nov. 2023, doi: 10.1016/j.measurement.2023.113460.

[66] G. Dell'Orto, G. Mastinu, R. Happee, and J. K. Moore, "Measurement of the lateral characteristics and identification of the Magic Formula parameters of city

and cargo bicycle tyres," *Vehicle System Dynamics*, pp. 1–26, 2024, doi: 10.1080/00423114.2024.2338143.

[67] European Commission, "EU economy and society to meet climate ambitions," *EU economy and society to meet climate ambitions*, no. July, 2021.

[68] European Commission, "Traffic Safety Basic Facts on Cyclists," no. June, p. 24, 2018.

[69] European Cyclists' Federation, "CYCLING BEYOND THE CRISIS: COVID-19 measures tracker," *European Cyclists' Federation*, p. 516256, 2020.

[70] "The Recovery and Resilience Facility – Joint ECF and CIE recommendations for the national recovery and resilience," no. October, 2020.

[71] Deloitte's TMT, "Technology, Media, and Telecommunications Predictions 2020," 2020.

[72] P. Liu and S. Marker, "Evaluation of contributory factors' effects on bicycle-car crash risk at signalized intersections," *Journal of Transportation Safety and Security*, vol. 12, no. 1, pp. 82–93, 2020, doi: 10.1080/19439962.2019.1591555.

[73] J. Tempia, M. Jiang, H. Sato, G. Mothafer, and T. Yamamoto, "Risk Factor Analysis of Bicycle Accidents Considering Geometric Features and Bicycle Road at Intersections," *Proceedings of the City Planning Institute of Japan, Chubu Branch*, vol. 31, pp. 31–36, 2020, doi: 10.11361/cpijchubu.31.0_31.

[74] P. Skoczyński, "Analysis of solutions improving safety of cyclists in the road traffic," *Applied Sciences (Switzerland)*, vol. 11, no. 9, 2021, doi: 10.3390/app11093771.

[75] A. D. Rostami, A. Katthe, A. Sohrabi, and A. Jahangiri, "Predicting critical bicycle-vehicle conflicts at signalized intersections," *J Adv Transp*, vol. 2020, 2020, doi: 10.1155/2020/8816616.

[76] M. Hamer, "Brimstone and bicycles," New Scientist, 2005, ch. issue 2428, pp. 48–49.

[77] A. Livesey, *Bicycle Engineering and Technology*. Routledge, 2020. doi: 10.1201/9780367816841.

[78] S. Evangelou, M. D. J. N. Limebeer, and M. T. Rodriguez, "Influence of road camber on motorcycle stability," *Journal of Applied Mechanics, Transactions ASME*, vol. 75, no. 6, pp. 0610201–06102012, 2008, doi: 10.1115/1.2937140.

[79] R. Lot and M. Massaro, "A Combined Model of Tire and Road Surface for the Dynamic Analysis of Motorcycles Handling," no. 14, 2006.

[80] A. Doria, E. Marconi, L. Munoz, A. Polanco, and D. Suarez, "An experimental-numerical method for the prediction of on-road comfort of city bicycles," *Vehicle System Dynamics*, 2020, doi: 10.1080/00423114.2020.1759810.

[81] MSC Software, “Introducing Adams/Tire”.

[82] G. P. Starr, “ADAMS Guide,” no. February, pp. 1–46, 2010.

[83] D. J. N. Limebeer and R. S. Sharp, “Bicycles, Motorcycles, and Models,” vol. 26, no. 5, pp. 34–61, 2006, doi: 10.1109/MCS.2006.1700044.

[84] Y. Wei, C. Oertel, X. Li, and L. Yu, “A theoretical model for the tread slip and the effective rolling radius of the tyres in free rolling,” *Proceedings of the Institution of Mechanical Engineers, Part D: Journal of Automobile Engineering*, vol. 231, no. 11, pp. 1461–1470, 2017, doi: 10.1177/0954407016675227.

[85] M. G. Pottinger, “The Pneumatic Tire,” 2006, *US Department of Transportation*.

[86] A. Dressel and J. Sadauckas, “Characterization and modelling of various sized mountain bike tires and the effects of tire tread knobs and inflation pressure,” *Applied Sciences (Switzerland)*, vol. 10, no. 9, May 2020, doi: 10.3390/app10093156.

[87] N. Baltus, “Literature research About bicycle tyre measurements and tyre models,” Literature Research for MSc. Thesis, Delft University of Technology , 2019.

[88] N. Baltus, “About the mechanical properties of bicycle tyres,” MSc. Thesis, Delft University of Technology, 2019.

[89] Y. H. K. D. J. Cole, “Prediction of vehicle stability using a ‘“back to back”’ tyre test method,” 2011, *International Journal of Vehicle Design*.

[90] M. Smurra and F. Spinella, “Advanced testing of bicycle tyres,” MSc. Thesis, Politecnico di Milano, 2018.

[91] E. Bakker, L. Nyborg, and H. B. Pacejka, “Tyre modelling for use in vehicle dynamics studies,” *SAE Technical Papers*, pp. 10–11, 1987, doi: 10.4271/870421.

[92] B. G. Joseph, M. Archibald, and P. Windes, “Experimental Testing for the Cornering Stiffnesses of Bike Tires,” 2012, *Proceedings of the 2012 ASEE North-Central Section Conference*.

[93] P. Windes, M. Archibald, and B. Joseph, “Experimental Determination of Bike Tire Stiffnesses,” 2013, *Proceedings of the 2013 ASEE North-Central Section Conference*.

[94] V. Cossalter, A. Doria, R. Lot, N. Ruffo, and M. Salvador, “Dynamic properties of motorcycle and scooter tires: Measurement and comparison,” *Vehicle System Dynamics*, vol. 39, no. 5, pp. 329–352, May 2003, doi: 10.1076/vesd.39.5.329.14145.

[95] V. Cossalter, A. Doria, R. Lot, N. Ruffo, and M. Salvador, “Dynamic properties of motorcycle and scooter tires: Measurement and comparison,” *Vehicle System Dynamics*, vol. 39, no. 5, pp. 329–352, May 2003, doi: 10.1076/vesd.39.5.329.14145.

[96] A. Dressel and A. Rahman, "Measuring sideslip and camber characteristics of bicycle tyres," in *Vehicle System Dynamics*, Aug. 2012, pp. 1365–1378. doi: 10.1080/00423114.2011.615408.

[97] H. B. Pacejka and I. J. M. Besselink, "Magic Formula tyre model with transient properties," 1997. doi: 10.1080/00423119708969658.

[98] O. Maier, S. Hillenbrand, J. Wrede, A. Freund, and F. Gauterin, "Vertical and Longitudinal Characteristics of a Bicycle Tire," *Tire Science and Technology, TSTCA*, vol. 46, no. 3, pp. 153–173, 2018, doi: https://doi.org/10.2346/tire.18.460301.

[99] G. Mastinu, M. Gobbi, G. Previati, G. Magnani, and F. Ballo, "Measurement of forces and moments of bicycle tyres," *Bicycle and Motorcycle Dynamics 2019 Symposium on the Dynamics and Control of Single Track Vehicles, 9 – 11 September 2019, University of Padova, Italy*, vol. 51, no. 3, pp. 405–420, 2019, doi: 10.1080/00423114.2012.754048.

[100] G. Dell'Orto, F. M. Ballo, G. Mastinu, and M. Gobbi, "Bicycle tyres – Development of a new test-rig to measure mechanical characteristics," *Measurement*, vol. 202, p. 111813, Oct. 2022, doi: 10.1016/J.MEASUREMENT.2022.111813.

[101] G. Mastinu, M. Pennati, and M. Gobbi, "Design and construction of a test rig for assessing tyre characteristics at rollover," *SAE Technical Papers*, no. 724, 2002, doi: 10.4271/2002-01-2077.

[102] L. Uslenghi and L. Vaccari, "Indoor testing of cycling tyres and quality assurance of 'Vetyt' test rig," MSc. Thesis, Politecnico di Milano, 2021.

[103] F. P. Crinò, "Measuring and identifying the mechanical properties of bicycle tyres," MSc. Thesis, Politecnico di Milano, 2021.

[104] A. Lattuada, G. Mastinu, and G. Matrascia, *Straight Motion of Road Vehicles*. 2020. doi: 10.4271/9781468601312.

[105] UN Members, "The Paris agreement," in *COP 21*, 2015. doi: 10.4324/9789276082569-2.

[106] A. Tsakalidis *et al.*, *Indicators for monitoring the Strategic Transport Research and Innovation Agenda*. 2020. doi: 10.2760/802211.

[107] J. Gao *et al.*, "Cycling comfort on asphalt pavement: Influence of the pavement-tyre interface on vibration," *J Clean Prod*, vol. 223, pp. 323–341, Jun. 2019, doi: 10.1016/j.jclepro.2019.03.153.

[108] J. Gao, A. Sha, Y. Huang, L. Hu, Z. Tong, and W. Jiang, "Evaluating the cycling comfort on urban roads based on cyclists' perception of vibration," *J Clean Prod*, vol. 192, pp. 531–541, Aug. 2018, doi: 10.1016/j.jclepro.2018.04.275.

[109] T. S. Fisher, P. Healthcare, G. J. Malppan, and T. Sunny, "A Review on Design Developments in Bicycle," *International Research Journal of Engineering and Technology*, 2015, [Online]. Available: www.irjet.net

[110] G. Dell'Orto, F. Ballo, and G. Mastinu, "Experimental methods to measure the lateral characteristics of bicycle tyres – a review," pp. 1–18.

[111] H. Unrau and J. Zamow, "TYDEX-Format Manual Release 1.3," *Description and Reference Manual*, pp. 1–55, 1997, [Online]. Available: http://scholar.google.com/scholar?hl=en&btnG=Search&q=intitle:TYDEX-Format#2

[112] L. I. U. Xi and L. I. U. Fang-gang, "Tire dynamics research Application based on ADAMS / Tire," no. 5, pp. 365–368, 2014.

[113] "Standard Test Method for Apparent Shear Strength of Single-Lap-Joint Adhesively Bonded Metal Specimens by Tension Loading (Metal-to-Metal)," *ASTM International*, vol. 01, no. D1002-10, pp. 1–5, 2019, doi: 10.1520/D1002-10R19.1.2.

[114] MTS Systems Corporation, "MTS Landmark Testing Solutions," 2019.

[115] P. T. M. SpA, "Poly-V Belts and Pulleys."

[116] Y. A. Çengel, *Introduction to Thermodynamics and Heat Transfer*, vol. Second Edi. 2019. doi: 10.1007/978-3-030-05105-1_2.

[117] Joint Committee For Guides In Metrology, "Evaluation of measurement data — Guide to the expression of uncertainty in measurement," *International Organization for Standardization Geneva ISBN*, vol. 50, no. September, p. 134, 2008.

[118] I. Farrance and R. Frenkel, "Uncertainty of Measurement: A Review of the Rules for Calculating Uncertainty Components through Functional Relationships," *Clin Biochem Rev*, vol. 33, no. 2, pp. 49–75, May 2012.

[119] F. P. Bowden and L. Leben, "The Friction of Lubricated Metals," *Mathematical and Physical Sciences*, vol. 239, no. 799, pp. 1–27, 1940, doi: 10.2307/j.ctt211qv60.7.

[120] R. J. M. Pijpers and H. M. Slot, "Friction coefficients for steel to steel contact surfaces in air and seawater," *J Phys Conf Ser*, 2020, doi: 10.1088/1742-6596/1669/1/012002.

[121] J. H. M. Brooks, R. Tingay, and J. Varney, "Social distancing and COVID-19: An unprecedented active transport public health opportunity," Apr. 01, 2021, *BMJ Publishing Group*. doi: 10.1136/bjsports-2020-102856.

[122] Y. Yang, X. Wu, P. Zhou, Z. Gou, and Y. Lu, "Towards a cycling-friendly city: An updated review of the associations between built environment and cycling behaviors (2007–2017)," *J Transp Health*, vol. 14, Sep. 2019, doi: 10.1016/j.jth.2019.100613.

[123] M. Corno, G. Panzani, E. Catenaro, and S. M. Savaresi, "Modeling and analysis of a bicycle equipped with in-wheel suspensions," *Mech Syst Signal Process*, vol. 155, Jun. 2021, doi: 10.1016/j.ymssp.2020.107548.

[124] S. W. Kresie, J. K. Moore, M. Hubbard, and R. A. Hess, "Experimental Validation of Bicycle Handling Prediction," in *6th Annual International Cycling Safety Conference*, Davis, California, USA, 2017. [Online]. Available: http://creativecommons.org/licenses/by/4.0/.1

[125] R. Hess, J. K. Moore, and M. Hubbard, "Modeling the manually controlled bicycle," *IEEE Transactions on Systems, Man, and Cybernetics Part A:Systems and Humans*, vol. 42, no. 3, pp. 545–557, May 2012, doi: 10.1109/TSMCA.2011.2164244.

[126] S. Evangelou, "The Control and Stability analysis of Two–Wheeled Road Vehicles," Dissertation, University of London, London, 2003. [Online]. Available: http://www3.ic.ac.uk/pls/portallive/docs/1/50172.PDF

[127] A. Swami, C. Liu, J. Kubenz, G. Prokop, and A. K. Pandey, "Experimental Study on Tire Contact Patch Characteristics for Vehicle Handling with Enhanced Optical Measuring System," *SAE Int J Veh Dyn Stab NVH*, vol. 5, no. 3, Apr. 2021, doi: 10.4271/10-05-03-0023.

[128] A. Carahalios, "An Analysis of the Bicycle-Rider Interface Forces in Stationary Road Cycling," *University of Portland*, no. July, p. 15275, 2015.

[129] F. Berto, "All About Tire Inflation," 2006.

[130] SAE International, "Surface vehicle information report," *J2047*, pp. 1–96, 2019.

[131] J. Heine, "Optimizing Your Tire Pressure for Your Weight," *Bicycle Quarterly*, vol. 5, no. 4, pp. 1–2, 2006.

[132] J. Phromjan and C. Suvanjumrat, "The Contact Patch Analysis of Solid Tire on Drum Testing by Finite Element Method," *IOP Conf Ser Mater Sci Eng*, vol. 886, no. 1, 2020, doi: 10.1088/1757-899X/886/1/012049.

[133] C. A. Schneider, W. S. Rasband, and K. W. Eliceiri, "NIH Image to ImageJ: 25 years of image analysis," *Nat Methods*, vol. 9, no. 7, pp. 671–675, 2012, doi: 10.1038/nmeth.2089.

[134] M. D. Abràmoff, P. J. Magalhães, and S. J. Ram, "Image processing with imageJ," *Biophotonics International*, vol. 11, no. 7, pp. 36–41, 2004, doi: 10.1201/9781420005615.ax4.

[135] F. Farroni, N. Mancinelli, and F. Timpone, "A real-time thermal model for the analysis of tire/road interaction in motorcycle applications," *Applied Sciences (Switzerland)*, vol. 10, no. 5, 2020, doi: 10.3390/app10051604.

[136] F. Farroni, D. Giordano, M. Russo, and F. Timpone, "TRT: Thermo racing tyre a physical model to predict the tyre temperature distribution," *Meccanica*, vol. 48, no. 3, pp. 707–723, 2014, doi: 10.1007/s11012-013-9821-9.

[137] J. S. Loeb, D. A. Guenther, H. H. F. Chen, and J. R. Ellis, "Lateral stiffness, cornering stiffness and relaxation length of the pneumatic tire," *SAE Technical Papers*, vol. 99, pp. 147–155, 1990, doi: 10.4271/900129.

[138] A. L. Schwab and J. P. Meijaard, "A review on bicycle dynamics and rider control," *Vehicle System Dynamics*, vol. 51, no. 7, pp. 1059–1090, Jul. 2013, doi: 10.1080/00423114.2013.793365.

[139] V. Cossalter, R. Lot, and F. Maggio, "The Modal Analysis of a Motorcycle in Straight Running and on a Curve," *Meccanica*, vol. 39, no. 1, pp. 1–16, Feb. 2004, doi: 10.1023/A:1026269926222.

[140] K. Guo, D. Lu, and H. Wu, "Tire Dynamics Collaborative Development Strategy," *Chinese Journal of Engineering Science*, vol. 20, no. 1, p. 91, 2018, doi: 10.15302/j-sscae-2018.01.013.

[141] D. Lu, L. Lu, H. Wu, W. Wang, and M. Lv, "Tire Dynamics Modeling Method Based on Rapid Test Method," *Chinese Journal of Mechanical Engineering (English Edition)*, vol. 33, no. 1, 2020, doi: 10.1186/s10033-020-00513-8.

[142] V. Cossalter, A. Doria, E. Giolo, L. Taraborrelli, and M. Massaro, "Identification of the characteristics of motorcycle and scooter tyres in the presence of large variations in inflation pressure," *Vehicle System Dynamics*, vol. 52, no. 10, pp. 1333–1354, 2014, doi: 10.1080/00423114.2014.940981.

[143] J. K. Moore, M. Hubbard, A. L. Schwab, and J. D. G. Kooijman, "Accurate Measurement of Bicycle Parameters," *Bicycle and Motorcycle Dynamics: Symposium on the Dynamics and Control of Single Track Vehicles*, no. October, pp. 20–22, 2010.

[144] R. T. Uil, A. J. C. Schmeitz, I. J. M. Besselink, and H. Nijmeijer, "Non-lagging effect of motorcycle tyres - An experimental study with the Flat Plank Tyre Tester," *Eindhoven University of Technology, Department of Mechanical Engineering*, 2006.

[145] F. Bucchi, F. Cerù, and F. Frendo, "Stability analysis of a novel four-wheeled motorcycle in straight running," *Meccanica*, vol. 52, no. 11–12, pp. 2603–2613, Sep. 2017, doi: 10.1007/s11012-017-0645-x.

[146] V. Cossalter, R. Lot, and M. Massaro, "An advanced multibody code for handling and stability analysis of motorcycles," *Meccanica*, vol. 46, no. 5, pp. 943–958, Oct. 2011, doi: 10.1007/s11012-010-9351-7.

[147] A. Doria and L. Taraborrelli, "Out-of-plane vibrations and relaxation length of the tyres for single-track vehicles," *Proceedings of the Institution of Mechanical*

Engineers, Part D: Journal of Automobile Engineering, vol. 230, no. 5, pp. 609–622, 2016, doi: 10.1177/0954407015590703.

[148] I. J. M. Besselink, A. J. C. Schmeitz, and H. B. Pacejka, "An improved Magic Formula/Swift tyre model that can handle inflation pressure changes," *Vehicle System Dynamics*, vol. 48, no. SUPPL. 1, pp. 337–352, 2010, doi: 10.1080/00423111003748088.

[149] F. Klinger, J. Nusime, J. Edelmann, and M. Plöchl, "Wobble of a racing bicycle with a rider hands on and hands off the handlebar," in *Vehicle System Dynamics*, Taylor and Francis Ltd., May 2014, pp. 51–68. doi: 10.1080/00423114.2013.877592.

[150] S. Roa, A. Doria, and L. Muñoz, "Optimization of the Bicycle Weave and Wobble Modes," in *ASME 2018 International Design Engineering Technical Conferences & Computers and Information in Engineering Conference IDETC*, Quebec City, Canada, Aug. 2018. doi: 10.1115/DETC2018-86132.

[151] M. Gobbi, G. Mastinu, and M. Pennati, "Indoor testing of road vehicle suspensions," *Meccanica*, vol. 43, no. 2, pp. 173–184, 2008, doi: 10.1007/s11012-008-9119-5.

[152] M. Mitschke and H. Wallentowitz, *Dynamik der Kraftfahrzeuge*. Springer Fachmedien Wiesbaden, 2014. doi: 10.1007/978-3-658-05068-9.

[153] E. Bakker, H. B. Pacejka, and L. Lidner, "A new tire model with an application in vehicle dynamics studies," *SAE Technical Papers*, vol. 98, pp. 101–113, 1989, doi: 10.4271/890087.

[154] A. G. Asuero, A. Sayago, and A. G. González, "The correlation coefficient: An overview," *Crit Rev Anal Chem*, vol. 36, no. 1, pp. 41–59, 2006, doi: 10.1080/10408340500526766.

[155] M. Gobbi, F. Giorgetta, P. Guarneri, G. Rocca, and G. Mastinu, "Experimental Study and Numerical Modeling of the Dynamic Behaviour of Tyre/Suspension While Running Over an Obstacle," in *ASME 2006 International Mechanical Engineering Congress and Exposition*, 2006, pp. 195–204.

[156] A. Ari *et al.*, "Surging Energy Prices in Europe in the Aftermath of the War: How to Support the Vulnerable and Speed up the Transition Away from Fossil Fuels," 2022.

[157] O. V. Casas, R. Dalazen, and A. Balbinot, "3D load cell for measure force in a bicycle crank," *Measurement (Lond)*, vol. 93, pp. 189–201, Nov. 2016, doi: 10.1016/j.measurement.2016.07.031.

[158] M. Ambrož, "Raspberry Pi as a low-cost data acquisition system for human powered vehicles," *Measurement (Lond)*, vol. 100, pp. 7–18, Mar. 2017, doi: 10.1016/j.measurement.2016.12.037.

[159] C. A. Manrique-Escobar, C. M. Pappalardo, and D. Guida, "On the Analytical and Computational Methodologies for Modelling Two-wheeled Vehicles within the Multibody Dynamics Framework: A Systematic Literature Review," *Journal of Applied and Computational Mechanics*, vol. 8, no. 1, pp. 153–181, Jan. 2022, doi: 10.22055/jacm.2021.37935.3118.

[160] M. Gobbi, G. Mastinu, F. Comolli, F. Ballo, and G. Previati, "Motorcycle smart wheels for monitoring purposes," *Bycicle and Motorcycle Dynamics*, no. September, pp. 9–11, 2019.

[161] M. Bartolozzi, G. Savino, and M. Pierini, "Novel high-fidelity tyre model for motorcycles to be characterised by quasi-static manoeuvres–rationale and numerical validation," *Vehicle System Dynamics*, vol. 60, no. 12, pp. 4290–4316, 2022, doi: 10.1080/00423114.2021.2013506.

[162] V. Cossalter and A. Doria, "The relation between contact patch geometry and the mechanical properties of motorcycle tyres," *Vehicle System Dynamics*, vol. 43, no. SUPPL., pp. 156–164, 2005, doi: 10.1080/00423110500141045.

[163] M. Massaro, V. Cossalter, and G. Cusimano, "The effect of the inflation pressure on the tyre properties and the motorcycle stability," *Proceedings of the Institution of Mechanical Engineers, Part D: Journal of Automobile Engineering*, vol. 227, no. 10, pp. 1480–1488, 2013, doi: 10.1177/0954407013496231.

[164] R. Lot, "A Motorcycle Tire Model for Dynamic Simulations: Theoretical and Experimental Aspects," *Meccanica*, vol. 39, no. 3, pp. 207–220, Jun. 2004, doi: 10.1023/B:MECC.0000022842.12077.5c.

[165] V. Cossalter, A. Doria, and R. Lot, "Steady Turning of Two-Wheeled Vehicles," *Vehicle System Dynamics*, vol. 31, no. 3, pp. 157–181, 1999, doi: 10.1076/vesd.31.3.157.2013.

[166] S. Derafshpour, M. Valizadeh, A. Mardani, and M. Tamaddoni Saray, "A novel system developed based on image processing techniques for dynamical measurement of tire-surface contact area," *Measurement (Lond)*, vol. 139, pp. 270–276, Jun. 2019, doi: 10.1016/j.measurement.2019.02.074.

[167] C. Zhang, W. Zhao, W. Wang, and J. Zhang, "Vision-based tire deformation and vehicle-bridge contact force measurement," *Measurement (Lond)*, vol. 183, Oct. 2021, doi: 10.1016/j.measurement.2021.109792.

[168] G. Mastinu and M. Fainello, "Study of the Pneumatic Tyre Behaviour on Dry and Rigid Road by Finite Element Method," *Vehicle System Dynamics*, vol. 21, no. 3, pp. 143–165, 1992.

[169] J. P. Pauwelussen, "Chapter Two - Fundamentals of Tire Behavior," in *Essentials of Vehicle Dynamics*, J. P. Pauwelussen, Ed., Oxford: Butterworth-Heinemann, 2015, pp. 7–74. doi: https://doi.org/10.1016/B978-0-08-100036-6.00002-9.

[170] M. Hubbard, J. K. Moore, R. Gilboa, A. Kubicki, A. Toribio, and J. K. Moore, "Practical Realization of a Theoretical Optimal-Handling Bicycle," 2019, doi: 10.6084/m9.figshare.9883328.v1.

[171] M. Blundell and D. Harty, "Tyre Characteristics and Modelling," in *The Multibody Systems Approach to Vehicle Dynamics*, Elsevier, 2015, pp. 335–450. doi: 10.1016/b978-0-08-099425-3.00005-4.

[172] B. Sankar Mohanta and A. Kumar, "A parametric analysis on the performance of vehicle tires," *Mater Today Proc*, 2022, doi: 10.1016/j.matpr.2021.03.167.

[173] N. Chicu, A.-L. Prioteasa, and A. Deaconu, "Current Trends and Perspectives in Tyre Industry," *Studia Universitatis „Vasile Goldis" Arad – Economics Series*, vol. 30, no. 2, pp. 36–56, Jun. 2020, doi: 10.2478/sues-2020-0011.

[174] I. M. Kalsbeek, "Experimental investigation into the shimmy motion of the bicycle for improving model-based shimmy estimations," 2016.

[175] L. Caggiani, A. Colovic, L. P. Prencipe, and M. Ottomanelli, "A green logistics solution for last-mile deliveries considering e-vans and e-cargo bikes," in *Transportation Research Procedia*, Elsevier B.V., 2021, pp. 75–82. doi: 10.1016/j.trpro.2021.01.010.

[176] C. Llorca and R. Moeckel, "Assesment of the potential of cargo bikes and electrification for last-mile parcel delivery by means of simulation of urban freight flows," *European Transport Research Review*, vol. 13, no. 1, Dec. 2021, doi: 10.1186/s12544-021-00491-5.

[177] G. Dell'orto, F. M. Ballo, G. Mastinu, R. Happee, and J. K. Moore, "Indoor measurement of the lateral characteristics of a cargo bicycle tyre," in *Bicycle and Motorcycle Dynamics 2023*, 2023. doi: 10.24404/644ba1e13c57633bb23a9dc6.

[178] "Babboe Carve - Tilting cargo bicycle." Accessed: Jun. 20, 2023. [Online]. Available: https://www.babboe.nl/

[179] G. Dell'Orto, J. K. Moore, G. Mastinu, and R. Happee, "Bicycle Tyre Data - Lateral Characteristics," Apr. 2023, doi: 10.5281/ZENODO.7866646.

[180] F. Farroni, G. N. Dell'annunziata, M. Ruffini, G. Mastinu, and G. Dell'orto, "Thermal model for bicycle tire internal temperature evaluation in various contact conditions," *The Evolving Scholar*, vol. 3, 2023, Accessed: Feb. 24, 2024. [Online]. Available: https://doi.org/10.59490/650dd6a3744cc87c1adcd283

[181] T. M. Inc., "MATLAB version 9.10.0.1684407 (R2021a) Update 3," 2021, *Natick, Massachusetts*.

[182] Ralf Bohle GmbH, "Schwalbe GmbH, 'Products.'" Accessed: Jun. 08, 2023. [Online]. Available: https://www.schwalbe.com/en/city-tour

[183] "CHENG SHIN RUBBER (XIAMEN) IND., LTD.," 2023. Accessed: Jun. 09, 2023. [Online]. Available: https://www.csttires.com/int/tire/brooklyn-pro-c1996/

[184] M. Blundell and D. Harty, "Tyre Characteristics and Modelling," in *The Multibody Systems Approach to Vehicle Dynamics*, Elsevier, 2015, pp. 335–450. doi: 10.1016/b978-0-08-099425-3.00005-4.

[185] G. Mastinu and E. Pairana, "Parameter identification and validation of a pneumatic tyre model," *Vehicle System Dynamics*, vol. 21, no. sup1, pp. 58–81, Jan. 1992, doi: 10.1080/00423119208969999.

[186] G. Dell'Orto, J. K. Moore, G. Mastinu, and R. Happee, "Magic Formula Parameters - Bicycle Tyres," May 2023, doi: 10.5281/ZENODO.7920415.

[187] G. Dell'Orto, "Magic Formula 89," https://github.com/mechmotum/Magic-Formula-89.

[188] "ETRTO - European Tyre and Rim Technical Organisation", Accessed: Jun. 21, 2023. [Online]. Available: https://www.etrto.org/home

[189] J. K. Moore, M. Hubbard, R. Hess, J. K. Moore, and R. A. Hess, "An Optimal Handling Bicycle", doi: 10.6084/M9.FIGSHARE.3806310.V1.

[190] M. Gobbi, F. Comolli, M. Hada, and G. Mastinu, "An instrumented steering wheel for driver model development," Dec. 01, 2019, *Elsevier Ltd*. doi: 10.1016/j.mechatronics.2019.102285.

[191] A. Doria, S. Roa, and L. Muñoz, "Stability analysis of bicycles by means of analytical models with increasing complexity," *Mechanical Sciences*, vol. 10, no. 1, pp. 229–241, Jun. 2019, doi: 10.5194/ms-10-229-2019.

[192] L. Alizadehsaravi and J. K. Moore, "Bicycle balance assist system reduces roll motion for young and old bicyclists during real-life safety challenges," 2023.

[193] G. A. Douglas and J. M. Bland, "Standard deviations and standard errors," *BMJ: British Medial Journal*, vol. 331, no. 903, 2005, doi: https://doi.org/10.1136/bmj.331.7521.903.

[194] L. B. Magalas and T. Malinowski, "Measurement techniques of the logarithmic decrement," in *Solid State Phenomena*, Trans Tech Publications Ltd, 2003, pp. 247–260. doi: 10.4028/www.scientific.net/ssp.89.247.

[195] J. K. Moore, "Bicycle Steer Control Github repo."

[196] J. K. Moore and G. Dell'Orto, "Bicycle Kickplate Model," Github.

[197] M. Rothhamel, "Measuring vertical tyre stiffness of bicycle tyres," in *The Evolving Scholar - BMD, 5th edition*, 2023. doi: https://doi.org/10.24404/63fd130ddf639dbecb55e672.

[198] C. Dembia, J. K. Moore, and M. Hubbard, "An object oriented implementation of the Yeadon human inertia model," *F1000Res*, vol. 3, pp. 1–15, 2015, doi: 10.12688/f1000research.5292.2.

[199] M. Plöchl and J. Edelmann, "Driver models in automobile dynamics application," *User Model User-adapt Interact*, vol. 45, no. 7–8, pp. 699–741, 2007, doi: 10.1080/00423110701432482.

List of publications

Journal papers

1. G. Dell'Orto, G. Mastinu, R. Happee, J.K. Moore, "Measurement of the lateral characteristics and identification of the Magic Formula parameters of city and cargo bicycle tyres," Vehicle System Dynamics, pp. 1–25, March 2024, https://doi.org/10.1080/00423114.2024.2338143
2. G. Dell'Orto, F. M. Ballo, G. Mastinu, M. Gobbi, and G. Magnani, "Racing bicycle tyres: experimental indoor evaluation of relaxation length," Meccanica, 2023, https://doi.org/10.1007/s11012-023-01684-z
3. G. Dell'Orto, F. M. Ballo, M. Gobbi, and G. Mastinu, "Twisting torque – A simplified theoretical model for bicycle tyres," Measurement, vol. 221, p. 113460, Nov. 2023, https://doi.org/10.1016/j.measurement.2023.113460
4. G. Dell'Orto, F. M. Ballo, G. Mastinu, M. Gobbi, and G. Magnani, "Racing bicycle tyres – Influence on mechanical characteristics of internal pressure, vertical force, speed and temperature," European Journal of Mechanics, A/Solids, vol. 100, Jul. 2023, https://doi.org/10.1016/j.euromechsol.2023.105010
5. G. Dell'Orto, F. M. Ballo, and G. Mastinu, "Experimental methods to measure the lateral characteristics of bicycle tyres – a review," Vehicle System Dynamics, pp. 1–23, Nov. 2022, https://doi.org/10.1080/00423114.2022.2144388
6. G. Dell'Orto, F. M. Ballo, G. Mastinu, and M. Gobbi, "Bicycle tyres – Development of a new test-rig to measure mechanical characteristics," Measurement (Lond), vol. 202, Oct. 2022, https://doi.org/10.1016/j.measurement.2022.111813

Conference contributions

7. G. Dell'Orto, G. Mastinu, "Indoor Test-Rig to Measure the Lateral Characteristics of Bicycle Tyres,". in Mastinu, G., Braghin, F., Cheli, F., Corno, M., Savaresi, S.M. (eds) 16th International Symposium on Advanced Vehicle Control. AVEC 2024. Lecture Notes in Mechanical Engineering. Springer, Cham. https://doi.org/10.1007/978-3-031-70392-8_128
8. G. Dell'Orto, F. M. Ballo, G. Mastinu, R. Happee, and J. K. Moore, "Indoor measurement of the lateral characteristics of a cargo bicycle tyre," Presentation

and extended abstract in Bicycle and Motorcycle Dynamics 2023, Delft, The Netherlands, October 18-20, 2023, doi: 10.24404/644ba1e13c57633bb23a9dc6

9. G. Dell'Orto, G. Mastinu,. "Bicycle tyres – A new test-rig for indoor tests," Presentation at Tire Technology Expo, Hannover, Germany, March 21-23, 2023.
10. G. Dell'Orto, G. Mastinu, "Performance of Bicycle Tyres. Effect of vertical load and inflation pressure," Poster presentation and extended abstract Science & Cycling, Bilbao, Spain, June 28-29, 2023.
11. G. Dell'Orto, L. Alizadehsaravi, R. Happee, J.K. Moore, "Kick-plate test for assessing bicycle dynamics and tyre effect," Poster presentation and extended abstract at International Cycling Safety Conference 2023, Den Haag, 2023.
12. G. Dell'orto, G. Mastinu, "Effect of temperature on the mechanical characteristics of bicycle tyres", Poster presentation and extended abstract at International Cycling Safety Conference 2022, Dresden, 2022, doi: 10.1080/00423114.2022.2144388
13. G. Dell'orto, G. Mastinu, "Indoor testing of bicycle tyres," Presentation at Eurobike Academy 2022, Frankfurt am Main, Germany, July 14-15, 2022.
14. G. Dell'Orto, "Are you able to ride a bike?," Presentation at EIT Urban Mobility Annual Forum 2021, Munich, Germany.

Online repositories & dataset

15. G Dell'Orto, G. Mastinu, "Dynamic measurements - Lateral characteristics of bicycle tyres," Zenodo, 2023, https://doi.org/10.5281/zenodo.7674873
16. G. Dell'Orto, G. Mastinu, "Static measurements - Lateral stiffness of bicycle tyres," Zenodo, 2023. https://doi.org/10.5281/zenodo.7677000
17. G. Dell'Orto, J.K. Moore, G. Mastinu, R. Happee, "Bicycle Tyre Data - Lateral Characteristics," Zenodo, 2023, https://doi.org/10.5281/zenodo.7866646
18. G. Dell'Orto, J.K. Moore, G. Mastinu, R. Happee, "Magic Formula Parameters - Bicycle Tyres," Zenodo, 2023, https://doi.org/10.5281/zenodo.7920415
19. G. Dell'Orto, "Kickplate test," Zenodo, 2024, https://doi.org/10.5281/zenodo.13890635

Additional online material & Socials

The reader can find further material related to this thesis online. I use professional social media for networking and posting updates. You can explore ResearchGate, LinkedIn or YouTube channel to stay in touch and be up to date on the progress of the research.

1. GitHub project repository for kickplate experiment: https://github.com/mechmotum/bicycle-kickplate-model
2. GitHub: https://github.com/GabrieleDello
3. ResearchGate: https://www.researchgate.net/profile/Gabriele-Dellorto-2
4. LinkedIn: www.linkedin.com/in/dellortogabriele
5. YouTube channel: https://www.youtube.com/@gabrieledellorto5006

Acknowledgments

I did not plan to pursue a PhD journey. It wasn't in my thoughts, I didn't know what a PhD was. At the end of my MSc thesis, I came across PhD offers at Polytechnic of Milan, Italy, just by chance, because I was looking for information for my MSc. thesis submission. I read about the opportunity to delve into the topic of bicycles and tyres, rather unusual I would say. And here we go, presenting and defending my "sweaty papers". It was by far the most engaging (also demanding) experience of my life. I am so proud and happy to have pursued that unknown journey. It wasn't easy at all, especially in the beginning: ups and downs happened on a daily basis, before I found finding my pace. But I would redo everything with no regrets.

I was not the only author of this research. First of all, I want to mention my promotors, Prof. dr. **Riender Happee** and Prof. dr. **Giampiero Mastinu**, along with my daily supervisor in Delft, Dr. **Jason Moore**. We had so many meetings to share and discuss ideas, proposals, and progress. I have learnt a lot, I have grown considerably when I look at myself four years ago. And I have to thank you all. Is it everything? Of course not. I have the pleasure of getting invaluable advice from Dr. **Federico Ballo**, Prof. dr. **Giorgio Previati**, and Prof. dr. **Massimiliano Gobbi**. They were among the first ones to help me with the new environment, rules, and way of thinking. I still remember the effort **Federico** made to correct my first paper draft… oh yes, it was a mess, I know. I could not have acquired writing skills without his feedback. I still have a document "Writing_advice", collecting the tips and advice on writing style. I am grateful for that.

I want to dedicate a special mention to Prof. dr. **Gianantonio Magnani**. He never formally supervised me, but with his wisdom, he helped me a lot in down moments, especially in the first period of the PhD, when it is hard to see any light.

The experimental devices that I have presented in this dissertation could not work without the help of lab technicians. Above all, Dr. **Mario Pennati** and **Dario Crema** eased the long and super-hot summer test days in the workshop. We had a lot of fun, always willing to help and make me laugh. **Mario** is the true soul of the LaST workshop, while **Dario Crema**, the drake of precision machining. I still remember the discussion to reinforce the VeTyT frame: the results I am publishing were also possible thanks to his effort.

And all the students who did the thesis with us. They strongly contribute to the advancement of VeTyT. I wish you all a brilliant career. In chronological order, we have: **Francesco Paolo Crino`**, **Lorenzo Uslenghi**, **Lorenzo Vaccari**, **Matheus Miguel Villa**, **Moaz Helmy Abdulrahman Aly Shaaban**, **Mohamed Ahmed Sanad Sanad Ibrahim**, and **Paolo Restelli**. I also acknowledge the students I had the honour to teach during the last four years, from Vehicle systems and Machine Design courses. I grew with you, I did my best to transmit curiosity and tips for your future career.

Then there are those whose contribution is more difficult to measure. If happiness is a fundamental part of life, they have done a lot to achieve it. My mate and friend **Luca** introduced me to the "Bovisa dark side", or "Bovisa Highlanders". We spent so a lot of fun times together, sharing a flat with six other people. I am still laughing while writing these sentences. I also met a big friend like **Renato**. We went on long and amazing trekking paths together, among others. Under the supervision of **Alessandro**, the "Ritter sketcher". The "Bovisa lovers" group also includes **Pier**, **Alberto** and **Francesco "Kekko"**. Together we shared amazing moments. I acknowledge the nice conversations about good food and whatever else with **Mauro**. It was nice to share the efforts of the university together. Thanks a lot for the last page drawing.

How can I forget Pareto's gang? First of all, **Alessandro Cocco**. Thanks to you I had probably the best and funniest cycling period of my life so far. I was lucky to meet you. Fantastic routes, and fantastic time together. We started riding together, expanding the group ride to include **Alessandro Vescovini** (also thanks for your Delft tips), and **Pietro** among others. I will bring with me our Dolomites experience forever. The rides with Alessandro often ended with Pizza in the evening. **Riccardo**, **Claudio**, and **Michael** also animated some pizza parties.

Well, it is time to write about Delft. Disclaimer: I will forget someone, for sure. The arrival in Delft was made much simpler thanks to my Biomechanical Engineering (BME department) colleagues. Ten days after my landing in Delft, I had the pleasure of being a guest at **Pier**'s birthday party. I knew him very little at the time, but I soon realised that I had met an amazing and wise friend. I am honoured to have him as a paranymph. The initial support of my bicycle lab mates was invaluable: a warm thank you to **Chris**, with **Nora**, **Rado**, **Leila**, **Sam** "the English loco", **Andrew**, **Jason**, with **Yumi**, and everyone who joined the lab. A special thank to **Timo**: he revealed to be a very kind and wise friend, always keen on helping. Another big thanks to my office mates: **Chris**, **Marit**, **Anthon** (still lost in ice bath), **Teddy** (still driving his Ferrari on his way to be my paranymph), **Suzanne**, **Martijn**, **Hassan**, **Emanuele**, and **Bart**. Please consider me a criminal if I don't cite the amazing legends I met in the fishtank: **Mauricio**, **Judith**, **Katerina**, **Chun-Feng**, again **Pier**. You all made my first weeks in Delft much easier.

And this was just the beginning. I still remember the amazing party we had at the PhD outing event. I had the honour of introducing **Teddy**, **Anthon**, **Niko** and others to the ritual of "Sbagliato". I leave the reader the license of googling it. And around a "Sbagliato" and an ice bath we set the team for the PhD sport event.

Somehow, somewhere, someone started to call me "Legend" (**Ebi**?). Again, I leave the reader the freedom to figure out why. Many "Maestro" and "Dottore" were dispensed left and right, especially when I struggled on kickplate or robot bike in the bicycle lab. Here I also spent hours chatting with Adam, who revealed to be an amazing and wise programmer. A coding genius, genuinely. Thanks to **Adam Kewley** I was able to run

many experiments and show results! **Tim Huiskens** was instead the robot bicycle helper, especially during the initial steps. I really appreciated his dedication and time in replying emails and giving valuable guidance.

Thanks also to technicians who helped us realise our "crazy" ideas: **Jan**, **Wouter**, **Hans**, **Spiridon**, and **Andre**.

During the breaks from the screen, I fell in love with walking through aisles and having short talks with whoever was around. Going to the third floor became a sort of ritual: the truly legend **Ebrahim**, **Nassim** (The Queen), **Edwin**, **Vahid** (Happy new year), **Jette**, true soul of the PhD council, and above all the unofficial king of Delft, **Sander Leeflang**. You always had nice explanations to our troubles, as only the legends can do.

It was so funny to spend hours with **Teddy** arguing about everything. He is keen on cycling, tennis, formula 1, airplanes, padel, medical devices, Madrenatura, and so on. One day, we will go together to Lake Como and Ferrari Museum, tasting tons of Mulino Bianco. I was super happy to see you all again at the Biomechanical Engineering conference in June 2024, it was worth the travel from Italy even though someone (**Teddy** or **Ebi**?) is still looking for **Alfredo**. **Ebi** was a perfect roommate, and after that stay I decided to propose him to be my paranymph. Why? Who knows.

I would have more to write, but I have now to conclude. Cooking masterclasses stated the highest peak of fine dining all over the Netherlands. We made amazing home-made pasta, specifically very thin and tasty tagliatelle with Bolognese. **Lennard**, **Jette**, **Monika**, **Nora** and others rolled out very thin tagliatelle. What did I do? Of course, I had to supervise the less skilled chefs, like **Nassim**, **Hassan** and my beloved friend **Ludo**. The result was much over the expectations, and **Judith**, **Monika**, **Teddy** and **Hassan** still remember the post-dinner effect. It was a pleasure to introduce **Nassim** to some difficult cooking preparations. She will remember how to chop (or cut) mozzarella for life.

Everyone was special: the Italians brought the energy everywhere. The spartan **Sara** (but she is actually like a chocolate lava cake), **Ludo** the racer (however she is better in playing football than in driving), **Fede** the wise (certified Rotterdam local guide) and **Bea** the Belgian (true chef) had the effect of an earthquake. You rock. It is impossible not to love them. Your office mates **Daniel**, **Rogier**, **Gavin**, **Alessia**, etc. are very lucky.

Thanks to **Eugenio** for the time spent together. He helped me, and it was very nice to talk about literally everything with him. Even in front of the chessboard. Thanks to my cycling mates at WTOS team, especially **Jonathan**, for the nice talks and rides. The time we had together was insufficient, I am sure we will meet again for some nice rides around the world, next time **Ruben** will also join us. Also nice time spent with Blue Falcons mates: above all, **Andrea** and the half-Belgian **Lex Niessen**.

Can I skip the padel matches? No, of course. We had very nice time on padel courts with **Teddy**, **Giovanni**, **Jules**, **Suzanne**, and **Christoph**. And sometimes we stopped by the bar for a "buonissima" and "bellissima" pizza with the crew. I am truly happy to creating these memories with you.

The time spent with the hermanos **Jose`**, **Vish**, **Giovanni**, **Ebi** and **Mohammad "Momo"** was so funny. I won't forget our Christmas holidays. Unbelievable karaoke, kapsalon and showers. We know that **Jose`** loves having shower (suuutrooo), same for **Gavin**. **Vish** also loves showers and durum. And I love you, hermanos.

I was "invited" to the CoR Christmas party. I sat at the table, hidden among colleagues **Vish**, **Gio**, and **Jules**, when I suddenly hear your voice, **Riender**, asking me "what are you doing here?", repeatedly. What would you do in these situations? We started to laugh loudly. Smart shortcut to skip the answer. LOL.

I am genuinely overwhelmed by nice memories. Nothing would have been possible without the open-minded and smart people I met in Delft. I cannot name everyone who made my stay in Delft special, I could write pages and pages. I am sure that I missed someone, my apologies for that.

A special thanks to my Doctoral Training Network mates. Prof. dr. **Benjamin Büttner**, **Corinna Niederreiter** and **Aaron Nichols** did something great with and for the DTN community. It was so lovely to participate in Annual Forums in Munich, Barcelona, Helsinki, and Ghent. Don't forget Tartu, with the special mates like **Miguel**, **Hannah**, the "lifter" **Mohamed**, **Mauricio**, and so on. I have also to mention **Luis**, **Serio**, **Jaime**, **Enrique**, **Shadi**, **Maria**, **Ahmad**, **Corneel**, **Gabriel**, **Peter**, **Misa**, **Sandra**, with whom I spent most of the time since the first annual forum. It was amazing to meet **Yunfei** and **Siyu** in Milan! We must organise again.

The last months of the PhD journey were made funnier by the strong competition for the podium of Fantacycling. Thank you guys, **Luca**, **Fausto**, **Alessandro**, **Paolo**, **Luigi**, **Daniele**, and **Martina**, for the wonderful moments spent together discussing race strategies and cheering along the roads of Zurich and Como.

Last but not least, I want to thank **Federica** and her family. We met by chance during a Summer School three years ago. She is also the hidden co-author of this dissertation, as she is a "formatting and layout" drake. Kiss kiss.

A big thank you to my family, in particular to my grandfather **Sergio** and my uncles **Paolo** and **Gianmario**. I know you have always trusted in me and cheered (a lot). **Gianmario** is also the artist who created the cover page drawings. Sorry for the misunderstanding, it wasn't me. I am a very bad painter.

You all contributed to the thesis you are reading. Thanks to everyone.

"We are creating memories. This is just the beginning", **Teddy** told me before leaving Delft. I agree, I will never forget it.